Computation of flow and heat transfer in a rotating cavity with peripheral inflow and outflow of cooling-air

Mirzaee, Iraj

Award date:
1997

Awarding institution:
University of Bath

COMPUTATION OF FLOW AND HEAT TRANSFER IN A ROTATING CAVITY WITH PERIPHERAL INFLOW AND OUTFLOW OF COOLING-AIR

submitted by
Iraj MIRZAEE
for the degree of Ph.D.
of the University of Bath
1997

COPYRIGHT

ProQuest LLC
789 East Eisenhower Parkway
P.O. Box 1346
Ann Arbor, MI 48106-1346

Dedicated to my father Haj Hassan Mirzaee

CONTENTS

ACKNOWLEDGEMENTS

I would like to express my gratitude to the many people who helped during the course of my work. Special thanks are due to my supervisor, Professor J.M. Owen for his continued enthusiasm, encouragements, guidance, as well as useful criticism throughout this project. I am indebted to him for all the help and advice that I received.

Many thanks also must go to Dr.M.Wilson for his co-supervison and help during different stages of this work. I would also like to thank Dr.D.A.S. Rees for his help and useful suggestions.

I gratefully acknowledge the receipt of a scholarship from my employer, Urmia University, Urmia, I.R.Iran, without whose financial support this research would not have been possible; also wish to thank BMW-Rolls-Royce for supporting the experimental study described in this study.

Finally, I must admit that without the patience and the sacrifices of my parents and my entire family this study would not have been completed. I am, therefore, grateful to my parents for their continuous and enduring love and support, to my wife (Batool) for all her help and encouragement, to my daughter (Mina) and my son (Reza) for their smiles and tenderness, which brighten our steps into the future.

SUMMARY

This thesis describes a combined numerical and experimental investigation into the flow and heat transfer characteristics in a rotating cavity with peripheral inflow and outflow of cooling air. A rotating cavity fitted with a stationary peripheral shroud is used as a simple model of the turbine rotors in air-cooled gas turbine engines. Investigation is carried out in two cases: peripheral flow with stationary flat and stepped shrouds.

For the numerical study, an axisymmetric elliptic multigrid CFD solver is used to solve for both laminar and turbulent flow. A low Reynolds number $k - \epsilon$ turbulence model is used to close the Reynolds-averaged Navier-Stokes equations. The code included the SIMPLEC pressure-correction scheme for the momentum equation.

For the flow field in the flat-shroud case, the basic flow structure showed two counter-rotating recirculating regions, symmetrical about the axial mid-plane ($z/s = 0.5$). Fluid in the boundary on both discs moved radially outwards, and there was a radial inflow in the core between two discs. For $C_W = 0$ and $Re_\phi = 10^4$, good agreement was obtained between the laminar and the LS turbulence model. Transition occurred at small values of x for $Re_\phi = 1.46$ x 10^5, and turbulent flow occurred in most of the cavity at the higher Reynolds numbers. The predicted tangential component of velocity, using the LS model, tended from a free-vortex-type to a forced vortex distribution prematurely, while in the experiments Rankine vortex flow occurred in most of the cavity. Agreement improved for the superposed flow case with increasing λ_T parameter. In order to improve the agreement between the computed and measured velocities, several modifications were considered in the low-Reynolds number $k - \epsilon$ model: Yap, rotation and Richardson-number corrections. It was found that the Richardson-number correction improves the computed results in comparison with the experimental data. The comparison between the LS model, DNS solution and the experimental data also showed that this type of flow is probably unstable and highly three dimensional.

For the heat transfer in the flat-shroud case, computations were carried out for superposed flow cases. The computed Nusselt numbers for the heated-disc were compared with the experimental data. There was a similar trend between the computed Nu and measurements, and the agreement improved where a radiation correction was included in the computed results.

For the stepped-shroud case, computations were made for three different outlet conditions: $\Gamma = 1, 0$ and $\Gamma \rightarrow \infty$. For each Γ parameter, twenty tests were carried out using the LS model at different values of Re_ϕ and C_W. The computed streamlines showed a complicated flow structure for each case involving a number of recirculating regions. Broadly similar flow structures were obtained for constant values of λ_T. In most of the cases, the computed Nusselt numbers showed a good agreement with the experimental data. It was also concluded that the λ_T parameter is important in the stepped-shroud case. At constant λ_T, computed Nu increases with increasing Re_ϕ and C_W.

Nomenclature

a	inner radius of disc
$a_{P,N,S,E,W}$	coefficients of algebraic equations
b	outer radius of disc
c	inlet swirl ratio ($=V_{\phi,I}/\Omega r$)
c_{eff}	effective swirl ratio
C_{gs}	Richardson number coefficient
C_p	specific heat at constant pressure
C_W	nondimensional mass flow rate ($=\frac{\dot{m}}{\mu b}$)
C_{W1}, C_{W2}	nondimensional mass flow rates in outlets 1 and 2
	respectively for the stepped-shroud configuration
$C_{\mu,\epsilon 1,\epsilon 2}$	constants in the $k-\epsilon$
	turbulence model
Ec	local Eckert number ($=\Omega^2 r^2/C_P\triangle T$)
E, F	source terms in ϵ-equation
f_μ	near-wall damping function
g	gravitational acceleration
G	gap ratio ($=s/b$)
Gr	Grashof number ($=b^4\Omega^2\beta\triangle T/\nu^2$)
h	total enthalpy ($=C_pT+(V_r^2+V_\phi^2+V_z^2)/2)$)
k	turbulent kinetic energy
k_f	thermal conductivity of fluid
$\dot{m}$	mass flow rate

max	maximum value
min	minimum value
Nu	Nusselt number ($=rq/k_f(T_s - T_{ref})$
P	production rate of turbulent kinetic energy
p	static pressure
Pr	Prandtl number ($= \mu C_p/k_e$)
p'	pressure-correction
q	heat flux
r, ϕ, z	radial, tangential and axial directions
Ra	Rayleigh number ($=GrPr$)
RMS^{Φ}	normalized root mean-square for Φ
Ro_T	thermal Rossby number ($=\Delta T/T_o$)
Ro	Rossby number ($=C_W/4\pi Re_\phi^{1/2}$)
R^{Φ}_{sum}	total absolute values of the residuals
R_T	turbulent Reynolds number ($= k^2/\epsilon\nu$)
Re_r	$\lvert C_w\rvert/2\pi x$; radial Reynolds number
Re_ϕ	$\Omega b^2/\nu$; rotational Reynolds number
Ri	Richardson number; ratio of an apparent body force to a typical inertial force
s	axial spacing between discs
S	source term; strain invariant
S_C	linearized part of source term
S_P	non-linearized part of source term
T	fluid temperature

T_{in}	inlet air temperature
T_o	average temperature between two discs
T_s	disc temperature
(V_r, V_ϕ, V_z)	radial, tangential and axial
	velocity components referred to stationary
	cylindrical coordinates (r, ϕ, z)
u_τ	friction velocity $(=\sqrt{\tau_w/\rho})$
x	r/b; nondimensional radial coordinate
y	normal distance from wall
y^+	nondimensional distance $(=u_\tau y/\nu)$
α	thermal diffusivity $(= k_f/\rho C_p)$
α_Φ	under-relaxation parameter
α_G	Gosman factor
α_P	under-relaxation factor for pressure
β	multigrid under-relaxation factor;
	volume expansion coefficient of fluid
ΔT	temperature difference between two discs
Λ	rotation parameter $(=(\Omega - S)^{2/3})$
θ	inlet air angle in the stepped-shroud (see Figure 6.1)
Γ	outlet ratio in the stepped shroud configuration
	$(=C_{W1}/C_{W2})$
$\Gamma_r, \Gamma_z, \Gamma_\phi$	diffusivity
ϵ	dissipation rate of turbulent kinetic energy
η	transformed z-coordinate $(=(\Omega/\nu)^{1/2}z)$
λ_L	laminar flow parameter $(=C_w Re_\phi^{-0.5})$

λ_T	turbulent flow parameter ($=C_w Re_\phi^{-0.8}$)
μ	dynamic viscosity
μ_T	turbulent viscosity
μ_{eff}	effective viscosity ($=\mu + \mu_T$)
ν	kinematic viscosity ($=\mu/\rho$)
ρ	density
τ_w	shear stress at wall
σ_ϵ	turbulent Prandtl number for ϵ
σ_k	turbulent Prandtl number for k
Φ	generalized dependent variable in transport equation
Ω	angular speed of discs; vorticity invariant

Subscripts

a	value at r=a
b	value at r=b
eff	effective value
I	refers to inlet
in	refers to inlet
i, j	cartesian grid
k	value in the k-equation
ϵ	value in the ϵ equation
max	maximum value

min	minimum value
n	value at northern face of control volume
nb	neighbouring nodes
ne	value at north-eastern corner of control volume
nw	value at north-western corner of control volume
N	value at northern node
NE	value at north-eastern node
NW	value at north-western node
P	value at central node
ref	reference value, defined as appropriate
s	value on the solid surface
s	value at southern face of control volume
se	value at south-eastern corner of control volume
sw	value at south-western corner of control volume
sum	total value
S	value at southern node
SE	value at south-eastern node
SW	value at south-western node
T	value in turbulent flow

Superscripts

new	new value
$old, *$	values from previous iteration or guessed values

List of Figures

Chapter 1

Introduction

The understanding of rotating flows, which occur in internal air systems of gas - turbine engines, is an important area of fluid dynamics and heat transfer. Figure 1.1 shows a typical internal cooling-air system used in gas-turbine engines, and the flow of the cooling air due to confined rotating discs is shown in Figure 1.2.

In order to improve engine performance and thermal efficiency, much work has been done to investigate the flow and heat transfer in such systems. These investigations have helped turbine manufacturers improve designs and run engines at extremely high temperatures , pressures and rotational speeds. Engine development since 1940 has resulted in an increase in turbine - entry temperature from about 900K to 1600K.

Rotating-disc systems can be used to model the flows which occur in the internal-air systems of gas turbine engines. For example, the

flow between corotating turbine or compressor discs can be modelled using the so-called rotating cavities shown in Figure 1.3. In the rotating cavity, plane rotating discs and a cylindrical rotating or stationary shroud are used as simple models to represent the more complex geometry that occurs inside the engine.

The enclosed corotating disc systems (Figures 1.3a 1.3b and 1.3c) simulate the rotating cavities in both compressor and turbine stages of engines. The radial outflow case in Figure 1.3d represents the flow that occurs between air-cooled corotating turbine discs; the radial inflow case in Figure 1.3e represents the flow that occurs when turbine cooling air is extracted between corotating compressor discs.

A significant amount of computational and experimental work has been devoted to the cases shown in Figures 1.3a, c, d and e, but systems with a stationary outer casing (Figures 1.3b, f and g) have received less attention. This type of system is relevant to some gas-turbine engines, where there is a peripheral flow of cooling air entering and leaving the cavity through outer casing. Figure 1.3b shows a sealed rotating cavity with stationary outer flat-shroud (this is, sometimes, referred as a no-superposed flow case). Figures 1.3f and 1.3g show the schematic diagrams of the rotating cavity with superposed peripheral flow for flat and stepped shrouds respectively. The cooling air enters the cavity through a series of holes, either in a stationary flat-shroud or through a rotating disc for the stepped-shroud case. Although this thesis is mainly concerned with the computation of these peripheral-flow cases, the radial outflow and

inflow cases provide a useful starting point for the validation of the computational fluid dynamics (CFD) technique.

The main object of this project is the numerical investigation of the flow and heat transfer in a rotating cavity with peripheral flow. The results are compared with experimental data obtained by Dr X. Gan and Dr P. Quinn for flat and stepped shrouds respectively. Computations are, mainly, carried out using the low Reynolds number $k-\epsilon$ Launder-Sharma (LS) turbulence model. For the flow field computation, the sensitivity of the results to source-term modifications in the ϵ equation is also considered for the flat-shroud case.

A review of previous work in this area is given in Chapter 2, and an outline of the numerical method and turbulence model is given in Chapter 3. In Chapter 4, the CFD code is validated using published experimental data for radial outflow and inflow cases. Since the computational results in this work are compared with experimental data, a brief description of the experimental apparatus for the flat and stepped shrouds is given in Chapter 5. Chapters 6 and 7 are concerned with flow-field and heat transfer results for the flat and stepped shrouds respectively. Conclusions and recommendations for future work are given in Chapter 8.

Chapter 2

Review of previous work

2.1 Introduction

The object of this chapter is to present a review of the work related to the fluid dynamics and heat transfer in rotating cavities. As mentioned in Chapter 1, rotating cavities can be divided into groups: sealed rotating cavity, rotating cavity with axial throughflow, rotating cavity with radial outflow, rotating cavity with radial inflow and rotating cavity with peripheral flow. The literature for the sealed cavity, outflow and inflow only is reviewed in this chapter. The work done on throughflow is less relevant to this study , and no previous work has been published for the superposed peripheral flow case.

Although an extensive review of the literature for rotating cavities has been provided by Bilimoria (1977), Onur (1980), Chew (1982), Northrop (1984), Long (1984), Firouzian (1986), Vaughan (1987), Ong (1988), Farthing (1988) and Owen and Rogers (1989, 1995), attention is paid here to those works making a contribution relevant to the current research. The relevant literature will be described in three main sections:

(i) sealed rotating cavities in section 2.2;

(ii) rotating cavity with radial outflow in section 2.3;

(iii) rotating cavity with radial inflow in section 2.4.

As shown in Chapter 1 (Figure 1.3), the rotating cavity with radial outflow and with radial inflow are known as source - sink flows. As described by Owen et al (1985), the flow structure in such flows may be divided into four regions: a source region, Ekman-type layers on the discs, a sink layer and an interior inviscid core of rotating fluid. The fluid enters the cavity in the source region, which distributes the fluid into two Ekman-type boundary layers on the discs. The fluid in the Ekman layers flows into the sink layer and out of the cavity. The inviscid core, which is surrounded by the above three regions, has tangential velocity less than that of the discs for radial outflow and greater for inflow.

For the following discussion, the notation used by various authors has been standardised, and is not necessarily that used by the original author. Some well-known nondimensional parameters are introduced here: the nondimensional radius (x), gap ratio (G), rotational Reynolds number (Re_ϕ), nondimensional flow rate (C_W), laminar flow parameter (λ_L), turbulent flow parameter (λ_T), radial Reynolds number (Re_r) and local Nusselt number (Nu). These parameters are defined below

$$\text{x}=\frac{r}{b} \ , \quad \text{G}=\frac{s}{b} \ , \qquad Re_\phi = \frac{\Omega b^2}{\nu} \ , \quad Re_r = \frac{C_W}{2\pi x}$$

. (2.1)

$$C_W = \frac{m}{\mu b} \ , \lambda_L = \frac{C_W}{Re_\phi^{0.5}}, \ \lambda_T = \frac{C_W}{Re_\phi^{0.8}}, \ Nu = \frac{rq_o}{k_f(T_s - T_{ref})}$$

Other symbols are defined where they are first used and a list of key symbols is given in the nomenclature.

2.2 Sealed rotating cavity

Before considering the rotating cavity with superposed flow, it is convenient first to study a sealed cavity. An enclosed cavity is, in general, taken to mean a cavity bounded by the discs and shrouds (either rotating or stationary).

For isothermal flow in a sealed rotating cavity, with rotating cylindrical surfaces which rotate at the same speed as the discs, solid body rotation occurs and there is no fluid velocity relative to that of the discs. However, for the non-isothermal case, there is fluid motion relative to that of the disc because of buoyancy effects. For the isothermal case with a stationary outer surface, solid body rotation cannot occur everywhere and a recirculation region exists inside the cavity. Much work has been done, by many authors, for a sealed cavity with rotating outer casing to investigate buoyancy effects, but less attention has been paid to the stationary outer shroud case. The work done on the former case is less relevant to this study, and only literature involving a stationary outer shroud is considered here.

2.2.1 Sealed cavity with stationary outer shroud

For a rotating cavity with a stationary outer shroud, Gosman and Spalding (1970) studied numerically the laminar flow between shrouded rotating discs. They used the finite-difference method described by Gosman et al (1969), and solved the Navier-Stokes equations in the form of the stream function-vorticity formulation. Computations were carried out for the rotational Reynolds number

up to 10^3 and the gap ratio, G=1. They found that the numerical method diverges beyond a limiting value of Re_ϕ. They improved numerical stability problems using the under-relaxation technique on the tangential component of velocity and refinement of the grid.

On the validation of low Reynolds number $k-\epsilon$ turbulence models for flows in sealed rotating disc systems, Morse (1991a) studied a case of co-rotating discs with a stationary outer shroud: G=0.1, a/b=0 and $Re_\phi = 10^6$. He obtained a flow structure with two symmetric recirculating flows about the mid-axial plane. He concluded that the direction of the flow is radially outwards over both discs and radially inwards in the centre of the cavity. He also showed that 5% of the recirculating mass reaches the mid-radial location. However, no comparisons with experimental data were made for the velocity profiles.

Abrahamson, Eaton and Koga (1989) conducted experimental work to study the flow between corotating discs with a stationary shroud in a computer disc-drive application. Experiments, using water as a working fluid, were carried out for varying Reynolds numbers in the range 1.5 x 10^5 to 1.5 x 10^6. Four different gap ratios were used: G=0.013, 0.025, 0.05 and 0.1. They observed the existence of three

important regions (see Figure 2.1): solid-body rotation near the inner cylindrical surface (inner region), an outer region dominated by two large contra-rotating vortices in the secondary flow , and a boundary layer region on the stationary shroud.

Flow visualization showed a sharp transition between the inner and outer regions (illustrated in Figure 2.1). For axisymmetric flow, the boundary between these two regions must be circular, while the existence of large vortical structures (which were confirmed by the flow visulization) create a polygonal boundary between the two regions in the circumferential plane.

They also showed that the thin shroud boundary layer region is three-dimensional and includes a pair of toroidal vortices whose vorticity was in $\pm\phi$ direction in cylindrical polar coordinates. The locus of the axes of these vortices was found to be a circle with diameter slightly smaller than the diameter of the shroud. They also concluded that the size of the outer region increases as the axial separation of the discs increases, and the strength of the shroud boundary layer region increases as Re_ϕ increases. In this region, there was a large velocity gradient from zero at the stationary shroud to the speed of the disc at the tip of the disc. The results suggest that the

axisymmetric assumption is not valid near the outer shroud and the flow is highly turbulent and three-dimensional.

Herrero, Humphrey and Giralt (1994) carried out a numerial study using the finite difference approach to solve for axisymmetric laminar flow and heat transfer between corotating discs with both rotating and stationary outer casings. The range of the Reynolds numbers in both cases was $3.7 \times 10^3 \leq Re_\phi \leq 1.8 \times 10^4$. They showed that for the stationary shroud case with isothermal boundary conditions ($\triangle T = 0$, where $\triangle T$ is the temperature difference between the two discs), there is a symmetric flow structure about the axial mid-plane. In the non-isothermal case, $\triangle T > 0$, the symmetric flow structure breaks down, and the degree of asymmetry increases with increasing thermal Rossby number ($Ro_T = \triangle T/T_o$, where T_o indicates the average temperature between the two discs) and with decreasing rotational speed. They tested the accuracy of the numerical method on enclosed rotor-stator and contra-rotating disc systems, but no experimental comparisons have been reported for the rotating cavity.

For a sealed rotating cavity with a stationary shroud, Arnold (1996), working in parallel with the author, studied the instability of these

flow structures in more detail. Computations were carried out using both laminar and turbulent axisymmetric models in the range $10^3 < Re_\phi < 1.5$ x 10^6.

As shown in Figure 2.2, while the values of root-mean-square (RMS) changes to the the dependent variables (see equation 3.17) decreased systematically by increasing the number of iterations, he obtained symmetrical flow structures at RMS values suggesting reasonable convergence level. For most of the cases he was able to minimise the RMS values to around 10^{-15}. From this point, where the RMS values were minimised, further iterations resulted in an increase in RMS values, and the solution never returned to the minimum point. A point was eventually reached where there was no significant further variation in the RMS values. Arnold showed that, by this stage, the flow structure was asymmetric and unstable. The predicted streamlines for the minimum point and for the last point are shown in Figure 2.2. He concluded that the flow becomes more stable as the rotational Reynolds number increases.

Lewis (1997) recently used the DNS method (Direct Numerical Simulation) to solve for the time-dependent axisymmetric flow in a sealed rotating cavity with stationary outer shroud, and revealed a highly unstable flow structure for $Re_\phi = 1.46$ x 10^5. The result

of this solution will be compared with experimental data and the steady flow solution in Chapter 6.

2.3 Rotating cavity with radial outflow

A rotating cavity with a radial outflow of fluid provides a simple model of the flow between co-rotating gas turbine discs. In the turbine, the cooling air usually enters axially through a central hole of radius r=a in one disc and leaves radially through a series of holes in a peripheral cylindrical shroud at r = b. The fluid flow and heat transfer in such cavities are discussed separately in sections 2.3.1 and 2.3.2 respectively.

2.3.1 Fluid flow

A rotating cavity with a radial outflow has been considered by many authors: Hide (1968), Bennetts and Hocking (1973), Bakke et al (1973) and Bennetts and Jackson (1974). By using the non-dimensional form of the governing equations, they introduced two important dimensionless parameters: Rossby number (Ro) and Ekman number (E). These two parameters can be defined as:

$$Ro = U/2\Omega L, \qquad E = \nu/\Omega L^2 \qquad (2.2)$$

where L is a length scale, U is a scale for the velocity relative to the rotation and ν is the kinematic viscosity.

Hide (1968) studied the structure of the isothermal laminar source-sink flow inside a rotating cavity. He revealed the existence of the four important regions mentioned in section 2.1: source region, sink region, interior core and Ekman-layers on the discs (see Figure 1.3d). At small values of Rossby and Ekman numbers, Hide used the linear theory (by neglecting the non-linear terms in the equation of motion), and obtained the linear Ekman-layer condition on the boundaries which occurred on the discs. The size of the source region was found to be proportional to the Rossby number (Ro), but on the sink region the thickness of this layer was proportional to the $E^{1/2}/Ro$. He also obtained an approximate formula for the thickness of these two regions in terms of Rossby and Ekman numbers.

Later, the accuracy of Hide's solution was investigated by other workers. Bennetts and Hocking (1973), in an analytical study, obtained a non-linear Ekman-layer solution for the case when the

Rossby number was increased. They found that the thickness of the sink layer was thinner than that for the linear theory. They also found that there was a lower limit to the thickness of this layer at $Ro = 1.34(E)^{1/4}$, and obtained solutions for Rossby numbers $Ro \leq 1.34(E)^{1/4}$. They suggested that this limit was due to numerical difficulties rather than more fundamental physical reasons.

Bennetts and Jackson (1974) carried out numerical and experimental work for source-sink flow. They used the stream function-vorticity formulation for the governing equations, and solved the full Navier-Stokes equations using a finite-difference scheme. They confirmed that there is indeed a solution when the Rossby number is greater than $1.34(E)^{1/4}$. The range of their investigation was $0 \leq Ro \leq 0.4$. They showed good agreement between numerical results and experimental data.

Bakke et al (1973) investigated the velocity distributions and pressure drop between corotating discs with turbulent radial outflow, using hot-wire techniques. The experiments were carried out at small gap ratios ($G < 0.05$) for rotational Reynolds numbers up to 6.5 x 10^5 and nondimensional mass flowrates, C_W, up to 2.5 x 10^4. The air entered the cavity, axially, through a hole in the centre of

the disc and there was no outer shroud.

They found that, at large radial positions, the effects of asymmetrical inlet conditions disappeared with increasing the rotational speed. They obtained good agreement, for high rotational speeds, between the measured tangential velocity and the 1/7th power law velocity distribution. They also found that the centrifugal forces tend to stablize the flow. Consequently, the turbulence intensity reduced by increasing the rotational speed of the disc. However, as the disc speed was increased further, it was found that the turbulence intensity increased again due to the shear force between the discs and fluid.

Owen and Pincombe (1980) used flow visualization (by introducing smoke to the cavity) to determine the flow structure inside an isothermal rotating cavity with a radial outflow. They used Laser-Doppler anemometry (LDA) to measure the velocity distribution inside the cavity for two cases: (i) outflow with axial inlet; (ii) outflow with radial inlet. They found the nature and size of the source region was dependent on whether the flow entered axially or radially; in the former case, a wall jet could form on the downstream disc, and the radial extent of the source region was greater than

that of the radial inlet case. For the latter case, they compared their experiments with Hide's solution, and good agreement was obtained apart from the extent of the source region. The size of the source region was found to be larger than in Hide's solution, and was correlated using a semi-empirical equation.

For small superposed flow rates, the flow visualization showed a relatively large "white" region near the outer shroud. This was evidence of ingress of fluid from outside the cavity through the holes in the shroud (in opposition to the superposed radial outflow). In the presence of ingress, the structure of the sink region was complex, and its radial extent was difficult to determine. Little investigation has been made of ingress in rotating cavities in comparison with the rotor-stator systems, details of which are given by Owen and Rogers (1989).

Kapinos (1965) and Owen et al (1985) used the integral momentum method to consider turbulent flow for a rotating cavity with a radial outflow, using a 1/7th power law for the velocity profile. Although the velocity predictions of Owen and his co-workers in the core were in good agreement with the experimental data of Owen and Pincombe (1980) the velocity profiles inside the boundary layers de-

parted significantly from the 1/7th power law profile assumed in the integral momentum method. Owen, Pincombe and Rogers (1985) suggested that the criterion for transition from laminar to turbulent flow in an Ekman-layer is $Re_r = 180$.

Numerical solution of the Navier-stokes equations, using the finite difference approach, for the case of axisymmetric isothermal laminar flow in a rotating cavity with a radial outflow, was investigated by Chew (1982). He developed the TEACH programme of Gosman and Ideriah (1976) using the SIMPLE algorithm of Patankar and Spalding (1972) for the pressure - correction scheme. Chew, Owen and Pincombe (1984) showed good agreement between the computations and experiments for isothermal laminar outflow.

For the turbulent outflow case, Morse (1988), Chew (1987) and Ong and Owen (1989) compared their computational results with the velocity measurments of Pincombe (1983). Morse used a low-Reynolds-number $k - \epsilon$ turbulence model to solve the turbulent elliptic equations. He obtained good agreement in terms of the velocity measurements inside the Ekman-layer and in the inviscid core. Chew used the mixing-length model of Koosinlin, Launder and Sharma (1974) and obtained reasonable agreement with experimen-

tal data. Ong and Owen also solved the linear and non-linear boundary layer equations using a Cebeci-Smith effective-viscosity model for turbulent flows. They used a Keller-Box numerical scheme for the numerical solutions, and they obtained good agreement between the computed velocity distributions and the LDA measurements of Pincombe.

Shirazi and Truman (1987) obtained solutions of the turbulent boundary layer equations with a relatively high rotation rate and narrow gap ratio (G = 0.05) using a $k - \epsilon$ turbulence model. In order to take into account anisotropy effects, they modified the two-equation turbulence model by introducing a model for the pressure-strain term. Their solutions were in good agreement with experimental data. However, they did not obtain solutions for high values of gap ratio where there is an inviscid core between the two discs.

Iacovides and Theofanopoulos (1991) used a zonal turbulence modelling approach to solve the elliptic equations. In this method either an isotropic $k - \epsilon$ model or an anisotropic algebraic-stress model was used in the fully turbulent region, and a mixing-length model was used in the thin viscous-dominated wall layers. They obtained good agreement with the experimental data of Pincombe (1983).

Vaughan et al (1989) used a multigrid elliptic solver incorporating a mixing-length model to investigate turbulent radial outflow at high rotational Reynolds numbers. Chiang and Eaton (1993) carried out an experimental investigation of a corotating cavity with a radial outflow. They used water as a working fluid, and obtained very similar flow structures to those found in previous work.

The axisymmetric instability of the radial outflow was investigated by Crespo et al (1996). They considered the axisymmetric incompressible flow in a rotating cavity with a radial outflow, and solved the time-dependent Navier-Stokes equations using the stream function-vorticity formulation. The values of the time step, δt, used in their computations were $3 \times 10^{-6} < \delta t < 4 \times 10^{-5}$ seconds. They conducted their investigations at very high rotation rates and varying mass flowrates. At the low mass flowrate, C_W =100, steady and symmetric flow was achieved. By increasing the mass flow rate, at constant Re_ϕ (=2.5 x 10^5), an oscillatory regime started in the source region, associated with a break of symmetry with respect to the mid-axial plane. The first transition from the steady flow to an oscillatory periodic-flow in the source region occured for $C_W = 120$. The frequency of this oscillation was close to the disc frequency, and the wavelength was about the size of the source

region. Further increases in the flowrate, up to $C_W = 132$, led to quasi-periodic behaviour in the source region. They found a chaotic flow at $C_W = 140$ and 150 with strong oscillations of the source region, associated with recirculation zones on both sides of the source region (see Figure 2.3). They concluded that the origin of the oscillatory region is not the instability of the Ekman-layers but the instability of the entry flow due to the importance of the nonlinear terms in cavities with small radius of curvature.

2.3.2 Heat transfer

Heat transfer between corotating discs with a radial outflow has been considered, theoretically and experimentally, by many authors. In his theoretical work, Kapinos (1965) obtained the heat transfer coefficient with the use of the Reynolds analogy. He showed that the heat transfer from a constant temperature heated disc is lower by about 15% from that obtained with a quadratic temperature distribution. Kreith (1966) carried out theoretical work on heat transfer in a rotating cavity with a laminar outflow at small gap ratios ($0.032 < G < 0.062$). Owen, Pincombe and Onur (1979) used the momentum integral method and Reynolds analogy to investigate the heat transfer in the Ekman - layer region. For a quadratic

disc temperature distribution, they obtained a formula to indicate the local Nusselt number as a function of C_W and x. Chew (1985) solved the full laminar energy equation for the case of radial outflow with either a radial or axial inlet using a finite-difference method. He assumed that the buoyancy forces and viscous dissipation terms were negligible. For the radial inlet case, he found that the heat transfer from the disc in the source region is very close to that for the free disc.

Bilimoria (1977), Onur (1980) and Northrop and Owen (1988) conducted experimental studies to measure the local and mean Nusselt numbers for a turbulent radial outflow case. Bilimoria described his heat transfer results in three separate regimes: in regime (I), called the source dominated regime, mean Nusselt number was independent of the rotational Reynolds number; in regime (II), called the intermediate developing Ekman layer regime, mean Nusselt number increases as Re_ϕ increases; in regime (III), called the fully developed Ekman-layer regime which occurs at high Re_ϕ , mean Nusselt number decreases as Re_ϕ increases. Onur extended the range of the heat transfer measurements and found a fourth regime (IV), which is dominated by buoyancy-driven convection. Onur obtained separate correlations for the mean Nusselt number at each regime as a func-

tion of G, C_W and Re_ϕ. His correlation for the fourth regime is only a function of gap ratio and Grashof number,$Gr = b^4\Omega^2\beta\triangle T/\nu^2$. Northrop and Owen (1988) investigated the heat transfer in the turbulent Ekman - layer for a symmetrically heated cavity. By neglecting buoyancy effects, they solved a linear form of the integral energy equation. They compared their results with the experimental data of Northrop (1984) who carried out measurements in a symmetrically heated cavity. Agreement between the computed and measured Nusselt numbers was mainly good.

Lapworth and Chew (1992) showed, in numerical work, the influence of disc geometery on heat transfer in the case of a rotating cavity with non-plane discs (discs with "cobs", see Figure 2.4). The cobs were located in the inner part of the cavity, making a model which was closer to the real geometry of turbine discs. They used a mixing-length turbulence model, and obtained good agreement with the findings of Farthing and Owen (1988).

Ong and Owen (1991) extended the Keller-Box numerical method to solve for heat transfer in a rotating cavity with a radial outflow. They found that the computed local Nusselt numbers were in good agreement with the solution of Chew (1982) for laminar flow, and

with the measurements of Northrop and Owen (1988) for turbulent flow.

Morse and Ong (1992) extended an existing elliptic solver to include the solution of the energy equation. They applied the solver to symmetrically heated discs with a radial outflow, and obtained reasonable agreements between the computed Nusselt numbers and measured values of Northrop and Owen (1988). They also showed that the maximum Nusselt number occurs at approximately the end of the source region. Inside the source region, Nusselt numbers increase with radius as air is entrained into the boundary layers. At large values of x, where the non-entraining the Ekman-type layer is developed, Nusselt number decreases with radius as air temperature increases with radius.

Wilson, Chen and Owen (1996) presented computational work on the flow and heat transfer in rotating disc systems. For the radial outflow case, a multigrid solver incorporating the low Reynolds number $k - \epsilon$ model was validated against the experimental data of Northrop and Owen (1988).

Long, Morse and Zafiropoulos (1993) carried out computations to

investigate the heat transfer for the case of radial outflow in an asymmetrically heated cavity. They used the finite-volume approach incorporating two different low Reynolds number $k-\epsilon$ models. The first model, which had previously been used for the symmetrically heated cavity, showed good agreement (within 10% error) for the Nusselt numbers on the downstream heated disc. However, poor agreement was achieved for the upstream cooler disc due to the high turbulence level in the computed core flow. As a result, the convective heat transfer to the upstream disc through the core region was overpredicted. They concluded that, in the basic model, the expression used for the radial-tangential components of the turbulent shear stresses ($\overline{V_r' V_\phi'}$) produces unrealistically high rates of turbulence generation in the core region. The problem was overcome by modifying the above term with the use of algebraic - stress modelling, and they showed improvement in the accuracy of the computed results with the use of the modified model. They also estimated the radiative heat exchange between the discs using a conventional view factor approach based on black-body emission.

2.4 Rotating cavity with radial inflow

2.4.1 Fluid flow

The basic flow structure for radial inflow, as shown in Figure 1.3e, is the same as for radial outflow, but the main flow is in the opposite direction. Instabilities inside the Ekman - layer for the case of radial inflow were investigated by Faller (1963) and by Tatro and Mollo-Christensen (1967). They observed two types of instabilities characterised by short and long wave-lengths. Later, Owen and Pincombe (1980) studied the instability inside the Ekman-layer. They also found the second type of instability, but with a different wavelength.

Firouzian et al (1985) used a flow visualization technique to investigate the flow structure for a radial inflow case. The flow visualization revealed the four important regions in the flow structure as described in section 2.1. Owen, Pincombe and Rogers (1985) made a basic study of source-sink flow in a rotating cavity. For radial inflow, they considered the nonlinear equations both for laminar and turbulent flows, and showed that at the nondimensional radius x = $c^{1/2}$ (where c is an empirically determined swirl ratio)

there was a stagnation point on the disc, and the value of $V_\phi/\Omega r$ was unity. Good agreement was achieved with measured values over wide range of rotational Reynolds numbers and mass flowrates.

Chew et al (1989) studied the effect of radial fins, which were attached to one of the two discs, in reducing the pressure drop. Farthing et al (1991) studied the use of rotating de-swirl nozzles to reduce the pressure drop for a rotating cavity with a radial inflow. They also showed the existence of a mixing layer in the source region, and modified the free vortex formula for the source region using the effective swirl ratio, c_{eff}, instead of inlet swirl ratio, c.

2.4.2 Heat transfer

Firouzian (1986) solved the Laplace equation to compute the local Nusselt numbers for a radial inflow, using measured temperatures for the front and back faces of the heated disc as a thermal boundary conditions. He showed the existence of negative Nusselt numbers at low values of x and high values of Re_ϕ or low values of C_W (or equivalently at low values of the $|\lambda_T|$ parameter). Firouzian et al (1986) compared experimental average Nusselt numbers for the radial inflow case for $2800 < C_W < 28000$ and $0.2 < Re_\phi/10^5 < 20$ with the correlations obtained by Owen and Onur (1983) for radial outflow. They showed that, under similar conditions, the magni-

tude of measured averaged Nusselt numbers for the inflow case was similar to those for the radial outflow case.

Reile, Radons and Hennecke (1985) carried out experimental work for the radial inflow case, and compared the results with theoretical predictions based on a finite element technique. They obtained reasonable agreement for both steady and transient cases. Rogers (1987) studied the heat transfer in a rotating cavity with a radial inflow, with an inlet swirl ratio of unity. She solved the momentum- and energy-integral equations for different radial temperature distributions on the disc, and with different Re_ϕ and C_W. She showed that the maximum local Nusselt number takes place at the radial location corresponding to the end of the source region. She also concluded that the effect of different disc temperature distributions on local Nusselt numbers is more pronounced for small values of x. She also predicted , under certain conditions, negative Nusselt numbers at small values of x.

Farthing et al (1991), in an experimental and theoretical study, investigated the heat transfer in a rotating cavity with a radial inflow. Two types of experimental data were available: (i) data from an experimental rig ; (ii) data from a compressor disc in a real gas-turbine engine. They compared measured Nusselt numbers with predicted values obtained from solutions of the integral equations, using the method described by Chew and Rogers (1988). They showed good agreement between the rig results and computations inside the Ekman layer, but poor agreement in the source region.

The real engine test results were consistent with the results from both the experimental rig and the computations.

Chapter 3

Numerical method and turbulence modelling

3.1 Introduction

Since the main interest of this study is to investigate the flow and heat transfer in a rotating cavity with peripheral flow , a code developed from that described by Vaughan et al (1989) (SURF) is used as the numerical method. The axisyimmetric code is based on the finite volume techniques explained by Patankar (1980), and is written in the cylindrical coordinate system (r, ϕ, z). The code is an elliptic solver and incorporates the multigrid method for convergence acceleration. Several turbulence models were incorporated in the code by Kilic (1993) to solve for turbulent flow. These in-

clude the mixing-length model, and the low-Reynolds-number $k-\epsilon$ models of Morse (1991b) and Launder and Sharma (1974). The application of the Launder and Sharma (LS) model is of principal interest in this thesis. The version of the code used by the author is that described by Kilic (1993) with an extra facility for the use of blockages within the computed grid, as used by Wilson et al (1995). This version of the code is now called BURF (Bath University Rotating Flow). The main contribution of the author in terms of code development is the implementation of modifications to the source term of the dissipation equation in the $k-\epsilon$ model. These modifications include the Yap correction (Yap, 1987), a rotation correction and a Richardson correction.

A brief description of the governing equations and numerical solution are given in sections 3.2 and 3.3 respectively, and the multigrid method is described in section 3.4. The source term modifications in the $k-\epsilon$ turbulence model for rotating flows are discussed in section 3.5.

3.2 Governing equations

3.2.1 Laminar flow

For steady , axisymmetric , laminar flow , the general form of the conservation equations for mass, momentum and energy may be written in the stationary cylindrical-polar coordinate system (r, ϕ, z) as:

$$\frac{\partial}{\partial r}(\rho r V_r \Phi) + \frac{\partial}{\partial z}(\rho r V_z \Phi) = \frac{\partial}{\partial r}\left(r\Gamma_r \frac{\partial \Phi}{\partial r}\right) + \frac{\partial}{\partial z}\left(r\Gamma_z \frac{\partial \Phi}{\partial z}\right) + S_\Phi \quad (3.1)$$

where V_r, V_ϕ, V_z are the velocity components in the cylindrical-polar coordinate system. The dependent variable Φ is taken as $1, V_r, V_\phi, V_z$ and h to give conservation equations for, respectively, mass, radial, tangential and axial components of velocities, and entalpy.

3.2.2 Turbulent flow

For turbulent flow, the approximation of the Reynolds stresses $(\overline{\rho V_i V_j})$, which appear in the time-average Navier - Stokes equations, for axisymmeteric isotropic flow, were written by Kilic (1993)

$$\rho\overline{V_r'}^2 = 2/3\rho k - 2\mu_T\frac{\partial V_r'}{\partial r}, \qquad \rho\overline{V_r'V_\phi'} = -\mu_T r\frac{\partial(V_\phi'/r)}{\partial r}$$
$$\rho\overline{V_\phi'}^2 = 2/3\rho k - 2\mu_T\frac{V_r'}{r}, \qquad \rho\overline{V_r'V_z'} = -\mu_T(\frac{\partial V_r'}{\partial z} + \frac{\partial V_z'}{\partial r}) \quad (3.2)$$
$$\rho\overline{V_z'}^2 = 2/3\rho k - 2\mu_T\frac{\partial V_z'}{\partial z}, \qquad \rho\overline{V_\phi'V_z'} = -\mu_T r\frac{\partial V_\phi'}{\partial r}$$

Where k is the turbulent kinetic energy ($= 0.5\overline{V_i'V_i'}$), and μ_T denotes the turbulent viscosity obtained from the Prandtl-Kolmogorov equation:

$$\mu_T = C_\mu f_\mu \frac{\rho k^2}{\epsilon} \quad (3.3)$$

The general form of the conservation equation (3.1) can be used for turbulent flow as well as for laminar flow. For turbulent flow, the transport equations for turbulent energy and dissipation of energy can be obtained by taking Φ as k or ϵ respectively.

For each dependent variable Φ, the values of Γ_r, Γ_z and S_Φ are given in Table 3.1, and for laminar flow the values of μ_T, k and ϵ are zero. For the low-Reynolds-number $k-\epsilon$ turbulence model, the effective viscosity shown in Table 3.1 can be defined as:

$$\mu_{eff} = \mu + \mu_T \quad (3.4)$$

Φ	Γ_z	Γ_r	S_Φ
1	0	0	0
V_z	$2\mu_{eff} - \mu$	μ_{eff}	$-\frac{\partial}{\partial z}\left(p + \frac{2}{3}\rho k\right) + \frac{1}{r}\frac{\partial}{\partial r}\left(r\mu_T \frac{\partial V_r}{\partial z}\right)$
V_r	μ_{eff}	$2\mu_{eff} - \mu$	$-\frac{\partial}{\partial r}\left(p + \frac{2}{3}\rho k\right) - (2\mu_{eff} - \mu)\frac{V_r}{r^2}$ $+\frac{\rho V_\phi^2}{r} + \frac{\partial}{\partial z}\left(\mu_T \frac{\partial V_z}{\partial r}\right)$
V_ϕ	μ_{eff}	μ_{eff}	$-\frac{\rho V_r V_\phi}{r} - \mu_{eff}\frac{V_\phi}{r^2} - \frac{V_\phi}{r}\frac{\partial \mu_T}{\partial r}$
k	$\mu + \frac{\mu_T}{\sigma_k}$	$\mu + \frac{\mu_T}{\sigma_k}$	$P - \rho\epsilon - D$
ϵ	$\mu + \frac{\mu_T}{\sigma_\epsilon}$	$\mu + \frac{\mu_T}{\sigma_\epsilon}$	$\frac{\epsilon}{k}(C_{\epsilon 1}P - C_{\epsilon 2}\rho\epsilon) + E - F$
h	K_f/C_p	K_f/C_p	$\frac{1\partial}{r\partial r}[(\mu_{eff}$ -$K_f/C_p)r\frac{\partial}{\partial r}(V_r^2 + V_\phi^2 + V_z^2)/2]$ $\frac{\partial}{\partial z}[(\mu_{eff}$ -$K_f/C_p)\frac{\partial}{\partial z}(V_r^2 + V_\phi^2 + V_z^2)/2]$ $\frac{1\partial}{r\partial r}[\mu_{eff}\ (\frac{1}{3}V_r\frac{\partial V_r}{\partial r} - \frac{2V_r^2}{3r} - \frac{2}{3}V_r\frac{\partial V_z}{\partial z} -$ $\frac{V_\phi^2}{2} + V_z\frac{\partial V_r}{\partial z})]$ $\frac{\partial}{\partial z}[\mu_{eff}\ (V_r\frac{\partial V_z}{\partial r} + \frac{1}{3}V_z\frac{\partial V_z}{\partial r} - \frac{2V_z}{3r}\frac{\partial(rV_r)}{\partial r})]$

Table 3.1. Components of the conservation equations (equation 3.1)

The term P in table 3.1 denotes the rate of production of turbulent kinetic energy, and is given by:

$$P = \mu_T[2\left(\left(\frac{\partial V_z}{\partial z}\right)^2 + \left(\frac{\partial V_r}{\partial r}\right)^2 + \left(\frac{V_r}{r}\right)^2\right) + \left(\frac{\partial V_z}{\partial r} + \frac{\partial V_r}{\partial z}\right)^2 + \left(\frac{\partial V_\phi}{\partial z}\right)^2 + \left(r\frac{\partial}{\partial r}\left(\frac{V_\phi}{r}\right)\right)^2] \tag{3.5}$$

Values and expressions for C_μ, f_μ and other turbulence quantities used by Kilic (1993) are given in Table 3.2.

Term	High R_T model	Launder and Sharma model (LS)	Morse model (M)
C_μ	0.09	0.09	0.09
$C_{\epsilon 1}$	1.44	1.44	1.44
$C_{\epsilon 2}$	1.92	$1.92 f_1$	$1.92 f_1$
D	-	$2\mu\left[\left(\frac{\partial\sqrt{k}}{\partial z}\right)^2+\left(\frac{\partial\sqrt{k}}{\partial r}\right)^2\right]$	$2\mu\left[\left(\frac{\partial\sqrt{k}}{\partial z}\right)^2+\left(\frac{\partial\sqrt{k}}{\partial r}\right)^2\right]$
E	-	$2\frac{\mu\mu_T}{\rho}[\left(\frac{\partial^2 V_r}{\partial z^2}\right)^2+\left(\frac{\partial^2 V_\phi}{\partial z^2}\right)^2 + \left(\frac{\partial^2 V_z}{\partial r^2}\right)^2+\left(\frac{\partial^2 V_\phi}{\partial r^2}\right)^2]$	$2\frac{\mu\mu_T}{\rho}[\left(\frac{\partial^2 V_r}{\partial z^2}\right)^2+\left(\frac{\partial^2 V_\phi}{\partial z^2}\right)^2 + \left(\frac{\partial^2 V_z}{\partial r^2}\right)^2+\left(\frac{\partial^2 V_\phi}{\partial r^2}\right)^2]$
F	-	-	$2\mu\left[\left(\frac{\partial\sqrt{\epsilon}}{\partial z}\right)^2+\left(\frac{\partial\sqrt{\epsilon}}{\partial r}\right)^2\right]$
f_1	1.0	$\left(1-0.3exp\left(-R_T^2\right)\right)$	$\left(1-0.22exp\left(-\frac{R_T^2}{6}\right)\right)$
f_μ	1.0	$exp\left[\frac{-3.4}{\left(1+\frac{R_T}{50}\right)^2}\right]$	$\left(1-exp\left(-\frac{y^+}{24.4}\right)\right)^2$
σ_k	1.0	1.0	1.0
σ_ϵ	1.3	1.3	1.3

Table 3.2. Terms appearing in the $k-\epsilon$ turbulence models

The terms $R_T(=k^2/\epsilon\nu)$ and y^+ in Table 3.2 denote turbulent Reynolds number and nondimensional distance from the solid surface respectively.

3.3 Numerical solution

3.3.1 Finite volume equations

Equation 3.1 can be discretized using a control-volume approach as described by Patankar (1980). Figure 3.1 shows the locations of the dependent variables with respect to the control volume around a grid node. As can be seen , the locations of the axial velocity (V_z) and radial velocity (V_r) are staggered in their own directions such that they are located at the faces of the principal control-volumes. This ovecomes to the difficulty of an oscillatory pressure field which can arise during the iterative solution, as described by Patankar (1980). Dependent variables (other than the radial and tangential components of velocity) are stored at the main grid nodes.

By discretizing the general conservation equation for the control-volume shown in the Figure 3.2, and by integrating over the control volume incorporating the second-order central-difference approximation, the following experession can be obtained:

$$(a_{P,\Phi} - S_P^{\Phi})\Phi = a_{N,\Phi}\Phi_N + a_{S,\Phi}\Phi_S + a_{E,\Phi}\Phi_E + a_{W,\Phi}\Phi_W + S_C^{\Phi} \tag{3.6}$$

where Φ represents one of the dependent variables, a is the coefficient at the specified location and $S_C^{\phi} + S_P^{\phi}\Phi$ is the linearized

representation of the source term S^{Φ}.

As described by Gilham (1990), using a second-order central-difference approximation for the convection terms can lead to divergence and numerical instability of the iterative scheme. This problem can be overcome by the use of the 'hybrid' scheme of Spalding (1972). This technique uses hybrid upwind differencing for the convection terms, which has been described in detail by Patankar (1980). Using the above scheme, the coefficients of the equation number (3.6) can be written as:

$$\begin{aligned} a_{N,\phi} &= max(\tfrac{|C_{N,\phi}|}{2}, D_{N,\phi}) - \tfrac{C_{N,\phi}}{2}, \\ a_{S,\phi} &= max(\tfrac{|C_{S,\phi}|}{2}, D_{S,\phi}) - \tfrac{C_{S,\phi}}{2}, \\ a_{E,\phi} &= max(\tfrac{|C_{E,\phi}|}{2}, D_{E,\phi}) - \tfrac{C_{E,\phi}}{2}, \\ a_{W,\phi} &= max(\tfrac{|C_{W,\phi}|}{2}, D_{W,\phi}) - \tfrac{C_{W,\phi}}{2}, \\ a_{P,\Phi} &= a_{N,\phi} + a_{S,\phi} + a_{E,\phi} + a_{W,\phi} \end{aligned} \tag{3.7}$$

where C and D are the representations of the convection and diffusion coefficients respectively. These coefficients and the source terms (S_C^{Φ}, S_P^{Φ}) are given in detail by Kilic (1993). Furthermore, an inconsistency in the order of the finite-difference approximation for the diffusion terms may occur at the boundaries. This problem may be overcome by introducing a second-order backward (or forward) difference formulation (see Kilic (1993)).

Special attention should be given to the treatment of boundary conditions. In general two types of boundary conditions are specified: either the values or the normal gradients of the variables are known. The former type of boundary conditions does not create a particular problem, and values are specified once at the beginning of the solution procedure. The second type of the boundary condition, however, needs to be updated at the end of each iteration. An additional equation is needed to evaluate the boundary value which involves the replacement of the gradient by a second-order forward or backward difference formula (depending on the positioning of the boundary node).

A geometrical expansion/contraction parameter is used to create a nonuniform distribution of the grid nodes. This gives a suitable grid refinement within the regions of a large velocity gradients. An upper limit of 1.3 is kept for the expansion factor , in order to limit the truncation error.

3.3.2 Under-relaxation

In the iterative solution of algebraic equations, it is sometimes desirable to speed up or slow down the changes from one iteration to the next. The former process is called *over − relaxation* and the second is called *under − relaxation*. According to Patankar (1980), the use of the over-relaxation is less common, and the under-relaxiation is very useful technique for the nonlinear problems in order to avoid divergence in the iterative solution. Using an under-relaxation factor, α_Φ, for the dependent variable Φ, equation (3.6) can be expressed in the form:

$$\frac{a_{P,\Phi}}{\alpha_\Phi}\Phi_P = \sum a_{nb,\Phi}\Phi_{nb} + S_C^\Phi + (\frac{1-\alpha_\Phi}{\alpha_\Phi})a_{P,\Phi}\Phi_P^* \tag{3.8}$$

where Φ and Φ^* refer to the current and previous iterative values respectively. The under - relaxation parameter can be varied from 0 to 1 ($0 < \alpha_\Phi \leq 1$) and $a_{P,\Phi}$ is given by

$$a_{P,\Phi} = \sum_{nb} a_{nb,\Phi} - S_P^\phi \tag{3.9}$$

For highly swirling flows, the centrifugal force and pressure gradient terms dominate the radial momentum equations and so a small discrepancy in these terms can cause a large error in the iterative solution. To overcome this problem and improve the stability, Vaughan et al (1989) added the damping function suggested by Gosman et al

(1976) to the source term of the radial momentum equation. This term may be written as:

$$\alpha_G \frac{\rho|V_\phi|}{r}(V_r^{old} - V_r^{new}) \tag{3.10}$$

where α_G is an emprical constant.

3.3.3 Solution procedure

Equation 3.6 can be written, for a two-dimensional grid, in the form:

$$\begin{aligned}[a_{P,\Phi}(i,j) - S_P^\phi(i,j)]\Phi_P(i,j) = a_{E,\Phi}(i,j)\Phi(i+1,j)+ \\ a_{W,\Phi}(i,j)\Phi(i-1,j)+ \\ a_{N,\Phi}(i,j)\Phi(i,j+1)+ \\ a_{S,\Phi}(i,j)\Phi(i,j-1) + S_C^\phi(i,j)\end{aligned} \tag{3.11}$$

The above equation can be converted to the one dimensional problem using a chosen line as shown in Figure 3.3 . In this method, the current values of variables at the grid points along the two neighbouring lines are used. Hence, the above equation may be written as:

$$\begin{aligned}a(i)\Phi(i) = b(i)\Phi(i+1) + c(i)\Phi(i-1) \\ +d(i)(i = 1,2,3,...,N)\end{aligned} \tag{3.12}$$

According to Patankar (1980), the solution of the above equations can be obtained by the standard Gauss-Seidel method. Owing to the particularly simple form of the equations, there is a convenient solution algorithm called the Thomas algorithm or the TDMA (Tri-Diagonal Matrix Algorithm). The value of $\Phi(i)$ can be obtained for all the grid points along the chosen line, and the sweeping process can be carried out for all the other lines in the direction normal to the chosen line. After completing one process for the domain, a different sweeping process may be carried out for the next steps as shown in Figure 3.3

3.3.4 Pressure-correction equation

In order to solve the momentum equations, it is assumed that the pressure distribution is either known or guessed. The corrected pressure, p', may be written as:

$$p = p^* + p' \tag{3.13}$$

where p^* is the guessed pressure and p' is the $pressure-correction$. Similarly, the corrected velocity field can be written as:

$$\begin{aligned} V_z &= V_z^* + V_z' \\ V_r &= V_r^* + V_r' \end{aligned} \tag{3.14}$$

where V_z^* and V_r^* are obtained using the axial and radial momentum equations respectively, and V_z' and V_r' are the corrections.

To obtain p', a pressure-correction equation is derived from the continuity equation. This equation has the dual purpose of determining the pressure and of ensuring that the velocity distributions satisfy the continuity equation. By considering the continuity equation and incorporating the radial and axial momentum equations, the pressure correction equation can be expressed as follows:

$$a_p p'_p = a_E p'_E + a_W p'_W + a_N p'_N + a_S p'_S + b \tag{3.15}$$

More details of the derivation of the above equation and coefficients are given by Kilic (1993). The velocity components and pressure are now available by solving the momentum and pressure correction equations.

Two algorithms that have been used to solve the momentum equations via a pressure correction equation are the SIMPLE algorithm proposed by Patankar and Spalding (1972) and the SIMPLEC algorithm proposed by van Doormaal and Raithby (1984). The SIMPLEC algorithm takes into account some velocity correction terms in the pressure-correction equation that are neglected in the SIMPLE formulation (see Kilic (1993)). The code used here employs

the SIMPLEC algorithm.

As can be seen, the pressure correction equation (3.15) has the same form as the general linear algebraic equation described in section 3.3.1, and a similar procedure can be used to obtain the pressure correction. As with the other algebraic equations, the pressure correction equation may lead to divergence unless underrelaxation is used. Therefore equation 3.13 can be rewritten as:

$$p = p^* + \alpha_p p' \tag{3.16}$$

where α_p is an under-relaxation parameter ($0 < \alpha_p \leq 1$).

The boundary condition for the pressure can be different in accordance with the type of the boundary condition imposed for the axial and radial momentum equations. As with the momentum equations, the boundary conditions for the pressure correction equation can be of two types (a) specified-value condition; (b) specified-gradient condition. If the velocity at the boundary is specified then the boundary condition for the pressure is of the gradient type (i.e. $\partial p'/\partial n = 0$, where n is the direction normal to the boundary). Alternatively, if the gradient - type boundary condition was applied on the momentum equations then the pressure on the boundary is fixed.

The important operations using the SIMPLEC algorithm can be

summarised as follows:

(1) guess a pressure distribution (p^*) and the velocity field (V_r, V_ϕ, V_z);

(2) solve the axial and radial momentum equations to obtain new V_r and V_z;

(3) solve the pressure correction equation to obtain p';

(4) correct the pressure and velocity field to obtain the new p, V_r and V_z;

(5) solve the tangential momentum equation to obtain V_ϕ;

(6) repeat the whole procedure starting from step (2) until the solution has converged.

3.3.5 Convergence criteria

Although there is no universal definition for convergence criteria, the criteria used by Kilic (1993) were found to be satisfactory for this study. Two convergence criteria were of importance: the normalized root mean-square (RMS) value of the dependent variables, and the normalized sum of the absolute values of the residuals.

Following Kilic (1993) and Vaughan et al (1989), the RMS residual

can be defined as:

$$RMS^{\Phi} = \sqrt{\frac{\sum_{ij}(\Phi^n - \Phi^{n-1})^2}{\sum_{ij}(\Phi^n)^2}} \tag{3.17}$$

where Φ^n and Φ^{n-1} represent the current and previous iterative values repectively, and $\sum_{ij}$ indicates summation over the grid nodes.

In some circumstances (e.g. where the underrelaxation parameters are very small, or the absolute values of the dependent variables are small) the RMS value is not a good identification of the level of convergence. Therefore, aditional criteria were also implemented to ensure that convergence had been obtained; these included checking overall balance in conserved quantities (e.g. mass, angular momentum and energy) and checking , cell-by-cell and in total, absolute values of the residuals for all the dependent variables. For the dependent variable Φ, the residual for each cell may be calculated as:

$$\begin{aligned} R_{ij}^{\Phi} &= (a_{P,\Phi} - S_P^{\phi})\Phi_P - a_{N,\Phi}\Phi_N \\ &-a_{S,\Phi}\Phi_S - a_{E,\Phi}\Phi_E - a_{W,\Phi}\Phi_W - S_C^{\Phi} \end{aligned} \tag{3.18}$$

The total absolute values of the residuals are then calculated from

$$R_{sum}^{\Phi} = \sum_{ij} |R_{ij}^{\Phi}| \tag{3.19}$$

The above equation can be normalized for each dependent variable using a different normalization parameter. The product of the

maximum tangential velocity of the disc (Ωb) and the mass flow rate is used to normalize the momentum equations; the residual for the pressure correction equation is normalized using the mass flow rate; the residuals of the k and ϵ equations are normalized using the product of the mass flow rate and characteristic values of k and ϵ. The characteristic values for k and ϵ were taken by Kilic (1993) as $\overline{k} = 10^{-2}(\Omega b)^2$ and $\overline{\epsilon} = (\overline{k})^2/100\nu$. For cases with no superposed flow ($C_W = 0$), the bulk recirculation in the cavity was calculated and this was used for the mass flowrate Kilic (1993).

In the work reported here, convergence was assumed when both the normalized root mean-square (RMS) value and the normalized value of R^{Φ}_{sum} for each dependent variable were less than 10^{-5} and 10^{-6} respectively. The solutions obtained corresponded with the "minimum-residual" solutions obtained by Arnold (1996), as described in Chapter 2.

3.4 Multigrid method

Rotating-flow problems sometimes require very fine grids (particularly if low-Reynolds-number turbulence models are used), and normally suffer from slow convergence and long computing times. In

order to decrease the computing time and overcome the slow convergence, a multigrid technique has been applied. A V-cycle nonlinear multigrid method, employing a series of progressively coarser grids m, m-1, m-2, ... was used to solve the nonlinear system of equations described in the previous section. The multigrid method employed in this code is described in detail by Kilic (1993), and only an outline of this method is illustrated here. The following procedures are carried out to complete the solution algorithm using the multigrid method.

(1) The discretized governing equations derived in section 3.3.1 are solved, using a fixed number of iterations, on the finest grid using the SIMPLEC algorithm described in section 3.3.4. This step is called the *relaxation* stage.

(2) The dependent variables are restricted from the fine to coarse grids using a *full weighting restriction operator*, as obtained by Stuben and Trottenberg (1982). This step, which is the transfer of the fine grid solution to the nodes of the coarse grid, is called *restriction* stage. As discussed previously, the location of the radial and axial velocity components in the main grid is staggered. Therefore, three different restriction operators are required: one for

axial velocity, one for radial velocity and one for all other dependent variables.

(3) At each grid level, relaxation is followed by restriction until the coarsest grid is reached.

(4) The process moves back from the coarsest grid to the finest grid using a prolongation process followed by relaxation. (The prolongation process is a bilinear interpolation operator used to apply corrections to the dependent variables from the coarse to finer grid.)

(5) All the procedures explained above are repeated until a converged solution is achieved.

As mentioned by Kilic (1993), the multigrid solution algorithm is unstable when the source terms contain derivatives. Because the k and ϵ equations are dominated by their source terms and these terms include many derivatives, it is difficult to obtain a stable convergence for k and ϵ using the multigrid solution algorithm. On the coarse grid, the calculated values of k and ϵ become greater than the fine grid solutions, and during the interpolation process some of the values of k and ϵ can become negative, which is physically impossi-

ble. This problem is overcome by solving the k and ϵ equations only on the finest grid (and using the restricted values on coarser grids); all other mean-flow variables are solved by applying the multigrid algorithm as described above.

3.5 Source term modifications for rotating flows

Since the aim of this study is to investigate the application of the $k-\epsilon$ turbulence model (particularly the Launder-Sharma model) to predict the flow and heat transfer in a rotating cavity , it is useful to consider some of the well-known modifications which have made to it. The dissipation rate transport equation is not exact, but is devised largely by analogy with the more precise transport equation for k. As a result, some physical effects on the dissipation of turbulence energy are not accounted for fully (or in some cases at all) by the standard form of the ϵ equation, the deficiencies arising from the empirical nature of the source terms.

Deficiencies of the $k-\epsilon$ model have been investigated by many authors and have been compiled by Sloan et al (1986). The isotropic eddy-viscosity assumption in the $k-\epsilon$ model, or alternatively, an invariant C_μ coefficient in the equation for the eddy viscosity (see

equation 3.3) is not valid for complex flow. Turbulent flows that are influenced by anisotropic effects cannot be fully predicted by the standard $k - \epsilon$ model, and extra terms are needed to take into account the stresses due to vorticity and pressure fluctuations. Many attempts have been made to improve the $k - \epsilon$ model, and most of them fall into two categories: 1) streamline curvature corrections for recirculating flows (not necessarily swirling flows); 2) corrections for swirling flows.

These semi-empirical corrections may be considered either for the source - term of the dissipation equation (see Table 3.1), or modification to the eddy-viscosity formulation by expressing the C_μ coefficient as a function of curvature or rotation. Source - term modifications for swirling flows only are considered in this section.

A comprehensive study of the source term modifications is given by Mirzaee (1995, 1996) and only three important corrections are considered here: the Yap correction, rotation correction and gradient Richardson-number correction.

3.5.1 Yap correction

Yap (1987) introduced an empirical correction term, referred to here as YC, into the source term of the ϵ equation in the LS turbulence model. This term attempts to reduce unrealistically large levels of near-wall turbulence that are returned by the LS model in regions of flow separation. Craft et al (1992) showed that the unrealistic large peak in Nusselt number predictions for impinging flows using the LS model can be improved with the use of the Yap correction term.

Iacovides and Toumpanakis (1993) used the Yap correction for the flow in an axisymmetric rotor-stator system. They obtained improved predictions of the velocity field near the outer shroud, and this suggested that the prediction of the flow near the outer shroud in the peripheral flow case might also be improved. The Yap correction has been added to the LS model in this study, and the effect of this correction on the flow field is investigated in chapter 6. The axisymmetric ϵ transport equation in cylindrical polar co-ordinates (r, ϕ, z) may be written:

$$\frac{\partial}{\partial r}(\rho r V_r \epsilon) + \frac{\partial}{\partial z}(\rho r V_z \epsilon) = \frac{\partial}{\partial r}\left(r\Gamma_r \frac{\partial \epsilon}{\partial r}\right) + \frac{\partial}{\partial z}\left(r\Gamma_z \frac{\partial \epsilon}{\partial z}\right) + S_\epsilon \tag{3.20}$$

where

$$\Gamma_r = \mu + \frac{\mu_T}{\sigma_\epsilon}$$

$$\Gamma_z = \mu + \frac{\mu_T}{\sigma_\epsilon}$$

$$S_\epsilon = \frac{\epsilon}{k}(C_{\epsilon 1}P - C_{\epsilon 2}\rho\epsilon) + E - F$$

The Yap correction term, YC, is added to the ϵ equation for the low Reynolds number $k - \epsilon$ model, and can be written as (see Iacovides and Toumpanakis (1993)):

$$YC = max[0.83(\frac{l_\theta}{l} - 1)(\frac{l_\theta}{l})^2\frac{\epsilon^2}{k}\ ,\ 0] \tag{3.21}$$

where

$$l_\theta = \frac{k^{1.5}}{\epsilon} \qquad , l = 2.55y$$

and y is the normal wall distance.

3.5.2 Rotation correction

The influence of rotation on turbulence transport terms is described by Shao et al (1991). In summary, rotation appears to trap the energy in the large scales of motion, thus reducing the transfer of energy to small eddies. This is equivalent to a reduction in the dissipation rate of turbulence. In order to take into account for

this mechanism, Bardina et al (cited by Iacovides et al (1996)) proposed rotation-related modifications to the dissipation equation of the $k-\epsilon$ model. An empirical rotation correction term was devised by Iacovides and Toumpanakis (1993) and applied to an enclosed rotor-stator flow. An empirical rotation parameter, Λ, was used to reduce the generation of ϵ in the presence of rotation. This parameter may be written as:

$$\Lambda = ((\Omega - S)^2)^{\frac{1}{3}} \tag{3.22}$$

where the vorticity and strain invariants , Ω and S, are given by

$$S = \frac{k}{\epsilon}\sqrt{\frac{1}{2}S_{ij}S_{ij}} \tag{3.23}$$

$$\Omega = \frac{k}{\epsilon}\sqrt{\frac{1}{2}\Omega_{ij}\Omega_{ij}} \tag{3.24}$$

and

$$S_{ij} = \frac{1}{2}(\frac{\partial U_i}{\partial x_j} + \frac{\partial U_j}{\partial x_i}) \tag{3.25}$$

$$\Omega_{ij} = \frac{1}{2}(\frac{\partial U_i}{\partial x_j} - \frac{\partial U_j}{\partial x_i}) \tag{3.26}$$

Vorticity and strain terms for axisymmetric flow in the cylindrical polar (r, ϕ, z) co-ordinates may be written as:

$$\Omega = \frac{k}{\epsilon}[(\frac{\partial V_\phi}{\partial z})^2 + (\frac{\partial V_r}{\partial z} - \frac{\partial V_z}{\partial r})^2 + (\frac{\partial V_\phi}{\partial r} + \frac{V_\phi}{r})^2]^{\frac{1}{2}} \tag{3.27}$$

$$S = \frac{k}{\epsilon}[2(\frac{\partial V_r}{\partial r})^2 + 2(\frac{V_r}{r})^2 + 2(\frac{\partial V_z}{\partial z})^2 + (\frac{\partial V_\phi}{\partial r} - \frac{V_\phi}{r})^2 + (\frac{\partial V_r}{\partial z} + \frac{\partial V_z}{\partial r})^2 + (\frac{\partial V_\phi}{\partial z})^2]^{\frac{1}{2}} \tag{3.28}$$

Iacovides and Toumpanakis (1993) decreased the dissipation rate, ϵ, by reducing $C_{\epsilon 1}$ in equation 3.20 by factors of $(1 + 5\Lambda)$ and $(1 + 10\Lambda)$ for different flows. The following reduction to dissipation rate, taking turbulence levels into account, was used by Iacovides et al (1996) to control the level of turbulence in the outer region and in the centre of the cavity for enclosed rotating-disc systems:

$$C'_{\epsilon 1} = \frac{C_{\epsilon 1}}{[1+\alpha exp(\frac{\beta - R_t}{\beta})\Lambda]} \tag{3.29}$$

They optimized the values of α and β using the data of Itoh et al (1985) and of Cheah et al (1992), and found $\alpha = 10$ and $\beta = 50$ for these cases. The effect of this modification on the flow field in the present study is considered in chapter 6.

3.5.3 Gradient Richardson-number correction

In rotating-disc systems, tangential velocity profiles can often be interpreted in terms of combined vortex flow (free vortex + solid-body rotation). The nondimensional tangential velocity ($V_\phi/\Omega r$) in the flow field must go to zero at the axis of symmetry, or will be unity at a rotating surface (e.g. the inner rotating cylinder in the peripheral-flow case). Therefore, solid-body rotation must exist near a rotating surface where $V_\phi \rightarrow \Omega r$. Also, the tangential velocity must go to zero at a stationary surface (e.g. the stationary outer shroud in the peripheral flow case). Therefore, a free vortex must exist near a stationary shroud. Consequently, the flow field inside a rotating disc system may be explained by two vortex distributions. However, it is not fully understood to what extent the free vortex and the forced vortex flow will occur inside the cavity.

Sloan et al (1986) indicated that the $k-\epsilon$ turbulence model fails to create the proper size of the free-vortex and forced-vortex regions for rotating flows. Furthermore, the predicted radial velocity goes to zero more rapidly than the experimental data. It is suggested by many authors that the use of the *gradient Richardson-number* in the source term of the ϵ equation will give improved predictions for

the $k-\epsilon$ model. The physical meaning of the gradient Richardson-number is the ratio of an apparent body force (e.g. buoyancy, centrifugal, etc.) to a typical inertial force (see Sloan et al (1986)). The gradient Richardson number may be defined in either of the following ways:

$$(1) \qquad Ri_1 = \frac{2(V_\phi/r^2)(\partial/\partial r)(rV_\phi)}{(\partial V_z/\partial r)^2+[r(\partial/\partial r)(V_\phi/r)]^2} \tag{3.30}$$

$$(2) \qquad Ri_2 = \frac{k^2}{\epsilon^2}\frac{V_\phi}{r^2}\frac{\partial}{\partial r}(rV_\phi) \tag{3.31}$$

The denominator of Ri_1 and the term ϵ^2/k^2 in Ri_2 have dimensions of reciprocal time squared, and these are called mean-time scale and turbulent-time scale formulations respectively. By considering the above equations, it can be seen that the mean time scale Richardson number ,Ri_1, will go to infinity at solid body rotation, while the turbulent time scale formulation shows more realistic behaviour.

The modified source term of the dissipation equation may be written as:

$$S_\epsilon = C_{\epsilon 1}P\frac{\epsilon}{k} - (C_{\epsilon 2})_{eff}(\frac{\rho\epsilon^2}{k}) + E - F \tag{3.32}$$

where the $(C_{\epsilon 2})_{eff}$ is the effective $C_{\epsilon 2}$ and different definitions are used by different authors. Launder et al (1977) and Rodi and

Leschziner (1981) used the following definition:

$$(C_{\epsilon 2})_{eff} = C_{\epsilon 2}(1 - C_{gs}Ri) \tag{3.33}$$

where C_{gs} is the Richardson number coefficient. This has not been optimized for swirling flows in general and may be case-dependent. Referring to the definition for Ri, a positive gradient of angular momentum will tend to produce a positive Richardson-number which tends to increase the dissipation rate and decrease the length scale and eddy viscosity; vice-versa is true for a negative gradient of angular momentum. Using the equation 3.33, an arbitrary limit must be placed on the magnitude of the Richardson number to ensure positive values for $(C_{\epsilon 2})_{eff}$. The effect of this correction on the peripheral-flow problem will be described in Chapter 6.

Chapter 4

Validation of the code

4.1 Introduction

As described in chapter 3, an axisymmetric elliptic multigrid CFD solver is used to solve both laminar and turbulent flows. Before using this code for the case of rotating cavity with peripheral flow, it was necessary to validate the code for other rotating-disc systems for which experimental data or theoretical results were available. The computer program described in chapter 3 is that validated by Kilic (1993) for the free disc, enclosed rotor-stator and contra-rotating systems. The findings from this earlier work are summarized below.

For laminar flow, good agreement was achieved between the computed results and experimental/or theoretical data for velocity pro-

files without any serious convergence problems.

Kilic used two different low-Reynolds-number $k-\epsilon$ models, Launder and Sharma (1974) (LS) and Morse (1991) (M), to predict turbulent flow. He concluded that neither model was universally suitable for all the cases attempted, but both models gave satisfactory prediction of velocity profiles in most of the cases.

In this chapter, the code validation is extended to a rotating cavities with either a radial outflow or a radial inflow of fluid. Attention has been focussed only on isothermal laminar and turbulent flows: the code has been successfully used by Karabay (1995) to calculate Nusselt numbers for nonisothermal radial outflow case.

The basic flow structure for a rotating cavity with outflow and inflow is shown in Figures 1.3d and 1.3e respectively. As described in chapter 2, there are four important regions inside the cavity: the source region, Ekman-type layers on the discs, a sink layer and an interior inviscid core of rotating fluid. The fluid in the interior core between the Ekman-type layers rotates at a tangential velocity that is less than that of the disc for outflow and greater than that of the disc for inflow. (For convenience, the nondimensional mass flow

rate, C_W, is regarded as positive for radial outflow and negative for inflow.)

Several test cases were carried out using different mass flow rates and rotational Reynolds numbers for outflow and inflow, the computational results were compared with the experimental data obtained by Pincombe (1983). For all the test cases, a constant gap ratio (G = 0.133) was used, and other geometric quantities were set according to the experimental rigs. More information about the geometry of the experimental rigs and shrouds is given by Owen, Pincombe and Rogers (1985).

The computations were carried out using 115 x 91 and 115 x 115 non-uniform grids in the r-z plane for outflow and inflow respectively as shown in Figures 4.1a and 4.1b. The grid density was increased near the wall to resolve the boundary layers, ensuring $y^+ < 0.5$ on the solid surfaces for implementation of the turbulence equations into the laminar sub-layer, and a coarser grid was used outside the boundary layers to save computer time. For radial inflow, the number of the grid points across the cavity in the mid-plane was increased to predict accurately the strong jet in the source region.

Three levels of multigrid were applied in the computations, with the multigrid under-relaxation factor $\beta = 0.8$ and the Gosman factor (α_G) varied between 10 and 100. In general, different relaxation factors (between 0.4 and 1) were used for the velocity field and flow parameters. In order to avoid excessive computational time, the numerical solution was assumed to be converged when both RMS_{max} (equation 3.17) and the normalized maximum absolute residual ($\overline{R}_{max}$, equation 3.19) were less than 10^{-6}. Kilic (1993) showed that these two criteria are sufficent to obtain the converged solutions independent of the relaxation parameters.

The results of laminar flow computations are described in section 4.2 below, and results for turbulent flow are detailed in section 4.3.

4.2 Laminar flow in a rotating cavity

4.2.1 Radial outflow

According to Owen and Rogers (1995), flow in a rotating cavity with a radial outflow is laminar for $Re_r < 180$, and transition from

laminar to turbulent begins for $Re_r = 180$. For the laminar outflow case, $Re_r < 180$, three test cases were considered: $C_W = 253,\ 487$ and 689 with rotational Reynolds number $Re_\phi = 5$ x 10^4. Computational results were compared with the experimental data obtained by Pincombe (1983). Air enters the cavity axially for all cases except $C_W = 689$, in which case there is a radial inlet for the flow. Although the flow for these three cases was presumed to be laminar, two different turbulence models (LS and M) were used to test for laminarization. The boundary conditions used were as follows:

(i) no slip velocity conditions at all the walls;

(ii) uniform inlet and outlet velocity distributions for the radial and axial components of velocities;

(iii) zero swirl at inlet;

(iv) Derivative boundary conditions for tangential component of velocity in the outlet region ($\frac{\partial V_\phi}{\partial r} = 0$ *or* $\frac{\partial V_\phi}{\partial z} = 0$).

Figure 4.2 shows the effect of C_W on the flow structure using both the (LS) and the (M) models. The radial extent of the source region increases as the mass flow rate increases. With reference to this figure, the source region divides the flow into two main parts: a wall jet on the downstream disc and-free disc behaviour on the upstream disc. There are only small differences between the streamlines pre-

dicted by the two models.

Figure 4.3 shows the effect of nondimensional mass flow rate, C_w, on the radial variation of the tangential component of velocity, ($V_\phi/\Omega r$, measured at $z/s = 1/2$), for laminar flow: $Re_r < 180$ and $Re_\phi = 5$ x 10^4. Referring to these plots, the measured velocities are in reasonable agreement with both the (LS) and the (M) turbulence models.

As there are no radial and axial components of velocity in the interior core for the results shown in Figure 4.3, a Rankine vortex would be expected to occur (see Owen and Rogers (1995)) such that

$$\frac{V_\phi}{\Omega r} = A + Bx^{-2} \tag{4.1}$$

where A and B are constant. For laminar source-sink flow, the exact solution of the Ekman-layer equation (see Hide 1968) is given by

$$\frac{V_\phi}{\Omega r} = 1 - \frac{1}{2\pi}\lambda_L x^{-2} \tag{4.2}$$

such that $A = 1$ and $B = -\lambda_L/2\pi$. Curves showing the Rankine vortex, with the above values of A and B, are shown in Figure 4.4 together with the computed results and the experimental measurements. It should be noted that the region where $x^{-2} < 1$ is outside the cavity and has no physical meaning. The Rankine-

vortex curves are not appropriate near $x = 1$, where the sink-layer occurs, or for small values of x, where the source-region is formed.

4.2.2 Radial inflow

In the second part of the laminar investigation for the rotating cavity, the code was applied to the laminar radial inflow case with $Re_r < 180$. The results were compared with the experimental data obtained by Pincombe (1983) with the use of different shrouds: F and A. Each shroud provides a different inlet swirl ratio: $c = 1.0$ for shroud F and $c = 0.59$ for shroud A was suggested by Owen and Rogers (1995).

For shroud F, three test cases were considered using the LS model at almost constant mass flow rate and three different Reynolds numbers: $Re_\phi = 3.45\text{x}10^5$ and $C_W = -399$, $Re_\phi = 1.97\text{x}10^5$ and $C_W = -440$ and $Re_\phi = 9.85\text{x}10^5$ with $C_W = -440$. Three cases were also considered for shroud A using the LS model: $Re_\phi = 6\text{x}10^5$ and $4\text{x}10^5$ with $C_W = -309$ and $Re_\phi = 1.97\text{x}10^5$ and $C_W = -440$. It should be noted that shroud A contained 30 holes in the middle, and the computational model was based on an equivalent area cir-

cumferential slot.

In the computations, the flow entered cavity radially at r=b with varying swirl ratio ($c = 0, 0.2, 0.4, 0.6, 0.8$ and 1.0) and left the cavity axially at r=a. For the computational model, a uniform radial velocity and zero axial velocity were used at the inlet and vice versa for the outlet. Derivative boundary conditions were applied for the tangential velocity at the outlet. Before comparing the computational results with the experimental data, particular attention is given to the effect of swirl ratio on the flow field.

Figure 4.5 shows the effect of inlet swirl ratio on the laminar flow structure. This figure illustrates four main regions inside the cavity as described in Chapter 2: source region, separate Ekman-type layers on each disc, sink region and an interior inviscid core. With reference to this figure , it can be seen that the mixing layer and entraining region are present inside the source region. The mixing layer and entraining region are located, respectively, above and below the source region. The radial extent of the source region increases with decreasing inlet swirl ratio.

Figure 4.6 illustrates the variation of the tangential component of

velocity with radius for laminar inflow using shroud F, $c = 1.0$. Referring to this figure, the computational results overestimate the experimental data. Figure 4.7 shows the variation of tangential component of velocity with x^{-2} for the above case. Referring to this figure, it can be observed that, although there is a systematic difference between the LS model and the experimental data, both show the Rankine vortex behaviour inside the core.

Figure 4.8 shows the variation of tangential component of velocity with radius for laminar inflow using shroud A, $c = 0.59$. Referring to these plots, and also to the variation of tangential component of velocity with x^{-2} shown in Figure 4.9, it can be seen that Rankine vortex behaviour exists inside the core for all of the cases, and the computational results overestimate the experimental data. Analyzing the results for shroud F and A shows that the nondimensional tangential velocity increases as rotational Reynolds number decreases for both experiments and computations.

In order to predict the effect of inlet swirl ratio, c , computer runs were carried out for laminar inflow with different values of c. Figure 4.10 shows the effect of c on the radial variation of the tangential component of velocity for $Re_\phi = 1.97\text{x}10^5$ and $C_w = -440$. The

experimental data are those reported by Pincombe (1983) using different shrouds F and A. It is apparent that there is no single value of c which gives good agreement between the computations and measurements for all values of x.

For a better understanding of the effect of inlet swirl ratio, the variation of tangential velocity with x^{-2} is plotted in Figure 4.11. This plot shows the existence of a thin mixing layer in vicinity of x=1 where there is a large tangential velocity gradient, a free-vortex region inside the source region and a Rankine-vortex region inside the core. It should be noted that for the free vortex and Rankine-vortex regions there is a linear variation between the nondimensional tangential velocity and x^{-2}, and it passes through the origin for the free vortex and far from origin for the Rankine-vortex case. The thin mixing layer, in which $c \rightarrow c_{eff}$, is followed by a quasi-inviscid region. In the free-vortex region, where the angular momentum is constant, the variation of tangential velocity may be written as:

$$V_\phi/\Omega r = c_{eff} x^{-2} \tag{4.3}$$

where c_{eff} is the effective swirl ratio, not in general equal to c. It follows that

$$c_{eff} = x_e^2 \tag{4.4}$$

where x_e is the nondimensional radius at which $V_\phi/\Omega r = 1$ in the midplane.

Referring again to Figure 4.11, although the experimental results and computer predictions are different, they show similar behaviour inside the cavity. The tangential velocity increases as the swirl ratio increases, but the predictions corresponding to c=0.59 for shroud A and c=1.0 for shroud F overestimate the experimental data.

4.3 Turbulent flow in a rotating cavity

As mentioned earlier, the flow in a rotating cavity with a radial outflow or a radial inflow can be considered to be turbulent when the radial Reynolds number, Re_r, is greater than 180. Several test cases were computed for turbulent radial outflow using both the LS and M models , and some tests were also undertaken for turbulent radial inflow using only LS model.

4.3.1 Radial outflow

Initially, attention is focussed on the effect of nondimensional mass flow rate, C_W, on the turbulent flow structures, as shown in Figure 4.12. It can be seen that similar streamlines are predicted using either the LS or M model. The radial extent of the source region increases as the mass flow rate increases. The existence of the four important regions mentioned previously (in chapter 2) are also well predicted.

Three test cases were considered with constant mass flow rate, $C_W = 2500$, and three different rotational Reynolds numbers: $Re_\phi =$ 8.17x10^5, 5.47x10^5 and 1.1x10^6. Variation of the computed tangential component of velocity with radius in the mid-plane ,z/s = 0.5, is shown in Figure 4.13 in comparison with experimental data. Both experimental and computed results were made with an axial inlet into the cavity. There is good agreement between the experimental results and the computations , particularly for the LS model. To explain more about the flow behaviour inside the core region, the variation of the tangential component of velocity with x^{-2} is shown in Figure 4.14. Similar to the laminar flow behaviour, this shows evidence of Rankine vortex flow inside the core region for both com-

putations and experiments.

Finally, four test cases were considered to investigate the effect of nondimensional mass flow rate on the axial distribution of the radial component of velocity, $V_r/\Omega r$, in the boundary layer: C_W = 772, 1092, 1544 and 2184 with $Re_\phi = 4\text{x}10^5$. This effect is shown in Figures 4.15 and 4.16 for x=0.633 and 0.833 respectively. The nondimensional axial direction, η, is defined as

$$\eta = (\Omega/\nu)^{1/2} z \tag{4.5}$$

Referring to these figures, the thickness of the boundary layer increases as C_W increases. There are only small differences between the velocity profiles computed from the two models, and the agreement between the computed results and the experimental data is mainly good.

4.3.2 Radial inflow

For turbulent radial inflow the effect of inlet swirl ratio, c , on the flow structure is considered first. Figure 4.17 shows the streamlines predicted using the LS model at different inlet swirl ratios (between 0 and 1) for $Re_\phi = 1.97\text{x}10^5$ and $C_W = -1415$. Comparing this

figure with the streamlines predicted for the laminar inflow, Figure 4.5, it can be seen that both figures indicate the existence of the four main regions already mentioned, and that the radial extent of the source region increases as inlet swirl ratio decreases.

Three test cases were carried out using the LS model with almost constant mass flow rate and three different Reynolds numbers: $C_W = -1425$ and $Re_\phi = 9.85$ x $10^4, C_W = -1396$ and $Re_\phi = 1.97$ x 10^5 and $C_W = -1310$ with $Re_\phi = 3.45$ x 10^5. The inlet swirl ratio, c , was assumed to be 1 for all three cases, and the computed results were compared with the experimental data obtained using shroud F, for which $c \simeq 1$. The computed radial variation of the nondimensional tangential component of velocity, $V_\phi/\Omega r$, with radius, and comparison with the experimental data are shown in Figure 4.18. The computational results overestimate the experimental data (this is consistent with the laminar radial inflow results illustrated in Figure 4.8, but the agreement is less good for turbulent flow). Figure 4.19 shows the variation of $V_\phi/\Omega r$ with x^{-2}. Rankine vortex behaviour occurs inside the core region, but for all three cases there is a systematic difference between the computations and experiments.

In further work, another three test cases were considered using the

LS model for shroud A (c = 0.59): $C_W = -1415$ and $Re_\phi = 1.97$ x 10^5, $C_W = -946$ and $Re_\phi = 4$ x 10^5 and $C_W = -946$ and $Re_\phi = 6$ x 10^5. Computational and experimental results for the radial variation of $V_\phi/\Omega r$ are shown in Figure 4.20. Referring to this figure, and also to the variation of $V_\phi/\Omega r$ with x^{-2} shown in Figure 4.21, it can be seen that Rankine vortex behaviour exists inside the core for all the cases, but again the computational results overestimate the experimental data.

The final investigation for the rotating cavity with a radial inflow is to compute the effect of inlet swirl on the tangential component of velocity. The code used to solve for turbulent inflow for $Re_\phi = 1.97$ x 10^5, $C_W = -1415$ and six different inlet swirl ratios (varying between 0 and 1). Four sets of experimental data were available using different shrouds A, B, E and F (where the swirl ratio of the incoming fluid, c, was less than unity). Figure 4.22 shows the effect inlet swirl ratio on the radial variation of $V_\phi/\Omega r$ together with the experimental data reported by Pincombe using the different shrouds. It is apparent that the tangential component of velocity increases as the inlet swirl ratio increases. For a better understanding of the effect of inlet swirl ratio , the variation of tangential component of velocity with x^{-2} is plotted in Figure 4.23. Although the computations

corresponding to c=0.59 for shrouds A and B, c=0.4 for shroud E and c=1 for shroud F overestimate the experimental data, they do show similar behaviour inside cavity.

4.4 Conclusions

Application of the CFD solver described in chapter 3 has been applied to rotating cavities with laminar and turbulent radial outflow and inflow. The computed results were compared with the experimental data obtained by Pincombe (1983).

For the case of radial outflow, good agreement between the experimental results and computations was achieved using both the LS and M models for laminar and turbulent flow. Rankine vortex behaviour occurred inside the core for all the cases.

For the case of radial inflow, several test cases were considered using the LS model for both laminar and turbulent flows. Computational results overestimated the experimental data for both laminar and turbulent flows, and the agreement is less good than for outflow. The overprediction of the experimental results may be due in part to the three-dimensional effect of discrete inflow nozzles in the experiment, or to the existence of recirculating flow near the inlet in the computations, which may not be predicted with complet ac-

curacy by isotropic $k - \epsilon$ turbulence models. Although there is a systematic difference between the computations and experiments, both show the Rankine vortex behaviour in the core region.

The performance of the LS model in computing the flow and heat transfer in a rotating cavity with stationary outer casing, where both radial inflow and outflow occur, will be discussed in Chapters 6 and 7.

Chapter 5

Experimental apparatus

5.1 Introduction

Since the experimental measurements presented in this thesis were not made by the author, and they are used solely for comparison with the computational results, only a short description of the rigs is presented. For more details of the design and construction the reader is referred to Gan (1994) and Quinn (1997).

The experimental rigs were developed in the School of Mechanical Engineering, University of Bath, under funding from the BMW-Rolls-Royce (BRR), to study a turbine disc-cooling arrangement in which cooling air entered and left at the periphery of the rotating cavity between the turbine discs. Two different rotating-cavity rigs

were used: the "flat-shroud" rig and the "stepped-shroud" rig. Experiments in these rigs were conducted by Dr X. Gan and Dr P. Quinn respectively.

Schematic diagrams of the rotating cavity with flat shroud and stepped-shroud are given in Figures 5.1a and 5.1b, and descriptions of these rigs are presented in sections 5.2 and 5.3 respectively.

5.2 Flat-shroud rig

Fig. 5.1a shows a schematic diagram for the rotating cavity with a stationary flat shroud. The test rig comprised two discs of 762 mm diameter spaced an axial distance of 113 mm apart (G=0.30). The inner rotating cylinder was 381 mm in diameter (2a=381mm), and the outer stationary cylinder was located at radius b=381 mm (a/b = 0.5). The two discs and inner cylinder which were linked together, could be rotated at the same speed using a single 15KW thyristor-controlled electric motor. Disc 1, which could be heated, was made from steel, and disc 2, which provided flow visualization and optical access for the LDA measurements, was made from transparent polycarbonate. Disc 2 allowed laser Doppler anemometry (LDA) tests to be conducted up to 1500 rev/min. For high-speed tests, not presented here, a steel disc was used for disc 2. The surfaces of

the outer stationary casing and inner rotating cylinder were insulated with Rohacell, a lightweight foam with thermal conductivity of k$\simeq$ 0.03 W/mK.

The two discs were located in a stationary steel casing, producing a rotor-stator system on each side. In these two regions, compressed air was used to balance the pressure in the central cavity and to reduce the air leakage across the radial seals at the tip of the discs (the seals had a clearance of 0.7 mm when the discs were stationary). The cooling air entered the rotating cavity with zero inlet swirl ratio, $c = 0$, through 38 holes of 11.3 mm diameter, located in the middle of the stationary outer shroud. The air left the cavity at its periphery through 1 mm clearances between the discs and the stationary casing.

Details of the LDA measurements and associated facilities are given by Gan (1994), and only an outline of the velocity measurements is considered here. In order to carry out the LDA tests, a window was provided in the steel casing next to the polycarbonate disc. The window was covered with a clear polycarbonate plate to keep the side cavity enclosed. In the axial direction, measurements were made in terms of tangential and radial components of velocity at

three radial locations: x=0.55 , 0.75 and 0.85. In the radial direction, only the tangential component of velocity was measured in the midplane of the cavity, z/s=0.5, and also in some cases at z/s=0.8. Using the LDA system, it was possible to obtain measurements on the solid polycarbonate disc. The measured tangential velocity, V_ϕ, on the polycarbonate disc was found to be within 1 percent of the disc speed; this gave confidence in the accuracy of the LDA measurements.

For heat transfer measurements, the back face of disc 1 was heated up to 100 C by six radiant heater elements with a total output of up to 21 KW. The heater elements were controlled by a three-phase thyristor controller. The front face of disc 1 was coated with a fibre glass mat, about 1 mm thick and with thermal conductivity k$\simeq$ 0.27 W/mK. Ten RdF fluxmeters were embedded in the fibre-glass coated disc, and also T-type thermocouples were mounted at the same radial location as the flux meters, with about a 7 degree angular separation from the flux meters. This instrumented disc had been calibrated and tested by Chen et al (1995) in experiments on contra-rotating discs. The signals from the thermocouples and fluxmeters were taken out through a silver/silver graphite slipring unit, and voltages were measured by a computer-controlled data-

logger and digital voltmeter with a resolution of $\pm 1\mu$V.

5.3 Stepped-shroud rig

The rig described above was subsequently modified for different geometries and flow conditions. Schematic diagram of the modified rig, called the stepped-shroud rig, is shown in Figure 5.1b. Compared with the previous rig, the following changes were made:

1) A stepped-shroud with a 76 mm x 58 mm (r x z) rectangular cross-section was used instead of the flat shroud.

2) The outer radius of the cavity was increased to b=411 mm, using carbon-fibre rings attached to the periphery of the discs. The inner radius, a , and the axial distance between the two discs, s , were also increased to 205.5 mm and 120 mm respectively, in order to keep the values for a/b (=0.5) and the gap ratio (G=0.3) the same for both cases.

3) The air entered the cavity with solid-body rotation and with a constant angle, $\theta = 24.5$ degrees, through 74 holes of 8.6 mm di-

ameter, located on the left-hand side of the carbon-fibre ring. The air left the cavity radially through either or both of the clearances illustrated in Figure 5.1b: The clearance number 1 is 3 mm and number 2 is 2mm.

The experiments were conducted for three different values of the parameter Γ, representing the distribution of flow between two outlets: $\Gamma = 1, 0$ and $\Gamma \rightarrow \infty$ where Γ is defined as

$$\Gamma = \frac{C_{W1}}{C_{W2}} \tag{5.1}$$

where C_{W1} and C_{W2} are nondimensional mass flow rates at clearances 1 and 2 shown in Figure 5.1b.

LDA velocity measurements were not made, and only heat transfer measurements are reported in this thesis. The nondimensional mass flow rate , C_W, was varied between -1500 and -24000 in five steps, and the rotational Reynolds numbers was varied between 3.8 x 10^5 and 3.5 x 10^6 in four steps.

Chapter 6

Flow and heat transfer for the flat-shroud case

6.1 Introduction

In this chapter, flow and heat transfer in a rotating cavity with peripheral inflow and outflow is considered for the flat-shroud case. The simplified computational model, corresponding to the experimental rig described in chapter 5, is shown in Figure 6.1. In the experiment, as discussed in chapter 5, air enters the cavity through series of holes ; in the computational model, an annular slot is used. The computations described in this thesis were performed using a slot width of 11mm (close to the diameter of the holes in the rig). The sensitivity of solutions to the prescribed inlet slot width is de-

scribed in section 6.4.

As shown in Figure 6.1, the model comprises two corotating discs of radius b (= 381 mm) spaced an axial distance s(=113 mm) apart (G = 0.30) , an inner cylindrical surface rotating at the same speed as the discs at radius a (a/b = 0.5), and an outer stationary cylindrical surface (or "flat-shroud") at radius b. A cylindrical-polar coordinate system (r, ϕ , z), with its origin at the centre of the left hand side disc, is used. Air enters at the periphery of the cavity with zero swirl, and leaves through 1 mm axial clearances between each of the rotating discs and the stationary outer cylinder.

For the flow investigation, attention is focussed in section 6.2 on the sealed cavity. Superposed flow is considered in section 6.3, and a parametric study is presented in section 6.4, varying the geometrical quantities (G, slot-width and slot spacing) and flow parameters (Re_ϕ, C_W and λ_T).

The heat transfer investigation is considered in section 6.5. The left-hand disc is heated and the computed Nusselt numbers, Nu, for this disc are compared with the experimental data. Conclusions for both the flow and heat transfer studies are given in section 6.6.

6.2 Sealed cavity

For the case of an isothermal rotating cavity with a rotating shroud, solid-body rotation occurs when there is no superposed radial inflow or outflow. For the case of a stationary outer shroud, however, solid-body rotation cannot occur throughout the cavity, owing to the shear stress exerted by the shroud. Therefore, it is useful to consider the zero flow case before showing the effect of superposed flow.

The sealed cavity investigation is described in three subsections. In section 6.2.1, the flow field is computed using both laminar and LS models, and the results are compared with the LDA measurements of Gan (1994). As described above, the dimensions of the computational domain are the same as those for the experimental rig, where G=0.3 and a/b = 0.5. The study of ingress and source term modifications for the LS model are described in sections 6.2.2 and 6.2.3 respectively.

6.2.1 Computation of flow in the sealed cavity

For the sealed cavity ($C_W = 0$), four cases were considered with different rotational Reynolds numbers: $Re_\phi = 10^4, 1.46$ x 10^5, 3.75 x 10^5, and 1.5 x 10^6. Computations were carried out using both laminar and LS models except for the highest Reynolds number case where only the LS model was considered.

In general, the computations were carried out using a 91 x 131 non-uniform grid in the r-z plane. For some cases, grid independence was demonstrated by also using a 67 x 67 grid. A typical grid distribution is illustrated in Figures 6.2. In order to keep y^+ values less than 0.5 at solid surfaces, and to obtain a converged solution, different geometric expansion factors were used for individual cases.

Figures 6.3a to 6.3d show the streamlines in the cavity for different Reynolds numbers using both laminar and LS models. For $Re_\phi = 10^4$, the predicted streamlines for both models are virtually the same and the source region occupies most of the cavity. For the higher Reynolds numbers , there is a difference between the streamlines predicted by the LS and laminar models, particularly at $Re_\phi = 3.75$ x 10^5 where the two flow structures are significantly

different.

In all cases, there is radial inflow in the mid-plane (z/s=0.5) and outflow in the boundary layers on the discs. Although the streamlines show symmetry with respect to the mid-plane, the wavy behaviour in the mid-plane for some cases may indicate a tendency toward instability. This may imply that although a steady axisymmetric solution is possible for these cases, the real flow may be unsteady and three-dimensional, as reported by Abrahanson et al (1989) and Arnold (1996).

Figures 6.4a to 6.4d show the variation of $V_\phi/\Omega r$ with x and x^{-2} for the four different rotational Reynolds numbers. For $Re_\phi = 10^4$, where the computed flow is laminar, Figure 6.4a shows good agreement between the two models.

For Re_ϕ = 1.46 x 10^5, Figure 6.4b shows that the laminar solution departs from the LS model for $x \leq 0.65$, and transition occurs in this region. Referring to the variation with x^{-2}, it can be seen that Rankine-vortex flow occurs over most of the cavity according to the experimental data. The comparison is made at $z/s = 0.8$, the locations at which the experimental data were obtained. The

figure reveals that the computed core rotation is significantly larger than the measured value.

For Re_ϕ = 3.75 x 10^5 and 1.5 x 10^6, referring to Figures 6.4c and 6.4d, although there is not good agreement between the experimental data and the LS model , both show Rankine-vortex behaviour (which is close to free-vortex behaviour) in much of the cavity. However, the results show that the extent of this region in the experiments is much greater than in the computations. This implies that most of the cavity is occupied by the source region in the experiments.

For some of the above mentioned cases, grid-independence results for the variation of the tangential velocity with x and x^{-2} are shown in Figures 6.5a to 6.5c. Two different grids were used: 67 x 67 and 91 x 131 in r-z plane. As can be seen, there are only very small differences between the two sets of computations, and the differences between them is much smaller than those between the measurements and the computations.

Figure 6.6 to 6.9 show the axial variation of the radial and tangential components of velocity. As discussed earlier, for $Re_\phi = 10^4$

there is good agreement between the laminar and turbulent models. An increase in the Reynolds number to Re_ϕ = 1.46 x 10^5 leads to transition, as shown in Figure 6.7. For the higher values of Re_ϕ, Figures 6.8 and 6.9 show that the tangential component of velocity is nearly invariant with z/s outside the boundary layer. For these cases, there is reasonable agreement between measured values of $V_r/\Omega r$ and the values computed with the LS model, especially for the boundary layers, but the agreement for the tangential velocity is poor.

Grid-independence results for these cases are shown in Figures 6.10 to 6.12 with the use of two different grids: 67 x 67 and 91 x 131 in the r-z plane. For Re_ϕ = 1.46 x 10^5, the results show slight grid-dependence for the radial component of velocity near the axial mid-plane. However, the results show good agreement for the boundary layers on the discs and for tangential velocity distributions, which are important for the disc moment coefficient and Nusselt number results. For the higher Reynolds numbers, there is very little grid-dependence in terms of both radial and tangential components of velocity.

As explained in Chapter 2, Abrahamson et al (1989) found that

the flow in a sealed cavity could be highly three dimensional due to the effect of a stationary casing. They also measured the tangential component of velocity in the mid-plane of a cavity with narrow gap ratio (G=0.05) for $Re_\phi = 4.5 \text{ x } 10^5$. In order to validate the code further, this case was computed using the LS model. Figure 6.13 shows the variation of the computed and measured values of $V_\phi/\Omega r$ with x^{-2}. Although agreement between the two results is reasonable, the computed values overestimate the experimental data in the source region.

Lewis (1997) carried out a numerical investigation of the flow in a sealed rotating cavity with stationary shroud. He used a Direct Numerical Simulation (DNS) procedure to study the stability of the flow. Direct numerical simulations of selected cases showed a highly unstable flow structure for $Re_\phi = 10^4$ and above. For $Re_\phi = 1.46 \text{ x } 10^5$, as shown in Figure 6.14, the DNS solution gave rise to time-averaged results in good agreement with experimental data for tangential velocity. Time-dependent computations for $Re_\phi = 1.46 \text{ x } 10^5$ were carried out on a nonuniform 97 x 129 grid in r-z plane using a time step (determined by numerical stability tests) of $\Delta t = 2.8 \text{ x } 10^{-4}$ seconds.

As discussed earlier, the agreement between the computations and experiments for the sealed system was relatively poor, particularly for the tangential component of velocity. In order to investigate this problem further, several possible reasons for the poor agreement including physical effects and computational deficiencies were considered. The effects considered included: roughness of the inner and outer cylindrical surfaces of the experimental rig (see Figure 5.1a); possible ingress of external fluid through the seals in the rig; inadequacy of the turbulence model; 3-D effects in this type of flow as mentioned by Abrahanson et al (1989); and instability of the flow as found by Lewis (1997).

The average roughness of the inner and outer surfaces was approximately 30 μm. In order to investigate the roughness effect, some velocity measurements were repeated after smoothing of the outer and inner surfaces to give average surface roughness of around 8 μm. (Computational results were used to confirm that the thickness of the viscous sublayer was greater than 8 μm, so that the smoothed surfaces were considered to be "aerodynamically smooth".) The new results will be shown in the next section together with the original results wherever appropriate.

The effect of ingress on the flow field is described in section 6.2.2. The testing of several modifications, for source-term in the ϵ equation of the low-Reynolds-number $k - \epsilon$ model, is considered in section 6.2.3.

6.2.2 Effect of ingress on the flow field

The possibility of ingress being present in the experimental rig may have been the cause of the poor agreement between experimental data and computed results. To investigate this effect further, the blockage method described by Patankar (1980) was used for computations of a sealed cavity with an extended solution domain.

Figure 6.15a shows the schematic diagram of the computational domain used to investigate the ingress problem. The grid distribution and streamlines for Re_ϕ = 1.46 x 10^5 are shown in Figures 6.15b and 6.13c respectively. Figure 6.15c shows that there is no flow in the extended domain used to permit ingress into the rotating cavity. For closer analysis of any ingress, Figure 6.16 illustrates the axial variation of the radial component of velocity at x=1 and x=0.84. As shown in this figure, insignificant ingress (see x=1) is present in the flow field and the effect can be neglected.

6.2.3 Source term modifications

The aim of this section is to investigate the effect of some source term modifications to the low Reynolds number $k - \epsilon$ Launder-Sharma (LS) model. The modifications, to the dissipation equation, ϵ, were described in chapter 3. Three corrections to the source-term of the ϵ equation are considered here: the Yap , the rotation and the Richardson number corrections (see equations 3.21, 3.29 and 3.33). For the Richardson correction, a wide range of values for the constant C_{gs} (between 0 and 1) was tested by Mirzaee (1996). It was found that a value of 0.7 optimised predictions for the peripheral flow case.

Figures 6.17a to 6.17c illustrate the effect of the corrections on the variation of $V_\phi/\Omega r$ with x and x^{-2}, for $C_W = 0$ and $Re_\phi = 1.46$ x 10^5, 3.75 x 10^5 and 1.5 x 10^6 respectively. It should be noted that two sets of experimental data are shown for the comparison with the computations: rough and smooth results as mentioned in the previous section, and the difference between the two sets of measurements increases as Re_ϕ increases.

These figures indicate that the Yap correction has no significant

effect, but the rotation correction and the Richardson correction both affect the $V_\phi/\Omega r$ values. Considering the effect of the rotation correction, the computed $V_\phi/\Omega r$ are improved at large values of x but not at small values. When $V_\phi/\Omega r$ is plotted against x^{-2}, as shown in the Figure 6.17, the experimental data shows the Rankine vortex behaviour, but the computed results with the rotation correction do not.

Referring to the Richardson correction results, it can be seen that this correction significantly improves the results from the LS model. The variation of $V_\phi/\Omega r$ with x^{-2} in the above figures shows that the Richardson correction tends to laminarize the flow field at small values of x (evidence of solid-body rotation at small values of x), and increases the level of the turbulence in the recirculation region: a stabilizing effect near the inner shroud and a destablizing effect in the recirculation region. The LS model with Richardson correction gives Rankine vortex behavior in most of the cavity, which is consistent with the experimental data.

Figs 6.18 to 6.20 show the effect of the corrections on the axial variation of $V_r/\Omega r$ and $V_\phi/\Omega r$ for $C_W = 0.0$ and $Re_\phi = 1.46$ x 10^5, 3.75 x 10^5 and 1.5 x 10^6 respectively. Again, two sets of experi-

mental data are shown for the comparison with the computations: rough and smooth results. For Re_ϕ = 1.46 x 10^5, Figure 6.18, the Yap correction has no significant effect but the rotation and the Richardson corrections affect both V_r and V_ϕ.

The rotation correction tends to create turbulent flow. This gives better agreement between the computed and measured values of V_r in the core (where the experimental data suggests turbulent flow and the computed LS model produces laminar flow) and worse agreement in the boundary layers (where the data and the LS model both indicate laminar flow). For $V_\phi/\Omega r$, the rotation correction gives better agreement at larger values of x (x $\geq$ 0.75) but worse agreement at small values of x (x $\leq$ 0.55). Broadly similar results can be seen in Figures 6.19 and 6.18, but the agreement between the computations of $V_\phi/\Omega r$ using the rotation correction terms and the experimental data becomes worse as Re_ϕ increases. It can also be seen that the magnitude of the correction itself decreases as Re_ϕ increases.

The agreement between experimental data and computed results is improved by the use of the Richardson correction. It is worth noting that although the Richardson-number correction improves

the tangential velocity distribution, it does not significantly affect the radial velocity distribution inside the boundary layers on the discs.

6.3 Superposed flow

In this section, computations for superposed flow cases are compared with the LDA measurements of Gan (1994). Four cases are considered, using two different Reynolds numbers and two mass flow rates: Re_ϕ = 1.5 x 10^6 and 3.75 x 10^5, $C_W = -1500$ and -3000, such that $|\lambda_T| = 0.0172,\ 0.034,\ 0.052$ and 0.104.

Although in the experimental rig the superposed flow entered through a series of holes located in the stationary shroud, computations were carried out using a slot in the middle of the shroud. The air was assumed to enter the cavity with uniform radial velocity, and the axial and tangential components of velocity were zero. Equal mass flow rates were fixed for both outlets, with uniform radial velocity imposed to ensure a mass balance between the inflow and outflows. Derivative boundary condition was used for the tangential component of velocity in the both outlets ($\frac{\partial V_\phi}{\partial r} = 0$).

No-slip boundary conditions were used for the velocity components parallel to the wall. A grid with 91 x 91 nodes in the r-z plane was used for the computations.

The flow field computed using the LS model is considered in section 6.3.1, and effects of the source term modifications are investigated in section 6.3.2.

6.3.1 Flow field using LS model

Figure 6.21 shows how the streamlines vary with Re_ϕ and C_W. It can be seen that the radial extent of the recirculating region increases with increasing $|\lambda_T|$.

Figures 6.22a to 6.22d show the variation of $V_\phi / \Omega r$ with x and x^{-2}, in the mid-plane (z/s=0.5), for $C_W = -1500$ and -3000, and $Re_\phi =$ 1.5 x 10^6 and 3.75 x 10^5 , such that $|\lambda_T| = 0.0172,\ 0.034,\ 0.052$ and 0.104 respectively. For $|\lambda_T| = 0.0034$ and 0.104, two sets of experimental data are shown: smooth data and rough data. For $|\lambda_T| = 0.0034$, there is a significant difference between the rough and smooth results. The differences between the two sets of mea-

surements reduces as $|\lambda_T|$ increases. This implies that the effect of the stationary shroud decreases as $|\lambda_T|$ increases, so that any roughness effect decreases as $|\lambda_T|$ increases.

The comparison between computations and experimental data given in Figures 6.22a to 6.22d show that, except for the largest value of λ_T and the smallest value of x for which tangential velocities were measured, the computed velocities are larger than the measured values. The experimental data follow the Rankine-vortex behaviour, and the trend is towards a free vortex as $|\lambda_T|$ increases, and agreement between the computations and experiments improves as $|\lambda_T|$ increases.

Figures 6.23 to 6.26 show the axial variation of $V_r/\Omega r$ and $V_\phi/\Omega r$ at x=0.55, 0.75 and 0.85 for values of $|\lambda_T|$ corresponding to those in Figs 6.22a to 6.22d. For $V_\phi/\Omega r$, there is a little axial variation in either the measured or computed values and, as noted above, agreement improves as $|\lambda_T|$ increases. For $V_r/\Omega r$, the agreement between the measured and computed values appears to be worse as $|\lambda_T|$ increases.

The following effects may explain some of the differences between

the computational results and the experimental data: 3-D effects; roughness effects; unsteadiness and turbulence model deficiencies. The experimental results showed that the roughness may be neglected as $|\lambda_T|$ increases. As explained in Chapter 5, the air enters the cavity through 38 holes while the computational model is based on a slot. Therefore, 3-D effects may be important at high values of $|\lambda_T|$, where there is an interaction of 3-D jets inside the cavity in practice. The effect of source-term modifications to the LS turbulence model for superposed flow cases is considered below.

6.3.2 Source term modification

The effect of three corrections (Yap, rotation and Richardson-number corrections) were investigated in section 6.2.3 for a sealed cavity. It was concluded that the effect of the Yap correction was negligible for such flows, therefore in this section the effect of only two corrections (rotation and Richardson-number) are considered for the superposed-flow case.

Figures 6.27a to 6.27d illustrate the effect of these two corrections on the variation of $V_\phi/\Omega r$ with x and x^{-2} for the superposed flow cases described in section 6.3.1. In all the cases, there is a signif-

icant effect of the rotation correction on the tangential velocity at large values of x, and the effect becomes negligible at small values of x. In general , the effect of the rotation correction decreases as $|\lambda_T|$ increases.

Referring to the curves for the Richardson-number correction, it can be seen that the agreement between the experimental data and the computed results is improved, particularly at small values of x. In spite of systematic differences between the measurements and computed results using the Richardson- number correction, both show Rankine-vortex behaviour over most of the cavity. The Richardson-number correction mainly improves computations in the entraining region, where $V_r/\Omega r$ decreases as x decreases.

The effect of the corrections on the axial variation of $V_r/\Omega r$ and $V_\phi/\Omega r$ for the above cases is shown in Figure 6.28 to 6.31. Referring to these figures, the rotation correction has a relatively small effect on the computed values of V_r and V_ϕ. In general, with the use of this correction, the thickness of the boundary layers on the discs increases slightly (the data and the LS model both indicate thin boundary layers on the discs). The Richardson-number correction creates laminar flow at small values of x which gives better

agreement between the computed and measured values of V_ϕ, and the radial velocity distribution inside the boundary layers is not greatly affected by the correction. However, the measurements of $V_r/\Omega r$ in mid-plane are much less peaky than either the corrected or uncorrected computations.

6.4 Parametric study

In this section, a parametric study of the flat-shroud case is described, in terms of the geometric and flow parameters. The effect of the gap ratio, G, on the flow field is investigated in section 6.4.1, and the effects of varying slot-width and slot spacing are considered in sections 6.4.2 and 6.4.3. The effects of rotational Reynolds number, nondimensional mass flow rate and turbulent flow parameter (Re_ϕ, C_W and λ_T) are given in sections 6.4.4, 6.4.5 and 6.4.6. All the computations were carried out using the LS model.

6.4.1 Effect of varying G

In order to investigate the effect of gap ratio, computations were carried out for $Re_\phi = 1.5$ x 10^5 with $C_W = 0$ and -3000, such that $|\lambda_T|$ =0 and 0.034, for G=0.1, 0.2 and 0.3. Figure 6.32 shows the

effect of gap ratio on flow structure for $C_W = 0$ and -3000. For constant λ_T, the size of the source region increases as gap ratio increases.

Figures 6.33a and 6.33b show the variation of $V_\phi/\Omega r$ with x and x^{-2} for the cases shown in Figure 6.32. It can be seen that, at a fixed value of λ_T, the tangential component of velocity increases as the gap ratio decreases. Referring to the variation with x^{-2}, there is Rankine-vortex behaviour (close to free vortex) at large values of x (source-dominated region), and forced-vortex-type behaviour at small values of x.

Figures 6.34 and 6.35 show the effect of gap ratio on the axial variation of the radial and tangential components of velocity for $\lambda_T = 0$ and -0.034 respectively. Considering the radial component of velocity with $\lambda_T = 0$, Figure 6.34, the magnitude of V_r in the boundary layers increases with gap ratio. In the source-region, outside the boundary layer, the radial velocity profile for G=0.1 is much flatter at x=0.85 than for G=0.2 or 0.3. Referring to the variation of the tangential component of velocity, it can be seen that there is no significant axial variation for this component outside the boundary layers: $V_\phi/\Omega r$ decreases as gap ratio increases. Similar effects can

be seen in Figure 6.35 for $\lambda_T = -0.034$.

6.4.2 Effect of varying slot-width

The aim of this section is to investigate the effect of the inlet slot width on the flow field. As already mentioned, the experimental rig contained a series of holes, 11 mm in diameter, in the mid-plane of the outer cylindrical surface, and the superposed flow entered the cavity through these holes. However, the computational model employed an axisymmetric centrally-located slot. In this investigation, the axial width of the slot, s_c, (see Figure 6.36a) was changed in steps from 1.5 mm to 33 mm.

Figure 6.37 shows the effect that different slot widths have on the radial and tangential components of velocity for $Re_\phi = 3.75$ x 10^5 and $C_w = -3000$ ($\lambda_T = -0.104$). As can be seen from this figure, increasing the slot width has no significant influence on the computed tangential velocity distribution, but there is an effect on the radial velocity profiles. The computed results polarize into two curves: one for $s_c = 1.5mm$ ($G_c = 0.004$) and one for $s_c \geq 3mm$ ($G_c \geq 0.0288$). It is apparent that increasing the slot width influences the agreement between the computed and measured values of

V_r, but significant differences still remain.

6.4.3 Effect of varying slot-spacing

As shown in Figure 6.36b, two slots of equal width were positioned symmetrically about $z/s = 0.5$. Figures 6.38 and 6.39 show the effect of slot spacing on the computed flow streamlines for $C_W = -1500$, $Re_\phi = 1.5$ x 10^6 and $C_W = -3000$, $Re_\phi = 3.75$ x 10^5 , such that $\lambda_T = -0.0172$ and -0.104 respectively. It can be seen that as $|\lambda_T|$ increases from 0.0172 to 0.104, the size of the recirculating region increases, as expected, and the effect of the spacing of the slots becomes more apparent: increasing the distance between the slots tends to reduce the extent of the recirculating region, as shown in Figure 6.39. In particular, for $D_1 = D_2 = 0.112$ and $D_1 = D_2 = 0.212$ in Fig 6.39, the streamlines near the slots show that there are contra-rotating vortices on either side of each jet, resulting in greater mixing with a consequent reduction in the radial momentum of the jet. It is this mechanism that is believed to be responsible for the reduction in the radial extent of the recirculating region. It is also probable that, in the experimental rig, the discrete jets would create greater mixing than the axisymmetric slot used in the computations. This would explain to some extent why, for

$|\lambda_T| > 0$, there is poor agreement between the computed and measured values of V_r presented above. It does not, however, explain the poor agreement for $|\lambda_T|$=0, where the geometry of the hole or slot should be of no consequence.

Figures 6.40a and 6.40b show the variation of $V_\phi/\Omega r$ with x and with x^{-2} for values of λ_T corresponding to those in Figs 6.38 and 6.39. The effect of the slot spacing on the computations is confined to larger values of x (i.e. the recirculation region); for smaller values of x, the effects are negligible. It can be seen that increasing the spacing decreases the difference between the computed and measured values of V_ϕ.

Figures 6.41 and 6.42 show the variation of $V_r/\Omega r$ and $V_\phi/\Omega r$ with z/s for the conditions corresponding to Figures 6.40a and 6.40b. It can be seen that increasing the slot spacing improves the agreement between the computed and measured values of $V_r/\Omega r$ but, as noted above, it makes the agreement worse for $V_\phi/\Omega r$.

6.4.4 Effect of varying Re_ϕ

In order to investigate the effect of Re_ϕ on the flow field, computations were carried out using the LS model for three different Reynolds numbers at two different mass flow rates: Re_ϕ = 3.75 x 10^5, 7.5 x 10^5, and 1.5 x 10^6, with $C_W = -1500$ and -3000. Figure 6.43 shows the effect of Re_ϕ on the computed streamlines. It can be seen that, as Re_ϕ increases, the size of the source region decreases.

The effect of Re_ϕ on the variation of the tangential velocity with x and x^{-2} is illustrated in Figures 6.44a and 6.44b for $C_W = -1500$ and -3000. Referring to Figure 6.44a, as Re_ϕ increases the magnitude of the tangential velocity increases and the extent of Rankine-vortex (close to free-vortex) region decreases. A similar trend exists in Figure 6.44b for $C_W = -3000$

Figures 6.45 and 6.46 show the effect of Re_ϕ on the axial variation of the radial and tangential components of velocity for $C_W = -1500$ and -3000 respectively. For the case $C_W = -1500$, Figure 6.45, the thickness of the boundary layer and the magnitude of the radial velocity increase as Re_ϕ decreases. In the source region, the amount of radial inflow increases as Re_ϕ decreases. There is a small axial

variation of the tangential component of velocity in the midplane, becoming less evident as Re_ϕ is increased. The tangential component of velocity increases as Re_ϕ increases.

6.4.5 Effect of varying C_W

For constant Re_ϕ , the effect of varying C_W on the flow field was considered. At $Re_\phi = 3.75$ x 10^5, the nondimensional mass flow rate was varied in four steps: $C_W = 0, -1500, -3000$ and -6000.

Figure 6.47 illustrates the effect of nondimensional mass flow rate on the computed streamlines using the LS model. As can be seen, the size of the source region increases as $|C_W|$ increases, and all the cavity is occupied by the source region at the highest values of $|C_W|$. The effect of C_W on the variation of $V_\phi/\Omega r$ with x and with x^{-2} is shown in Figures 6.48a and 6.48b respectively. An increase in $|C_W|$ causes a decrease in $V_\phi/\Omega r$, and the size of the free vortex region increases.

Figure 6.49 shows the effect of C_W on the axial variation of $V_r/\Omega r$ and $V_\phi/\Omega r$ for $Re_\phi = 3.75$ x 10^5. Referring to this figure, the radial

component of velocity in the midplane and also in the disc boundary layer increases when $|C_W|$ is increased. However, the tangential component of velocity decreases as $|C_W|$ increases.

6.4.6 Effect of varying λ_T

The λ_T parameter in general gives particular insight for understanding the flow field. In this section, the effect of varying λ_T ($|\lambda_T| = 0$, 0.0172, 0.104 and 0.2) is studied. Figure 6.50 shows the effect of λ_T on the computed streamlines obtained with the LS model. As can be seen, the size of the source region increases as $|\lambda_T|$ increases. The effect of λ_T on the variation of $V_\phi/\Omega r$ with x and with x^{-2} is shown in Figures 6.51a and 6.49b respectively. The tangential component of velocity decreases and the free-vortex region increases as $|\lambda_T|$ increases.

Figure 6.52 shows the effect of λ_T on the axial variation of the radial and tagential components of velocity. The thickness of the boundary layer on the disc increases as $|\lambda_T|$ increases. There is little axial variation of the tangential velocity in the midplane, and $V_\phi/\Omega r$ decreases as $|\lambda_T|$ increases.

6.5 Heat transfer

In this section heat transfer computations together with experimental measurements are considered for the flat-shroud case. Only the left-hand disc is heated and the Nusselt number, Nu, refers to this disc. The reference temperature, T_{ref}, for the Nusselt number is assumed to be equal to the inlet air temperature.

Computations were carried out using the LS model, and the flow results were presented in the previous sections. The flow boundary conditions were also described, and here attention is focused on the thermal boundary conditions for the energy equation. For the left-hand disc (the heated disc), a polynomial fit to measured temperatures was used to provide the boundary condition. The inner and outer shrouds were assumed to be adiabatic (these surfaces were insulated in the experiments).

The thermal boundary conditions for the right-hand disc (the unheated disc) and the correction for radiation are described in sections 6.5.1 and 6.5.2 respectively. Comparisons between the computed results and measurements are given in section 6.5.3.

6.5.1 Boundary conditions for the unheated disc

As described in section 5.2, the unheated disc for the flat-shroud geometery was made from polycarbonate to provide optical access. The disc could not be insulated and its temperature was not measured. For the computations, it is difficult to prescribe an appropriate thermal boundary condition for the unheated disc, and two different assumptions were considered. These are referred to as: the adiabatic-disc assumption and the conducting-disc assumption.

In the conducting-disc assumption, the heat loss through the unheated disc is calculated assuming free-disc behaviour outside the cavity (between the unheated disc and stationary steel casing). Iteration is necessary, and the calculated wall temperature is updated after each iteration. Details of the conducting-disc assumption are given in Appendix A.

6.5.2 Radiation correction

In order to take into account the radiation heat flux from each solid surface, the total Nusselt number (Nu), measured by the fluxmeters

in the experiments, can be considered to comprise two components:

$$Nu = Nu_{conv} + Nu_{rad} \tag{6.1}$$

where Nu_{conv} and Nu_{rad} represent the Nusselt numbers for convection and radiation heat transfer respectively.

The radiation correction was added to the BURF code by Karabay (1995), allowing calculation of the radiative Nusselt number, Nu_{rad} for a simple cavity.

6.5.3 Comparisons between computed results and measurements

Figures 6.53a to 6.53d show the computed and measured variations of the temperature and Nusselt numbers with nondimensional radius x, together with the computed streamlines and isotherms, for $|\lambda_T| = 0.104, 0.052, 0.034$ and 0.017 respectively. The following comments apply to the presentation of the heat transfer results:

(i) both the measured and fitted temperature distributions are shown for the the heated-disc. Two computed temperature distributions are shown for the unheated-disc, corresponding to the adiabatic-disc and the conducting-disc assumptions.

(ii) for the Nusselt number distributions, measurements and computations are shown for the heated-disc. Three computed results may be seen for each case: (1) computed Nusselt numbers using the adiabatic-disc assumption; (2) computed Nusselt numbers using the conducting-disc assumption and (3) the computed Nusselt numbers using the conducting-disc assumption and including the radiation correction.

Figure 6.53a shows the results for $C_W = -3000, Re_\phi = 3.75$ x 10^5, $\lambda_T = -0.104$. The computed streamlines, Fig 6.53a(i), show that the source region fills the cavity. The computed isotherms, Fig 6.53a(ii), show large temperature gradients near the heated disc and adiabatic shroud and in the mixing region. Outside the boundary layers on the heated disc and outer shroud, temperature gradients are relatively small and are further reduced towards the inner cylinder at x=0.5.

Referring to the temperature variation, Figure 6.53a(iii), it can be seen that, as expected, the temperature of the conducting-disc is slightly lower than that of the adiabatic disc. Referring to the Nusselt number variation, Figure 6.53a(iv), there is no significant

difference between the adiabatic-disc and conducting-disc assumptions. However, the conducting-disc assumption with radiation correction significantly increases the computed Nusselt number. The computed Nusselt numbers are slightly lower than the experimental data, particularly at large values of x, but show a similar distribution to the measurements.

Broadly similar results, as described for $\lambda_T = -0.104$, are shown for $|\lambda_T| = 0.052, 0.034$ and 0.017 in Figures 6.53b, 6.53c and 6.53d. Some general conclusions may be drawn with respect to the influence of the λ_T parameter for these cases, as described below.

The difference in the computed temperatures for the unheated-disc, between the adiabatic-disc and conducting-disc assumptions, increases as $|\lambda_T|$ decreases. The radial variation of the computed unheated-disc temperature using the conducting-disc assumption increases as $|\lambda_T|$ decreases. For the computed Nusselt numbers, differences due to these two assumptions increase as $|\lambda_T|$ decreases.

The solid curves in Figures 6.53a(iv) to 6.53d(iv) show the computed Nusselt numbers for the conducting-disc assumption including the radiation correction. Referring to the comparisons between

these curves and measurements, it can be seen that the computed Nu values display the measured trends but tend to underestimate the measurements at large values of x. A possible reason for this underestimate is that the inner and outer cylindrical surfaces of the experimental rig were rough (this affected the tangential component of velocity) and this roughness was not allowed for in the numerical model. Deficiencies in the turbulence model may also have contributed to the underestimates of Nu. Furthermore, at x$\simeq$0.95, Figs 6.53a(iv) to 6.53d(iv) show a significant difference between the computed Nusselt number and experimental data. This difference for $C_W = -3000$, shown in Figures 6.53a(iv) and 6.53c(iv), is larger than for $C_W = -1500$ (shown in Figures 6.53b(iv) and 6.53d(iv)). Apart from the possible reasons mentioned above, some of this discrepancy may also be due to 3-D effects in the experimental rig.

6.6 Conclusions

An axisymmetric CFD multigrid solver has been used to compute the flow and heat transfer in a rotating cavity with a flat stationary casing and a peripheral flow of cooling-air. The main conclusions are given below.

6.6.1 Fluid flow

a) Sealed cavity

Four test cases were considered using both laminar and turbulent models, and the results were compared with experimental data. In an attempt to improve the agreement between computed and measured velocities, several modifications to the computational model were tested, such as extending the computational domain to investigate ingress and making source-term modifications to the dissipation equation of the LS model. The following conclusions were made.

• There is good agreement between laminar and LS models for the lowest Reynolds number, $Re_\phi = 10^4$, where the flow is fully laminar. Transition occurred at small values of x when Re_ϕ was increased.

• In the main, the results for the LS model were not in good agreement with the velocity measurements. For the tangential component of velocity, the computed LS model overestimated the experimental data at large values of x and underestimated the data at small values of x. The LS model predicted tangential velocities which tended from free-vortex to forced-vortex distributions prema-

turely, while the experimental profiles maintained a large Rankine-vortex element. For the radial component of velocity, except for Re_ϕ = 1.46 x 10^5, good agreement was achieved between the LS model and measurements. For Re_ϕ = 1.46 x 10^5, agreement was good for the disc boundary layers but poor in the axial mid-plane.

Several possible reasons were considered for the poor agreement between the computed results and the experimental data: roughness of the inner and outer cylinderical surfaces; ingress of external fluid through the seals in the rig; inadequacy of the turbulence model and flow instability.

• Some of the experimental test cases were repeated using smooth outer and inner shrouds.For the higher rotational Reynolds numbers there were significant differences in the tangential component of velocity between the two experimental results. However, the fundamental differences between the LS model and the smooth results were not changed.

• The computations suggest that ingress does not appear to be a significant problem. It does not explain the poor agreement between the experiments and computations.

• Three source-term modifications in the ϵ equation were investigated: the Yap, the rotation and the Richardson-number corrections. It was concluded that the Yap correction has no significant effect on the computed results. The rotation correction made the agreement between computed and measured values better at the large values of x and worse at small values of x. The Richardson-number correction improved the computed results in comparison with experimental data. The radial variation of $V_\phi/\Omega r$ using the Richardson-number correction showed Rankine-vortex behaviour as expected from the experiments. This correction also improved the sharp radial velocity profile located in the mid-plane for $Re_\phi = 1.46$ x 10^5, but the velocity profiles for radial and tangential components were unaffected near the discs.

• The experimental study of Abrahamson et al (1989) showed that this type of flow may be unsteady and three-dimensional. The work done by Lewis (1997) and by Arnold (1996) revealed instability of the flow structure for some cases. This instability, or time-dependency, appears to be the most probable reason for the disagreement between the current axisymmetric steady computations and the experimental data.

b) superposed flow

Four test cases were studied for superposed peripheral flow: $|\lambda_T| =$ 0.0172, 0.034, 0.052 and 0.104. The experimental data was compared with the computed results using the LS model. The main conclusions are as follows.

• Computed streamlines showed that the size of the source region increases with increasing values of $|\lambda_T|$. Comparing the computed results with experimental data, the agreement for the tangential component of velocity improved with increasing $|\lambda_T|$. For the radial component of velocity, the agreement appeared to be better for the boundary layers on the two discs than for the core; in the core, the experimental variation of $V_r/\Omega r$ with z/s is much flatter than the computed variation.

As mentioned for the sealed cavity, several possible reasons were proposed to explain the poor agreement between the LS model and experimental data: roughness on the inner and outer cylinderical surfaces; 3-D effects, inadequacy of the turbulence model and instability of the flow.

• For $V_\phi/\Omega r$, there was a significant difference between " smooth and rough " experimental results. For $V_r/\Omega r$, there were no significant differences between the two sets of measurements. It was also shown that the effect of roughness decreased with increasing $|\lambda_T|$. There were still significant differences between the LS model results and the smooth data.

• Two types of the three dimensionality may occur in the superposed flow case: 3-D effects due to the stationary outer shroud, which may also be present in the sealed cavity (as discussed by Abrahamson et al (1989)), and 3-D effects due to the discrete inlet holes in the experimental rig, producing interactions between inlet jets inside the cavity.

• In the turbulence modelling aspect, two source-term modifications were investigated for the superposed flow case: the rotation and the Richardson-number corrections. As concluded for the sealed cavity, there is a significant effect of the rotation correction on the tangential component of velocity at large values of x, and a negligible effect at small values of x; the effects become smaller as $|\lambda_T|$ is increased. Agreement between the computed results and experimental data is

improved using the gradient Richardson correction.

c) parametric study

A parametric study has been carried out using the LS model in terms of gap ratio, slot-width, slot spacing, and in terms of the flow parameters C_W, Re_ϕ and λ_T. The conclusions are as follows:

• As gap ratio, G, increases the effect of stationary outer shroud on the flow field increases, leading to an increase in the size of the recirculating region and a decrease in $V_\phi/\Omega r$.

• Varying slot-width had no significant effect on the tangential component of velocity. Similar radial velocity profiles were obtained for the higher values of slot-width.

• Increasing the axial spacing between the two inlet slots tended to reduce the size of the recirculating region. At high values of $|\lambda_T|$, the computed streamlines showed the existence of two contra-rotating vortices on either side of each jet, resulting in greater mixing with a consequent reduction in the radial momentum of the jet.

• As Re_ϕ increases, the magnitude of $V_\phi/\Omega r$ tangential velocity increases and the size of the free-vortex type region decreases. The thickness of the boundary layers and the magnitude of the radial velocity increases as Re_ϕ decreases.

• An increase in C_W decreases $V_\phi/\Omega r$ (as inlet swirl is zero) and increases the size of the source region. The radial component of velocity in the midplane and also in the disc boundary layer increases with increasing C_W.

• As $|\lambda_T|$ increases, the size of the source region increases (there is greater inward radial penetration of the flow) and $V_\phi/\Omega r$ decreases.

6.6.2 Heat transfer

Heat transfer computations were made in a rotating cavity with a stationary flat-shroud. Two different thermal boundary conditions for the unheated disc were used to solve the energy equation: an adiabatic-disc assumption and conducting-disc assumption; the conducting-disc solutions were modified to include a radiation correction. Four test cases were considered by varying the turbulent flow parameter, λ_T, in four steps from -0.104 to -0.017. The computed Nusselt numbers for the heated-disc were compared with the experimental data obtained by Gan (1994). The main conclusions

are given below.

• The computed isotherms showed a large temperature gradient near the heated-disc and in the mixing region located at the top of the cavity.

• The computed temperatures on the adiabatic-disc were higher than those on the conducting-disc, and the difference increased as $|\lambda_T|$ decreased.

• There was a small difference between the computed Nusselt numbers with the adiabatic-disc assumption and conducting-disc assumption at $|\lambda_T| = 0.104$, but the difference increased as $|\lambda_T|$ decreased.

• The conducting-disc assumption including a radiation correction produced a significant increase in Nusselt numbers, particularly for $|\lambda_T| = 0.104$. The radial distributions of Nusselt numbers were similar to the experimental results, but the computations tended to underestimate the measurements at large values of x.

• Roughness in the experimental rig, deficiencies in the turbulence model and 3-D effects were proposed as possible reasons for the above underestimation.

Chapter 7

Flow and heat transfer in a rotating cavity with stepped-shroud

7.1 Introduction

In this chapter fluid flow and heat transfer are considered for a rotating cavity with a stepped-shroud. The simplified computational model, corresponding to the experimental rig described in chapter 5, is shown in Figure 7.1a. On the experimental rig, a shaped rotating ring was attached to the left-hand disc, increasing the maximum radius of the cavity to b=411 mm. The stepped-shroud was represented by a stationary block in the computational model, reducing

the effective radius of the solution domain near the right-hand disc to 335 mm. The clearance between the stationary block and the rotating ring is 3 mm (clearance 1 in Figure 7.1a), and between the stationary block and right-hand disc is 2 mm (clearance 2).

In the experiments, as discussed in Chapter 5, air entered the cavity through a series of holes; in the computational model, an equivalent area slot is used. Air entered the cavity with a fixed flow angle $\theta = 24.5^o$ to the radial direction (as shown in Figure 7.1a) with solid-body rotation ($V_\phi/\Omega r = 1$). Air could be extracted from the cavity in one of three different arrangements: $\Gamma = 1, 0$ and $\Gamma \rightarrow \infty$ (see Figure 7.1).

In this study, the stepped-shroud case is investigated computationally using the LS turbulence model. A typical grid distribution in the r-z plane is given in Figure 7.1b. For each Γ parameter, computations are carried out at four different rotational Reynolds numbers and five different mass flow rates. The flow field results for the above cases are described in section 7.2. No velocity measurements were made in the rig, but the computed heat transfer results are compared with measured values in section 7.3. Conclusions are given in section 7.4.

7.2 Fluid flow

The superposed flow for the stepped-shroud case was considered computationally using the LS model over a wide range of mass flow rates and rotational Reynolds numbers. Computations for $\Gamma = 1, 0,$ and $\Gamma \rightarrow \infty$ (see Figure 7.1) are considered in sections 7.2.1, 7.2.2 and 7.2.3.

7.2.1 Fluid flow for $\Gamma = 1$

For $\Gamma = 1$, twenty tests were investigated at five different mass flow rates ($C_W = -24000, -12000, -6000, -3000$ and-1500) and at four different rotational Reynolds numbers ($Re_{\phi 1}, Re_{\phi 2}, Re_{\phi 3}$ and $Re_{\phi 4}$). More details of Re_ϕ and λ_T for each case are shown in Table 7.1.

Figure 7.2 shows the effect of C_W , Re_ϕ and λ_T on the computed streamlines for $\Gamma = 1$. There is a complicated flow structure for each case involving a number of recirculating regions. There is a radial inflow on the left-hand disc, creating anti-clockwise circulation near the inlet. The size of this recirculation zone decreases as Re_ϕ increases or as $|C_W|$ decreases. The clockwise circulation near the periphery next to the radial face of the step is like flow over a stator, where the flow in the boundary layer is radialy inward. This flow increases as Re_ϕ increases, creating a strong boundary-layer on the step-shroud.

C_W	$Re_{\phi 1}$ x 10^{-6} λ_T T_{ref} (C)	$Re_{\phi 2}$ x 10^{-6} λ_T T_{ref} (C)	$Re_{\phi 3}$ x 10^{-6} λ_T T_{ref} (C)	$Re_{\phi 4}$ x 10^{-6} λ_T T_{ref} (C)
-24000	0.43 -0.74 35.9	0.87 -0.42 32.5	1.74 -0.24 33.2	3.43 -0.14 35.7
-12000	0.39 -0.4 23.3	0.77 -0.23 26.2	1.53 -0.13 31.5	3.02 -0.07 38.9
-6000	0.41 -0.19 26.1	0.83 -0.11 28.9	1.64 -0.063 36.3	3.28 -0.036 49.9
-3000	0.38 -0.1 28.5	0.76 -0.06 34.1	1.54 -0.033 44.8	3 -0.019 67.6
-1500	0.36 -0.053 33.0	0.72 -0.03 39.3	1.48 0.017 53.3	2.92 -0.01 86.7

Table 7.1. Test parameters for stepped-shroud: $\Gamma = 1$.

The computed streamlines for cases joined by diagonal dashed lines in Figure 7.2 represent cases with approximately constant λ_T. It can be seen that, in most cases, broadly similar flow structures are predicted when λ_T remains constant. The size of the recirculation

near the inlet decreases as $|\lambda_T|$ decreases, which implies that the effect of inlet angle becomes negligible at small values of $|\lambda_T|$. As $|\lambda_T|$ decreases the radial outflow on both rotating discs and radial inflow on the stationary step increases, creating an anti-clockwise circulation next to the right-hand disc (see the cases with $|\lambda_T| \leq 0.034$).

Due to the broadly similar flow structures at constant λ_T, attention is focussed on the axial and radial variations of the velocity components with varying λ_T. Figures 7.3a and 7.3b show the variation of $V_\phi/\Omega r$ with x and x^{-2} at z/s=0.2 for $|\lambda_T| = 0.4, 0.22, 0.1, 0.034$ and 0.01. Referring to the variations with x, Figure 7.3a, at small values of x the $V_\phi/\Omega r$ increases as $|\lambda_T|$ increases. Referring to the variations with x^{-2}, Figure 7.3b, it can be seen that by increasing $|\lambda_T|$ the size of the recirculating region (characterised by free-vortex type flow) increases. At small values of x, the flow is influenced by the rotating discs rather than by the inlet conditions and, therefore, forced-vortex flow dominates in this region.

Figure 7.4 shows the axial variation of the $V_r/\Omega r$ and $V_\phi/\Omega r$ for $|\lambda_T| = 0.4, 0.22, 0.1, 0.034$ and 0.01. Due to the lack of experimental data, it is difficult to discuss distributions in detail, however, some general conclusions may be drawn as follows.

Referring to the radial velocity distributions, it can be seen that radial inflow occurs on the left-hand disc for higher values of $|\lambda_T|$ (=0.4 and 0.22). Decreasing $|\lambda_T|$ tends to reduce the radial velocity component, therefore, an attachment point (where $V_\phi/\Omega r = 1$) occurs for low values of $|\lambda_T|$. For radii lower than this, radial outflow occurs on the disc (as magnified in Figure 7.5), and the nondimensional tangential velocity ($V_\phi/\Omega r$) is less than unity. Referring to the tangential components of velocity for x < 0.85, it can be seen that $V_\phi/\Omega r$ increases with increasing $|\lambda_T|$, and the tangential velocity distribution is much flatter for low values of $|\lambda_T|$. The difference in the tangential component of velocity becomes smaller with decreasing $|\lambda_T|$.

7.2.2 Fluid flow for $\Gamma = 0$

Similar cases as for $\Gamma = 1$ are also considered for $\Gamma = 0$, where the middle clearance (number 1, Figure 7.1b) is blocked. The flow parameters for each case (C_W, Re_ϕ and λ_T) are given in Table 7.2.

Figure 7.6 shows the effect of C_W , Re_ϕ and λ_T on the computed streamlines for $\Gamma = 0$. The flow structures are similar to those for $\Gamma = 1$ for $|\lambda_T| > 0.034$. For $|\lambda_T| \leq 0.034$, the size of the recirculating region formed on the right hand side of the cavity for $\Gamma = 1$ is

greater than for $\Gamma = 0$. This implies that the effect of the stationary surface is reduced for $\Gamma = 0$.

Variation of $V_\phi/\Omega r$ with x and x^{-2} at z/s = 0.2 are shown in Figures 7.7a and 7.7b for $|\lambda_T| = 0.4, 0.22, 0.1, 0.034$ and 0.01.

C_W	$Re_{\phi 1}$ x 10^{-6} λ_T T_{ref} (C)	$Re_{\phi 2}$ x 10^{-6} λ_T T_{ref} (C)	$Re_{\phi 3}$ x 10^{-6} λ_T T_{ref} (C)	$Re_{\phi 4}$ x 10^{-6} λ_T T_{ref} (C)
	0.49	0.98	1.97	
-24000	-0.66	-0.39	-0.22	
	35.2	35.9	36.0	
	0.4	0.79	1.580	3.07
-12000	-0.4	-0.22	-0.13	-0.07
	29.6	33.3	36.6	42.2
	0.4	0.92	1.83	3.69
-6000	-0.176	-0.1	-0.058	-0.033
	32.2	35.4	41.1	48.7
	0.38	0.75	1.5	3
-3000	-0.1	-0.059	-0.034	-0.0197
	32.8	38.8	47.9	69.9
	0.36	0.72	1.46	2.93
-1500	-0.053	-0.03	-0.017	-0.010
	37.0	42.4	52.7	86.1

Table 7.2. Test parameters for stepped-shroud: $\Gamma = 0$.

A similar description as for Figures 7.3a and 7.3b can be given for

these results. Figure 7.8 shows the axial variation of the $V_r/\Omega r$ and $V_\phi/\Omega r$ for $|\lambda_T| = 0.4, 0.22, 0.1, 0.034$ and 0.01. The radial outflow formed on the discs at small values of $|\lambda_T|$ can be seen in Figure 7.9 in more detail. Again, the results follow the descriptions given for $\Gamma = 1$ in Figure 7.4.

7.2.3 Fluid flow for $\Gamma \rightarrow \infty$

Similar test cases were investigated for $\Gamma \rightarrow \infty$, where the right-hand clearance (number 2) is closed. The flow conditions for each case are shown in Table 7.3.

Figure 7.10 shows the effect of C_W , Re_ϕ and λ_T on the computed streamlines for $\Gamma \rightarrow \infty$. Comparing these streamlines with those for $\Gamma = 1$ and $\Gamma = 0$, it can be seen that there is a significant difference in the recirculating flow formed on the right-hand-side of the cavity. The size and number of the recirculating regions are more pronounced than for $\Gamma = 1$ and $\Gamma = 0$, and the effect of the stationary surface in creating the recirculating flow is more important for the $\Gamma \rightarrow \infty$ case.

Figures 7.11a and 7.11b show the variation of $V_\phi/\Omega r$ with x and x^{-2} for $|\lambda_T| = 0.4, 0.22, 0.1, 0.034$ and 0.01. Figures 7.12 and 7.13 show the axial variation of $V_r/\Omega r$ and $V_\phi/\Omega r$ for $|\lambda_T| = 0.4, 0.22, 0.1, 0.034$ and 0.01. The same description as for the $\Gamma = 1$ case applies to these results.

C_W	$Re_{\phi 1}$ x 10^{-6} λ_T T_{ref} (C)	$Re_{\phi 2}$ x 10^{-6} λ_T T_{ref} (C)	$Re_{\phi 3}$ x 10^{-6} λ_T T_{ref} (C)	$Re_{\phi 4}$ x 10^{-6} λ_T T_{ref} (C)
-24000	0.48 -0.66 19.4	1.01 -0.38 23.3	1.97 -0.22 30.4	3.89 -0.12 32.5
-12000	0.38 -0.41 36.8	0.76 -0.23 37.6	1.53 -0.13 36.7	3.01 -0.078 44.1
-6000	0.46 -0.176 25.9	0.91 -0.1 30.4	1.84 -0.058 33.9	3.62 -0.034 51.5
-3000	0.4 -0.097 30.9	0.79 -0.056 37.2	1.58 -0.033 47.3	3.07 -0.019 69.1
-1500	0.37 -0.053 35	0.73 -0.03 42.4	1.47 -0.0174 54.2	3 -0.0098 80.3

Table 7.3. Test parameters for stepped-shroud: $\Gamma \rightarrow \infty$.

7.3 Heat transfer

In this section heat transfer computations together with experimental comparisons for a rotating cavity with stepped-shroud are considered for $\Gamma = 1,0$ and $\Gamma \rightarrow \infty$. The left-hand disc is heated and the Nusselt number ,Nu, refers to this disc. The reference temperature, T_{ref}, for the Nusselt number is assumed to be equal to the measured inlet air temperature. In the experiments, two different air temperatures were recorded: the air temperature at the point very close to the inlet nozzle and the temperature inside the inlet pipe (see Figure 5.1b). The measurements showed that there is a significant difference between these two temperatures at high values of Re_ϕ, which causes an uncertainty in the experimental data at high values of Re_ϕ. Therefore, it is convenient to define a nondimensional correction for the inlet temperature, cor, as:

$$cor = \frac{T_{ref1} - T_{ref2}}{T_s - T_{ref2}} \tag{7.1}$$

where T_{ref1} and T_{ref2} are the measured air temperatures at the inlet pipe and inlet nozzle respectively, and T_s is the disc temperature at an arbitrary radius.

For each Γ value, twenty tests were investigated at five different mass flow rates and four different rotational Reynolds numbers.

More details of Re_ϕ, C_W, λ_T and inlet air temperature (T_{re_5}) for each test case are given in Tables 7.1, 7.2 and 7.3 for $\Gamma = 1, 0$ and $\Gamma \rightarrow \infty$ respectively.

The right-hand disc (or unheated-disc) was made from steel but there were no thermocouples to measure the temperature. The thermal boundary conditions for the computations were the same as those described for the flat-shroud case in Chapter 6: a polynomial fit to the measured temperatures on the heated-disc (left-hand disc); adiabatic assumptions for the inner cylinder and outer stepped-shroud and two assumptions for the unheated-disc (right-hand disc): adiabatic-disc and conducting-disc assumptions. It should be noted that the radiation correction described in Chapter 6 for a simple cavity is also used for the stepped-shroud case.

7.3.1 Heat transfer for $\Gamma = 1$

Heat transfer for the stepped-shroud was first considered for $\Gamma = 1$, and Figures 7.14 to 7.18 illustrate the results, for varying Re_ϕ, for $C_W = -24000, -12000, -6000, -3000$ and -1500 respectively.

Figure 7.14a to 7.14d show the computed and measured variations

of the temperature and Nusselt numbers with nondimensional radius x, together with the computed streamlines and isotherms for $C_W = -24000$ and for the four different values of Re_ϕ and λ_T.

It is convenient to remind the following statements, as described in Chapter 6, before describing any results.

(i) For the temperature distributions, the measurements and curve-fit are shown for the heated-disc. Two computed temperature distributions are shown for the unheated-disc using the alternatives: adiabatic-disc and conducting-disc assumptions.

(ii) For the Nusselt number distributions, both measurements and computations are shown for the heated-disc. Three computed results may be seen for each case: (1) computed Nusselt numbers using the adiabatic-disc assumption; (2) computed Nusselt numbers using the conducting-disc assumption and (3) the computed Nusselt numbers using the conducting-disc assumption and including the radiation correction.

Referring to Figure 7.14a(i), the results for $Re_\phi = 4.34$ x 10^5 and $\lambda_T = -0.742$, the computed streamlines show a large recirculating

region which is located next to the heated disc, and there is radial inflow inside the boundary layer on the heated disc (as shown in Figure 7.2). The computed isotherms, Figure 7.14a(ii) show a large temperature gradient near the heated disc and a more uniform temperature distribution in the rest of the cavity. Referring to the temperature variation, Figure 7.14a(iii), it can be seen that the temperature of the conducting-disc is lower than that of the adiabatic-disc. Referring to the Nusselt number variation, Figure 7.14a(iv), there is no clear difference between the Nusselt number variations obtained from the conducting-disc and adiabatic-disc assumptions. However, the conducting-disc assumption with radiation correction (solid curve) gives an increase in the computed Nusselt numbers. These computations overestimate the experimental data, particularly at large values of x.

Figure 7.14b shows the results for $Re_\phi = 8.77$ x 10^5, $\lambda_T = -0.42$. The computed streamlines, 7.14b(i) show that the size of the recirculating region decreases as rotational Reynolds number increases. Referring back to the axial variation of the radial component of velocity in Figure 7.5, there is radial inflow in the boundary layer on the heated disc. This gives a large temperature gradient at the heated disc, as shown in the computed isotherms, Figure 7.14b(ii).

Again, the conducting-disc assumption including the radiation effect gives a significant improvement in the agreement between the computed and measured values of Nu. Agreement between these computed Nusselt numbers and experimental data is good, except at large values of x.

Figure 7.14c shows the results for $Re_\phi = 1.74$ x 10^6, $\lambda_T = -0.242$. The anti-clockwise recirculating region in the computed streamlines is smaller than those of Figures 7.14a and 7.14b. A similar effect to that shown in Figures 7.14a and 7.14b is obtained using a conducting-disc assumption including the radiation correction, however, the computed Nusselt numbers tend to underestimate the experimental data.

Referring back to Figure 7.5, it can be seen that there is outflow and inflow on the heated disc at small and large values of x respectively. This implies that there is a stagnation point on the heated disc where all the components of velocity in the rotating frame are zero. Both experiment and computation indicate a significant rise in the Nusselt number where the stagnation point is predicted.

Figure 7.14d shows the results for $Re_\phi = 3.43$ x 10^6, $\lambda_T = -0.141$.

In the computed streamlines, Figure 7.14d(i), there is a small anti-clockwise recirculating region which is located at top of the cavity. There are high temperature gradients near the surface of both discs (particularly the heated disc) and an almost uniform temperature distribution exists inside the core region, Figure 7.14d(ii). There is a good agreement between the computed Nusselt numbers using the conducting-disc assumption with radiation correction (solid curve) and experimental data. Referring to the computed streamlines, and back to Figure 7.5, there is no stagnation point on the heated disc and radial outflow occurs on both discs. This may be the reason why the agreement is better in Figure 7.14d(iv) than in Figure 7.14c(iv).

Broadly similar results to those described above are shown for $C_W = -12000$, -6000 , -3000 and -1500 in Figures 7.15 to 7.18 respectively. Some cases with behaviour different from that described above are disccussed below.

For all the cases discussed above, the temperature of the conducting-disc is lower than that of the corresponding adiabatic-disc. However, there is no significant effect on the computed Nusselt numbers, except where the inlet temperature is very large (Figs 7.15d 7.16d, 7.17c, 7.17d and 7.18d) and where there is also a strong mix-

ing process. Figure 7.16d shows the results for $Re_\phi = 3.28$ x 10^6, $C_W = -6000$ and $\lambda_T = -0.036$. The computed streamlines show radial outflow on both discs, and strong mixing between two recirculating regions. Referring to the Nusselt number variation, Figure 7.16d(iv), the computed Nusselt numbers using the conducting-disc assumption are significantly higher than for adiabatic-disc assumption. The agreement between the computed Nusselt numbers using the conducting-disc assumption with radiation correction (solid curve) and experimental data is good.

Figure 7.18d shows the results for $Re_\phi = 2.92$ x 10^6 , $C_W = -1500$ and $\lambda_T = -0.01$. Again, there is radial outflow on both discs together with strong mixing between two recirculating regions. Referring to the Nusselt number variation, Figure 7.18d(iv), it can be seen that the adiabatic disc assumption gives rise to negative Nusselt numbers on the heated disc. This implies that the local fluid temperature is higher than the heated disc temperature.

The negative Nusselt number indicates that the effect of viscous dissipation (or frictional heating) is higher than the forced cooling effect. The frictional heating effect can be described quantitatively by the Eckert number, $Ec = \Omega^2 r^2 / C_P(T_S - T_I)$, Ong (1988). When

Ec is small, the effect of frictional heating is negligible. Ong found a significant viscous dissipation effect for Eckert number $Ec = 0.9$. In the current case, the Eckert number is greater than 1, and a large viscous dissipation effect is expected. The computed Nusselt numbers using the conducting-disc assumption are much higher than that those for the adiabatic disc assumption. In contrast to most of the previous cases, the conducting-disc assumption with radiation correction (solid curve) tends to overestimate the experimental data for Nu. The reason may be due to the degree of the uncertainty in the measured air temperature for the highest Reynolds number, which will be discussed in section 7.3.4.

7.3.2 Heat transfer for $\Gamma = 0$

Figures 7.19 to 7.23 show the heat transfer results for $\Gamma = 0$, where the centre-clearance (number 1) is closed. Apart from some exceptional cases, the same description as for $\Gamma = 1$ also applies for $\Gamma = 0$. As discussed in section 7.2.1, the anti-clockwise recirculating region in the right hand-side of the cavity is the result of the rotating disc and stationary surface. For $\Gamma = 0$, the mass flow rate in outlet number 2 is double that of $\Gamma = 1$ for the corresponding case. This reduces the size of the recirculating region created on the right hand

side of the cavity. For $\Gamma = 1$, there were some cases where mixing, due to this recirculating, caused a significant rise in Nusselt numbers for conducting-disc assumption. For $\Gamma = 0$, there are fewer of these cases (see Figs 7.2 and 7.6). In general, however, there is similar behaviour, as for $\Gamma = 1$, between the experimental data and computed Nusselt numbers using the conducting-disc assumption with radiation correction. Apart from a few cases in which the computed Nusselt numbers underestimate the experimental data, there is good agreement between computations and experiment.

7.3.3 Heat transfer for $\Gamma \rightarrow \infty$

Figures 7.24 to 7.28 show the results for $\Gamma \rightarrow \infty$, for which outlet number 2 is blocked. For $\Gamma \rightarrow \infty$, the effect of the stationary stepped-shroud in creating the recirculating region on the right-hand side of the cavity is more pronounced. Therefore, strong mixing occurs in the cavity for most of the cases. This mixing process, where used with the conducting-disc assumption, reduces the air temperature near the heated-disc. Consequently, the effect of the conducting-disc assumption on Nusselt numbers is more significant than for the $\Gamma = 1$ and $\Gamma = 0$ cases. Referring to the Figures 7.24 to 7.28, it can be seen that the agreement between the computed

Nusselt numbers, using the conducting - disc assumption with radiation correction, and measured values is generally good. However, there are a few cases (the highest rotational Reynolds number cases, Figs 7.24d, 7.25d, 7.26d and 7.27d) in which the computed results overestimate the experimental data.

7.3.4 Parametric variation of Nu with λ_T

From Figures 7.14 to 7.28 it can be concluded that there is no simple variation of the Nusselt number with respect either to Re_ϕ or to C_W. The reason can be found by analysing the flow structure. As discussed in section 7.2, the flow structure for the stepped-shroud geometery is more complicated than for the flat shroud. In cases where there is a strong superposed flow, radial inflow occurs over the entire heated disc. However, as the Reynolds number increases, a region of radial outflow develops on the inner part of the disc, so that there is both radial inflow and outflow on the disc with a stagnation point in between (see Figs 7.5, 7.9 and 7.13). In other cases, there is no stagnation point on the heated disc, and radial outflow occurs over the entire surface (see agian Figs 7.5, 7.9 and 7.13). Consquently, the heat transfer response will be different for those three groups (inflow on the disc, outflow on the disc and a

combination of inflow and outflow), and there is, in general, no simple behaviour in terms of either Re_ϕ or C_W.

Attempts have been made to find a flow parameter for which the Nusselt number variation is systematic. Referring to section 7.2, it was concluded that the flow structure does not change significantly with C_W and Re_ϕ if the turbulent flow parameter, λ_T, is kept constant. It should, therefore, be easier to interpret the variation of Nu with C_W and Re_ϕ for these cases where λ_T is kept constant. Figures 7.29 to 7.31 show the effects of C_W, Re_ϕ and λ_T on the computed and measured Nusselt numbers for $\Gamma = 1$, $\Gamma = 0$ and $\Gamma \to \infty$ respectively. It should be noted that in these figures only the computed Nusselt number using the conducting-disc assumption with radiation correction is compared with the experimental data.

For $\Gamma = 1$, Figures 7.29a to 7.29e illustrate the results for $\lambda_T = -0.22, -0.10, -0.06, -0.034$ and -0.017 respectively. Referring to the Figures 7.29a to 7.29d, both computed and measured Nusselt numbers increase as C_W and Re_ϕ increase. In Figure 7.29e ($\lambda_T = -0.017$), the computations show similar trend to Figures 7.29a to 7.29d, while the experiments show the opposite trend. Referring to the nondimensional correction for the inlet temperature

,cor (see equation 7.1), the magnitude of this correction for the case shown by the solid triangle is higher than the other cases. This implies that the inlet temperature is close to the temperature of the heated disc. Referring to the definition of the Nusselt number, any small uncertainty in the measured inlet temperature may give rise to a large variation in the Nusselt number.

For $\Gamma = 0$, Figures 7.30a to 7.30e present the results for $\lambda_T = -0.22, -0.10, -0.06, -0.034$ and -0.017 respectively. Referring to these figures, both computed and measured Nusselt numbers increase as C_W and Re_ϕ increase.

For $\Gamma \rightarrow \infty$, Figures 7.31a to 7.31e show the results for $\lambda_T = -0.22, -0.10, -0.06, -0.034$ and -0.017 respectively. Again, referring to Figures 7.31a to 7.31c, both computed and measured Nusselt numbers increase as C_W and Re_ϕ increase. In Figures 7.31d and 7.31e, the computed Nusselt numbers increase as C_W and Re_ϕ increase. The measurements in Figures 7.31d and 7.31e for the highest Re_ϕ (shown by triangles) do not follow the same rules. The *cor* parameter in these two exceptional cases is high, and any small uncertainty in the inlet air temperature will cause a large variation in the Nusselt number.

Due to the large variation of the *cor* parameter for the experiments, it is difficult to describe the effect of different Γ values on the Nusselt number. However, there are some similarities and differences in the distributions of the Nusselt numbers for $\Gamma = 1, 0$ and $\Gamma \rightarrow \infty$. For $|\lambda_T| = 0.22$, the computed streamlines in Figs 7.2, 7.6 and 7.10 show that the size of the anti-clockwise recirculation region on the left-hand side of the cavity decreases as Γ increases. Referring also to the computed radial and axial velocity components in Figs 7.5, 7.9 and 7.13, it can be seen that there is a mixture of radial inflow and outfow on the left-hand disc for $|\lambda_T| = 0.22$. The stagnation points, where $V_\phi/\Omega r = 1$, are located at approximatly x=0.65, 0.85 and 0.9 for $\Gamma = 0, 1$ and $\Gamma \rightarrow \infty$ respectively. The Nusselt number variations for $|\lambda_T| = 0.22$, Figs 7.29a, 7.30a and 7.31a, show a sharp peak near the stagnation point, and the magnitude of this peak increases as the position of the stagnation point moves radialy outwards. For $|\lambda_T| \leq 0.06$, the computed streamlines and the computed radial and tangential components of velocity show that radial outflow only occurs on the left-hand disc. For these cases, the variation of the Nusselt number in Figs 7.29 to 7.31 show similar shapes for $\Gamma = 1, 0$ and $\Gamma \rightarrow \infty$.

7.4 Conclusions

Flow and heat transfer computations were made in a rotating cavity with a stationary stepped-shroud using the LS turbulence model. The main conclusions for fluid flow and heat transfer are given in sections 7.4.1. and 7.4.2. respectively.

7.4.1 Fluid flow

The flow field for the stationary stepped-shroud and peripheral flow was considered for three different cases: $\Gamma = 1,0$ and $\Gamma \rightarrow \infty$. Twenty tests were carried out for each conditions, at different values for Re_ϕ and C_W. There were no experimental data for velocity comparison with the computations. The main observations arising from the predictions are given below.

• The computed streamlines showed a complicated flow structure for each case involving a number of recirculating regions for $\Gamma = 1,0$ and $\Gamma \rightarrow \infty$.

• Broadly similar flow structures were obtained for constant values of the $|\lambda_T|$ parameter.

• For cases with large values of $|\lambda_T|$, there is radial inflow on the left-hand disc, creating a large anti-clockwise recirculation region near the inlet. Free-vortex type flow occurs in this region and the size of the recirculation decreases as $|\lambda_T|$ decreases.

• In the free vortex region, at large values of x, $V_\phi/\Omega r$ decreases with increasing $|\lambda_T|$. However, for the forced vortex region at small values of x, $V_\phi/\Omega r$ increases as $|\lambda_T|$ increases.

• For some cases, an attachment point is formed on the left-hand disc. The position of the attachment point moves radially outwards as the $|\lambda_T|$ parameter is decreased. For small values of $|\lambda_T|$, outflow occurs everywhere on the left-hand disc.

• Broadly, similar conclusions apply for $\Gamma = 0$ and $\Gamma \to \infty$. The size of the recirculating region formed on the right-hand side of the cavity for $\Gamma \to \infty$ is greater than for $\Gamma = 1$ and 0.

7.4.2 Heat transfer

Heat transfer in the rotating cavity with stepped-shroud was considered at four rotational Reynolds numbers and five different mass flow rates for $\Gamma = 1,0$ and $\Gamma \rightarrow \infty$. For the computations, two different thermal boundary conditions for the unheated-disc were used to solve the enrgy equation: an adiabatic-disc assumption and conducting-disc assumption; the conducting-disc solutions were modified to include a radiation correction. The computed Nusselt numbers for the heated-disc were compared with the experimental data obtained by Quinn (1996). The main conclusions are given below.

• As concluded for the flat-shroud case in Chapter 6, the computed temperature for the adiabatic-disc was higher than for the conducting-disc, and the difference increased as Re_ϕ increased.

• At low values of Re_ϕ, there was little difference in the computed Nusselt numbers between the adiabatic-disc and conducting-disc assumptions, but the difference increased as Re_ϕ increased.

• For most of the cases, where either inflow or outflow occurred over the entire surfaces of the heated disc, the agreement between the computed Nusselt numbers and experiment was mainly good. For the cases where there was a mixture of inflow and outflow on the heated disc, the computed Nusselt number showed a strong peak around the stagnation point. This shows a deficiency in the LS tur-

bulence model near the stagnation point which has been noted by other authors.

• The most important parameter in all three cases ($\Gamma = 0, 1$ and $\rightarrow \infty$) appears to be the turbulent flow parameter, λ_T. At constant λ_T, computations show that Nu increases with increasing Re_ϕ and $|C_W|$. This statement also applies to most of the experiments, the exceptions being those cases of greatest experimental uncertainty in the measurements of the inlet temperature.

Chapter 8

Conclusions

In this thesis, a computational study of the fluid flow and heat transfer for a rotating cavity with a peripheral inflow and outflow of cooling air has been carried out, and comparisons made with experimental data. The rotating cavity comprised two corotating discs connected by an inner rotating cylindrical hub and enclosed by an outer stationary cylindrical casing, or shroud. Cooling air entered and left at the periphery of the system, and two different outer shroud geometeries were tested: the flat-shroud and the stepped-shroud cases.

For the computations, an axisymmetric elliptic multigrid CFD solver has been used to solve for steady laminar and turbulent flow. A low-Reynolds number $k - \epsilon$ turbulence model was used to close the

Reynolds-averaged Navier-Stokes equations. The numerical solution procedure included the SIMPLEC pressure-correction scheme of van Doormal and Raithby (1984) for the momentum equations.

Before using the CFD solver to investigate the peripheral flow problem, the program was used to compute the flow for rotating cavities with either a radial outflow or a radial inflow. For validation, the computed results (using both the Launder-Sharma (LS) and Morse (M) turbulence models) were compared with published experimental data. Although neither model was perfect for all the cases considered, both models showed satisfactory results for velocity profiles in most cases.

For the peripheral flow case, the experimental results were obtained at Bath University by Dr X. Gan for the flat-shroud case, and by Dr P. Quinn for the stepped-shroud case. The main conclusions of this study for the flat-shroud and stepped-shroud are given in sections 8.1 and 8.2 respectively. Recommendations for future work are given in section 8.3.

8.1 Flat-shroud case

The main conclusions for the fluid flow and heat transfer are given in sections 8.1.1 and 8.1.2 respectively.

8.1.1 Fluid flow

Incompressible isothermal flow in a rotating cavity with a flat-stationary shroud was considered. Attention was focussed on three aspects: fluid flow in a sealed cavity, the effect of superposed flow and a parameteric study.

a) Sealed cavity

For the sealed cavity, four cases were considered with different rotational Reynolds numbers ($10^4 \leq Re_\phi \leq 1.5$ x 10^6) using both laminar and the LS turbulence model, and the results were compared with experimental data. In an attempt to improve the agreement between computed and measured velocities, several modifications to the computational model were tested, such as extending the computational domain to investigate ingress and making source-term modifications to the dissipation equation of the LS model. The fol-

lowing conclusions could be made.

• The basic flow structure showed two counter-rotating recirculating regions, symmetrical about the axial mid-plane (z/s = 0.5). Fluid in the boundary layers on both discs moved radially outwards and there was a radially inflow in the core between the two discs.

• For $Re_\phi = 10^4$, good agreement was obtained between the laminar and the LS models. Transition occurred at x $\leq$ 0.65 for $Re_\phi = 1.46$ x 10^5, and turbulent flow occurred in most of the cavity at the higher Reynolds numbers.

• For Re_ϕ = 1.46 x 10^5 , 3.75 x 10^5 and 1.5 x 10^6, the numerical results were compared with experimental data obtained by Gan (1994). For the radial velocity, good agreement was obtained between the LS model and experimental data inside the boundary layers on both discs, but not in the mid-axial plane where inflow was overpredicted. However, the agreement in the mid-plane improved with increasing Re_ϕ. For tangential velociy, the computed results using the LS model overestimated the experimental data at large values of x (in the recirculating region), and underestimated at small values of x (near to the inner cylinder). Furthermore, the pre-

dicted tangential velocity distribution, using the LS model, changed from a free-vortex type to a forced-vortex distribution prematurely, while in the experiments Rankine vortex flow (close to the free-vortex) occurred in most of the cavity.

• In order to improve the agreement between the computed and measured velocities, several possible ideas were (computationally and experimentally) considered: roughness of the inner and outer cylindrical surfaces; ingress of external fluid through the seals in the rig; inadequacy of the turbulence model; and flow instability.

• Some of the experimental test cases were repeated using smooth outer and inner shrouds.For the higher rotational Reynolds numbers there were significant differences in the tangential component of velocity between the two experimental results. However, the fundamental differences between the LS model and the smooth results were not changed.

• Computations suggest that ingress does not appear to be a significant problem and does not explain the poor agreement between the experiments and computations.

• Three source-term modifications in the ϵ equation were investigated: the Yap, the rotation and the Richardson-number corrections. It was concluded that the Yap correction has no significant effect on the computed results. The rotation correction made the agreement between computed and measured values better at the large values of x and worse at small values of x. The Richardson-number correction improved the computed results in comparison with experimental data. The radial variation of $V_\phi/\Omega r$ using the Richardson-number correction showed Rankine-vortex behaviour as expected from the experiments. This correction also improved the sharp radial velocity profile located in the mid-plane for $Re_\phi = 1.46$ x 10^5, but the velocity profiles for radial and tangential components were unaffected near the discs. Overall, it was concluded that none of the three corrections produced satisfactory computations of both V_r and V_ϕ over the range of the conditions tested.

• The experimental study of Abrahamson et al (1989) showed that this type of flow may be unsteady and highly three dimensional. The work done by Lewis (1997) and by Arnold (1996) revealed instability of the flow structure for some cases. In particular, the axisymmetric DNS solutions of Lewis for $Re_\phi = 1.46$ x 10^5 produced

time-average results in good agreement with the experimental data. This suggests that instability of the real flow was the probable reason for the disagreement between the computations presented in this thesis and the measured values.

b) Effect of superposed flow

For the superposed flow case, four test cases were considered with varying $|\lambda_T|$ ($= 0.017, 0.034, 0.052$ and 0.104) using the LS model. The main conclusions are as follows.

- Computed streamlines showed that the size of the source region increases with increasing values of $|\lambda_T|$. Comparing the computed results with experimental data, the agreement for the tangential component of velocity improves as $|\lambda_T|$ increases. However, for the radial component of velocity, the agreement appeared to be better for the boundary layers on the two discs than for the core. In the core region the experimental variation of $V_r/\Omega r$ with z/s is much flatter than the computed variation.

- As mentioned for the sealed cavity, several possible reasons were

proposed to explain the poor agreement between the LS model and experimental data: roughness on the inner and outer cylindrical surfaces, 3-D effects, inadequacy of the turbulence model and instability of the flow.

• For $V_\phi/\Omega r$, there was a significant difference between the smooth and rough surface data. For $V_r/\Omega r$, there were no significant differences between the two sets of measurements. It was also shown that the effect of roughness decreased as $|\lambda_T|$ increased. It was concluded that roughness effects did not explain the differences between the measurements and the computations.

• Two types of the three dimensionality may occur in the superposed flow case: 3-D effects due to the stationary outer shroud, which may also be present in the sealed cavity (as discussed by Abrahamson et al (1989)), and 3-D effects due to the discrete inlet holes in the experimental rig, producing interactions between inlet jets inside the cavity.

• In the turbulence modelling, two source-term modifications were investigated for the superposed flow case: the rotation and the Richardson-number corrections. As concluded for the sealed cav-

ity, there is a significant effect of the rotation correction on the tangential component of velocity at large values of x, and a negligible effect at small values of x. However, the effects become smaller as the $|\lambda_T|$ parameter is increased. Agreement between the computed results and experimental data is slightly improved using the Richardson correction.

c) Parametric study

A parametric study has been carried out using the LS model in terms of gap ratio, slot-width, slot spacing, and in terms of the flow parameters C_W, Re_ϕ and λ_T. The conclusions are as follows:

- As gap ratio, G, increases the size of the recirculating region increases and $V_\phi/\Omega r$ decreases.

- Varying slot-width has no significant effect on the tangential component of velocity. Similar radial velocity profiles were obtained for high values of slot-width.

- Increasing the axial spacing between the two inlet slots tended to

reduce the size of the recirculating region. At high values of $|\lambda_T|$, the computed streamlines showed the existence of two contra-rotating vortices on either side of each jet, resulting in greater mixing with a consequent reduction in the radial momentum of the jet.

• As Re_ϕ increases the magnitude of the tangential velocity increases and the size of the free-vortex type region decreases. The thickness of the boundary layers and the magnitude of the radial velocity increases as Re_ϕ decreases.

• An increase in C_W decreases $V_\phi/\Omega r$ and increases the size of the source region. The radial component of velocity in the midplane and also in the disc boundary layer increases with increasing C_W.

• As $|\lambda_T|$ increases the size of the source region increases and the tangential component of velocity decreases.

8.1.2 Heat transfer

Heat transfer computations were made in a rotating cavity with a stationary flat-shroud. Two different thermal boundary conditions for the unheated disc were used to solve the energy equa-

tion: an adiabatic-disc assumption and a conducting-disc assumption; the conducting-disc solutions were modified to include a radiation correction. Four test cases were considered by varying the turbulent flow parameter, λ_T, in four steps from -0.104 to -0.017 ($Re_\phi = 3.75$ x10^5 and 1.5 x 10^6). The computed Nusselt numbers for the heated-disc were compared with the experimental data obtained by Gan (1994). The main conclusions are given below.

• There was a small difference between the computed Nusselt numbers with the adiabatic-disc assumption and conducting-disc assumption at $|\lambda_T| = 0.104$, but the difference increased as $|\lambda_T|$ decreased.

• The conducting-disc assumption including a radiation correction produced a significant increase in computed Nusselt numbers, particularly for $|\lambda_T| = 0.104$, and improved agreement with the measured values. The radial distributions of Nusselt numbers were similar to the experimental results, but the computations tended to underestimate the measurements at large values of x. Roughness in the experimental rig, deficiencies in the turbulence model and 3-D effects were proposed as possible reasons for this underestimate.

8.2 Stepped-shroud

The flow field and heat transfer computations for stepped-shroud were made over a wide range of mass flow rates and rotational Reynolds numbers ($1500 \leq |C_W| \leq 24000$ and $3 \text{ x } 10^5 < Re_\phi < 4 \text{ x } 10^6$). Computations were carried out using the LS model for three different distributions of outlet flow: $\Gamma = 1, 0$ and $\Gamma \rightarrow \infty$.

8.2.1 Fluid flow

Twenty tests were carried out for each Γ parameter at different values of Re_ϕ and C_W. There were no experimental data for velocity comparison with the computations. The main conclusions are given below.

- The computed streamlines show a complicated flow structure for each case involving a number of recirculating regions for $\Gamma = 1, 0$ and $\Gamma \rightarrow \infty$.

- Broadly similar flow structures were obtained for constant values of the $|\lambda_T|$ parameter.

• For cases with large values of $|\lambda_T|$, there is radial inflow on the left-hand disc, creating a large anti-clockwise recirculation region near the inlet. Free-vortex type flow occurs in this region and the size of the recirculation decreases as $|\lambda_T|$ decreases.

• In the free vortex region, at large values of x, $V_\phi/\Omega r$ decreases as $|\lambda_T|$ increases. However, for the forced vortex region at small values of x, $V_\phi/\Omega r$ increases as $|\lambda_T|$ increases.

• For some cases, where there is both radial inflow and outflow on the left-hand disc, an attachment point is formed, the position which moves radially outwards as $|\lambda_T|$ decreases. For small values of $|\lambda_T|$, outflow occurs everywhere on the left-hand disc.

• Broadly similar conclusions apply for $\Gamma = 0$ and $\Gamma \to \infty$. The size of the recirculating region formed on the right-hand side of the cavity for $\Gamma \to \infty$ is greater than for $\Gamma = 1$ and 0.

8.2.2 Heat transfer

Heat transfer in the rotating cavity with a stepped-shroud was considered at four rotational Reynolds numbers and five different mass flow rates ($1500 \leq |C_W| \leq 24000$ and $3 \text{ x } 10^5 < Re_\phi < 4 \text{ x } 10^6$) for $\Gamma = 1, 0$ and $\Gamma \rightarrow \infty$. For the computations, two different thermal boundary conditions for the unheated-disc were used to solve the enrgy equation: an adiabatic-disc assumption and a conducting-disc assumption; the conducting-disc solutions were modified to include a radiation correction. The computed Nusselt numbers for the heated-disc were compared with the experimental data obtained by Quinn (1996). The main conclusions are given below.

• At low values of Re_ϕ, there was little difference in the computed Nusselt numbers between the adiabatic-disc and conducting-disc assumptions, but the difference increased as Re_ϕ increased.

• For most of the cases, where either inflow or outflow occurred over the entire surfaces of the heated left-hand disc, the agreement between the computed Nusselt numbers and experiment was very good. For the cases where there was a mixture of inflow and outflow on the heated disc, the computed Nusselt number showed a strong

peak around the attachment point; this peak is associated with the behaviour of the LS turbulence model near the attachment point, as has been noted by other authors.

• The most important parameter in all three cases ($\Gamma = 0, 1$ and $\Gamma \rightarrow \infty$) appears to be the turbulent flow parameter, λ_T. At constant λ_T, computations show that Nu increases with increasing Re_ϕ and $|C_W|$. This statement also applies to most of the experiments.

8.3 Recommendation for future work

From the results of this study it is possible to suggest certain problems that require further investigation.

As discussed in the literature review in Chapter 2, the flow in a rotating cavity with a stationary outer casing may be unsteady and three dimensional. Further experimental and theoretical investigations should be carried out to study the instability and three dimensionality of this flow.

The beneficial effects of a correction to the isotropic $k-\epsilon$ turbulence model used in this work suggests that improved flow predictions may be obtained using more sophisticated anisotropic models such as the low-Reynolds-number differential stress model tested by Iacovides

et al (1996), or a non-linear variant of the $k - \epsilon$ model as described by Craft et al (1996).

For the stepped-shroud case, no velocity measurements were available to validate the computations. It was recommended that velocity measurements should be obtained, if possible.

References

Abrahamson, S.D., Eaton, J.K. and Koga, D.J., 1989, 'The flow between shrouded corotating discs', *Phys. Fluids A, vol. 1, No 2, pp.241-251.*

Arnold, P. 1996, 'Instability and Transition in a rotating cavity with a peripheral flow of cooling air', *Report No 1., School of Mech. Eng., Univ. of Bath.*

Bakke, E., Kreider, J.F. and Kreith, F., 1973, 'Turbulent source flow between parallel stationary and rotating discs', *J. Fluid Mech. vol. 58, pp.209-231.*

Bennetts, D.A. and Hocking, L.M., 1973, 'On nonlinear Ekman and Stewartson layers in a rotating fluid' *Proc. R. Soc. Lond., A 333, pp.469-489.*

Bennetts, D.A. and Jackson, W.D.N., 1974, 'Source-sink flow in a rotating annulus; a combined laboratory and numerical study' *J. Fluid Mech., vol. 66, pp.689-705.*

Bilimoria, E.D., 1977, 'Heat transfer in rotating cylindrical cavities', *PhD thesis, University of Sussex, U.K.*

Cheah, S.C., Iacovides, H., Jackson, D. C., Ji, H., and Launder, B.E., 1992, 'LDA measurements of an enclosed rotor-stator disc

flow' , *Symp on LDA on reciprocating, reacting, or rotating flows, Swansea, 7-9, April 1992.*

Chen, J-X, Gan, X. and Owen, J.M., 1995, 'Heat transfer from air-cooled contra-rotating discs', *40th ASME Int. Gas Turbine Cong., Houston, Paper 95-GT-184.*

Chew, J.W., 1982, 'Computation of flow and heat transfer in rotating cavity', *PhD thesis, University of Sussex, U.K.*

Chew, J.W., 1985, 'Computation of forced laminar convection in rotating cavities', *J. Heat Transfer, vol. 107, pp.277-282.*

Chew, J.W., 1987, 'Computation of flow and heat transfer in a rotating disc systems', *Proc. 2nd ASME-JSME Thermal Eng. Joint Conf., vol. 3, pp.361-367.*

Chew, J.W., Farthing, P.R., Owen, J.M. and Stratford, B., 1989, 'The use of fins to reduce the pressure drop in a rotating cavity with a radial inflow', *J. Turbomachinery, vol. 111, pp.349-356.*

Chew, J.W., Owen, J.M. and Pincombe, J.R., 1984, 'Numerical Predictions for laminar source-sink flow in a rotating cylindrical cavity', *J. Fluid Mech., vol. 143, pp.451-466.*

Chew, J.W. and Rogers, R.H., 1988, 'An integral method for the calculation of turbulent forced convection in a rotating cavity with

radial outflow', *Int. J. Heat and Fluid Flow, vol. 9, pp.37-48.*

Chiang, C. and Eaton, J.K., 1993, 'An experimental investigation of corotating discs and single disc flow structures', *Report No MD-62, Thermosciences Division, Dept. of Mech. Eng., Univ. of Stanford, Stanford, California*

Craft, T.J., Launder B.E. and Suga, K., 1996, 'Development and application of a cubic eddy-viscosity model of turbulence', *Int. J. Heat Fluid Flow, vol. 17, pp.108-115.*

Crespo Del Arco, E., Maubert, P., Randriamanina, A. and Bontoux, P., 1996 'Spatio-temporal behaviour in a rotating annulus with a source-sink flow', *J. Fluid Mech. vol. 328, pp.271-296.*

Faller, A.J., 1963, 'An experimental study of the instability of the laminar Ekman boundary layer', *J. Fluid Mech., vol. 15, pp.560-576.*

Farthing, P.R., 1988, 'The effect of Geometry on flow and heat transfer in a rotating cavity', *PhD thesis, University of Sussex, U.K.*

Farthing, P.R. and Owen, J.M., 1988, 'The effect of disc geometry on heat transfer in a rotating cavity with a radial outflow of fluid', *J. Engng. Gas Turbines Power, vol. 110, pp.70-79.*

Farthing, P.R. and Owen, J.M., 1991, 'De-swirled radial inflow in a

rotating cavity', *Int. J. Heat Fluid Flow, vol. 12, No 1, pp.63-70.*

Firouzian, M., 1986, 'Flow and heat transfer in a rotating cylindrical cavity with a radial inflow of fluid', *M.Phil thesis, Univ. of Sussex, UK*

Firouzian, M., Owen, J.M., Pincombe, J.R. and Rogers, R.H., 1985, 'Flow and heat transfer in a rotating cavity with a radial inflow of fluid. Part I: The flow structure', *Int. J. Heat Fluid Flow, vol. 6, No 4, pp.228-234.*

Firouzian, M., Owen, J.M., Pincombe, J.R. and Rogers, R.H., 1986, 'Flow and heat transfer in a rotating cavity with a radial inflow of fluid. Part II: Velocity, pressure and heat transfer measurements', *Int. J. Heat Fluid Flow, vol. 7, No 1, pp.21-27.*

Gan, X., 1994, 'Experimental study of rotating discs with peripheral flow', *Report No 014/94, School of Mech. Eng., Univ. of Bath.*

Gan, X., 1995, 'Private communication'

Gosman, A.D. and Ideriah, F.J.K., 1976, 'Teach-T: A general computer program for two dimensional turbulent recirculating flows' in 'Calculation of recirculating flows', *Mech. Eng. Dept. Imperial College, Univ. of London*

Gosman, A.D., Pun, W.M., Runchal, A.K., Spalding, D.B. and

Wolfshtein, M., 1969 'Heat and mass transfer in recirculating flows', *Academic Press, London*

Gosman, A.D. and Spalding, D.B., 1970, 'Computation of laminar flow between shrouded rotating disc', *Dept. of Mech. Eng., Imperial College, Univ. of London, Report No. EF.TN/A/30*

Hide, R., 1968, 'On source-sink flows in a rotating fluid' *J. Fluid Mech., vol. 32, pp.737-764.*

Herrero, J., Humphery, J.A.C., and Giralt, F., 1994, 'Comparative analysis of coupled flow and heat transfer between corotating discs in rotating and fixed cylindrical enclosures' *HTD-vol. 300, Heat Transfer in Gas Turbines, ASME 1994, pp.111-121.*

Iacovides, H. and Theofanopoulos, 1991, 'Turbulence modeling of axisymmetric flow inside rotating cavities', *Int. J. Heat Fluid Flow, vol. 12, pp.2-11.*

Iacovides, H., and Toumpanakis, P., 1993, 'Turbulence modeling of flow in axisymmetric rotor-stator systems' , *5th Int. symp. on refined flow modeling and turbulence measurements, Paris, September 7-10.*

Iacovides, H., Nikas, K.S., and Te Braak, A.F., 1996, 'Turbulent flow computations in rotating cavities using low-Reynolds-number models', *ASME conference, Birmingham, UK, June 10-13, GT-159.*

Itoh, M., Yamada, Y. and Nishioka, K., *et al*, 1985, 'Transition of the flow due to an enclosed rotating disk' *Trans. Japan. Soc. Mech Eng., vol. 51, pp.452-460 (in Japanese).*

Kapinos, V.M., 1965, 'Heat transfer during the flow of a stream from the centre to the periphery between two rotating discs', *International Chemical Eng., vol. 5, pp.461-466.*

Karabay, H., 1995, 'An adiabatic pre-swirl rotor-stator system with cover-plate ', *Report, No 040/95, School of Mech. Eng., Univ. of Bath.*

Kilic, M., 1993, 'Flow between contra-rotating discs', *PhD thesis, University of Bath, U.K.*

Koosinlin, M.L., Launder, B.E. and Sharma, B.I., 1974, 'Prediction of momentum, heat and mass transfer in swirling turbulent boundary layers', *J. Heat Transfer, vol. 96, pp.204-209.*

Kreith, F., 1966, 'Transfert de chaleur et de masse danse un encoulement radial entre deux disques paralleles fixes ou tournant a la meme vitesse', *Int. J. Heat Mass Transfer, vol. 9, pp.265-282.*

Kreith, F. and Viuiand, H., 1967, 'Laminar source flow between two parallel coaxial discs rotating at different speeds', *J. Applied Mech., Trans. of ASME, Series E, vol. 34, pp.541-547.*

Lapworth, B.L. and Chew, J.W., 1992, 'A numerical study of the influence of disc geometry on the flow and heat transfer in a rotating cavity', *J. Turbomachinery, vol. 114, pp.256-263.*

Launder, B. E., Priddin, C. H. and Sharma, B. I.,1977, 'The calculation of turbulent boundary layers on spinning and curved surfaces ' , *J. Fluids Engng vol 99, pp.231-239*

Launder, B.E. and Sharma, B.I., 1974, 'Application of energy dissipation model of turbulence to the calculation ofthe flow near a spinning disc.', *Letters in Heat and Mass Transfer, vol. 1, pp.131-138.'*

Lewis, T.W., 1997, 'Private communication.'

Long, C.A., 1984, 'Transient heat transfer in a rotating cylindrical cavity', *PhD thesis, University of Sussex, U.K.*

Long, C.A., Morse, A.P. and Zafiropoulos, N., 1993, 'Buoyancy-affected flow and heat transfer in asymmetrically-heated rotating cavities', *38th ASME International Gas Turbine and Aeroengine Congress and Exposition, Cincinnati, Ohio, U.S.A*

Mirzaee, I., 1995, 'Computation of flow in a rotating cavity with a peripheral flow of cooling air', *Report, No 054/95, School of Mech. Eng., Univ. of Bath, UK.*

Mirzaee, I., 1996, 'Computation of flow in a rotating cavity with a peripheral flow of cooling air: Source term modifications', *Report, No 062/96, School of Mech. Eng., Univ. of Bath, UK.*

Morse, A.P., 1988, 'Numerical prediction of turbulent flow in rotating cavities', *J. Turbomachinery, vol. 110, pp.202-215.*

Morse, A.P., 1991a, 'Assesment of laminar-turbulent transition in closed disc geometries', *J. Turbomachinery, vol. 113, pp.131-138.*

Morse, A.P., 1991b, 'Application of a low Reynolds number $k - \epsilon$ turbulence model to high-speed rotating cavity flows', *J. Turbomachinery, vol. 113, pp. 98-105.*

Morse, A.P. and Ong, C.L., 1992, 'Computation of heat transfer in rotating cavities using a two-equation model of turbulence', *J. Turbomachinery, vol. 114, pp.247-256.*

Northrop, A., 1984, 'Heat transfer in a cylindrical rotating cavity', *PhD thesis, University of Sussex, U.K.*

Northrop, A. and Owen, J.M., 1988, 'Heat transfer measurements in rotating-disc systems. Part II: The rotating cavity with a radial outflow of cooling air', *Int. J. of Heat and Fluid Flow, vol. 9, pp.27-36.*

Ong, C.L., 1988, 'Computation of fluid flow and heat transfer in

rotating disc-systems', *PhD thesis, University of Sussex, U.K.*

Ong, C.L. and Owen, J.M., 1989, 'Boundary layer flows in rotating cavities', *J. Turbomachinery, vol. 111, pp. 341-348.*

Ong, C.L. and Owen, J.M., 1991, 'Prediction of heat transfer in a rotating cavity with a radial outflow', *J. Turbomachinery, vol. 113, pp.115-122.*

Onur, H.S., 1980, 'Convective heat transfer in rotating cavities', *PhD thesis, University of Sussex, U.K.*

Owen, J.M., Pincombe, J.R. and Rogers, R.H., 1985, 'Source-sink flow inside a rotating cylindrical cavity', *J. Fluid Mech., vol. 155, pp.233-265.*

Owen, J.M. and Pincombe, J.R., 1980, 'Velocity measurements inside a rotating cylindrical cavity with a radial outflow of fluid.' *J. Fluid Mech., vol. 99, pp.111-127.*

Owen J.M., Pincombe, J.R. and Onur, H., 1979, 'Flow and heat transfer in a rotaing cylindrical cavity with a radial outflow of coolant', *Report No 79/Me/104, School of Eng. and Applied Science, Univ. of Sussex, UK.*

Owen, J.M. and Rogers, R.H., 1989, 'Flow and heat transfer in rotating-disc systems; Volume 1: Rotor-stator systems', *Research*

Studies Press, Taunton, U.K.; Wiley, New York, U.S.A.

Owen, J.M. and Rogers, R.H., 1995, 'Flow and heat transfer in rotating-disc systems; Volume 2: Rotating cavities', *Research Studies Press, Taunton, U.K.; Wiley, New York, U.S.A.*

Patankar, S.V. , 1980, 'Numerical heat transfer and fluid flow', *Hemisphere , New York.*

Patankar, S.V. and Spalding, D.B., 1972, 'A calculation procedure for heat, mass and momentum transfer in three dimensional parabolic flow', *Int. J. Heat Mass Transfer, vol. 15, pp.1787-1805.*

Pincombe, J.R., 1983, 'Optical measurements of the flow inside a rotating cylinder', *PhD thesis, University of Sussex, U.K.*

Quinn, P., 1996, 'Experimental study of a rotating cavity with peripheral flow, Report 6: Heat transfer measurements with a stationary "Step-Shroud"', *Report No 077/96, School of Mech. Eng., Univ. of Bath, UK.*

Reile, E. Radons, U. and Hennecke, D.K., 1985, 'Transient behaviour of a compressor rotor with ventilation. Test results under simulated conditions', *AGARD CP390, p. 36-1*

Rogers, R.H., 1987, 'The use of an integral method for the computation of heat transfer on the discs of a rotating cavity with radial in-

flow. Part I: Solid-body rotation at inlet', *Report No 87/TEMRC/103, School of Eng. and Applied Science, Univ. of Sussex, UK.*

Shao, L., Michard, M. and Bertoglio, J.P., 1991, 'Effects of solid body rotation on the transport of turbulence' , *Eighth Symposium on Turbulent Shear Flows, Technical Univ. of Munich, September 9-11*

Shirazi, S.A. and Truman, C.R., 1987, 'Prediction of turbulent source flow between corotating discs with an anisotropic two equation turbulence model', *J. Turbomachinery, vol. 110, pp.187-194.*

Sloan, D. G., Smith, P. J. and Douglas Smoot, L., 1986, 'Modeling of swirl in turbulent flow systems ' , *Prog. Energy Combust. Sci., vol 12, pp.163-250.*

Spalding, D.B., 1972, 'A novel finite-difference formulation for differential expressions involving both first and second derivatives', *Int. J. Num. Methods Eng., vol. 4, pp.551-559.*

Stuben, K. and Trottenberg, G., 1982, 'Multigrid methods: fundemental algorithms, model problem analysis and applications', *Multigrid Methods, Lecture Notes in Mathematics, vol. 960, Springer Verlag*

Tatro, P.R. and Mollo-Christensen, E.L., 1967, 'Experiments on Ekman-Layer instability', *J. Fluid Mech. vol. 28, pp.531-543*

Vaughan, C., 1987, 'A numerical investigation into the effect of an external flow field on the sealing of a rotor-stator cavity', *PhD thesis, University of Sussex, U.K.*

Vaughan, C.M., Gilham, S. and Chew, J.W., 1989, 'Numerical solutions of rotating disc flows using a non-linear multigrid algorithm', *Proc. 6th Int. Conf. Num. Meth. Lam. Turb. Flow., Swansea, pp.66-73 (Pineridge Press).*

Wilson, M., Chen, J.X. and Owen, JM., 1996, 'Computation of flow and heat transfer in rotating-disc systems ' , *IMechE Conference Transaction, London, 9-10 January, pp.41-50.*

Yap, C.R., 1987, 'Turbulent heat and momentum transfer in recirculating and impinging flows.', *PhD thesis, Dept. of Mech. Eng. University of Manchester.*

APPENDIX A

Conduction model for the unheated disc

For steady flow, the heat flux q through the unheated disc can be written (see Fig. A1):

$$q = h_{tot}(T_W - T_E) = K_{air}(dT/dZ)|_W \qquad \text{(A1)}$$

where h_{tot} is the total heat transfer coefficient, defined by:

$$h_{tot} = \frac{1}{(\Delta Z_{disc}/K_{disc})+(1/h_{ext})} \qquad \text{(A2)}$$

For the flat-shroud case, the unheated-disc was made from polycarbonate with thickness $\Delta Z_{disc} = 10$ mm and conductivity $K_{disc} = 0.2$W/mK. For the stepped-shroud case, the unheated-disc was made from steel with thickness $\Delta Z_{disc} = 10$ mm and conductivity $K_{disc} = 54$W/mK. The heat transfer coefficient at the exterior disc surface (Fig. A1), h_{ext}, was deduced from the relationship $Nu = 0.015 Re_\phi^{0.8}$, for heat transfer from an isothermal free disc rotating in air (see Owen and Rogers, 1989).

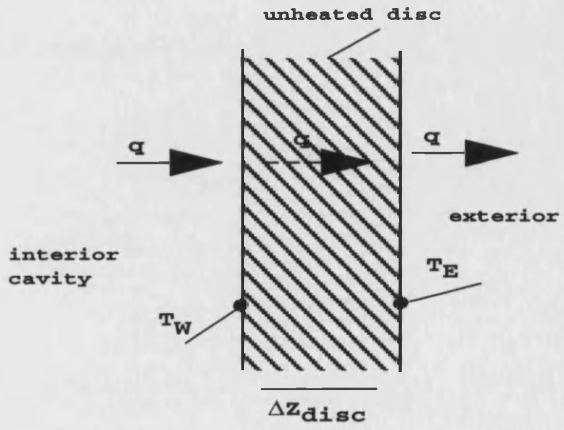

Figure A1. Conduction model definition sketch

The temperature gradient at the interior wall (in equation (A1)) was expressed using a second order formula involving the interior surface temperature, T_W, and computed fluid temperatures (Kilic, 1993). Equation (A1) was then solved to give the interior wall temperature of the unheated disc, with the exterior temperature T_E taken to be the same as that of the cooling air at inlet.

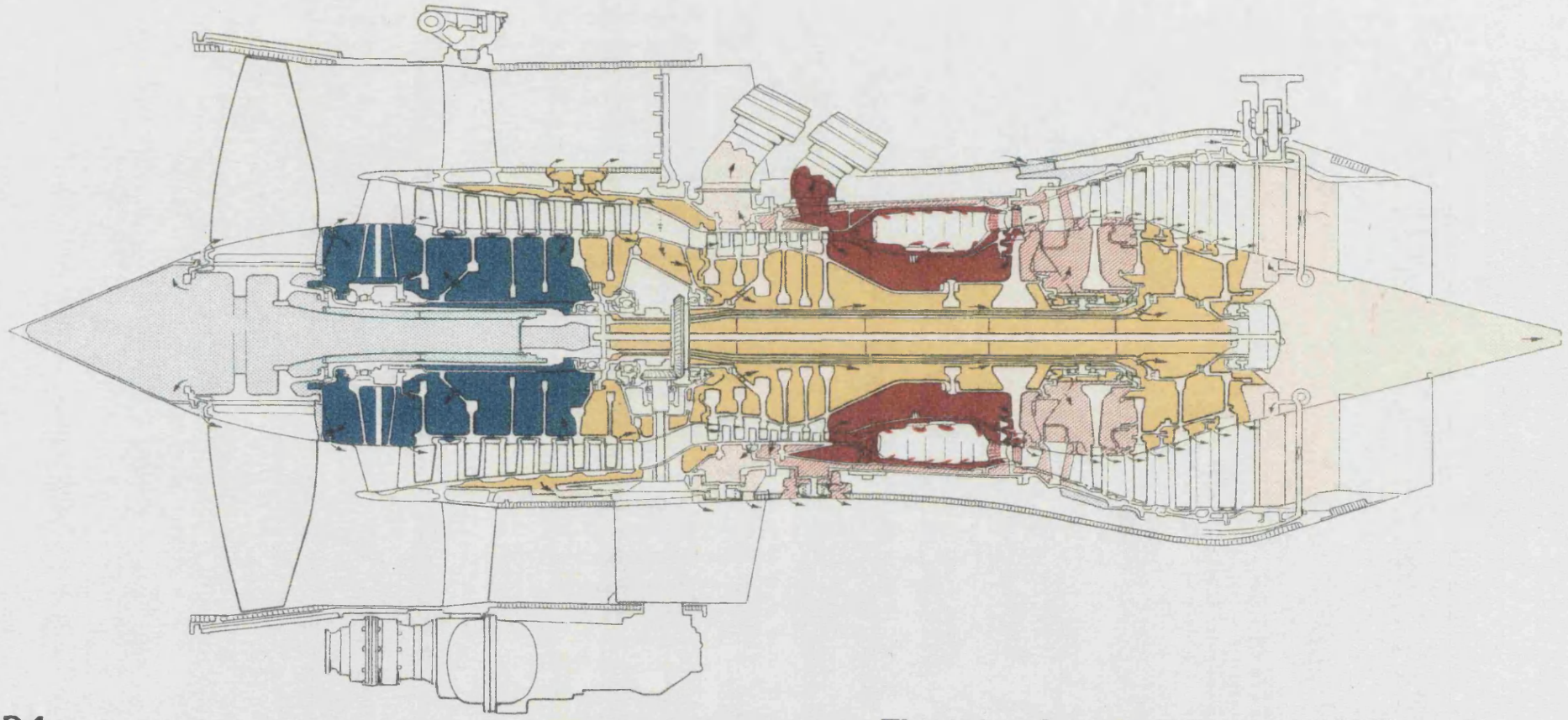

Fig 1.1 A typical Internal Airflow diagram (Rolls-Royce RB211)

94842

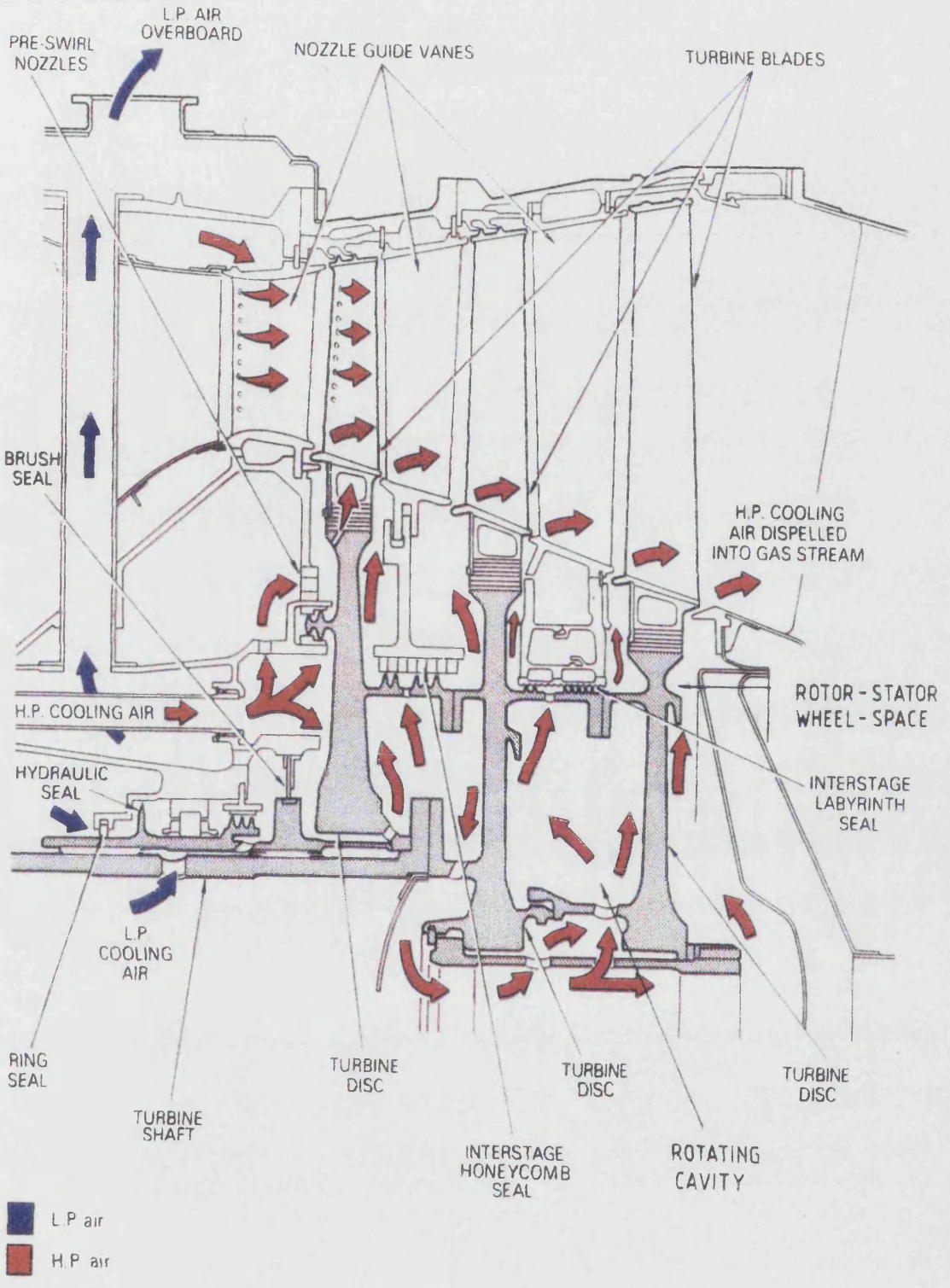

Fig 1.2. Typical turbine cooling (The Jet Engine - Rolls-Royce PLC)

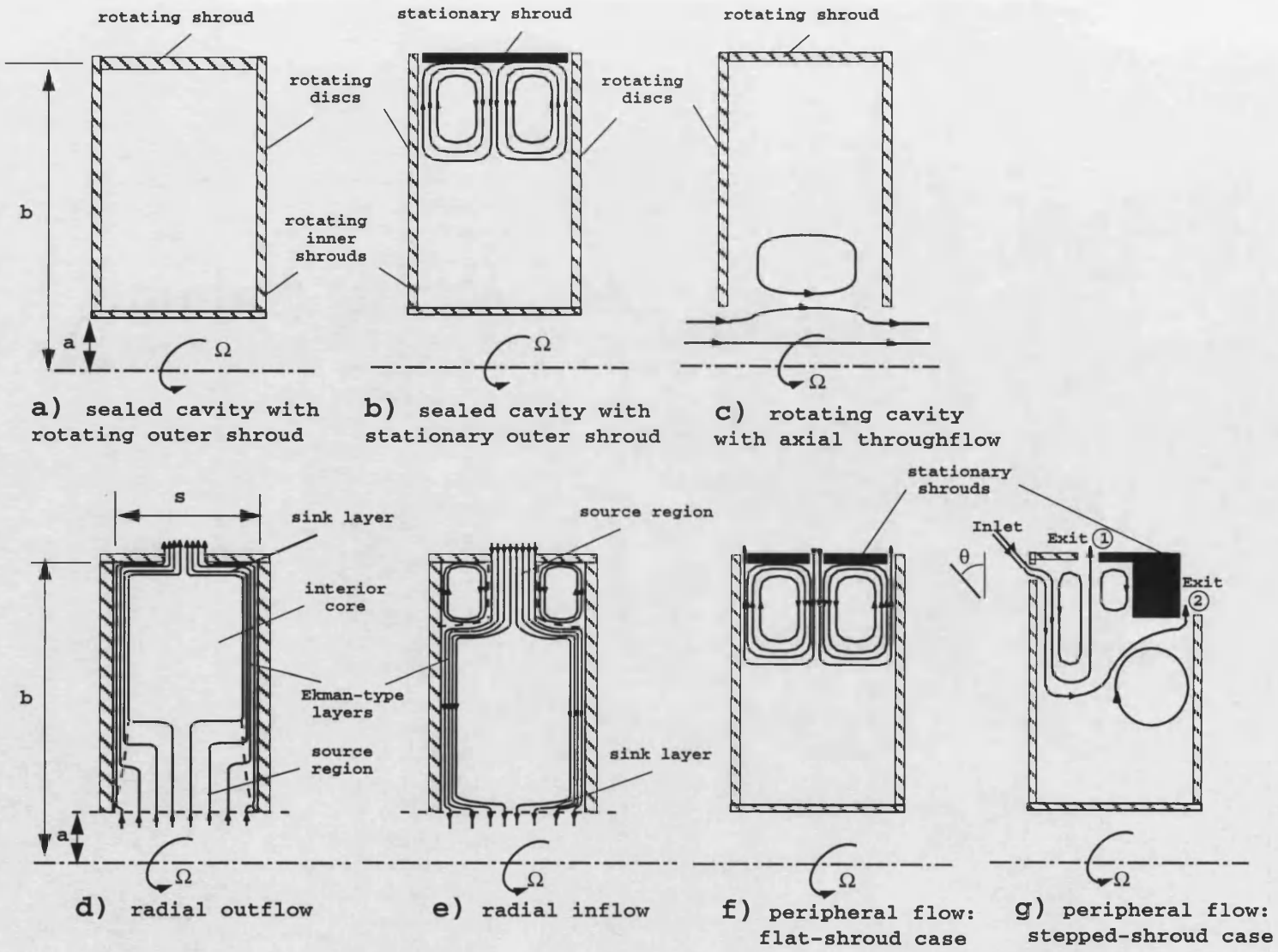

Figure 1.3. Schematic diagrams of corotating-discs

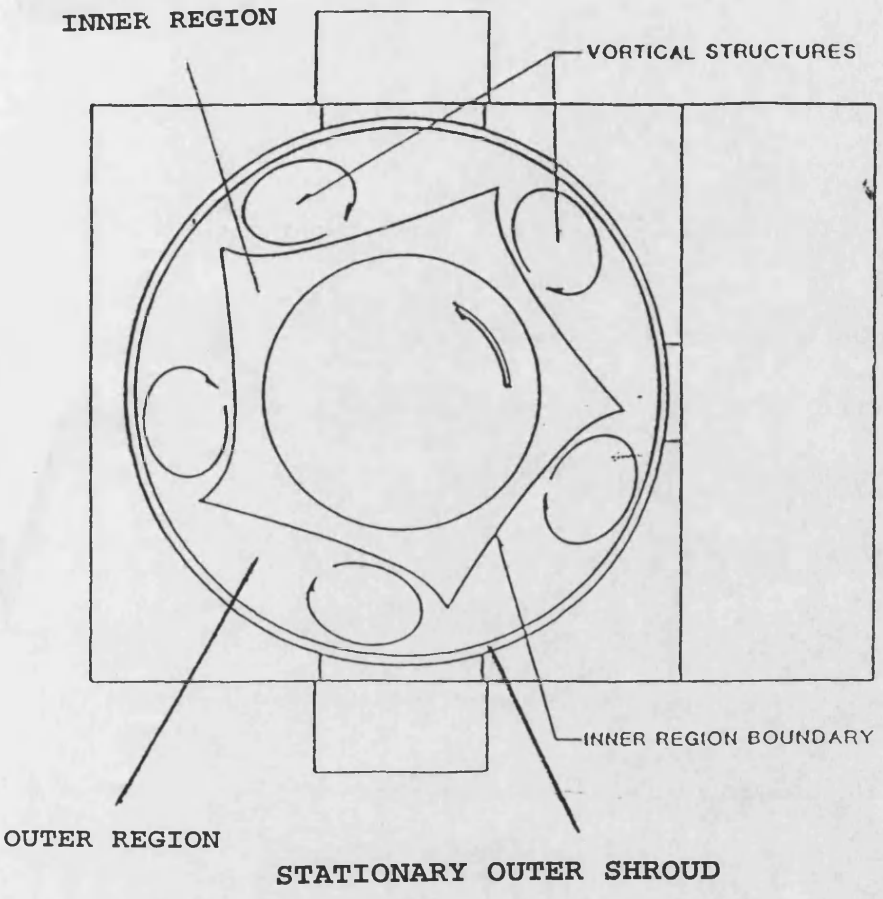

Figure 2.1. Sketch of the flow structure, Abrahamson et al (1989)

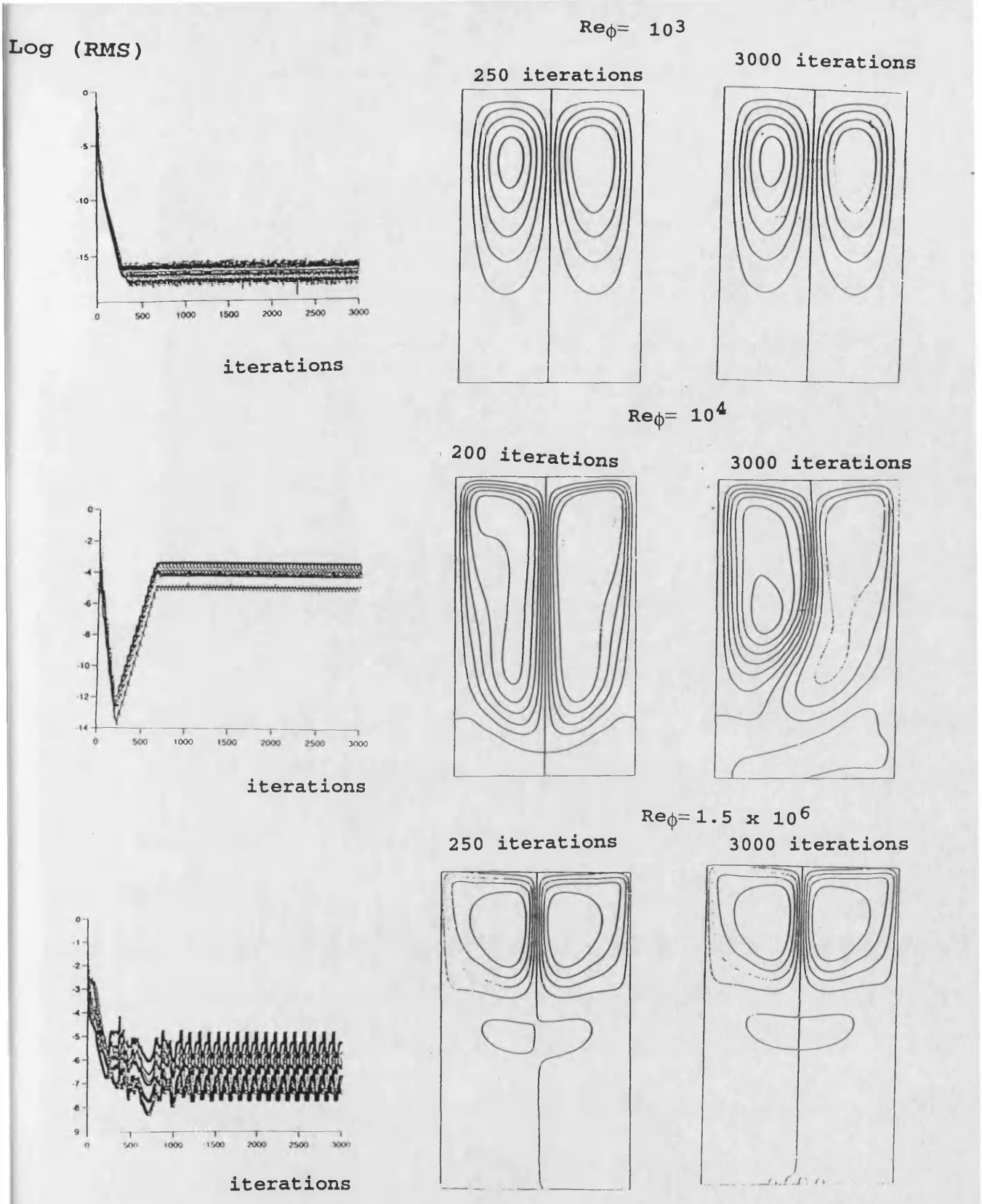

Figure 2.2. Computed streamlines and RMS changes for a sealed rotating cavity with stationary outer shroud. Arnold (1996)

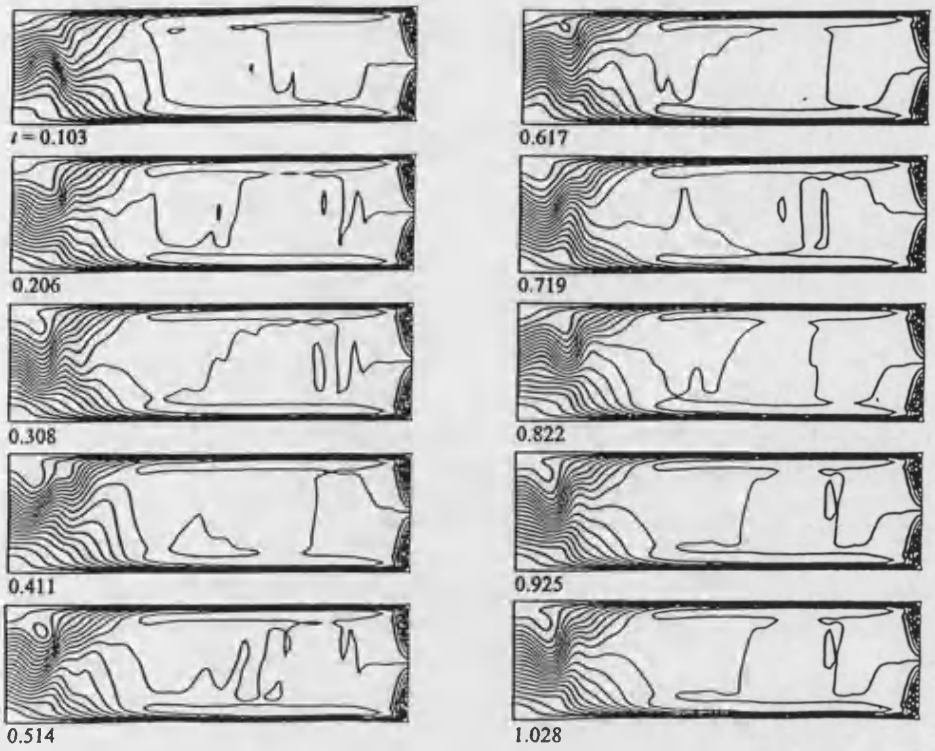

Figure 2.3. Computed instantaneous streamlines for rotating cavity with a radial outflow: C_W = 140 and E = 2.24 x 10^{-3}. Crespo et al (1996)

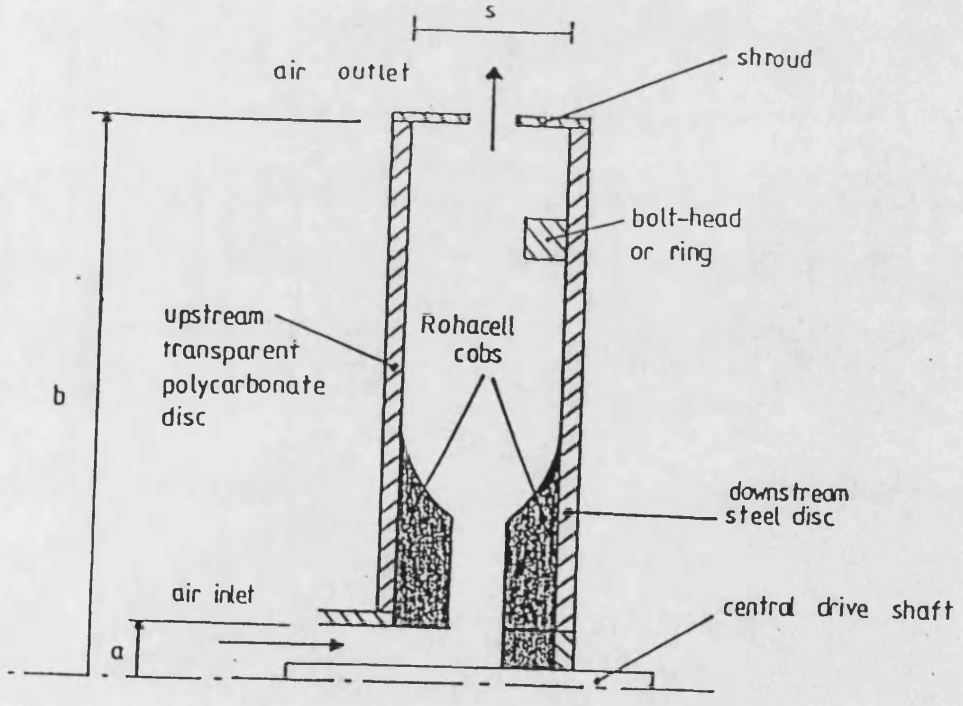

Figure 2.4. Simplified diagram of the rotating cavity with cobs.

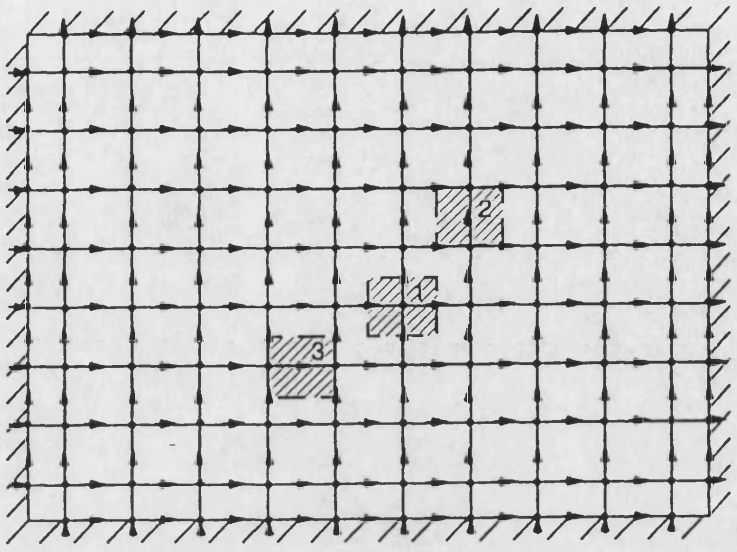

Figure 3.1. Typical finite-volume grid, control volumes for (1) Φ – cell, (2) V_r - cell, (3) V_z - cell.
Reported from Kilic (1993)

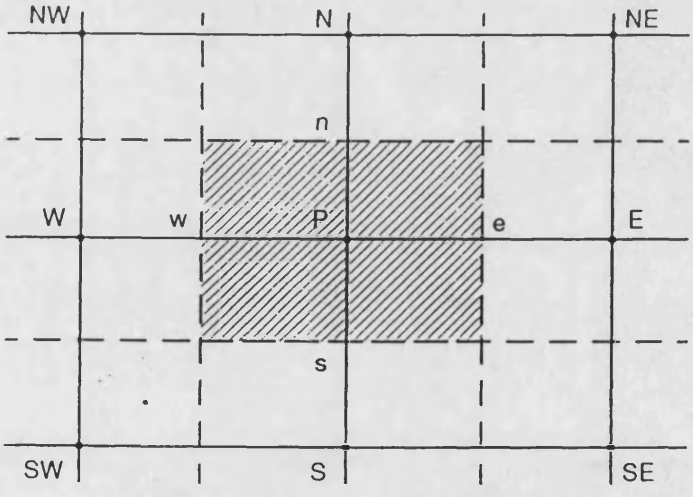

Figure 3.2. Locations of the faces of the control-volume.
Reported from Kilic (1993)

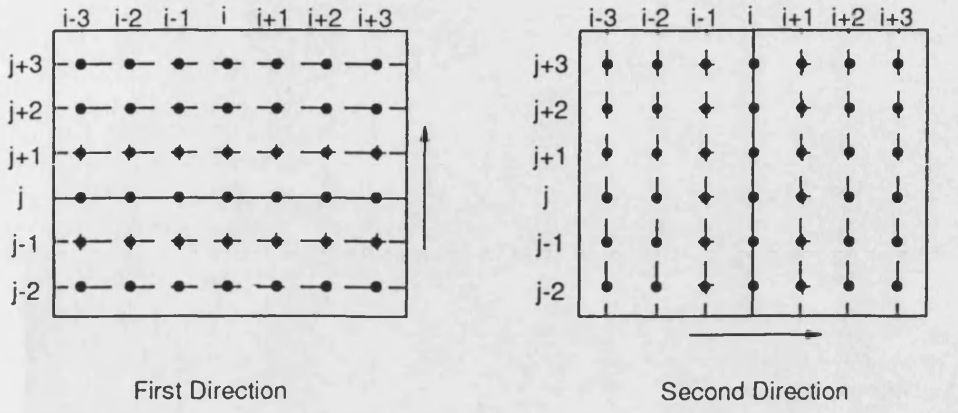

(a) Alternating - direction sweeps

grid points along the chosen line

grid points along the neighboring lines

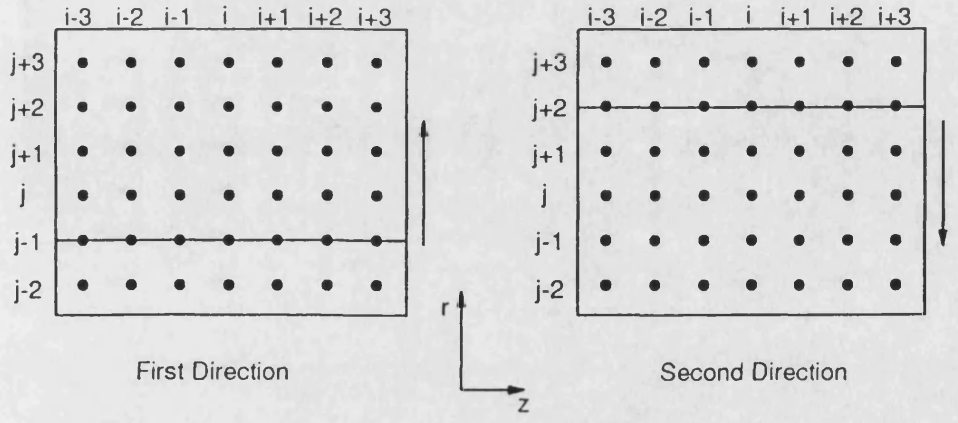

(b) Unidirectional sweeps

Figure 3.3. **Schematic representation of the smoothing process Reproduced from Kilic (1993)**

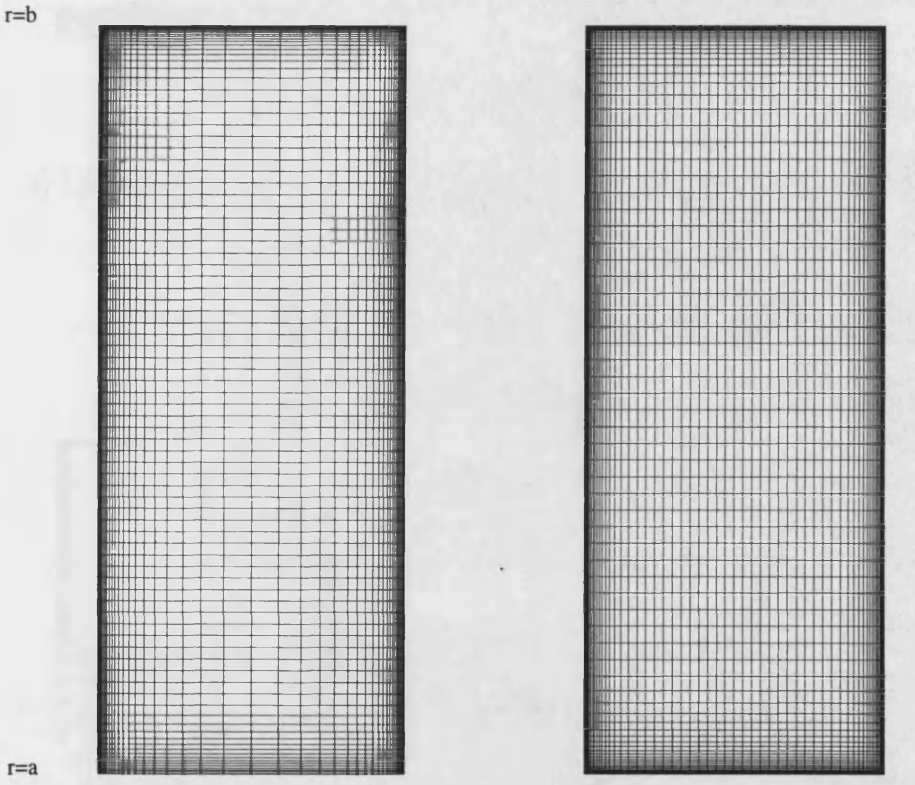

a) 115 x 91 grid nodes in r-z plane

b) 115 x 115 grid nodes in r-z plane

Figure 4.1 Typical grid distributions for rotating cavity

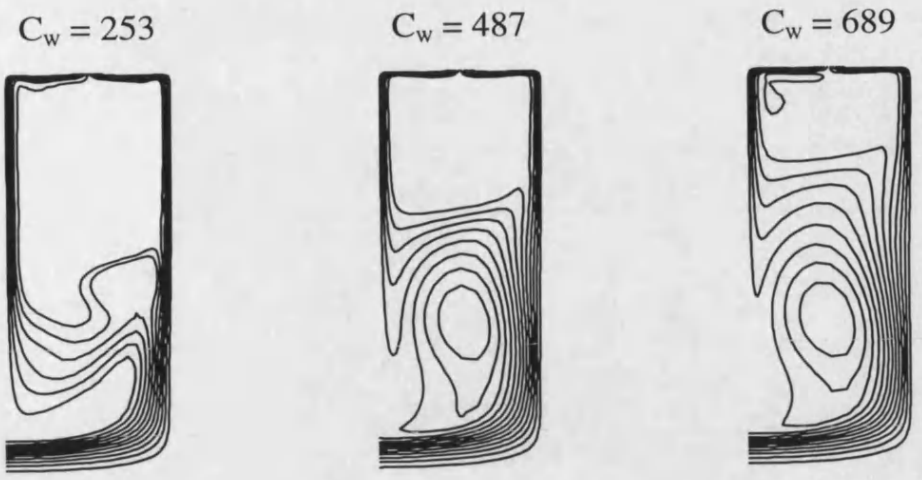

a) LS model

b) Morse model

Figure 4.2. Effect of C_w on laminar flow structure in rotating cavity with a radial outflow: G=0.133, $Re_r < 180$ and $Re_\phi = 5 \times 10^4$.

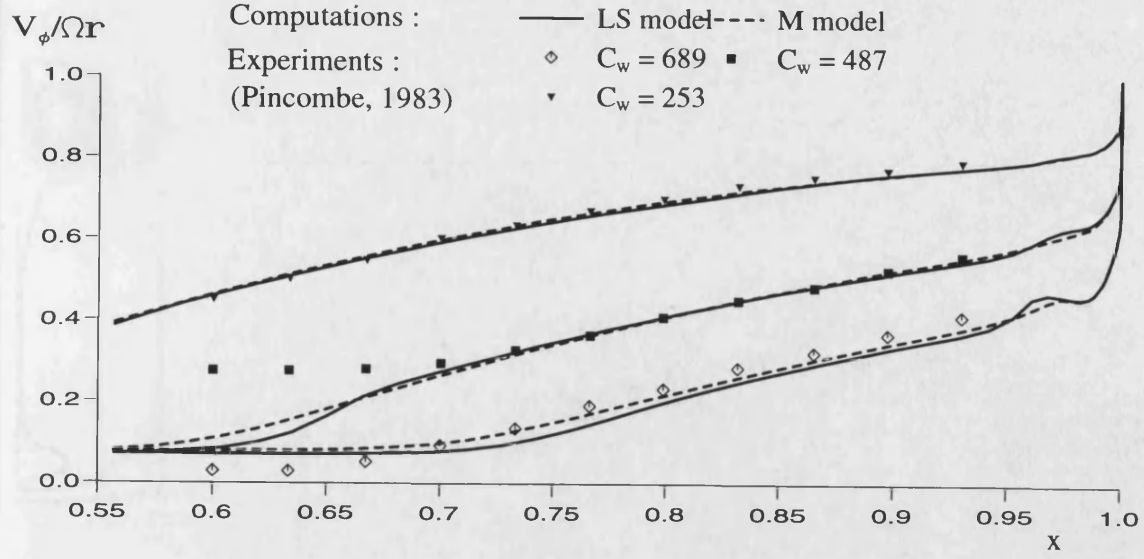

Figure 4.3. Effect of C_w on the radial variation of the tangential component of velocity for rotating cavity with a laminar outflow (Re_r<180) : G=0.133, z/s=0.5 and $Re_\phi=5x10^4$.

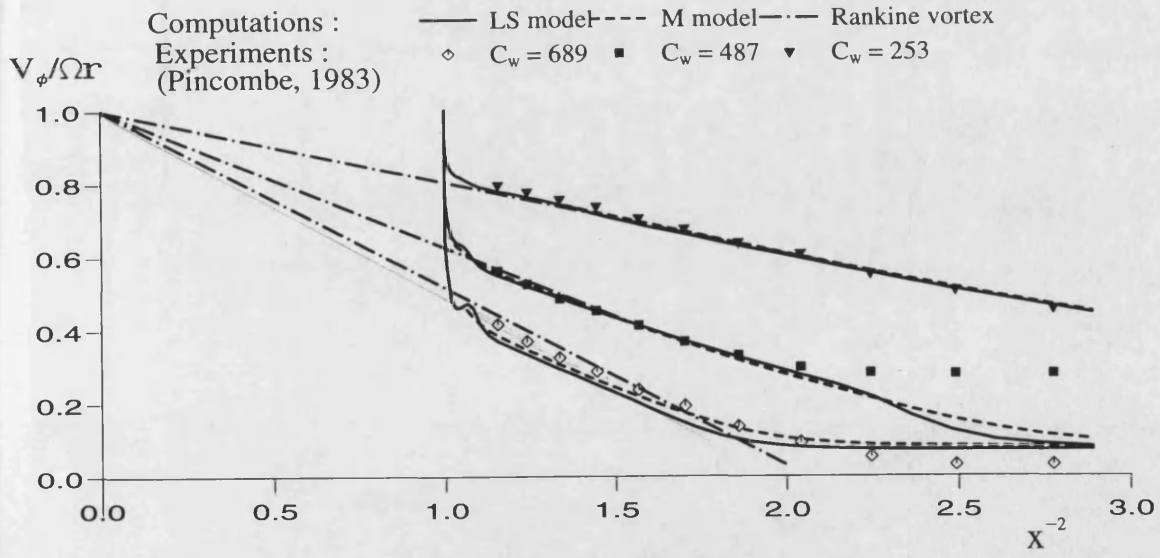

Figure 4.4. Effect of C_w on the variation of tangential component of velocity with x^{-2} for rotating cavity with a laminar radial outflow (Re_r<180) : G=0.133, z/s=0.5 and $Re_\phi=5x10^4$.

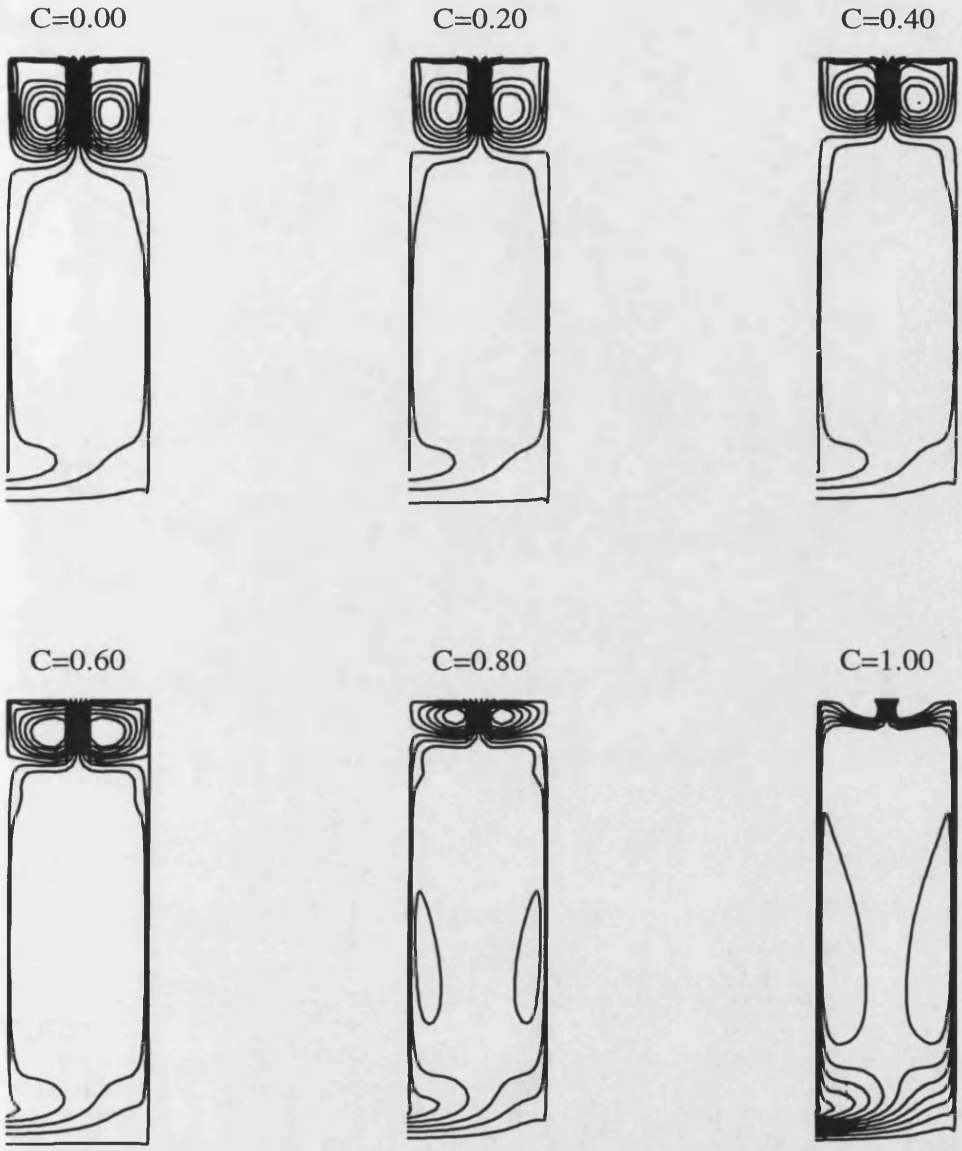

Figure 4.5. The effect of different swirl ratios on flow structure for rotating cavity with a laminar radial inflow (Re_r<180): G=0.133, Re_ϕ=1.97x10^5 and C_w=-440. (LS model)

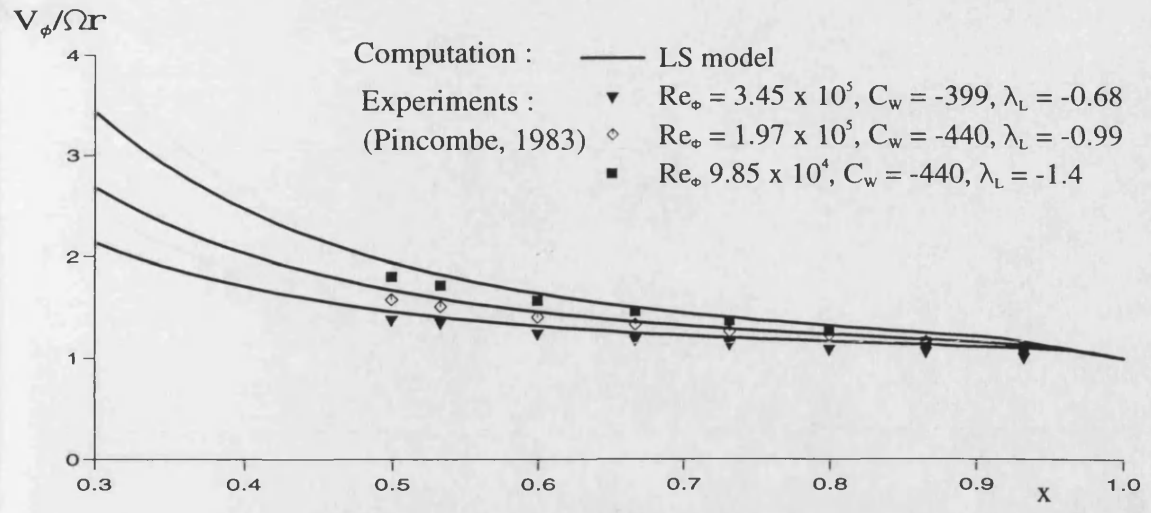

Figure 4.6. Radial variation of tangential component of velocity for rotating cavity with a laminar radial inflow (Re_r<180): shroud F, C=1.0, G=0.133 and z/s=0.5.

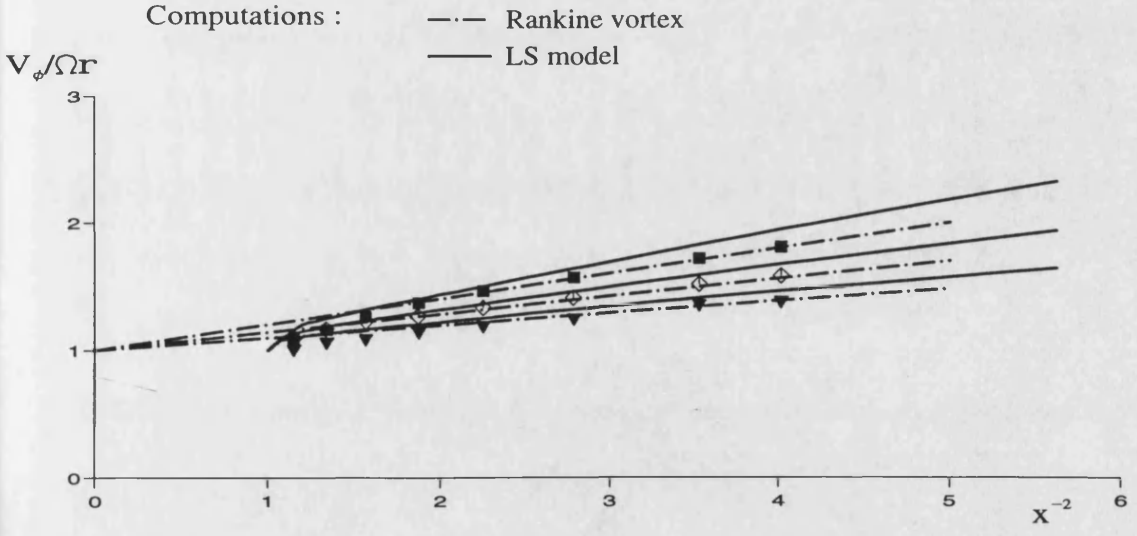

Figure 4.7. Variation of tangential component of velocity with x^{-2} for rotating cavity with a laminar radial inflow (Re_r<180): shroud F, C=1.0, G=0.133 and z/s=0.5. (symbols same as for Figure 4.6)

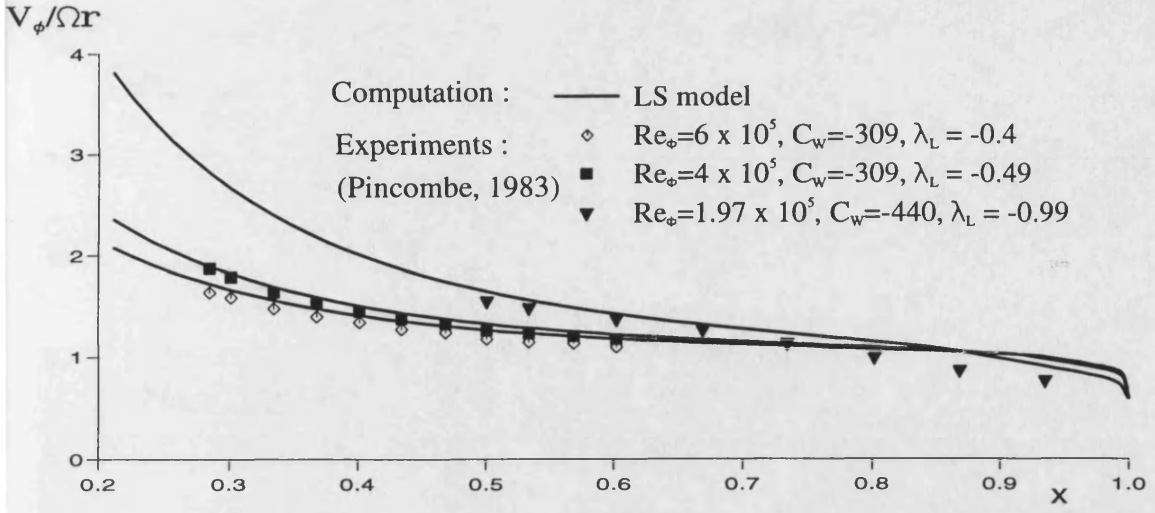

Figure 4.8. Radial variation of tangential component of velocity for rotating cavity with a laminar radial inflow (Re_r < 180): shroud A, C=0.59, G=0.133 and z/s=0.5.

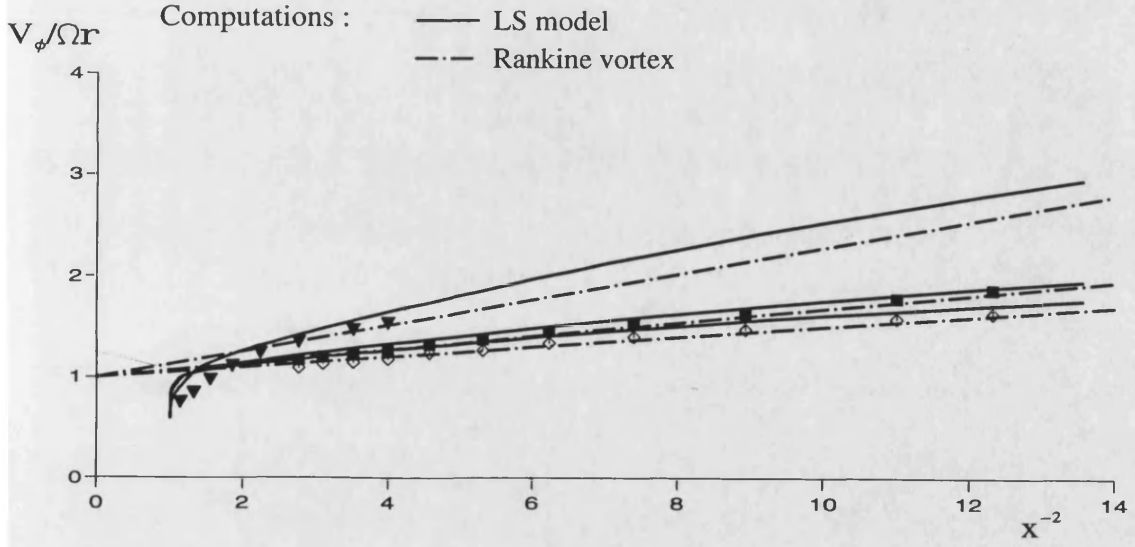

Figure 4.9. Variation of tangential component of velocity with x^{-2} for rotating cavity with a radial laminar inflow (Re_r < 180):shroud A, C=0.59, G=0.133 and z/s=0.5 (symbols same as for Figure 4.8)

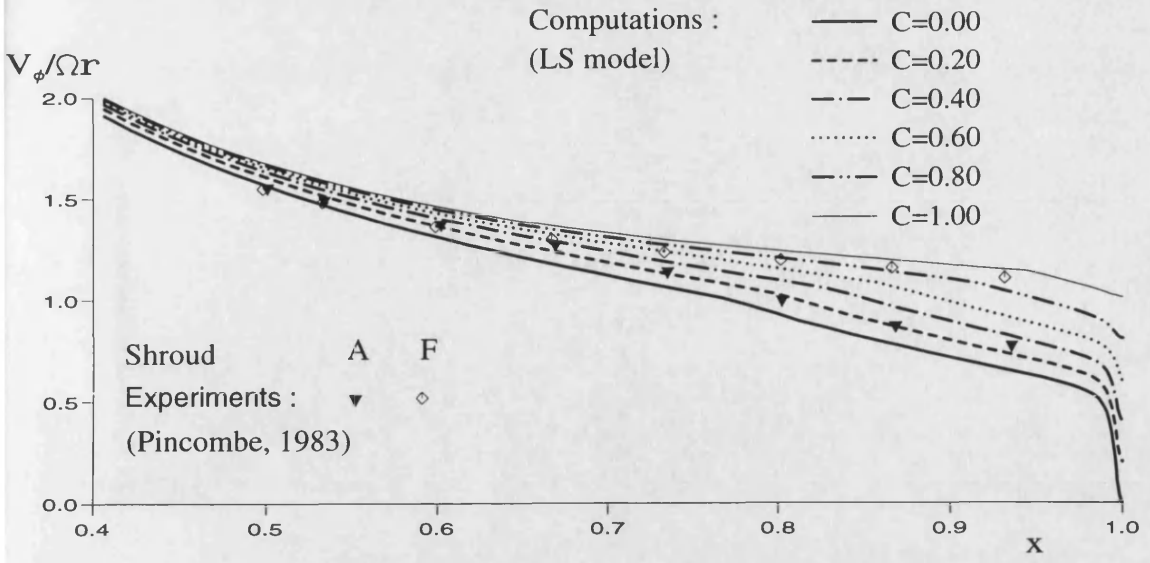

Figure 4.10. Effect of the inlet swirl ratios on the variation of tangential component of velocity with radius for rotating cavity with a laminar inflow (Re_r<180): G=0.133, z/s=0.5, Re_ϕ=1.97 x 10^5, C_w=-440 and λ_L = -0.99.

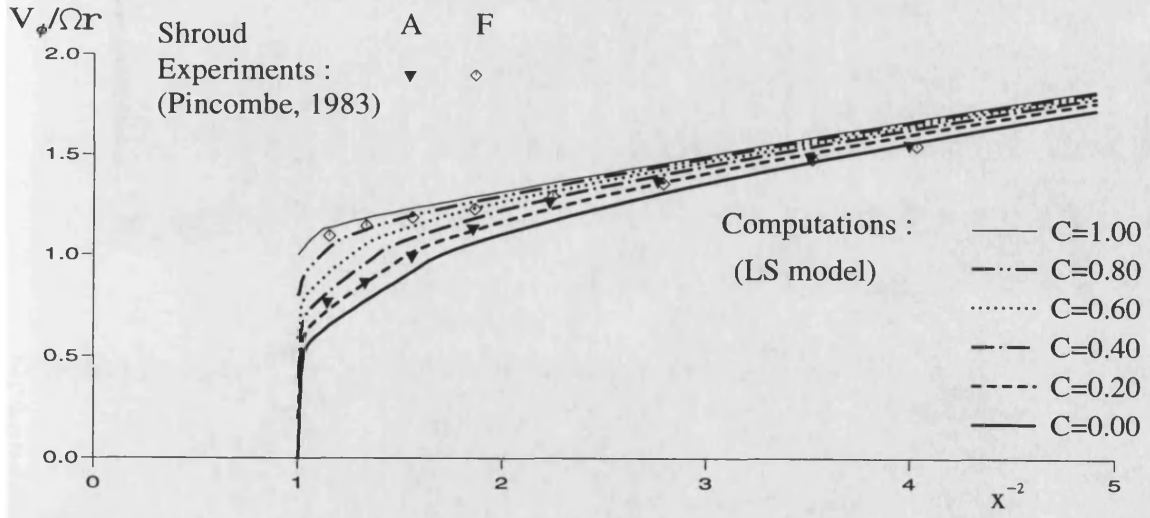

Figure 4.11 Effect of the inlet swirl ratio on the variation of tangential component of velocity with x^{-2} for rotating cavity with a laminar radial inflow (conditions same as for Figure 4.10)

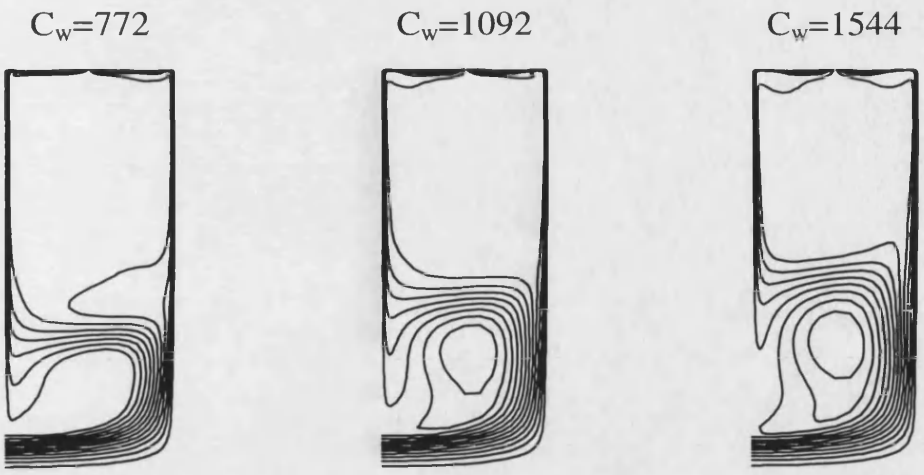

a) LS model

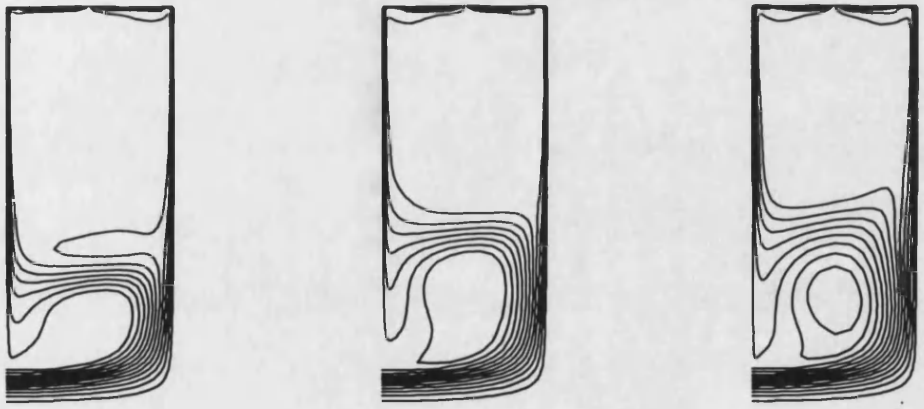

b) Morse model

Figure 4.12. Effect of C_w on turbulent flow structure in rotating cavity with a radial outflow : G=0.133 and $Re_\phi=4x10^5$.

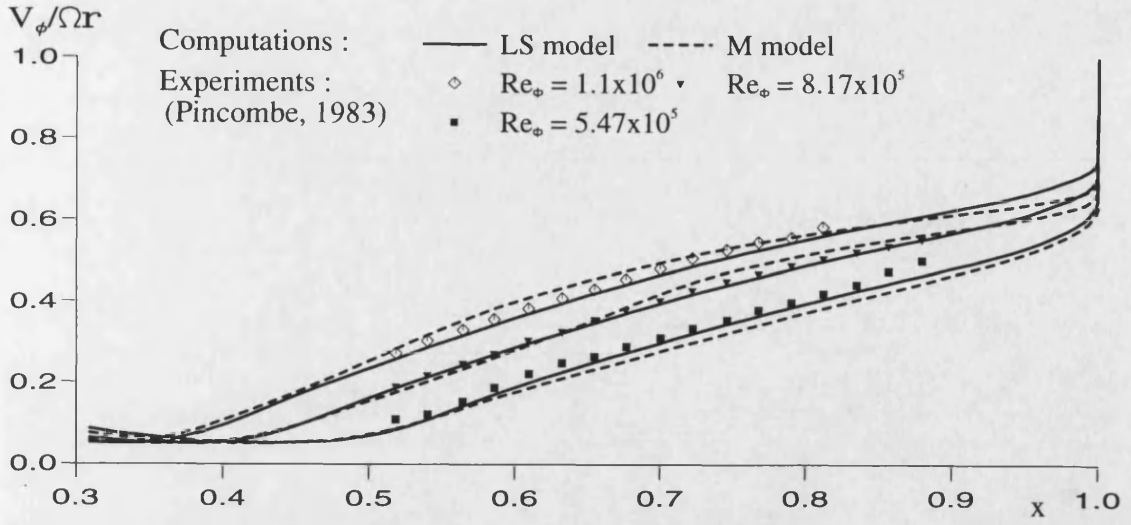

Figure 4.13 Effect of Re_Φ on the radial variation of the tangential component of velocity for rotating cavity with a turbulent radial outflow (Re_r>180) : G=0.133, z/s=0.5 and C_w=2500.

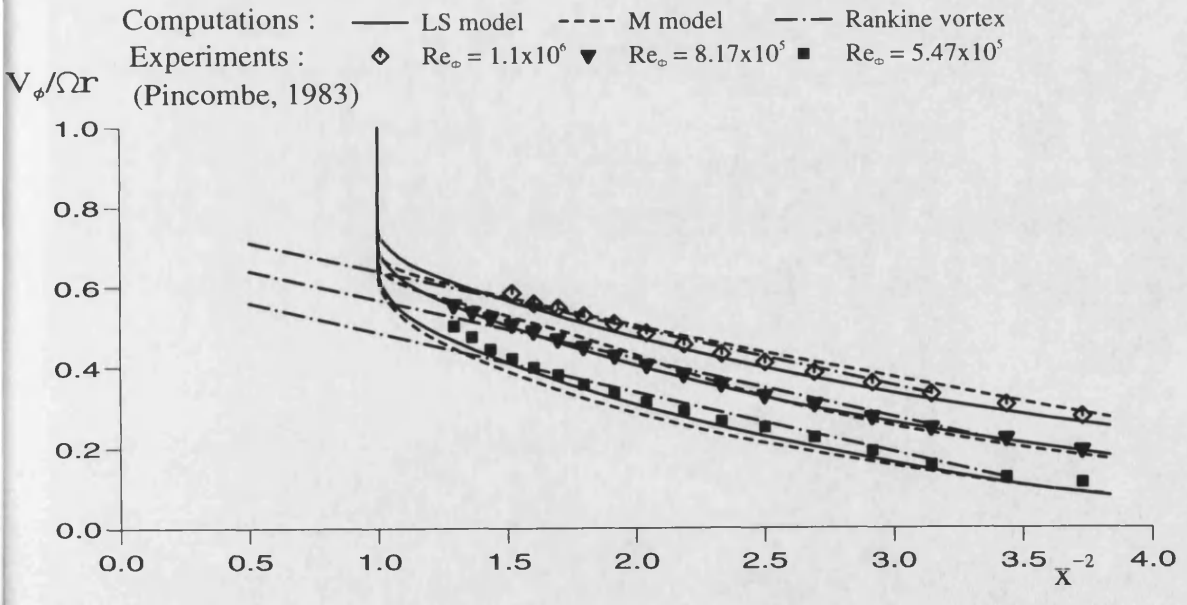

Figure 4.14 Effect of Re_ϕ on the variation of tangential component of velocity with x^{-2} for rotating cavity with a turbulent radial outflow (Re_r>180) : G=0.133, z/s=0.5 and C_w=2500.

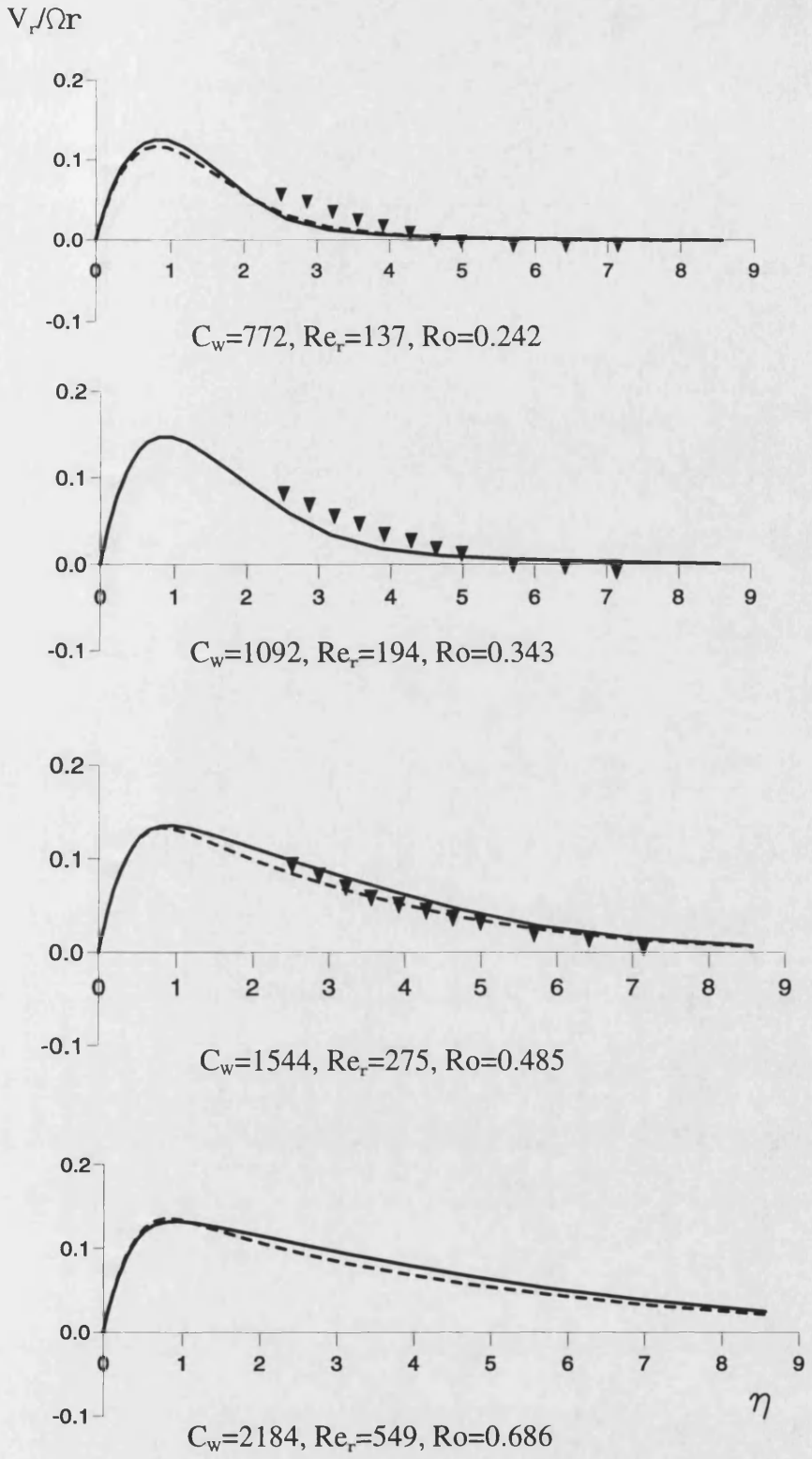

Figure 4.15. Axial distribution of the radial component of velocity in the boundary layer for rotating cavity with a radial outflow: G=0.133, x=0.633 and $Re_\phi=4x10^5$

____ LS model

- - - - M model

▼ Pincombe (1983)

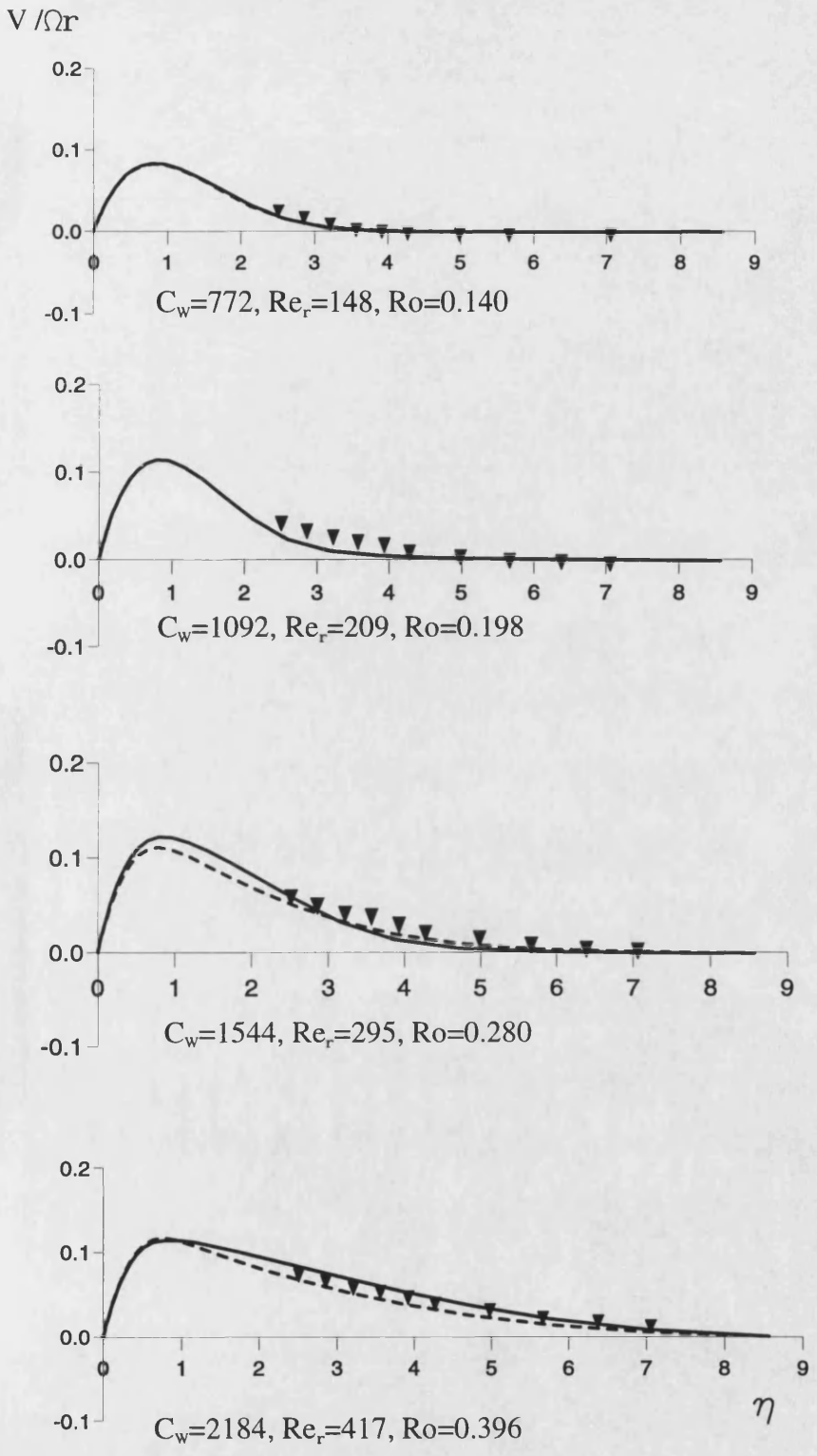

Figure 4.16. Axial distribution of the radial component of velocity in the boundary layer for rotating cavity with a radial outflow: G=0.133, x=0.833 and $Re_\phi=4x10^5$

—— LS model

- - - M model

▼ Pincombe (1983)

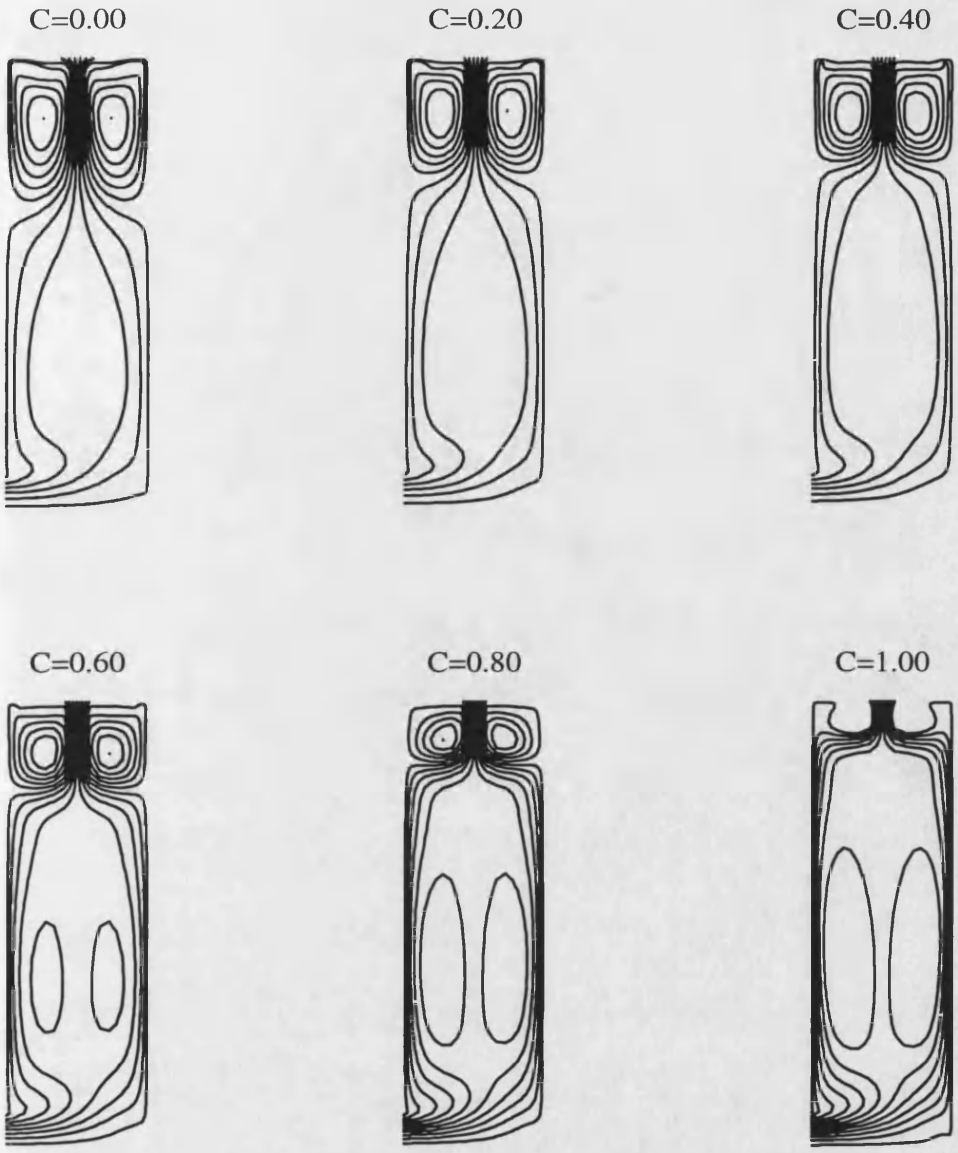

Figure 4.17. Effect of different swirl ratios on flow structure for rotating cavity with a turbulent radial inflow (Re_r>180):G=0.133, Re_ϕ=1.97x10^5 and C_w=-1415. (LS model)

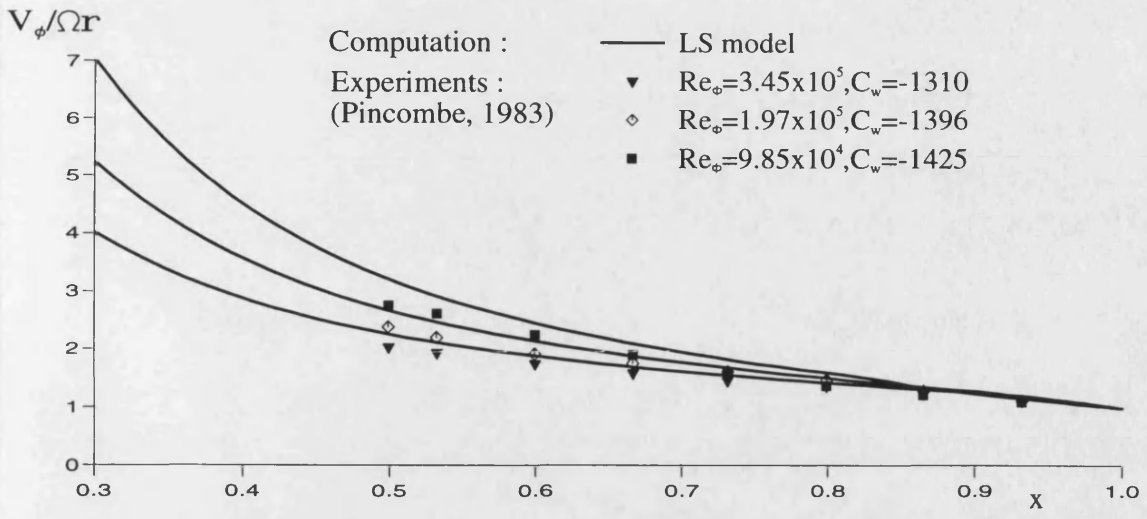

Figure 4.18. Radial variation of tangential component of velocity for rotating cavity with a turbulent radial inflow (Re_r>180): shroud F, c=1, G=0.133 and z/s=0.5.

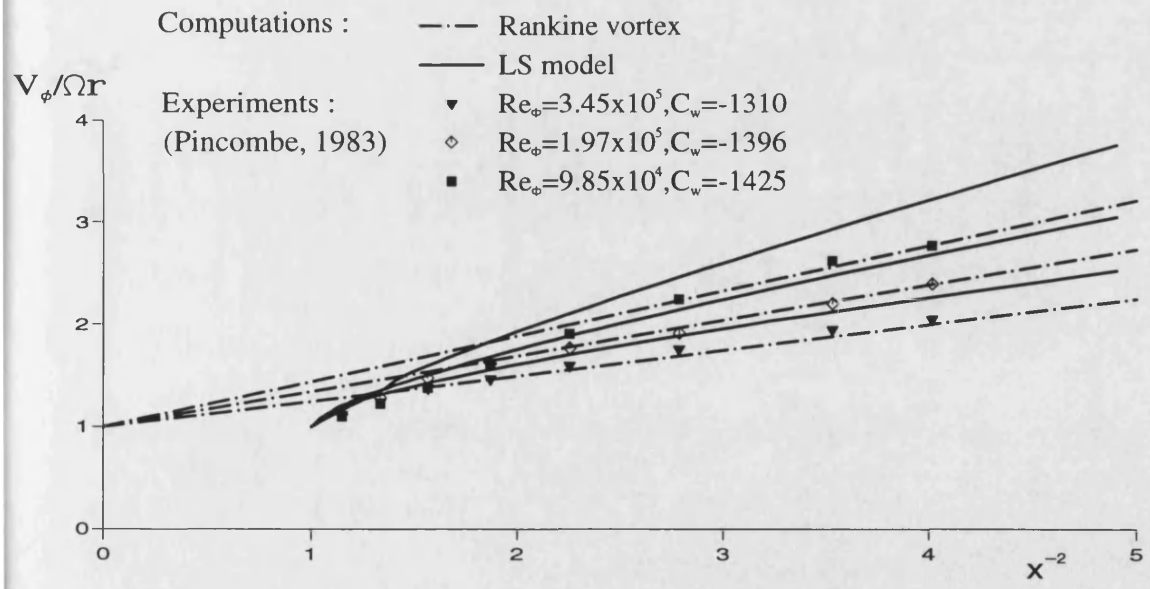

Figure 4.19 Variation of tangential component of velocity with x^{-2} for rotating cavity with a turbulent radial inflow (Re_r>180): shroud F, c=1.0, G=0.133 and z/s=0. z/s=0.5.

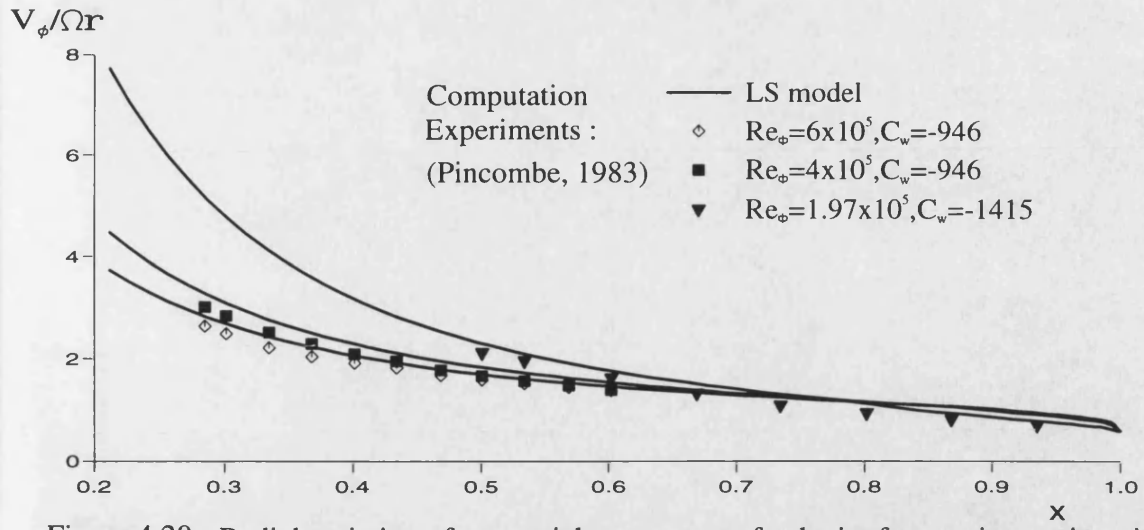

Figure 4.20 Radial variation of tangential component of velocity for rotating cavity with a turbulent radial inflow (Re_r>180): shroud A, c=0.59, G=0.133 and z/s=0.5.

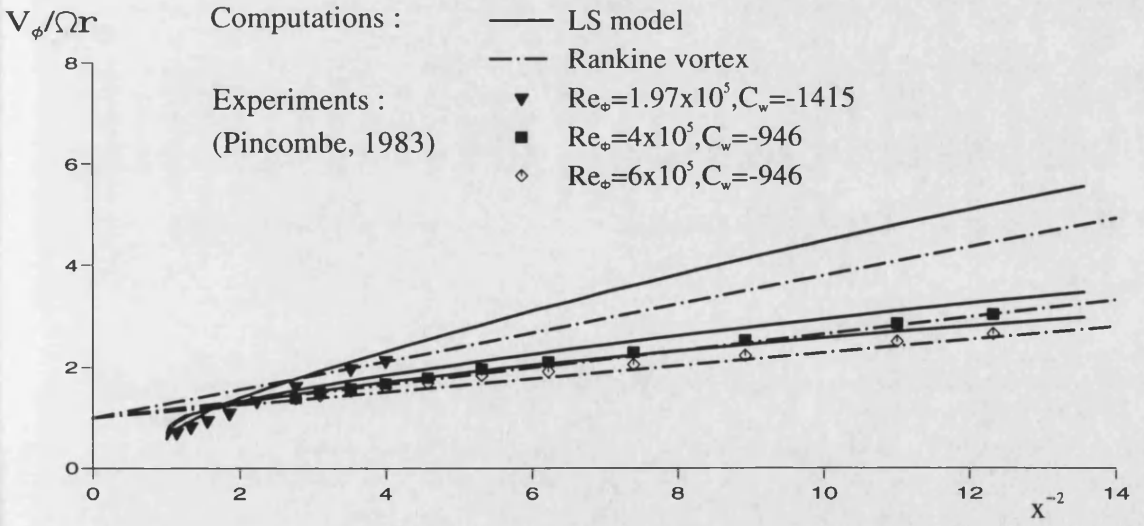

Figure 4.21 Variation of tangential component of velocity with x^{-2} for rotating cavity with a turbulent radial inflow (Re_r>180): shroud A, c=0.59, G=0.133 and z/s=0.5.

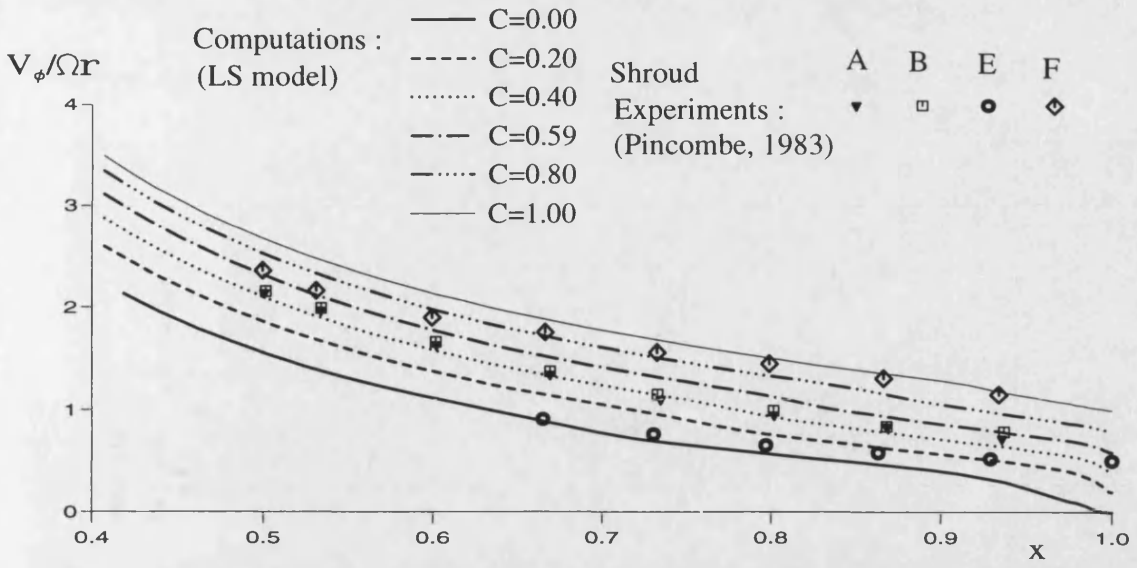

Figure 4.22. Effect of the inlet swirl ratios on the variation of tangential component of velocity with radius for rotating cavity with a turbulent radial inflow (Re_r>180): G=0.133, z/s=0.5, Re_ϕ=1.97 x 10^5, C_w=-1415 and λ_T=-0.082

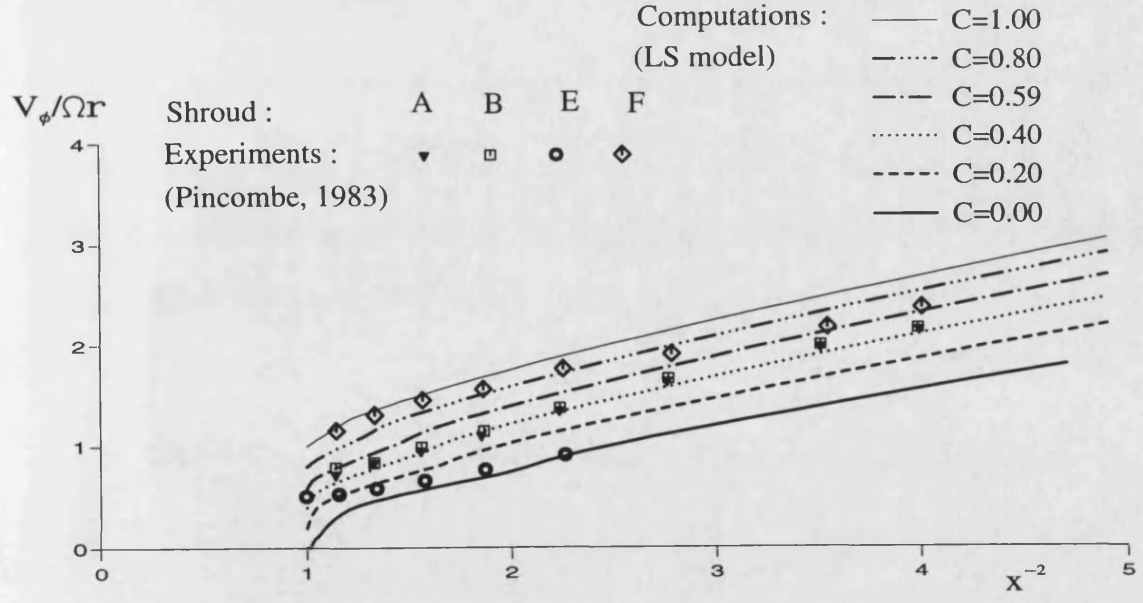

Figure 4.23. Effect of the inlet swirl ratio on the variation of tangential component of velocity with x^{-2} for rotating cavity with a turbulent radial inflow (Re_r>180): G=0.133, z/s=0.5, Re_ϕ=1.97 x 10^5, C_w=-1415 and λ_T=-0.082

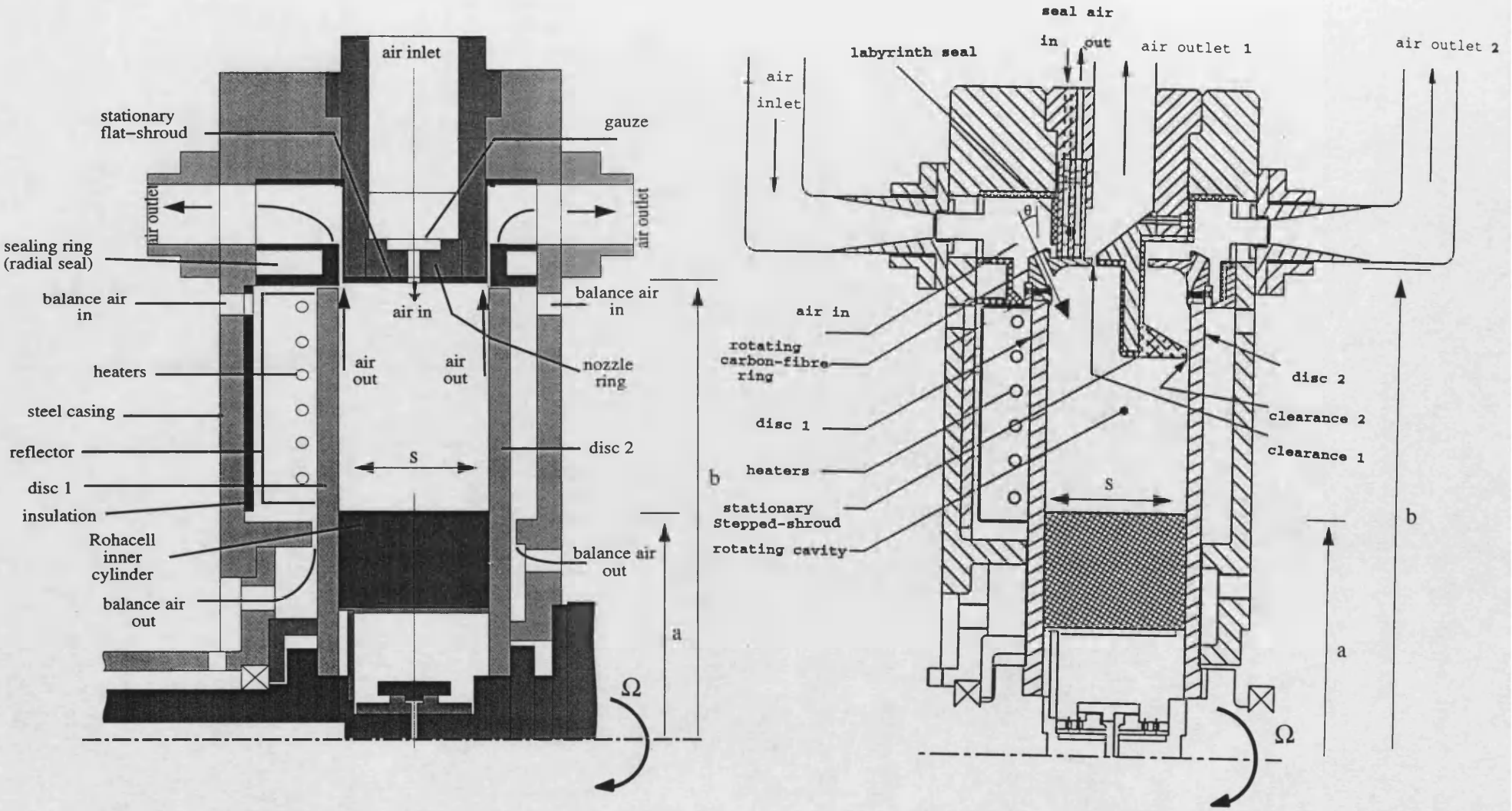

Figure 5.1. Schematic diagrams of the peripheral flow rigs

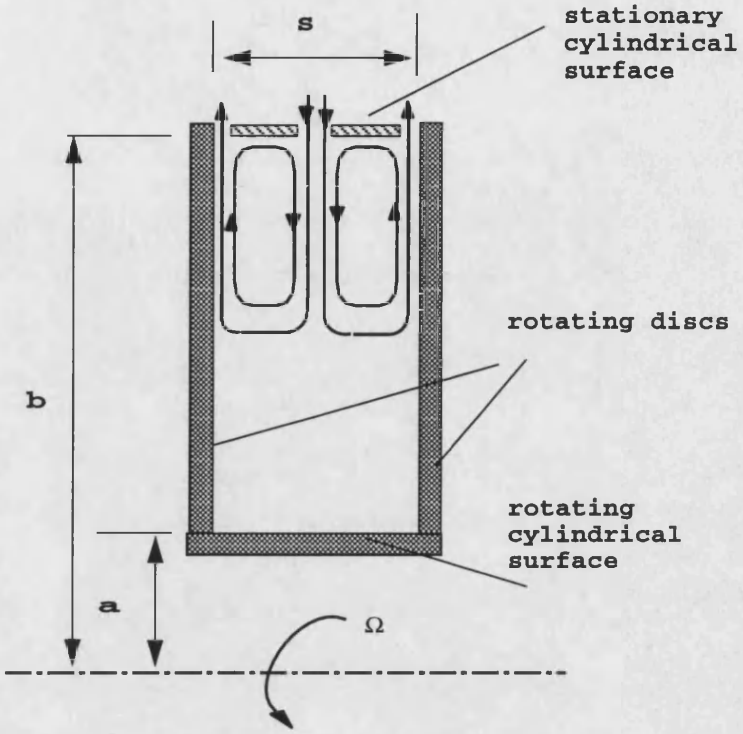

Figure 6.1. Schematic diagram of peripheral flow for flat-shroud case

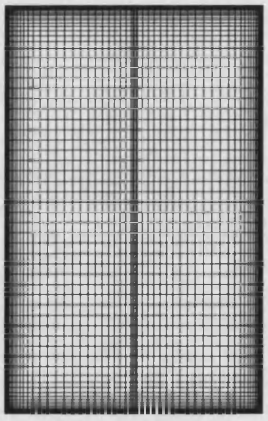

91 x 91 grid nodes in r-z plane

Figure 6.2 Typical grid distribution for flat-shroud

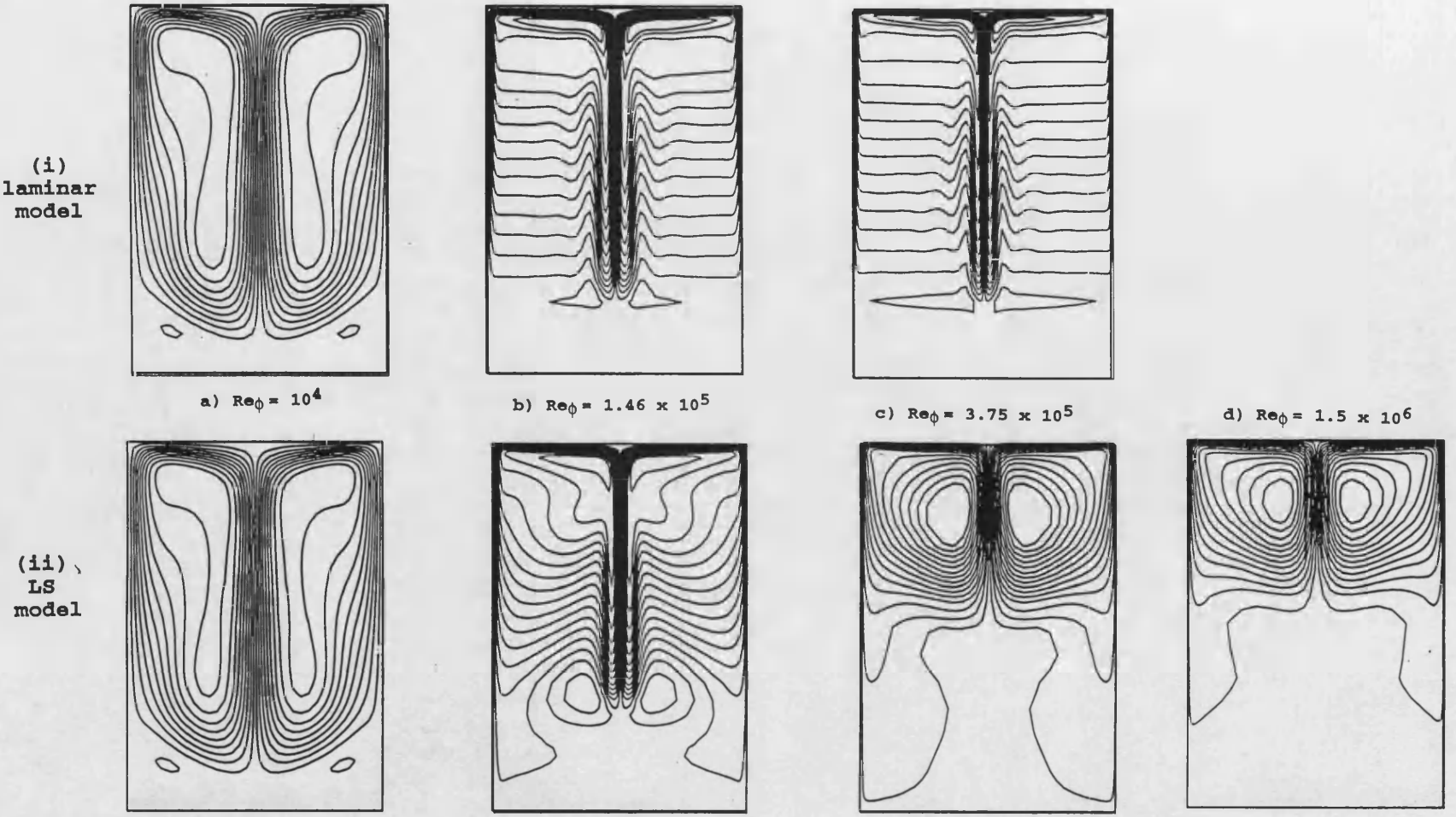

Figure 6.3. Effect of Re_ϕ on computed streamlines for sealed rotating cavity with flat-shroud

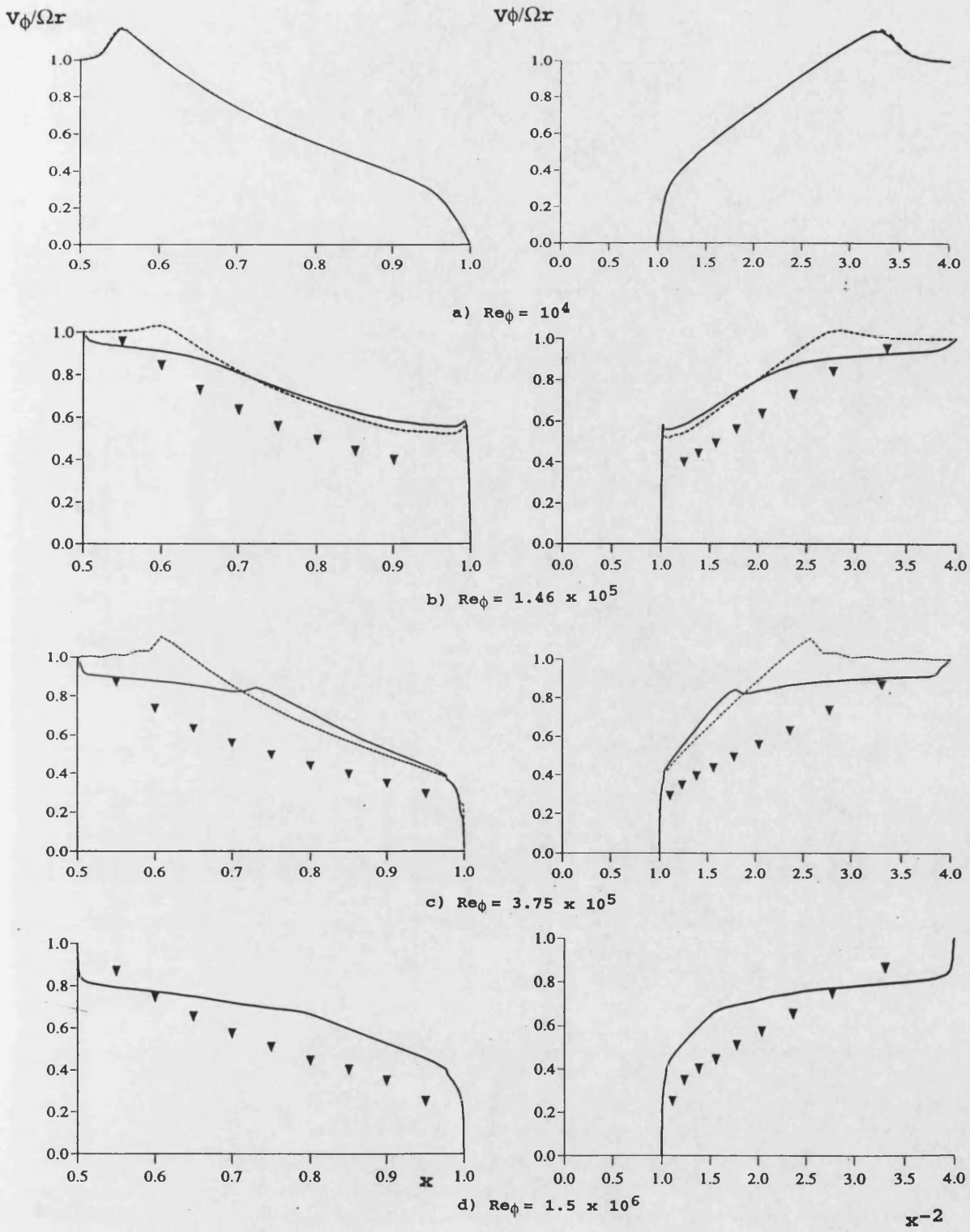

Figure 6.4. Effect of Re_ϕ on variation of $V_\phi/\Omega r$ with x and x^{-2} for sealed rotating cavity with flat-shroud

——— LS model -------- laminar model

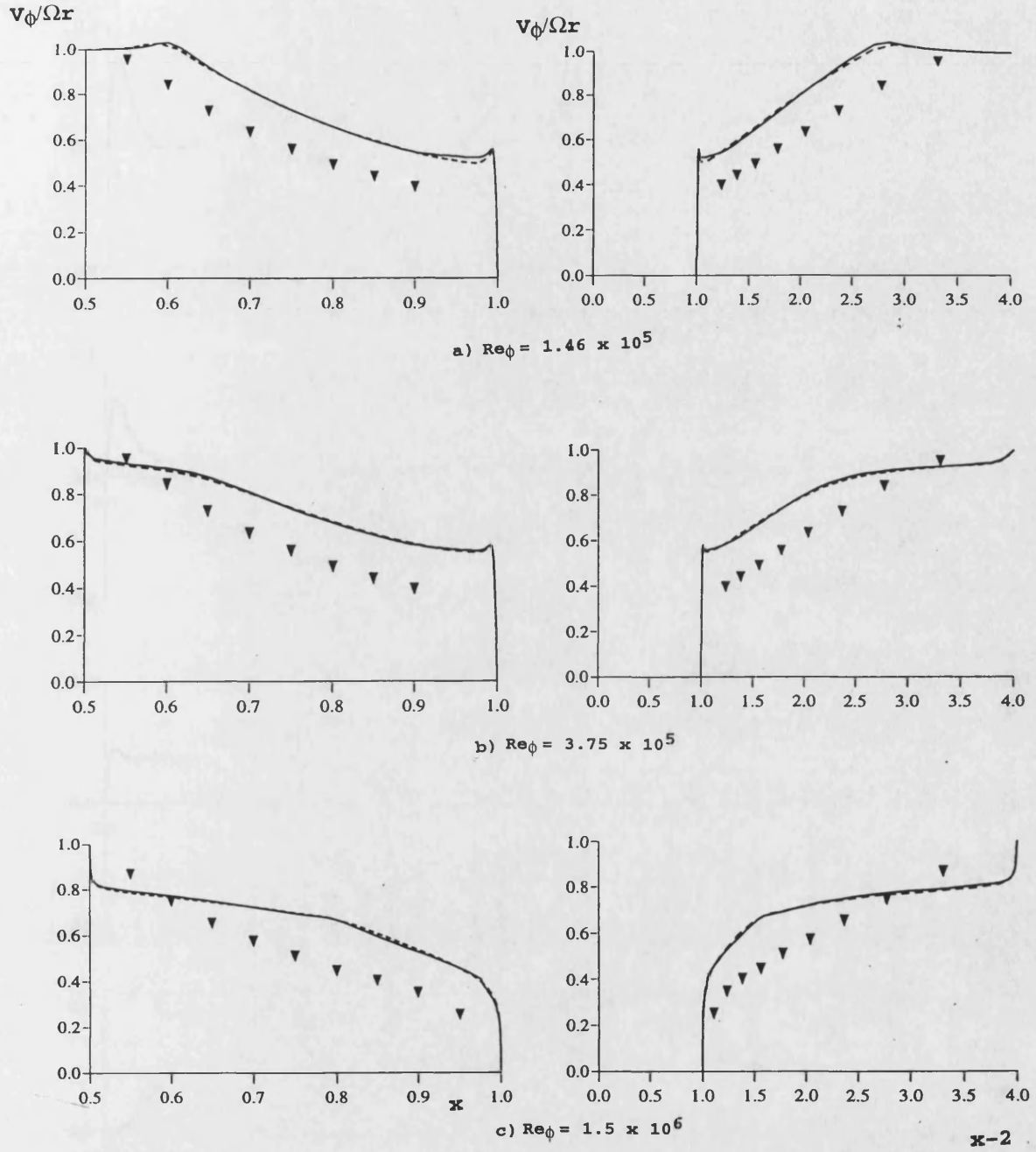

Figure 6.5. Effect of Re_ϕ on variation of $V_\phi/\Omega r$ with x and x^{-2} for sealed rotating cavity with flat-shroud (grid-independence results)

——— LS model (67 x 67 grid nodes)

- - - - LS model (91 x 131 grid nodes)

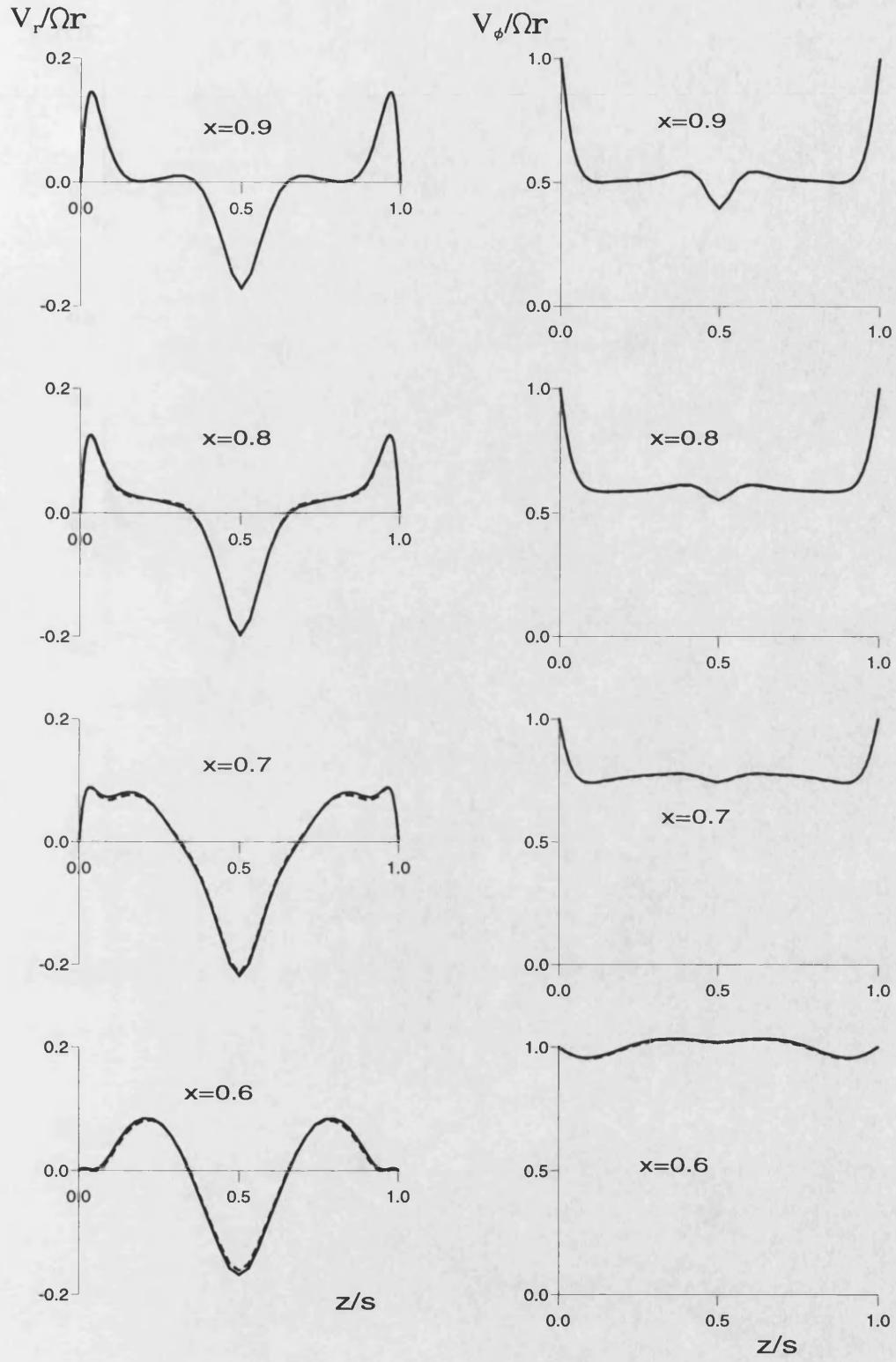

Figure 6.6. Axial variation of $V_r/\Omega r$ and $V_\phi/\Omega r$ for sealed rotating cavity with flat-shroud: $Re_\phi = 10^4$.

——LS model ----- Laminar model

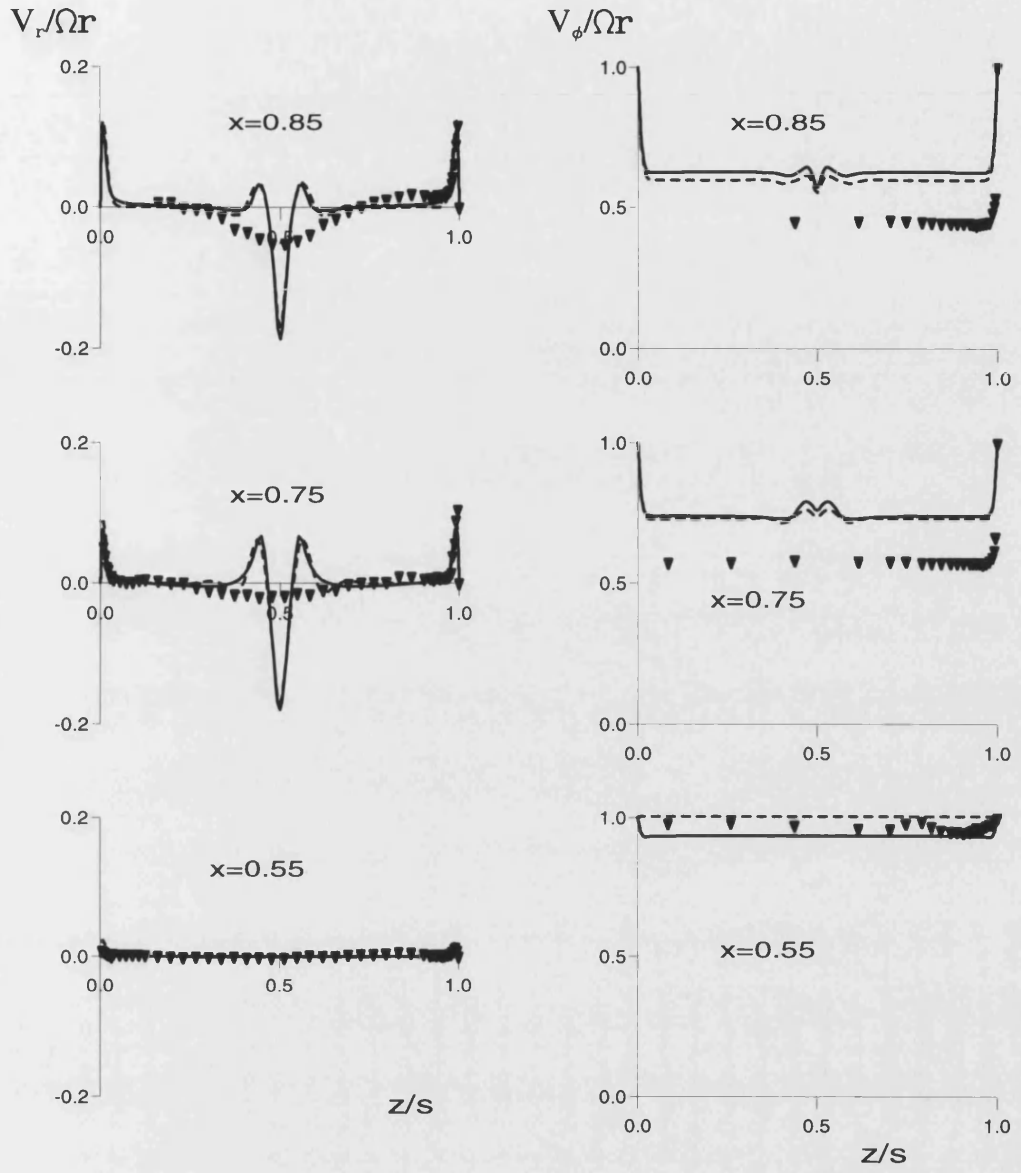

Figure 6.7. Axial variation of $V_r/\Omega r$ and $V_\phi/\Omega r$ for sealed rotating cavity with flat-shroud: $Re_\phi = 1.46 \times 10^5$.

——— LS model

----- Laminar model

▼ Data of Gan (1994)

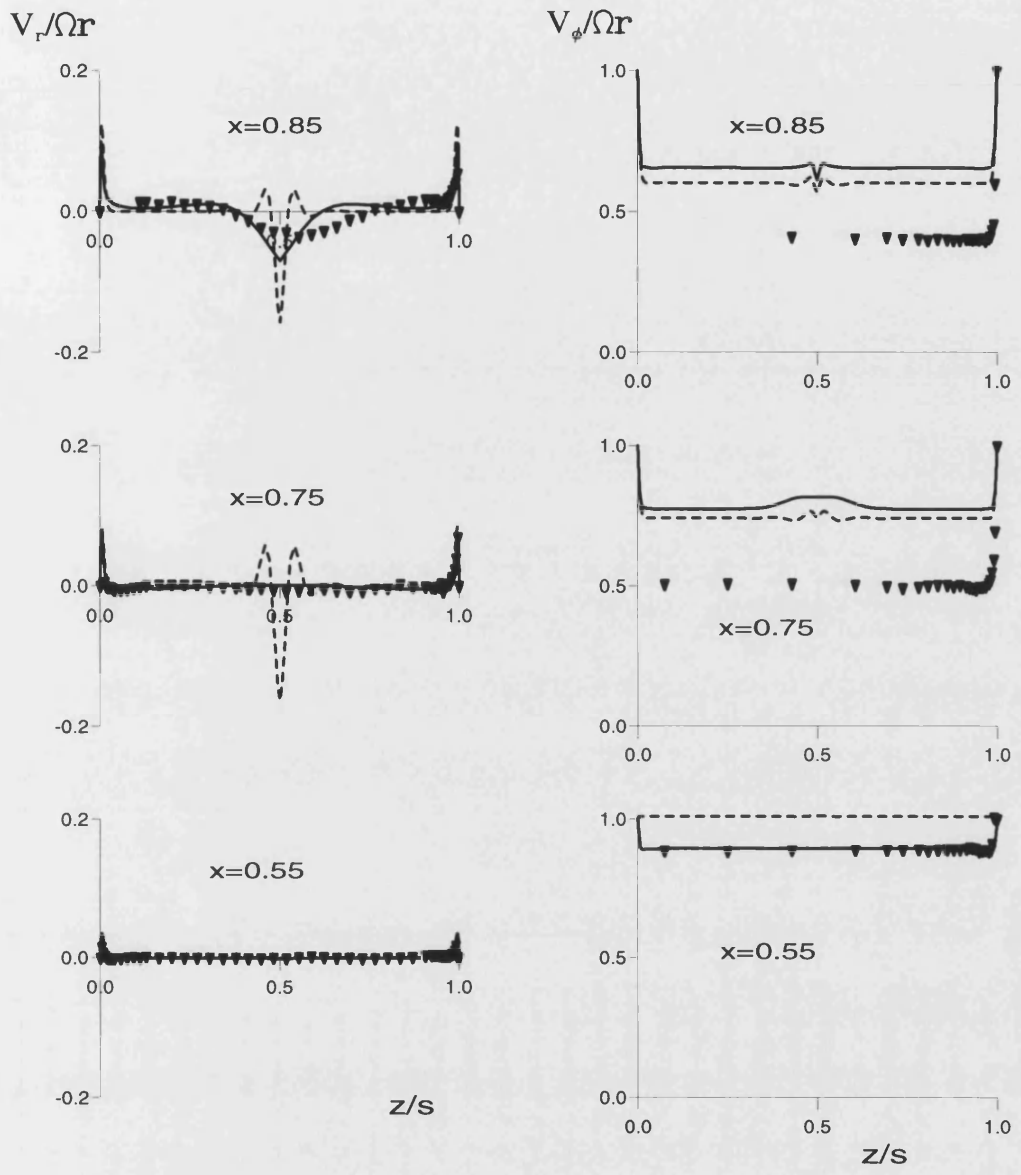

Figure 6.8. Axial variation of $V_r/\Omega r$ and $V_\phi/\Omega r$ for sealed rotating cavity with flat-shroud: $Re_\phi = 3.75 \times 10^5$.

——— LS model

----- Laminar model

▼ Data of Gan (1994)

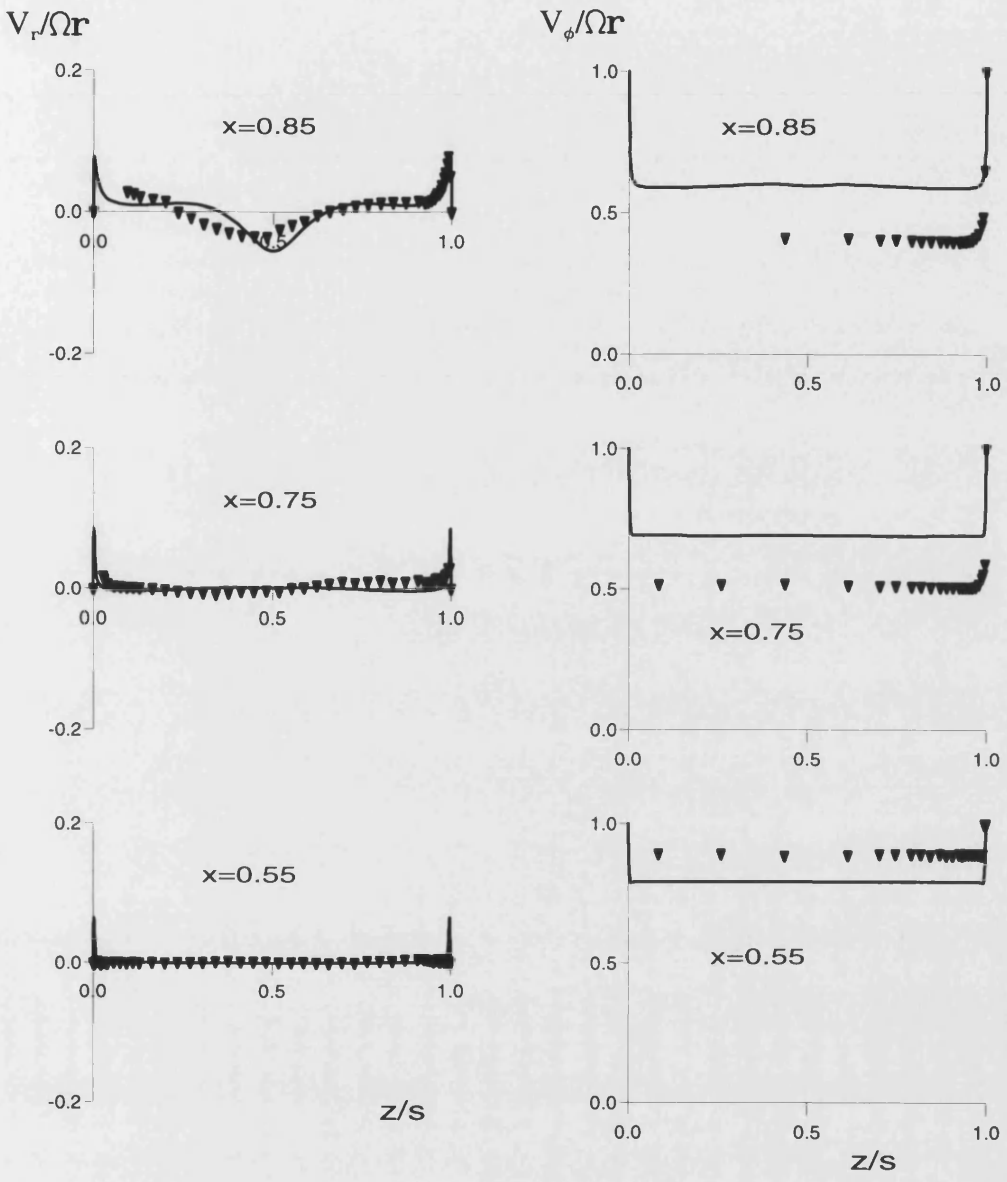

Figure 6.9. Axial variation of $V_r/\Omega r$ and $V_\phi/\Omega r$ for sealed rotating cavity with flat-shroud: $Re_\phi = 1.5 \times 10^6$.

—— LS model

▾ Data of Gan (1994)

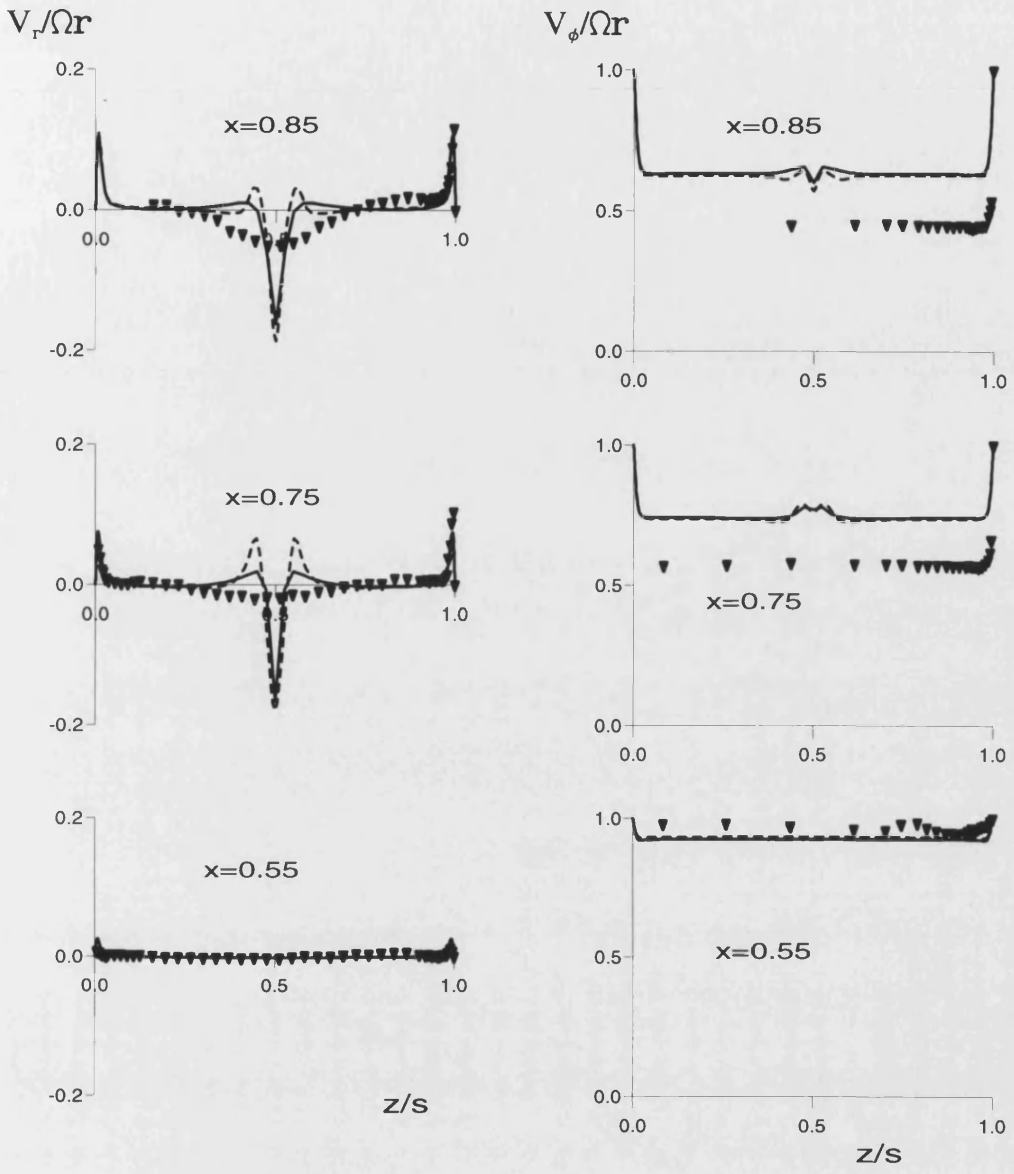

Figure 6.10. Axial variation of $V_r/\Omega r$ and $V_\phi/\Omega r$ for sealed rotating cavity with flat-shroud: $Re_\phi = 1.46 \times 10^5$.

—— LS model (67x67 grid nodes)
--- LS model (91x131 grid nodes)
▼ Data of Gan (1994)

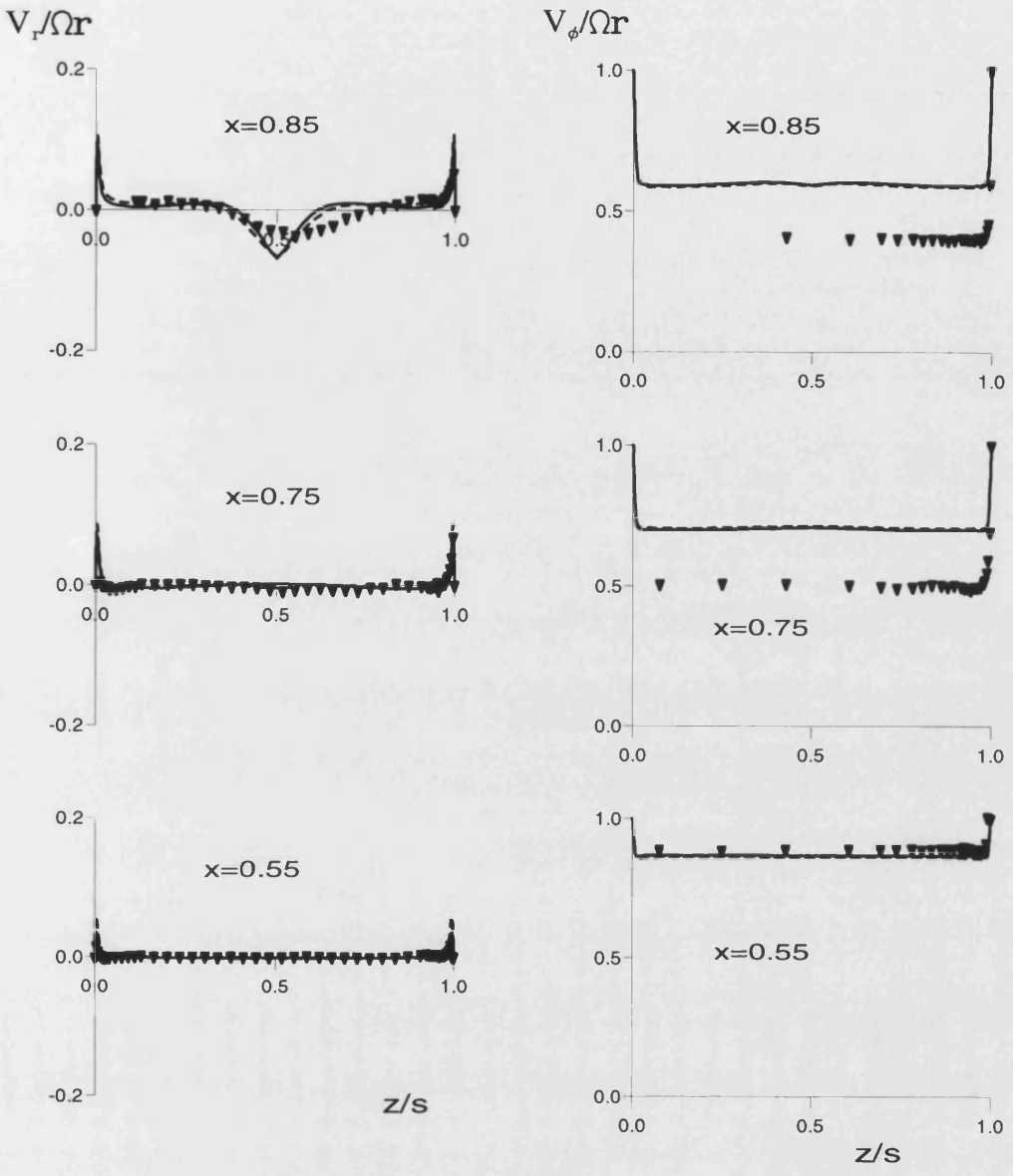

Figure 6.11. Axial variation of $V_r/\Omega r$ and $V_\phi/\Omega r$ for sealed rotating cavity with flat-shroud: $Re_\phi = 3.75 \times 10^5$.

—— LS model (91x131 grid nodes)

--- LS model (67x67 grid nodes)

▼ Data of Gan (1994)

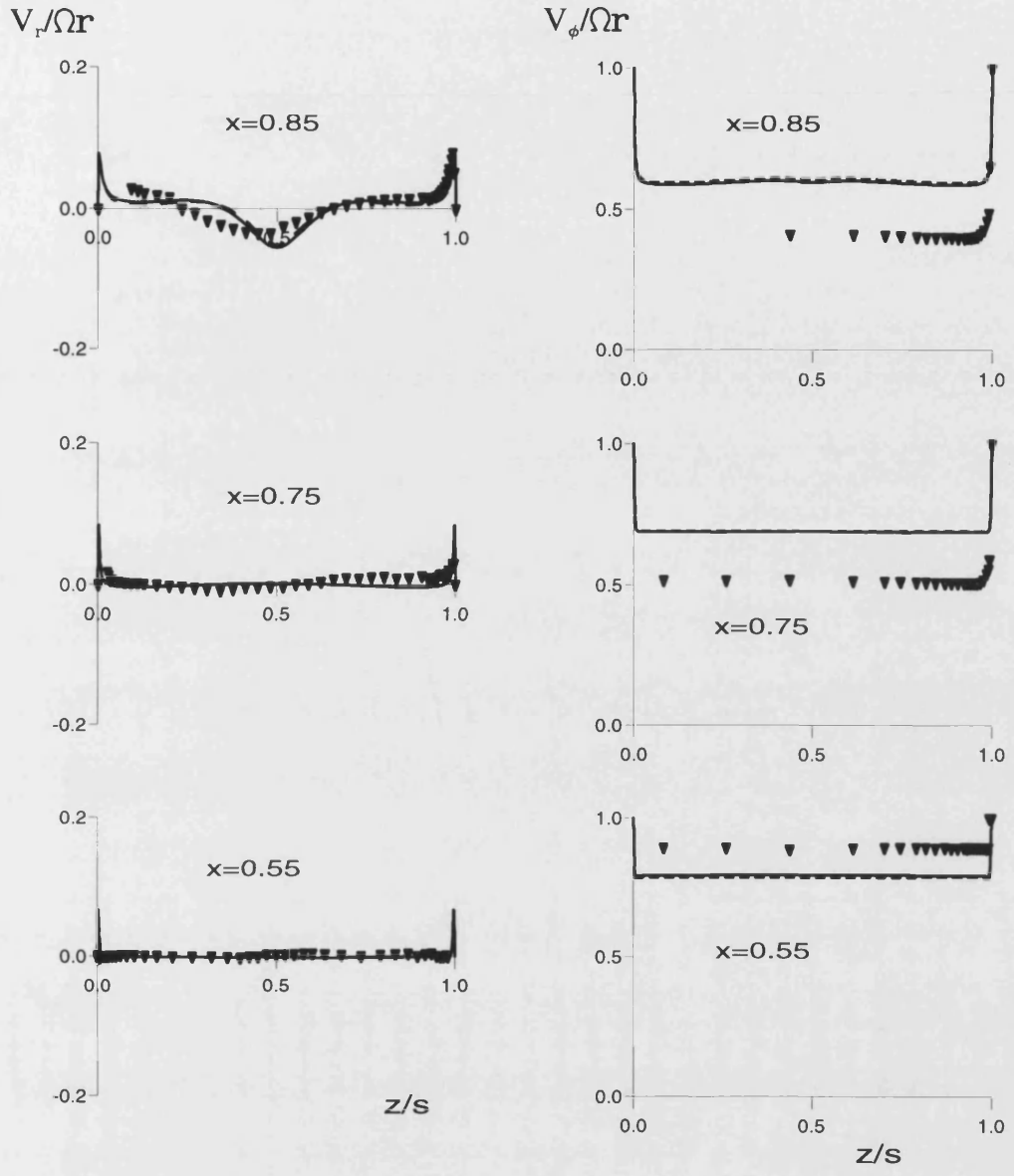

Figure 6.12. Axial variation of $V_r/\Omega r$ and $V_\phi/\Omega r$ for sealed rotating cavity with flat-shroud: $Re_\phi = 1.5 \times 10^6$.

—— LS model (91x131 grid nodes)

---- LS model (67x67 grid nodes)

▾ Data of Gan (1994)

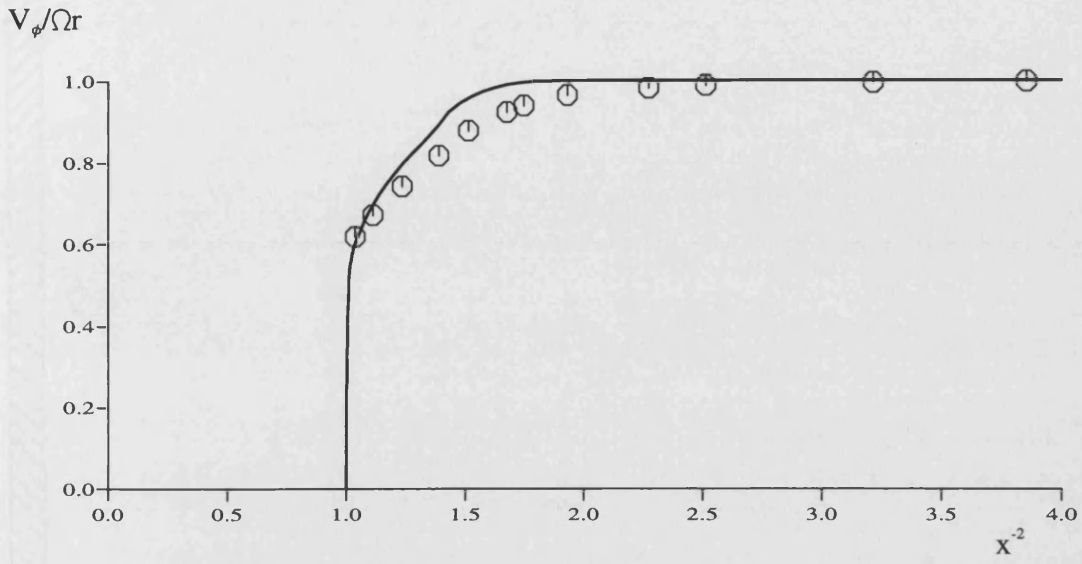

Figure 6.13. Variation of tangential component of velocity with x^{-2} for rotating cavity with flat-shroud: G=0.05, z/s=0.5, C_w = 0 and Re_ϕ = 4 x 10^5.

⏲ Data of Abrahamson et al (1989)

—— LS model

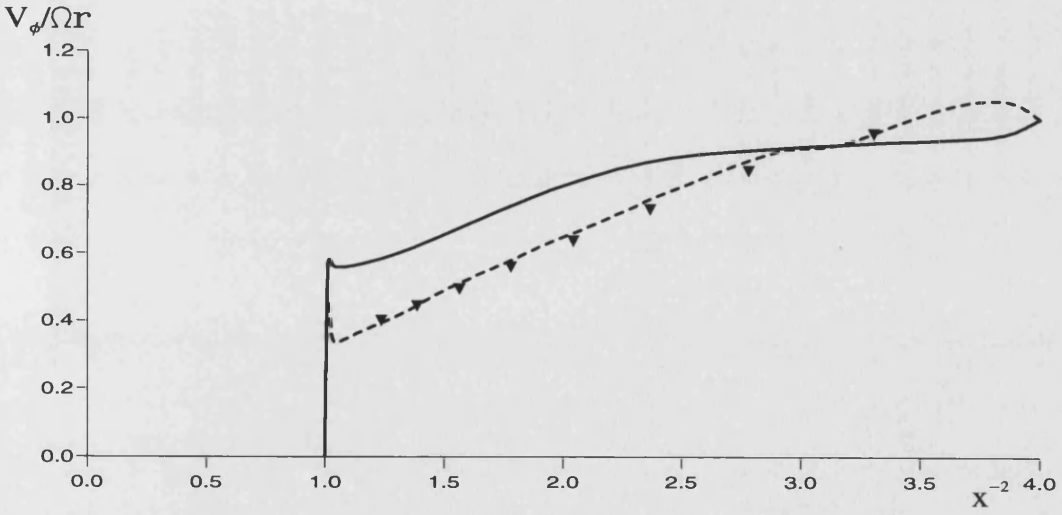

Figure 6.14. Variation of tangential component of velocity with x^{-2} for rotating cavity with peripheral flow: G=0.30, z/s=0.80, C_w=0 and Re_ϕ=1.46x10^5.

—— LS model

---- DNS model (Lewis, 1997)

▾ Data of Gan (1994)

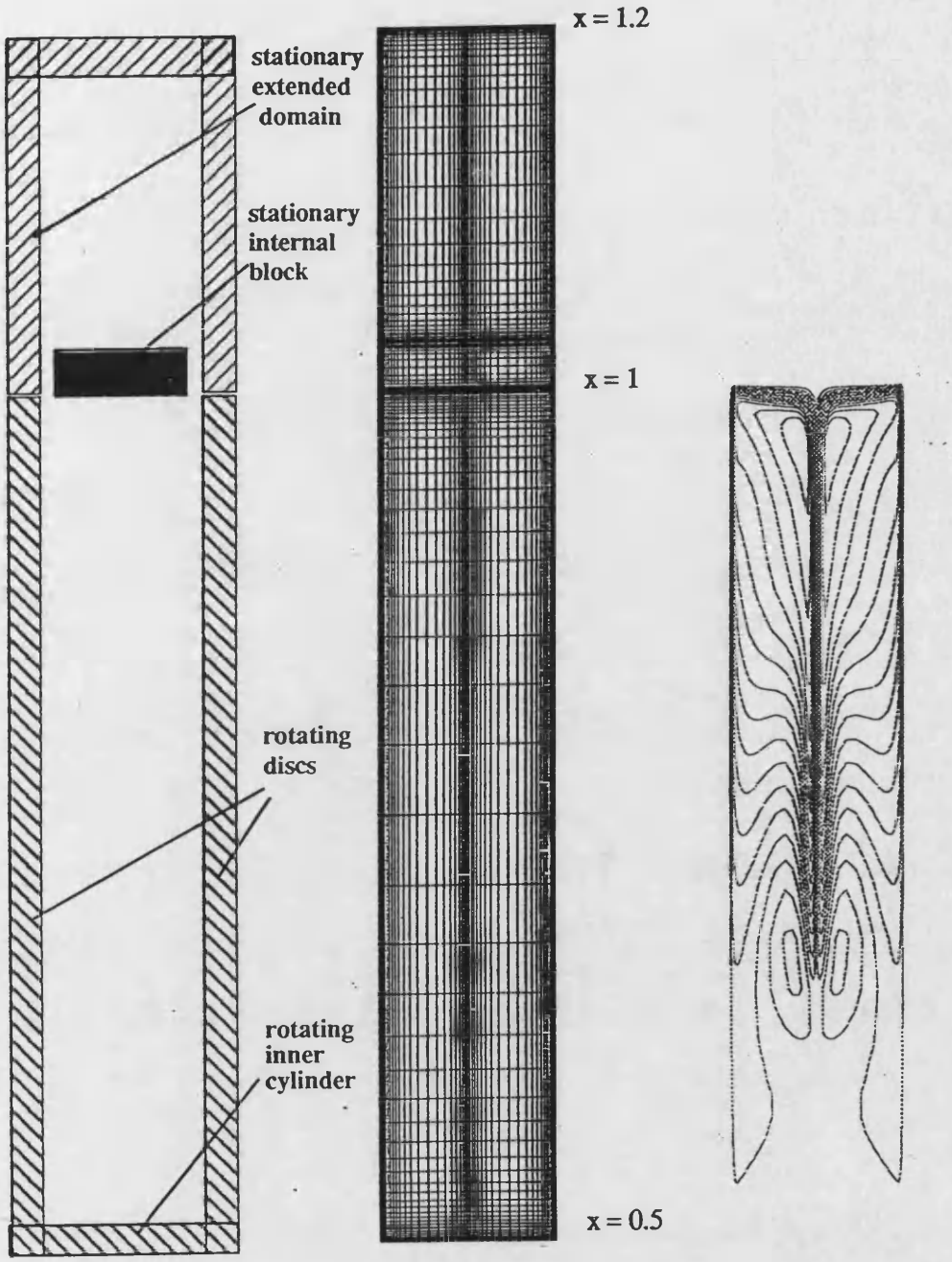

Figure 6.15. Schematic diagram, grid distribution and computed flow streamlines using internal blockage for rotating cavity with peripheral flow: G=0.30, C_w=0.0, Re_ϕ=1.46x10^5 and L-S model.

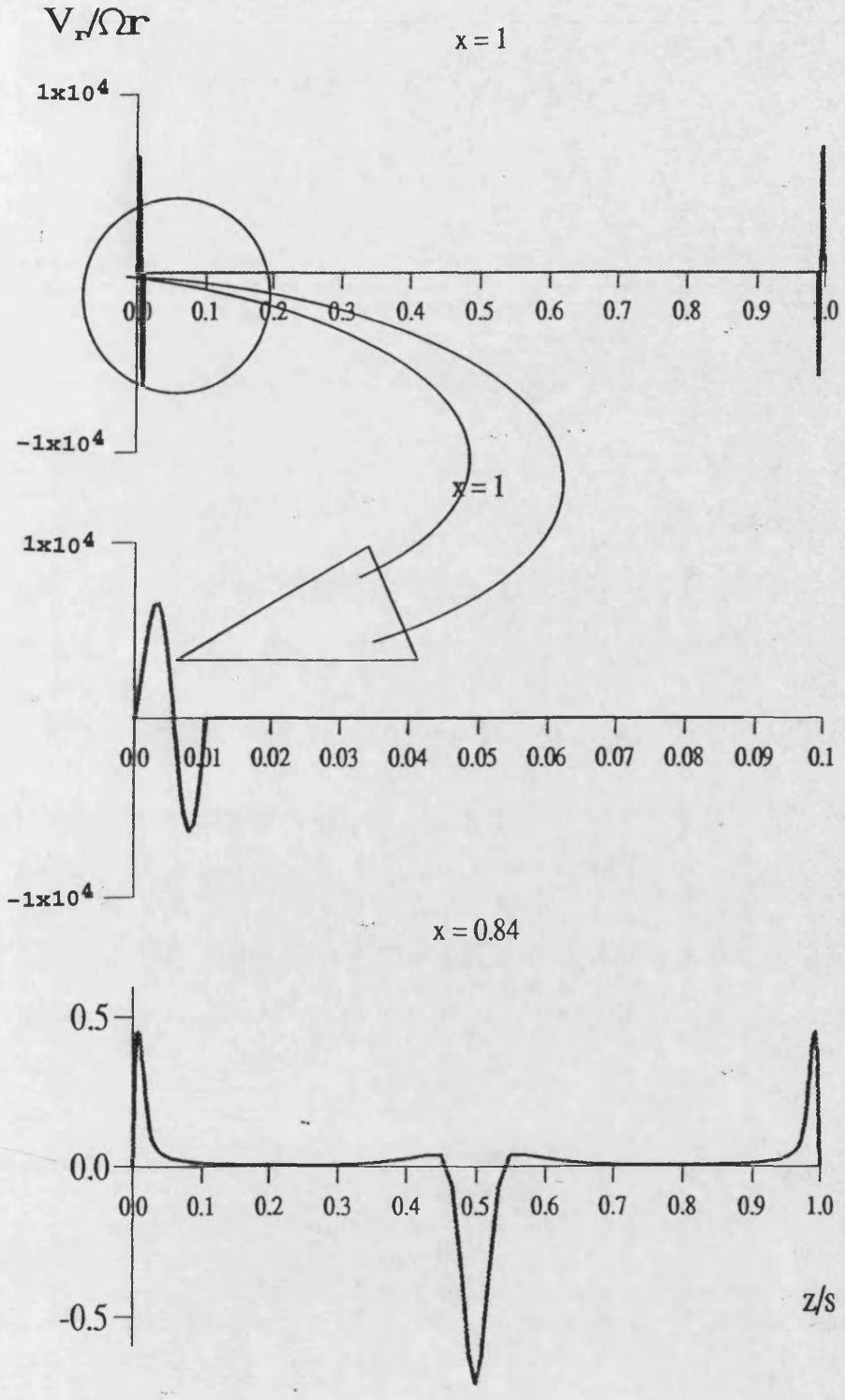

Figure 6.16. Effect of ingress on the axial variation of radial velocity for rotating cavity with peripheral flow: G=0.30, C_w=0.0, Re_ϕ=1.46x10^5 and L-S model.

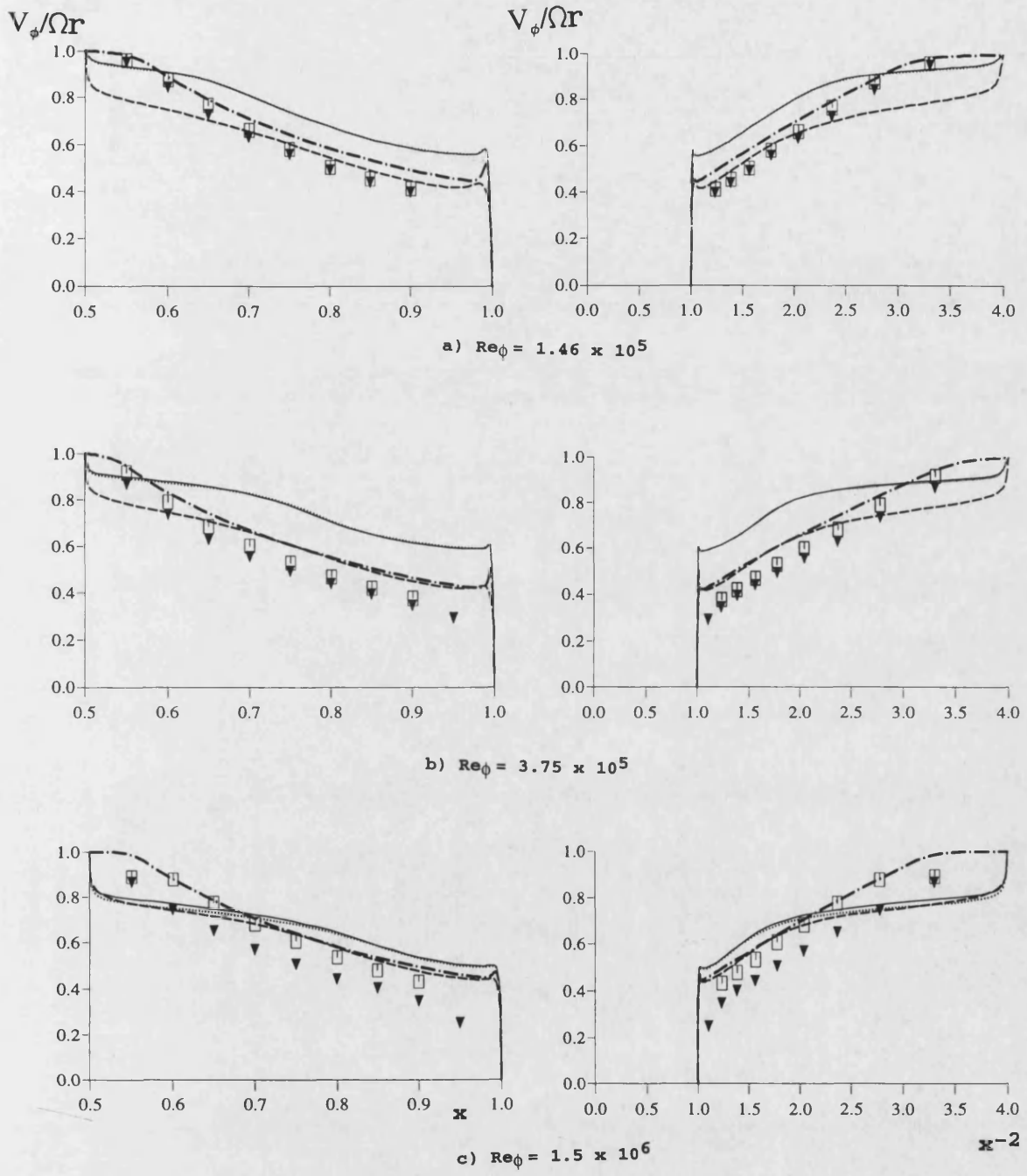

Figure 6.17. Effect of corrections on variation of $V_\phi/\Omega r$ with x and x^{-2} for sealed rotating cavity with flat-shroud.

——— LS model

····· LS model + Yap correction

---- LS model + rotation correction

—·— LS model + Richardson correction

▼ "rough data" (Gan, 1994)

▯ "smooth data" (Gan, 1995)

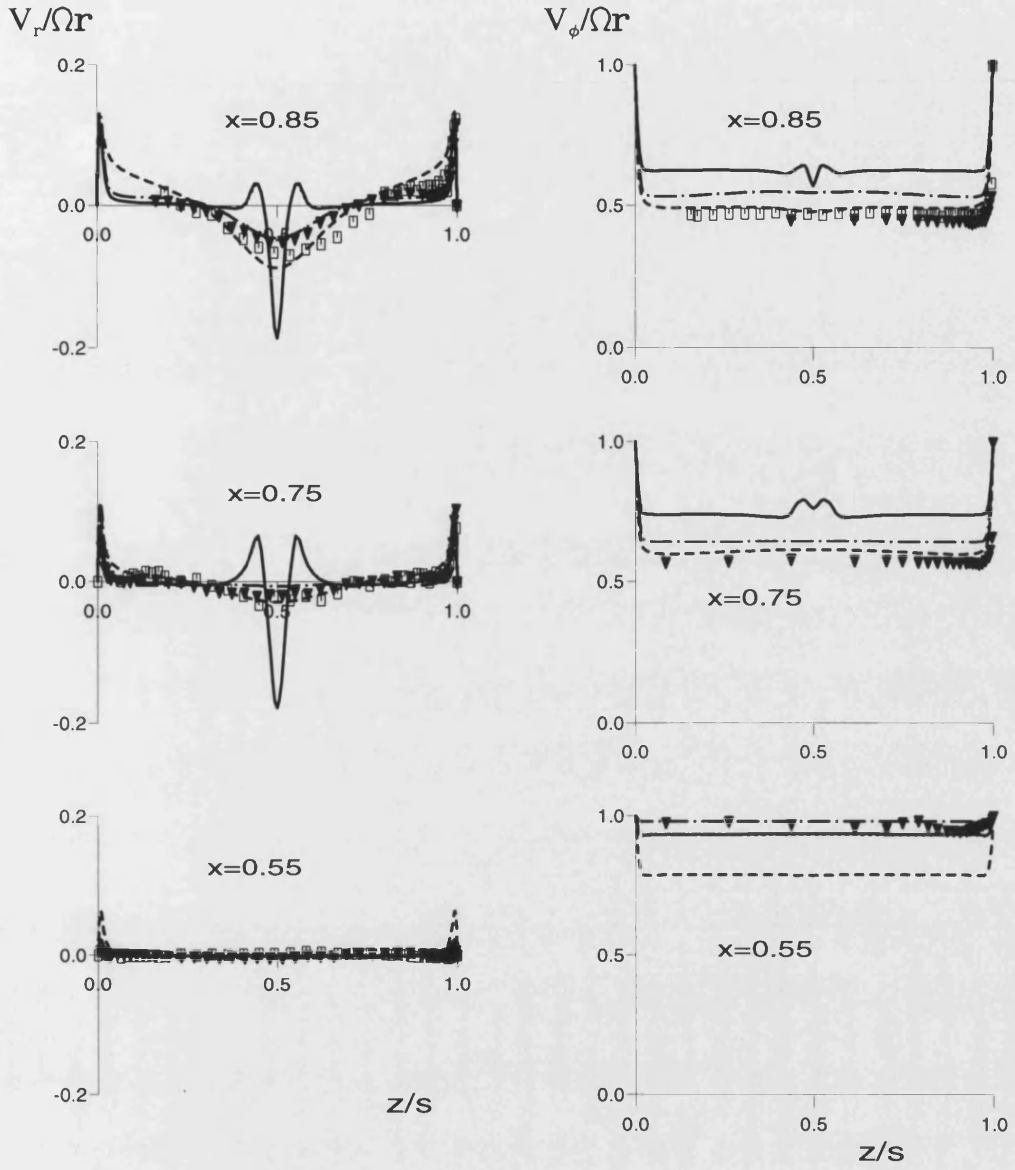

Figure 6.18. Effect of corrections on axial variation of $V_r/\Omega r$ and $V_\phi/\Omega r$ for sealed rotating cavity with flat-shroud: $Re_\phi = 1.46 \times 10^5$.

——— LS model

····· LS model + Yap correction

- - - - LS model + rotation correction

—·— LS model + Richardson correction

▾ "rough data" (Gan, 1994)

▯ "smooth data" (Gan, 1995)

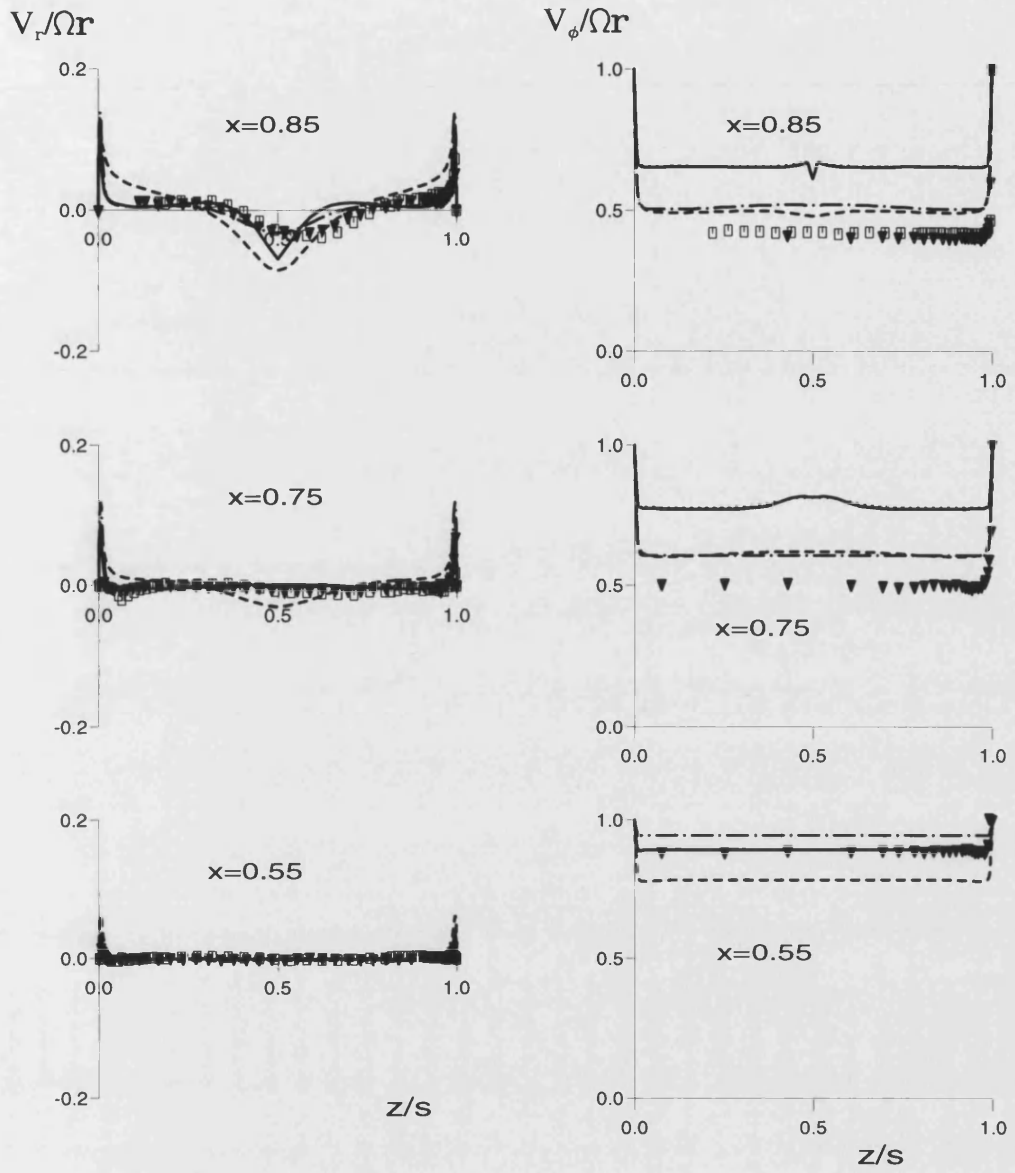

Figure 6.19. Effect of corrections on axial variation of $V_r/\Omega r$ and $V_\phi/\Omega r$ for sealed rotating cavity with flat-shroud: $Re_\phi = 3.75 \times 10^5$.

——— LS model

····· LS model + Yap correction

- - - - LS model + rotation correction

—·— LS model + Richardson correction

▼ "rough data" (Gan, 1994)

▯ "smooth data" (Gan, 1995)

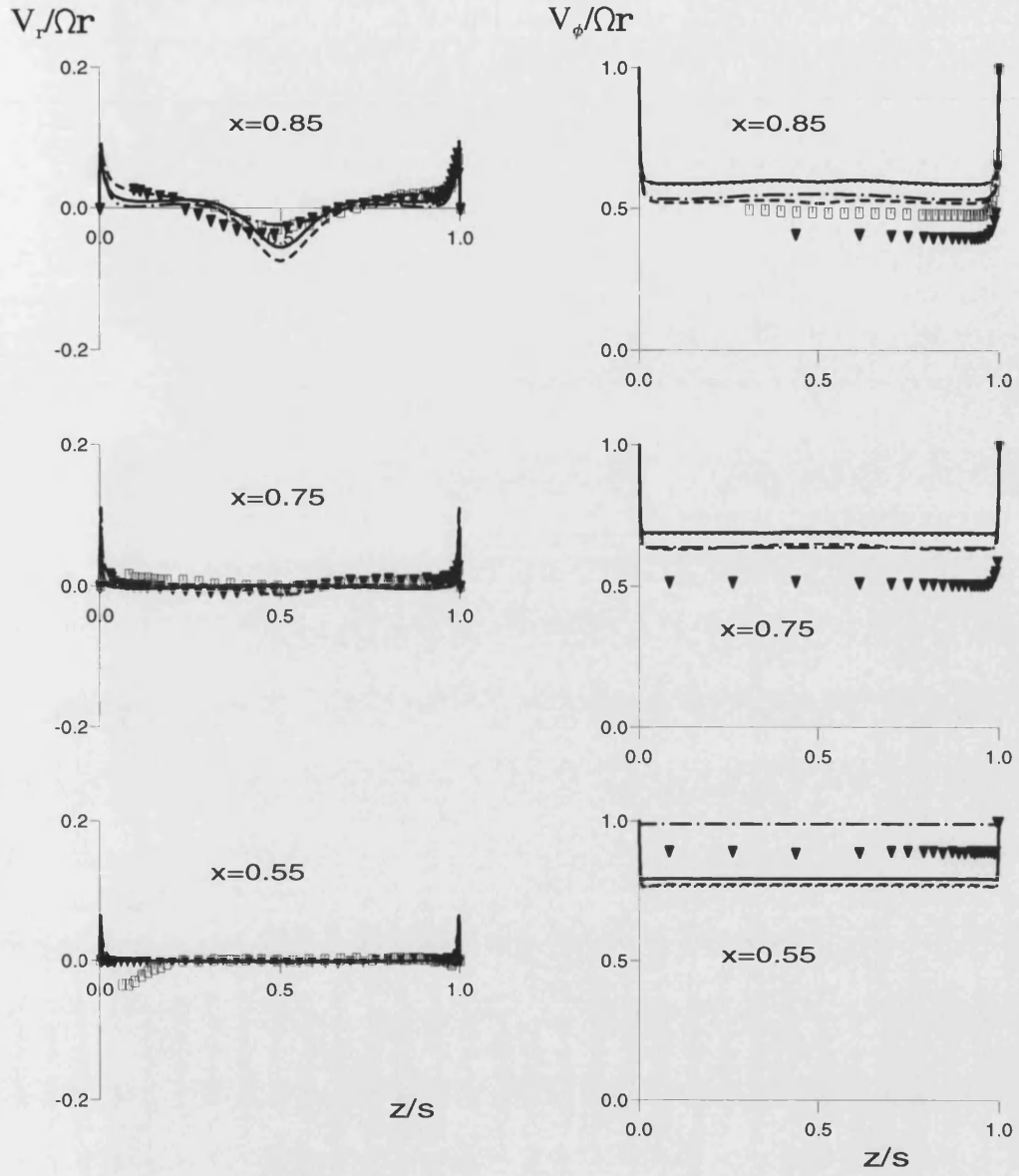

Figure 6.20. Effect of corrections on axial variation of $V_r/\Omega r$ and $V_\phi/\Omega r$ for sealed rotating cavity with flat-shroud: $Re_\phi = 1.5 \times 10^6$.

——— LS model

..... LS model + Yap correction

- - - - - LS model + rotation correction

—·— LS model + Richardson correction

▾ "rough data" (Gan, 1994)

▯ "smooth data" (Gan, 1995)

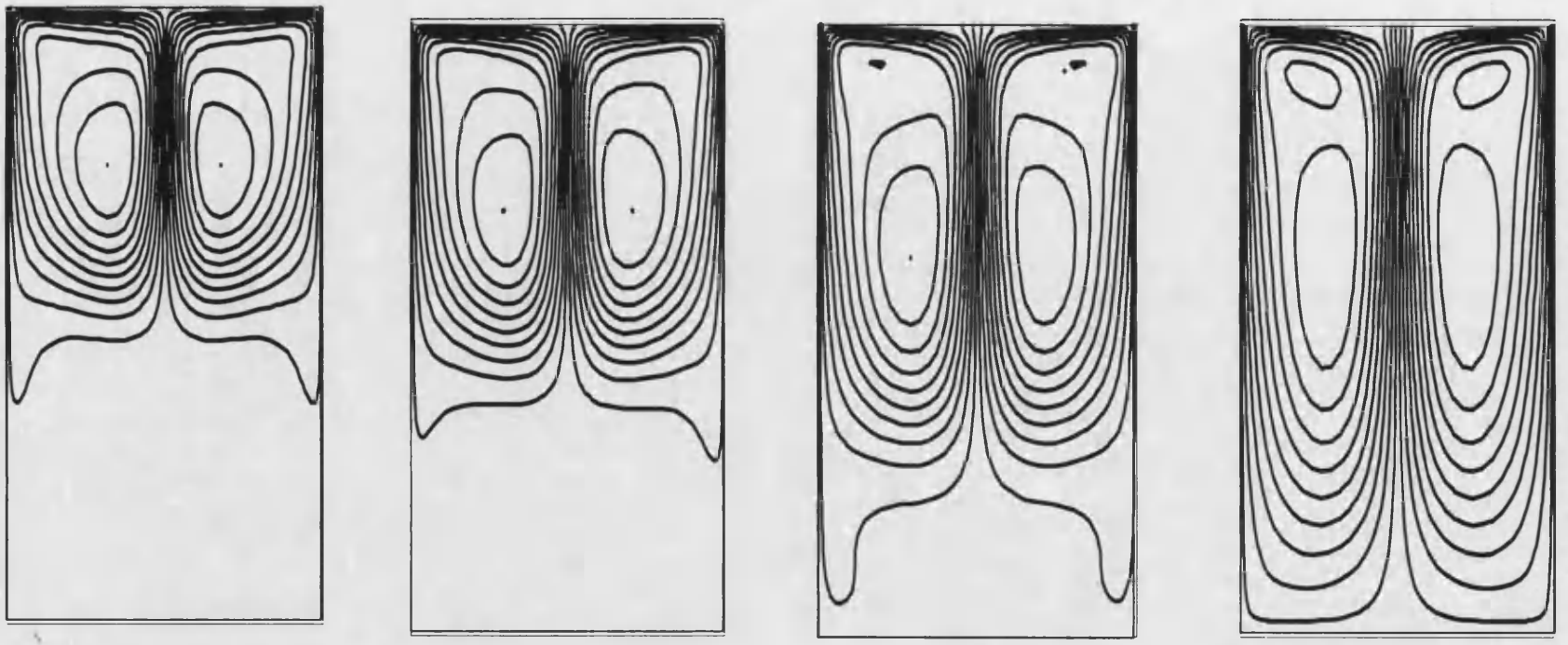

a) λ_T = -0.017 (C_W = -1500, Re_ϕ = 1.5 x 10^6)

b) λ_T = -0.034 (C_W = -3000, Re_ϕ = 1.5 x 10^6)

c) λ_T = -0.052 (C_W = -1500, Re_ϕ = 3.75 x 10^5)

d) λ_T = -0.104 (C_W = -3000, Re_ϕ = 3.75 x 10^5)

Figure 6.21. Computed streamlines for superposed rotating cavity with flat-shroud.

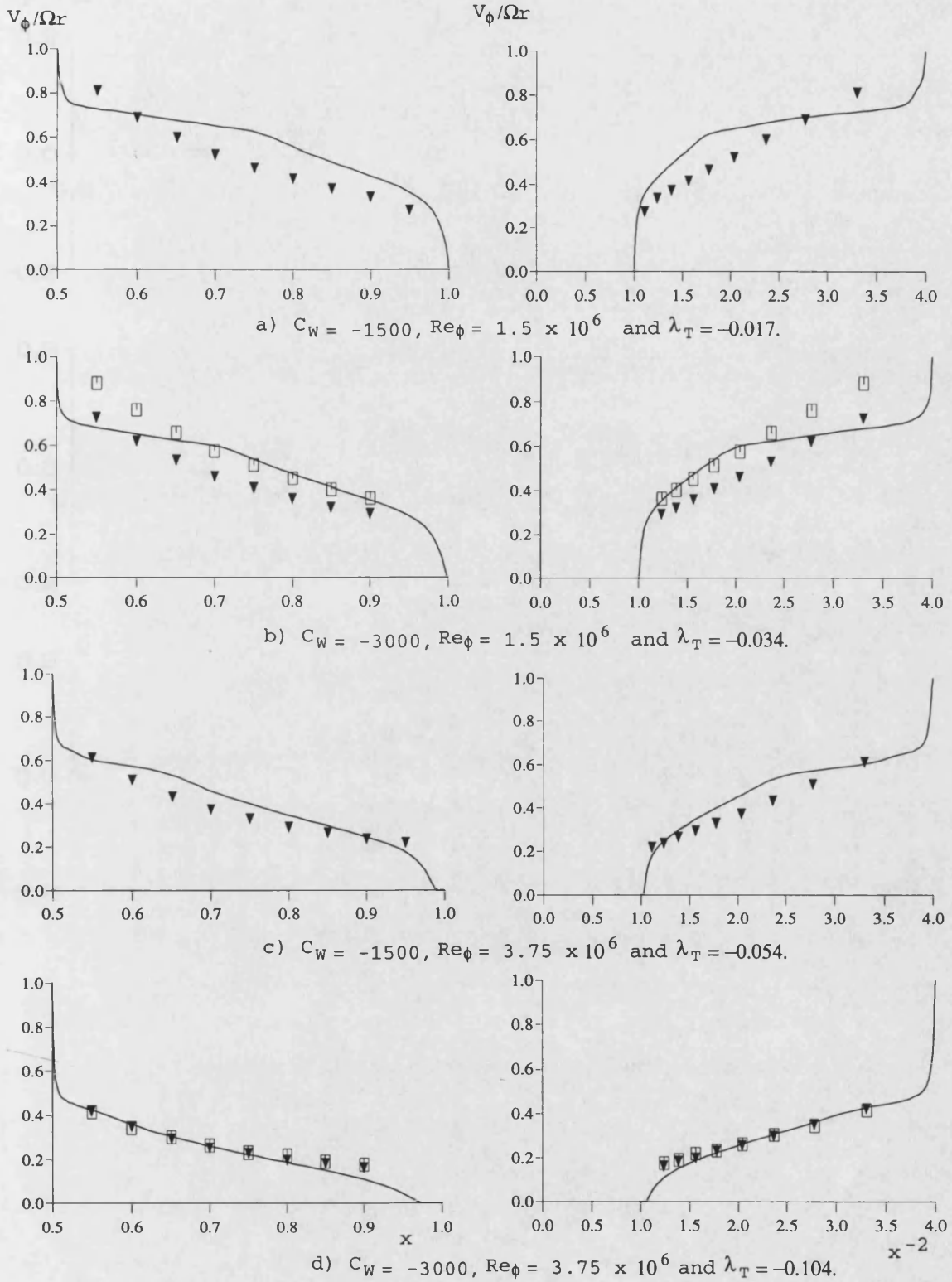

Figure 6.22. Effect of Re_ϕ , C_W and λ_T on variation of $V_\phi/\Omega r$ with x and x^{-2} for rotating cavity with flat-shroud.

▼ "rough data" (Gan, 1994)

▯ "smooth data" (Gan, 1995)

—— LS model

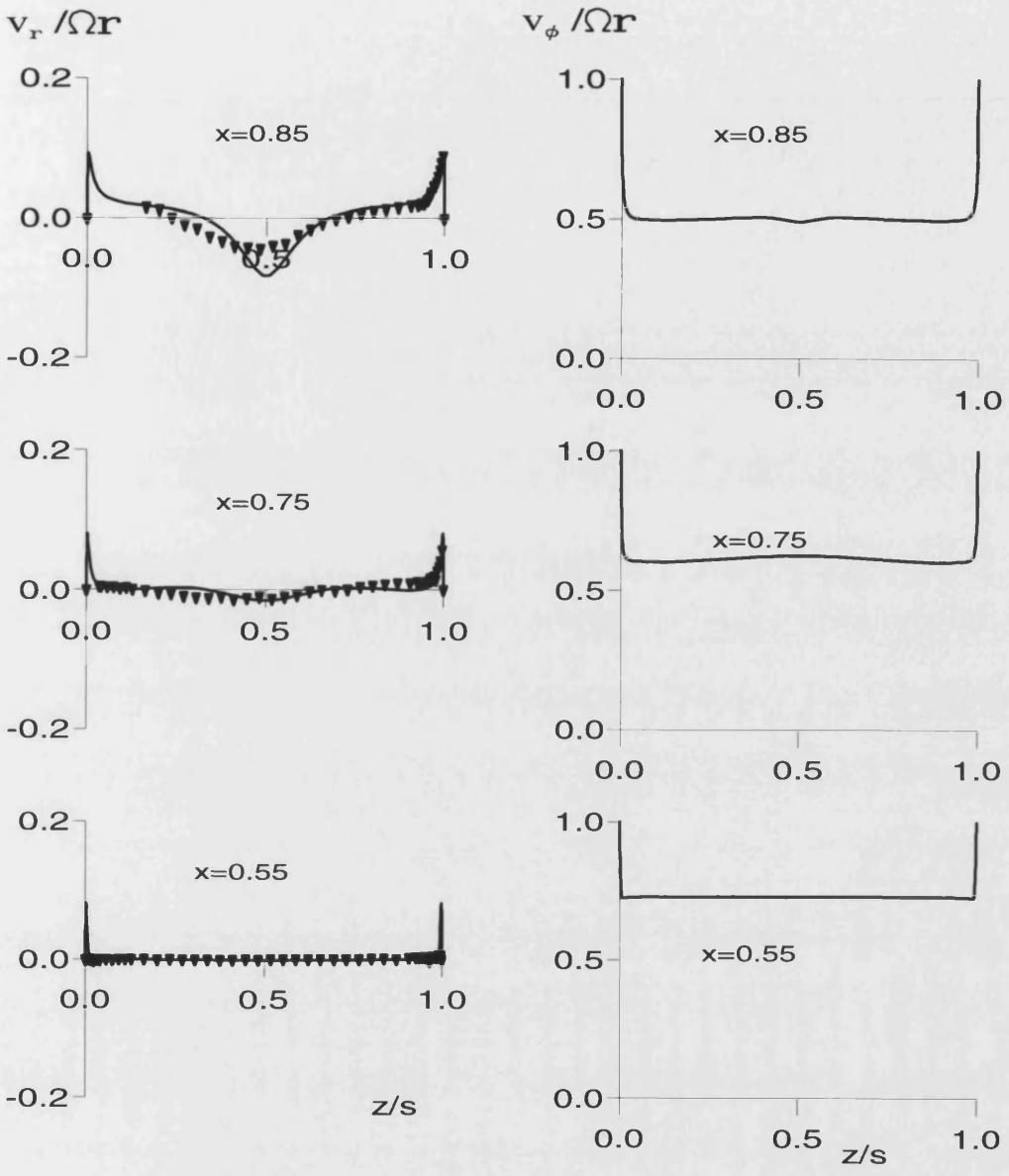

Figure 6.23. Axial variation of $V_r/\Omega r$ and $V_\phi/\Omega r$ for rotating cavity with flat-shroud: $C_w = -1500$, $Re_\phi = 1.5 \times 10^6$ and $\lambda_T = -0.017$.

▾ Data of Gan (1994)

—— LS model

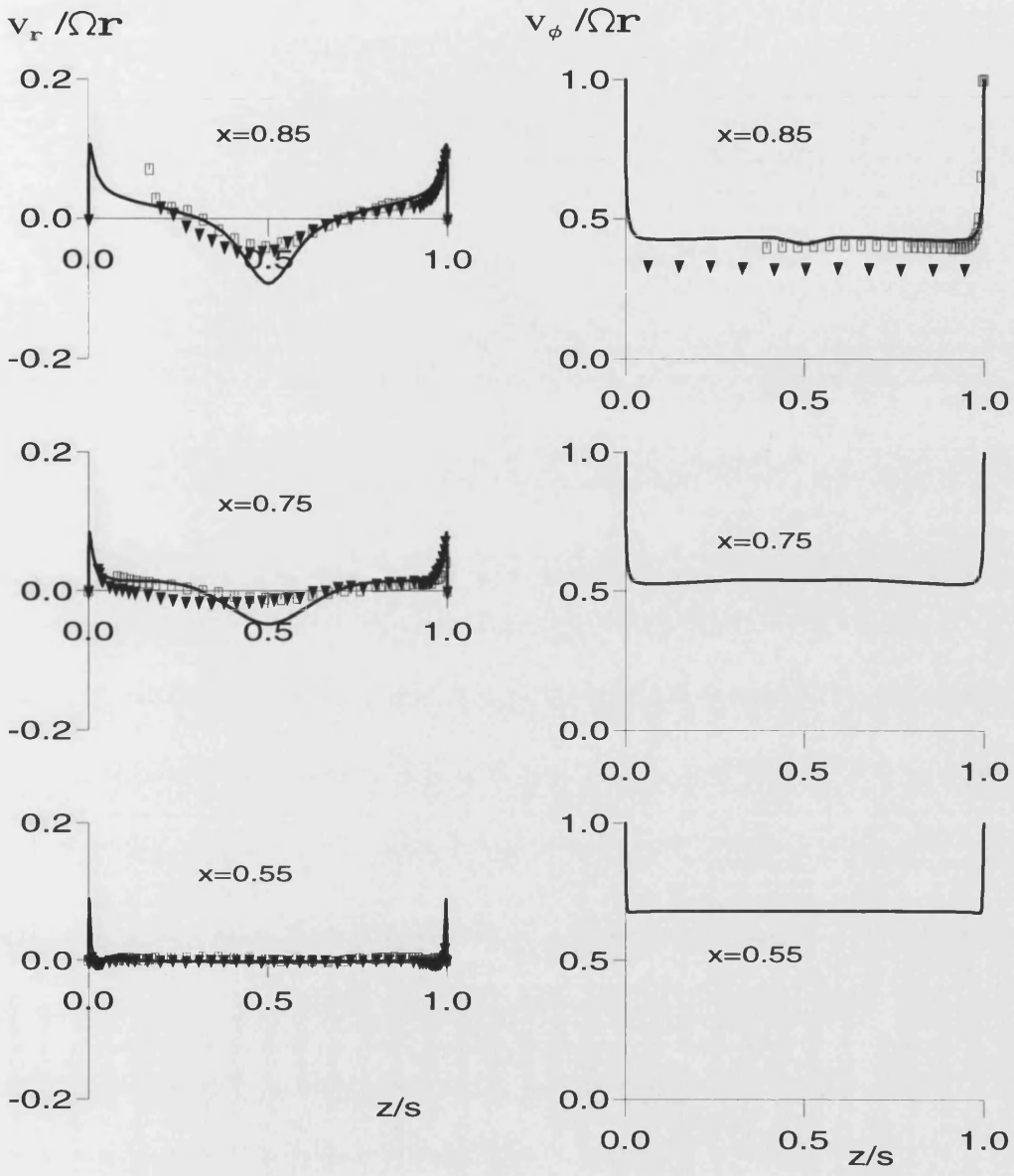

Figure 6.24. Axial variation of $V_r/\Omega r$ and $V_\phi/\Omega r$ for rotating cavity with flat-shroud: C_w = -3000, Re_ϕ = 1.5 x 10^6 and λ_T = -0.034.

▼ "rough data" (Gan, 1994)

▯ "smooth data" (Gan, 1995)

—— LS model

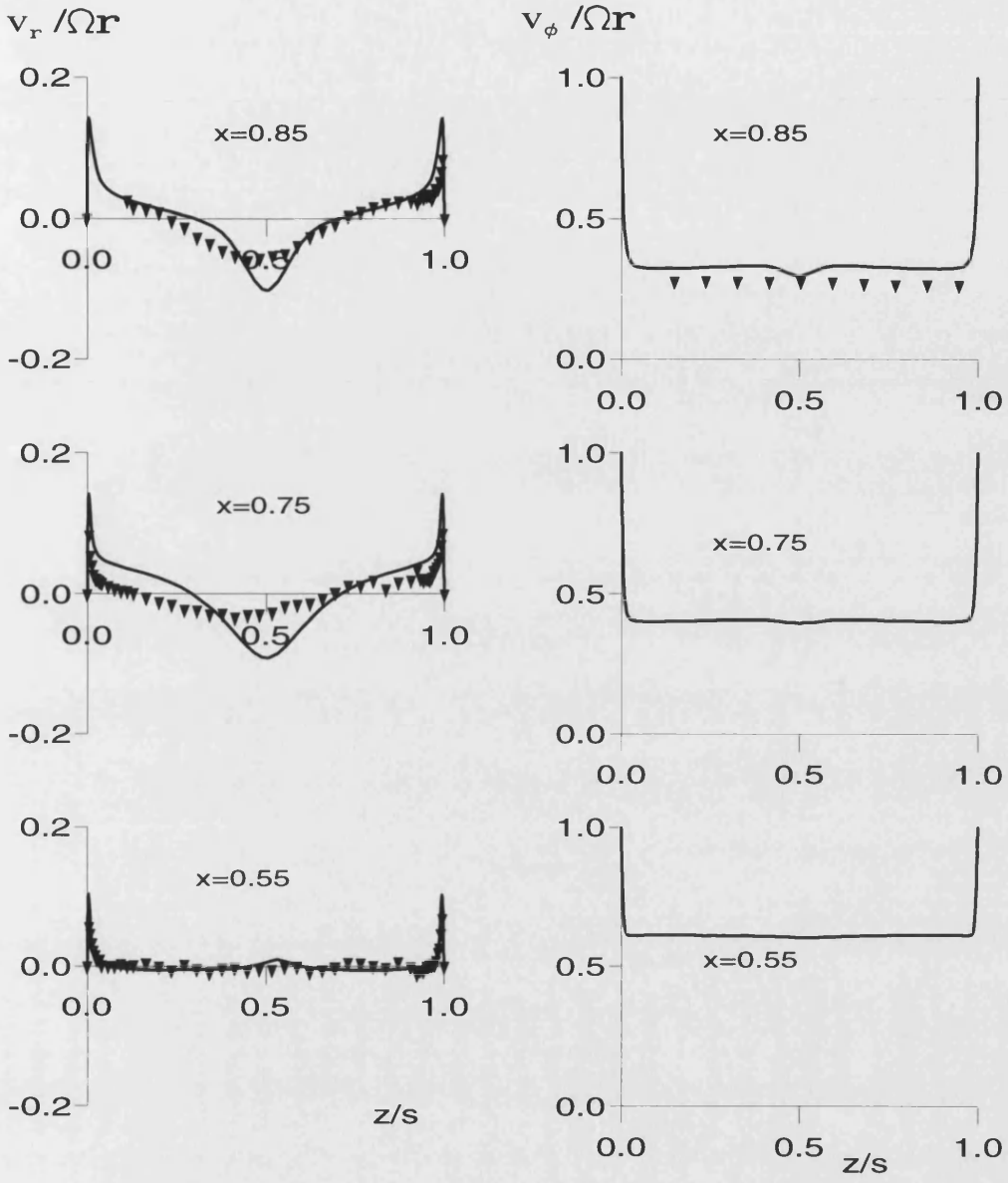

Figure 6.25. Axial variation of $V_r/\Omega r$ and $V_\phi/\Omega r$ for rotating cavity with flat-shroud: C_w = -1500, Re_ϕ= 3.75 x 10^5 and λ_T = -0.052.

▼ Dtata of Gan (1994)

—— LS model

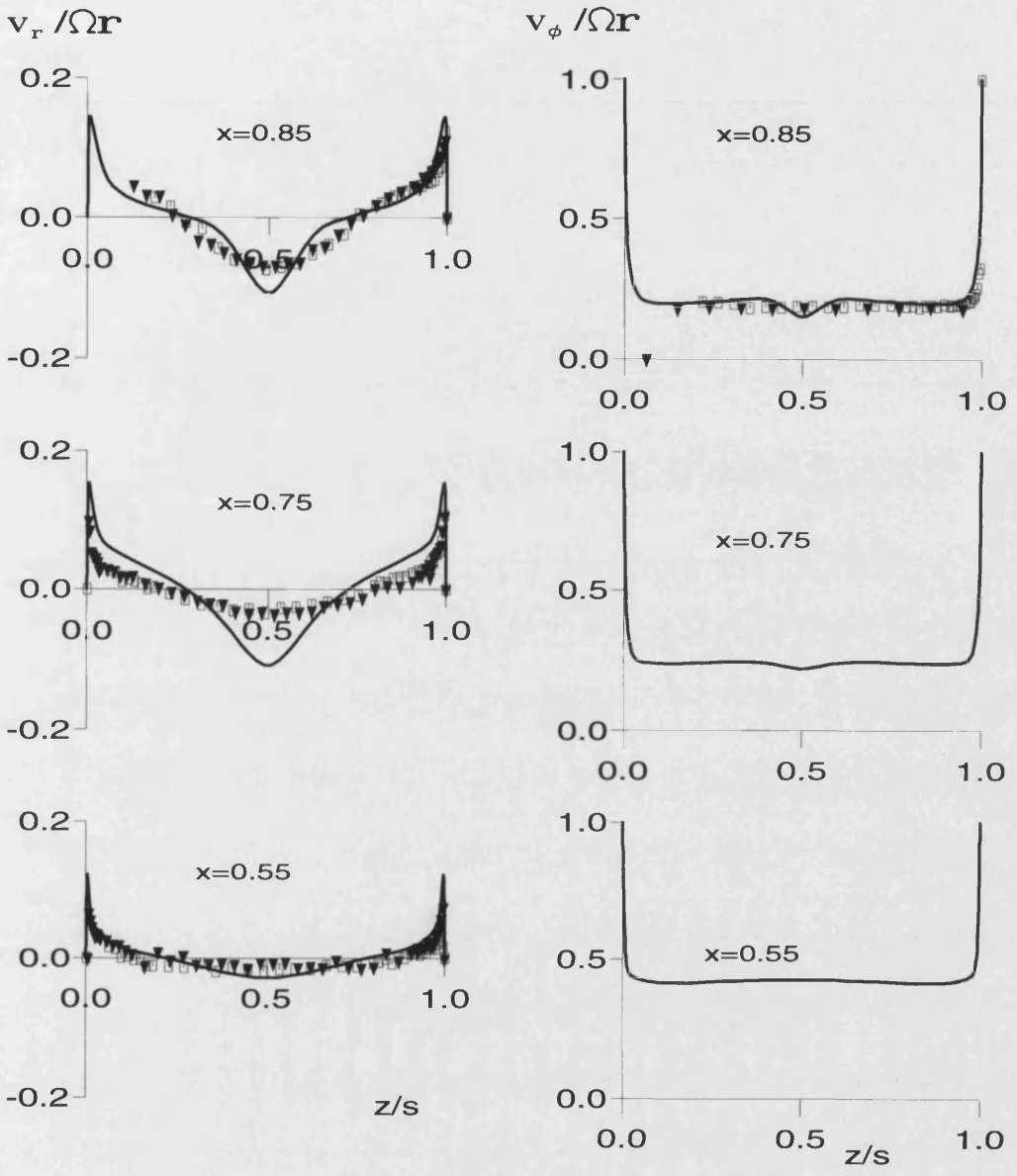

Figure 6.26. Axial variation of $V_r/\Omega r$ and $V_\phi/\Omega r$ for rotating cavity with flat-shroud: C_w=-3000, Re_ϕ=3.75 x 10^5 and λ_T = -0.104.

▼ "rough data" (Gan, 1994)

▯ "smooth data" (Gan, 1995)

____ LS model

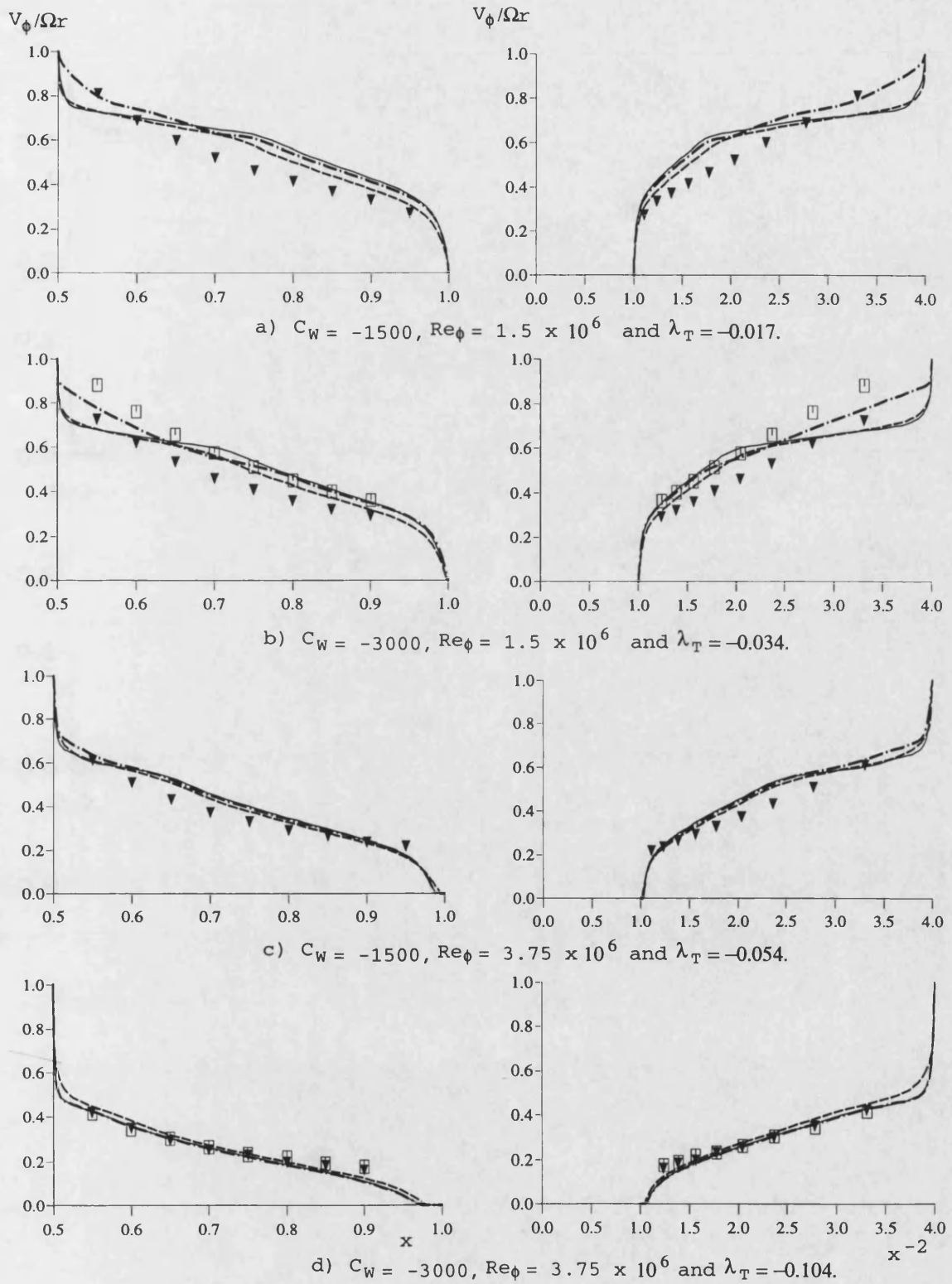

Figure 6.27. Effect of corrections on variation of $V_\phi/\Omega r$ with x and x^{-2} for rotating cavity with flat-shroud.

▼ "rough data" (Gan, 1994) —— LS model

▯ "smooth data" (Gan, 1995) ---- LS model + rotation correction

—·— LS model + Richardson correction

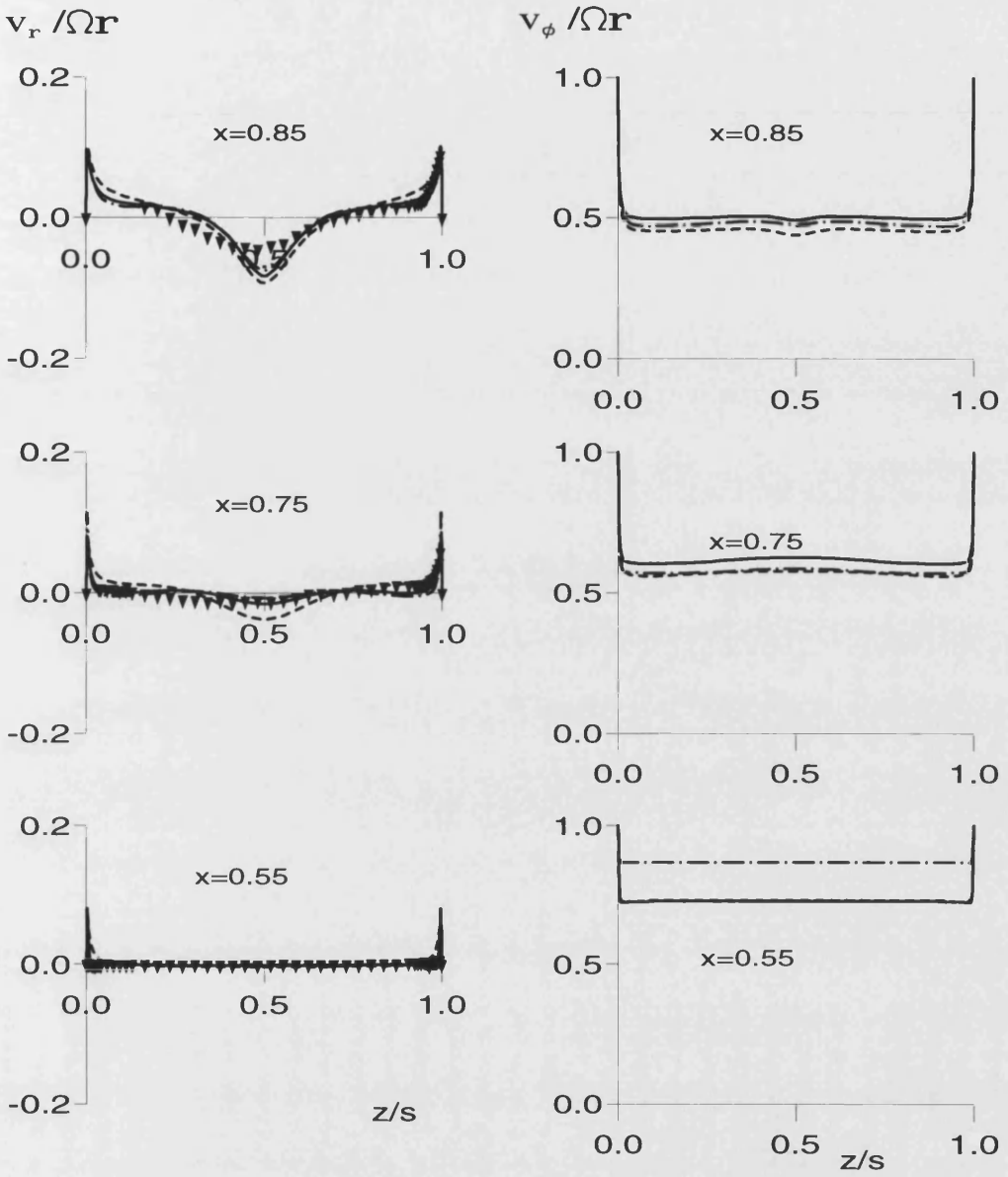

Figure 6.28. Effect of corrections on axial variation of $V/\Omega r$ and $V_\phi/\Omega r$ for rotating cavity with flat-shroud:
$C_w = -1500$, $Re_\phi = 1.5 \times 10^6$ and $\lambda_T = -0.017$.

▼ Data of Gan (1994)

—— LS model

---- LS model + rotation correction

—·— LS model + Richardson correction

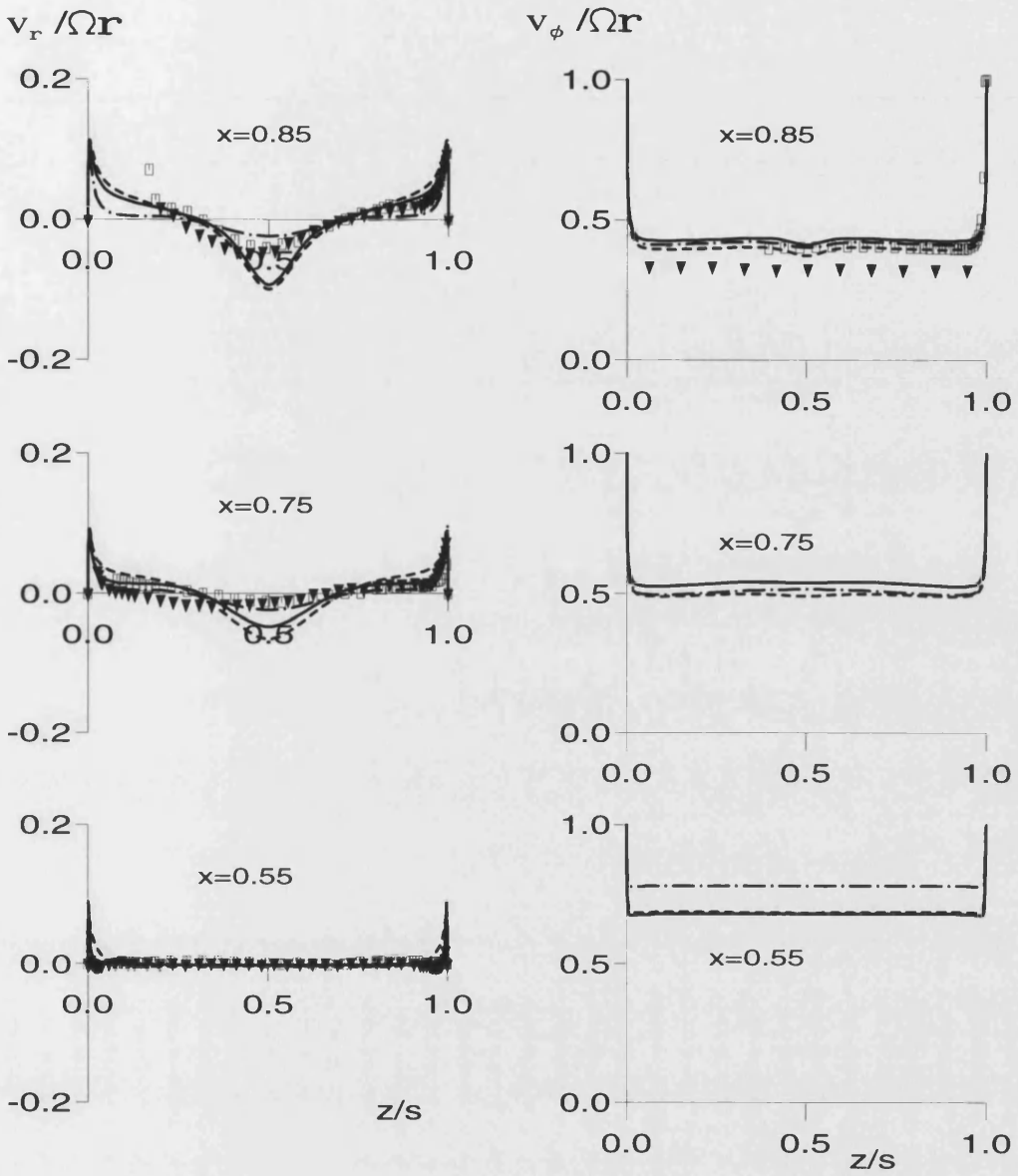

Figure 6.29. Effect of corrections on axial variation of $V_r/\Omega r$ and $V_\phi/\Omega r$ for rotating cavity with flat-shroud:
$C_w = -3000$, $Re_\phi = 1.5 \times 10^6$ and $\lambda_T = -0.034$.

▼ "rough data" (Gan, 1994)

▯ "smooth data" (Gan, 1995)

—— LS model

---- LS model + rotation correction

—·— LS model + Richardson correction

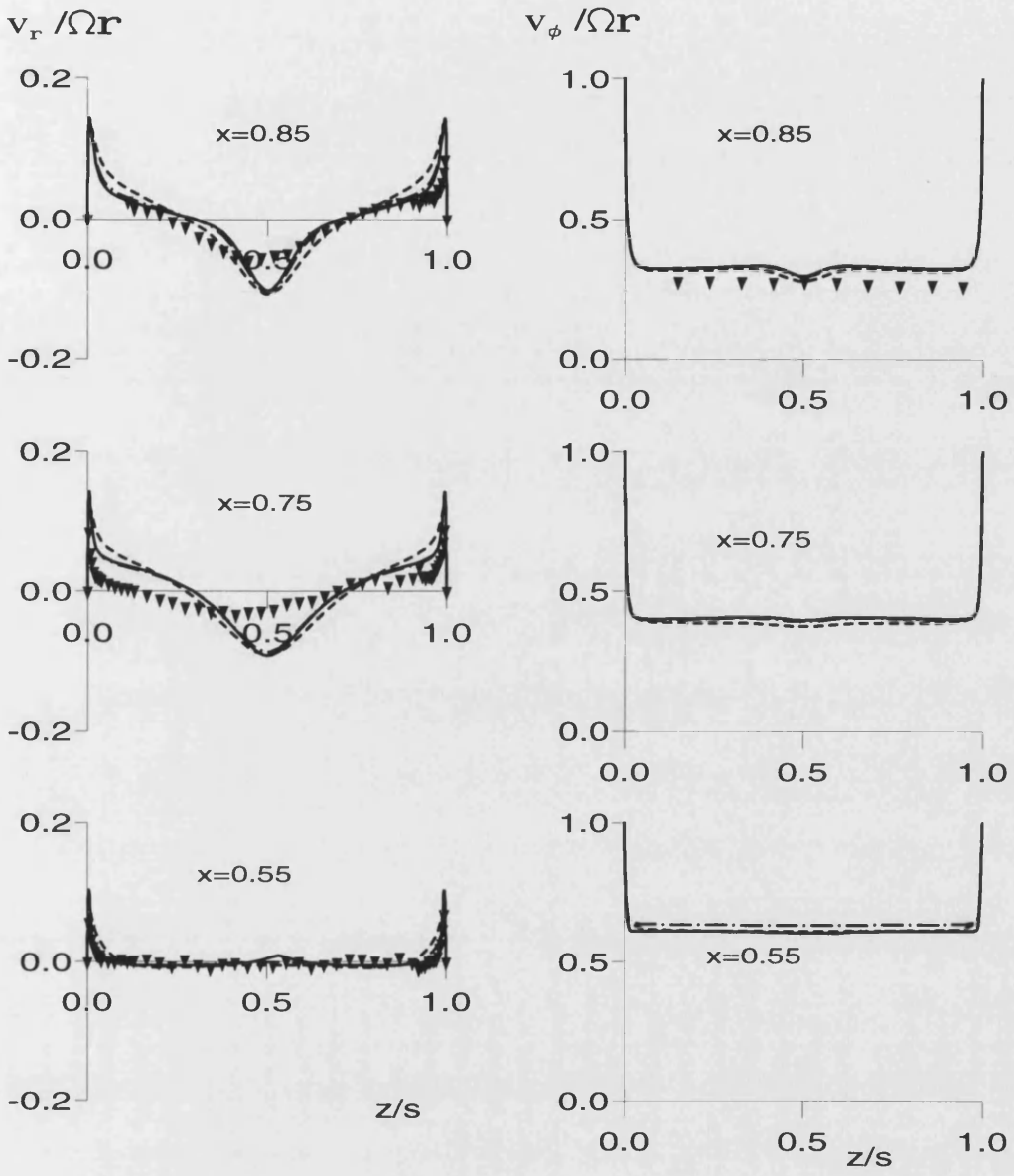

Figure 6.30. Effect of corrections on axial variation of V /Ωr and V_ϕ/Ωr for rotating cavity with flat-shroud:

C_w = -1500, Re_ϕ = 3.75 x 10^5 and λ_T = -0.052.

▼ Data of Gan (1994)

——— LS model

- - - - LS model + rotation correction

—·— LS model + Richardson correction

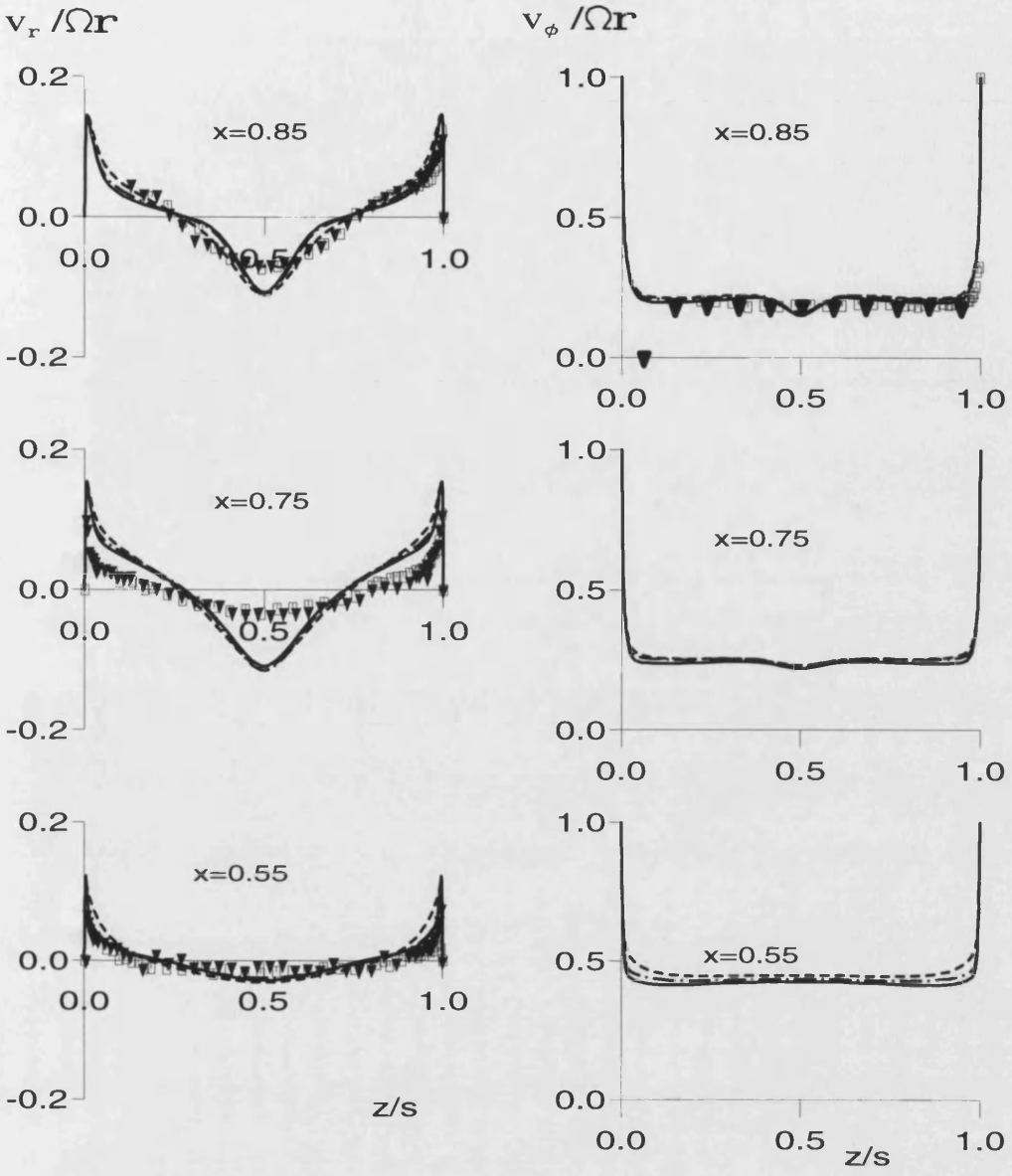

Figure 6.31. Effect of corrections on axial variation of $V_r/\Omega r$ and $V_\phi/\Omega r$ for rotating cavity with flat-shroud:

$C_w = -3000$, $Re_\phi = 3.75 \times 10^5$ and $\lambda_T = -0.104$.

▼ "rough data" (Gan, 1994)

▯ "smooth data" (Gan, 1995)

—— LS model

---- LS model + rotation correction

—·— LS model + Richardson correction

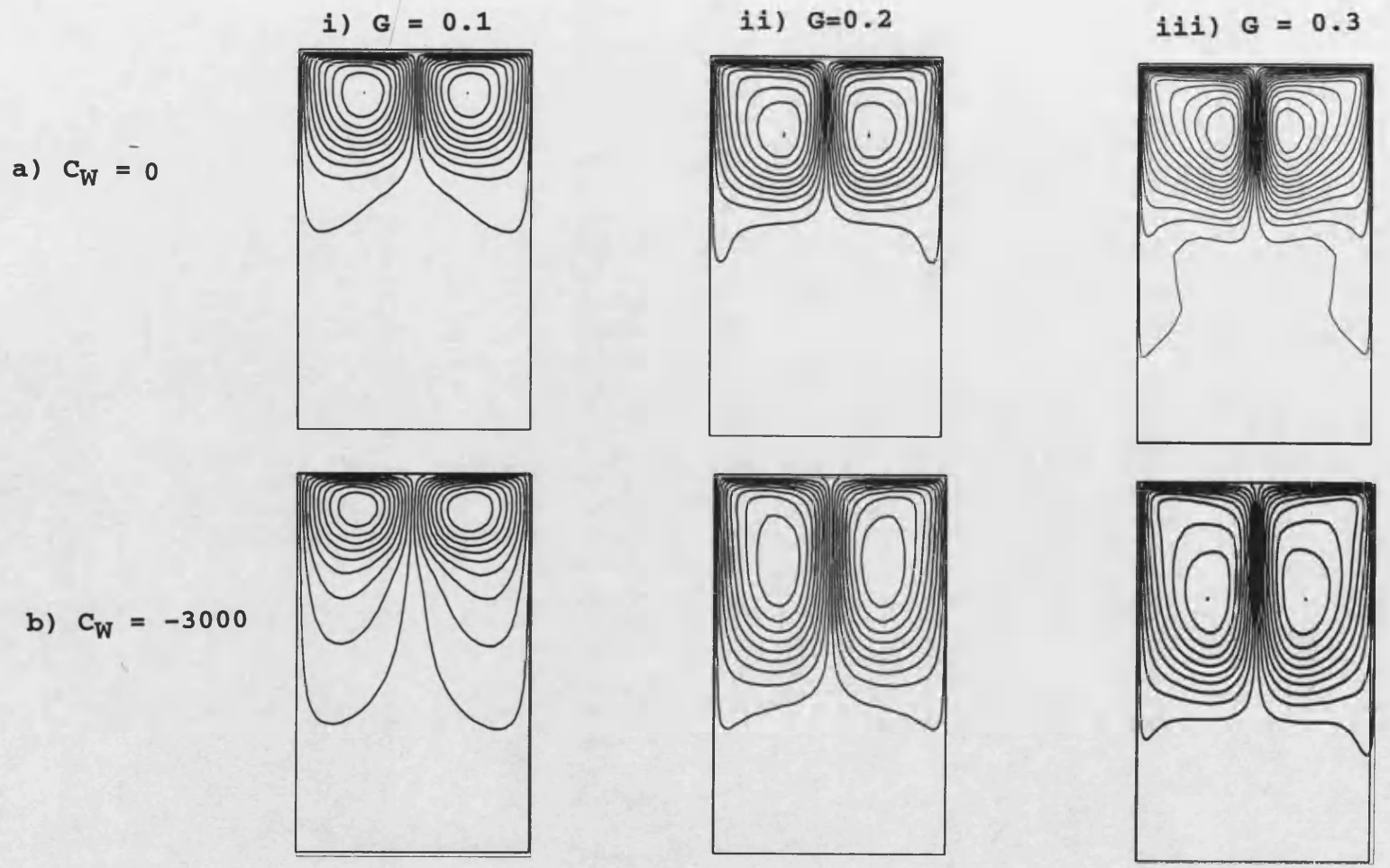

Figure 6.32. Effect of gap ratio on computed streamlines for rotating cavity with flat-shroud: $Re_\phi = 1.5 \times 10^6$.

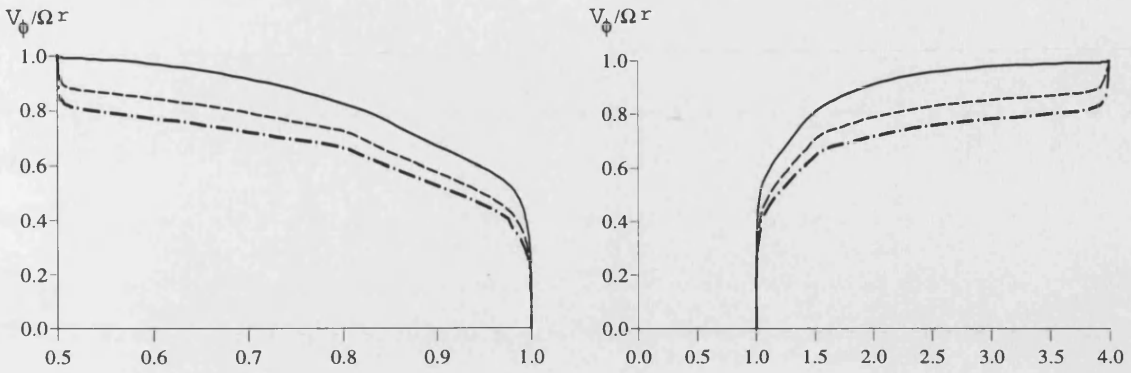

a) C_W =0 and Re_ϕ = 1.5 x 10^6

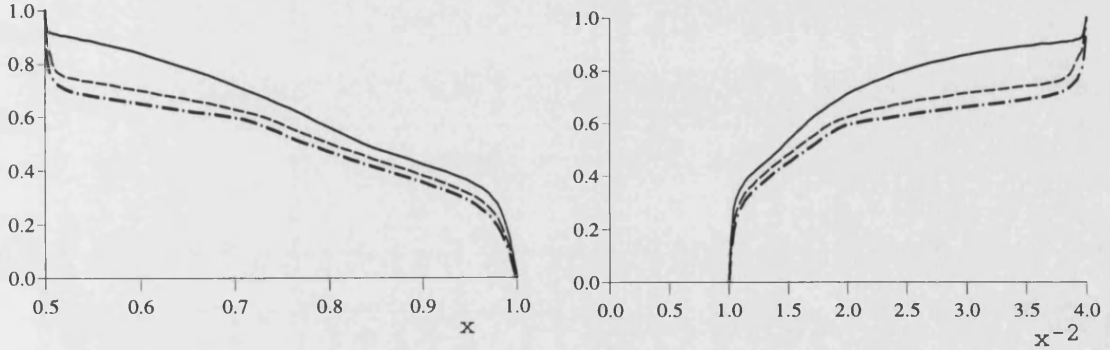

b) C_W = -3000 and Re_ϕ = 1.5 x 10^6

Figure 6.33. Effect of gap ratio on variation of computed $V_\phi/\Omega r$ with x and x^{-2} for rotating cavity with flat-shroud.

——— G = 0.1
– – – – G = 0.2
—·—·— G = 0.3

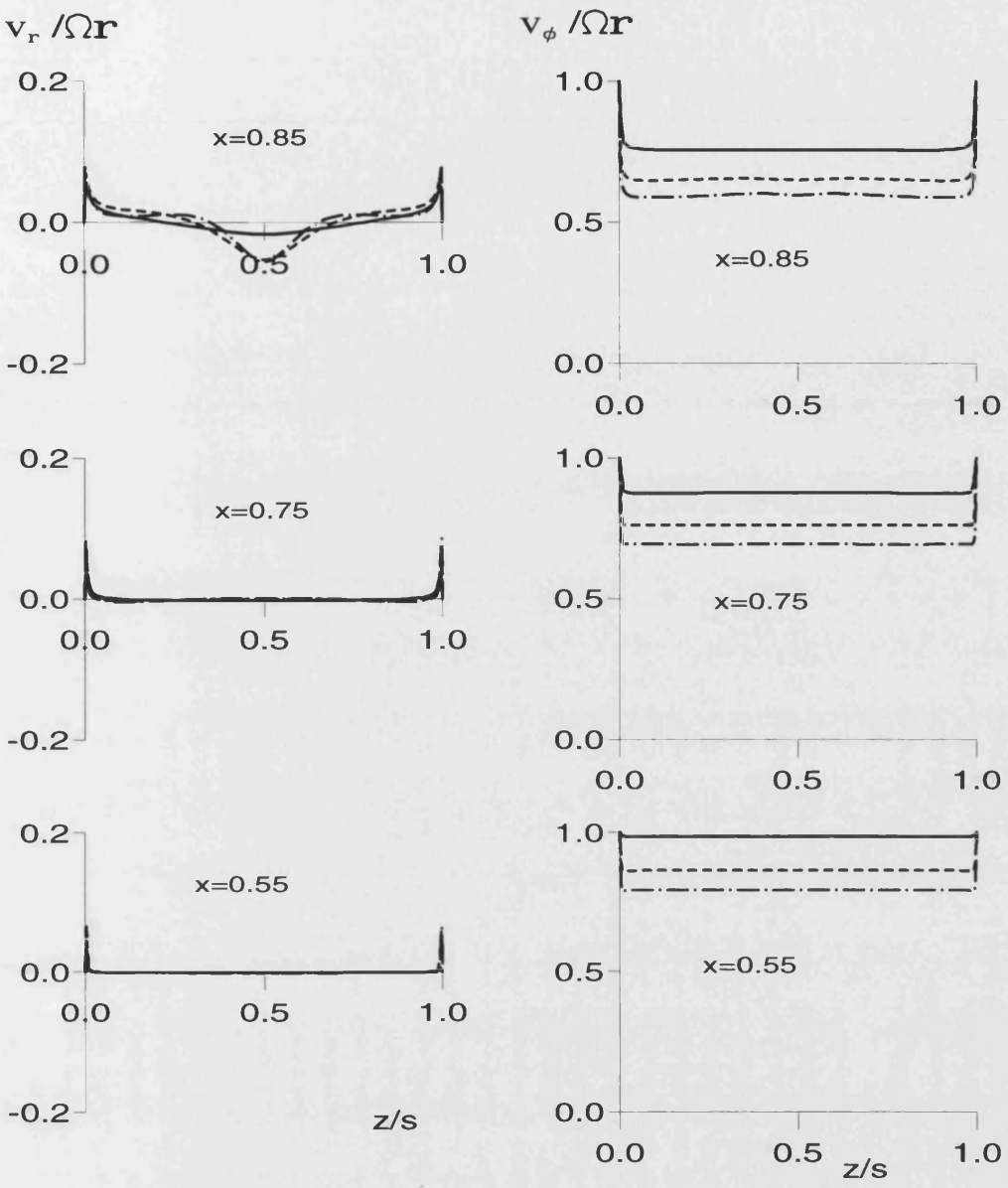

Figure 6.34. Effect of gap ratio on axial variation of radial and tangential components of velocity for rotating cavity with flat-shroud:
$Re_\phi = 1.5 \times 10^6$ and $C_w = 0.0$

—— G = 0.1

---- G = 0.2

—·— G = 0.3

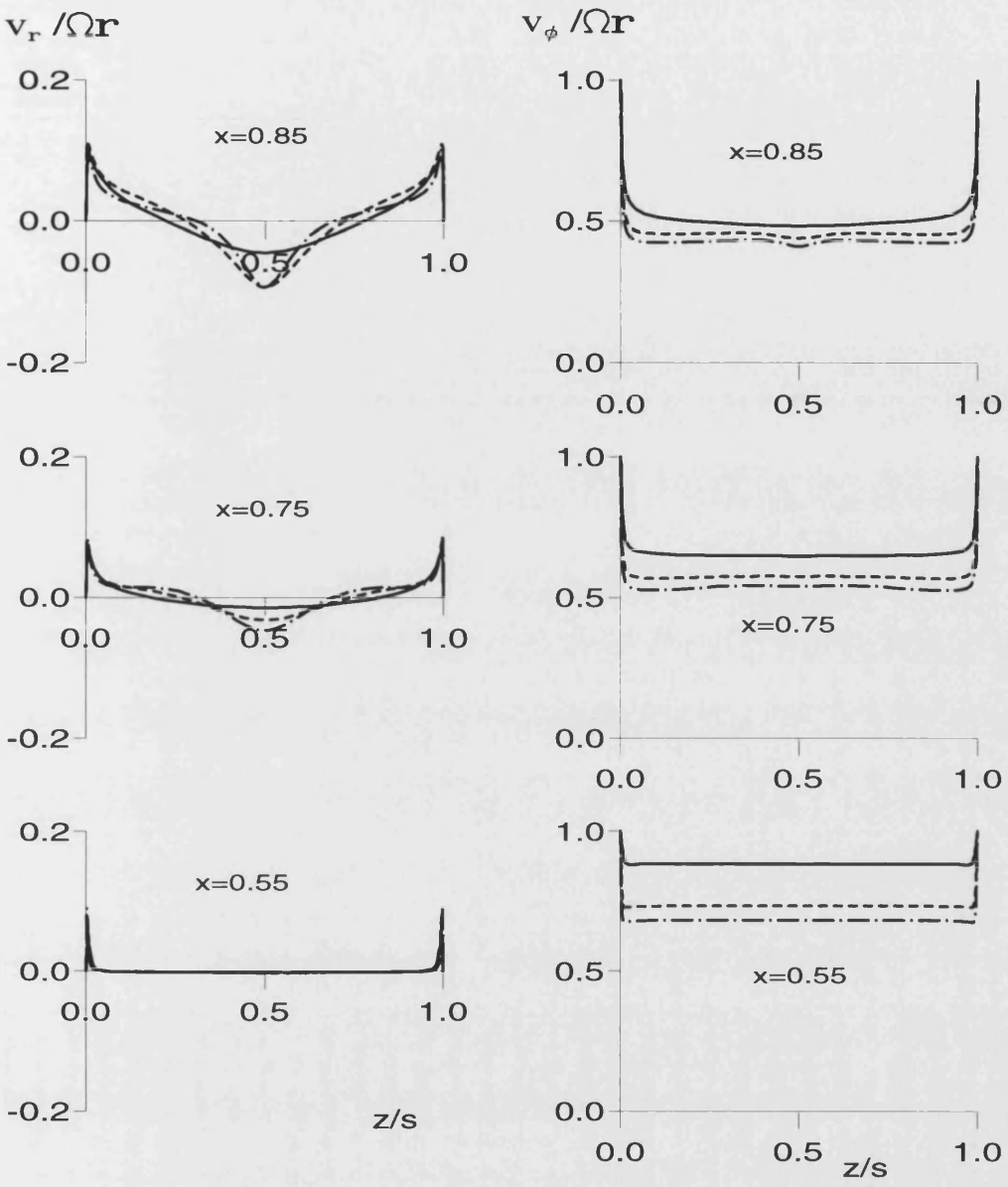

Figure 6.35. Effect of gap ratio on axial variation of radial and tangential components of velocity for rotating cavity with flat-shroud:
$Re_\phi = 1.5 \times 10^6$ and $C_w = -3000$.

—— G = 0.1

---- G = 0.2

—·— G = 0.3

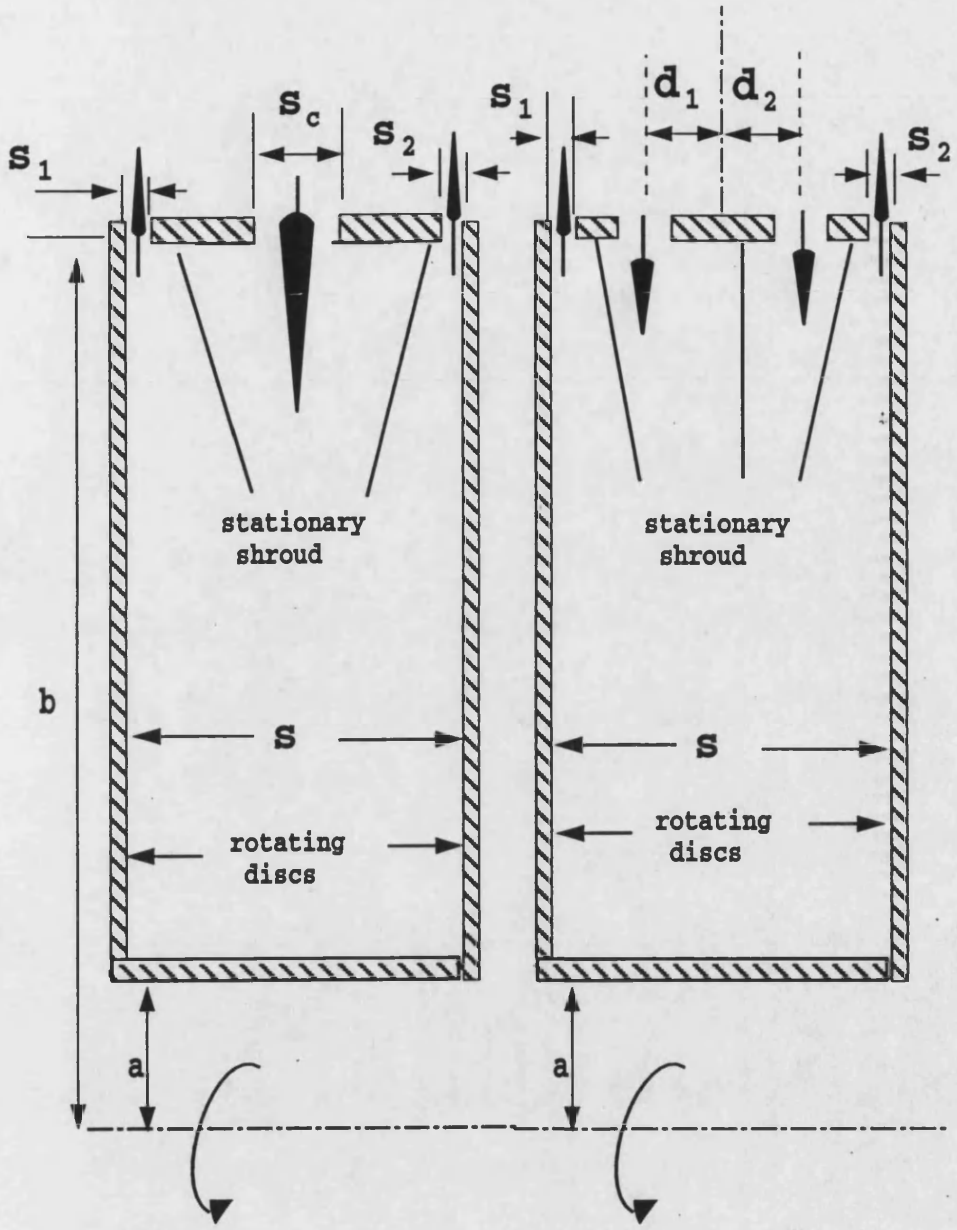

Figure 6.36. Schematic diagrams of slot geometry

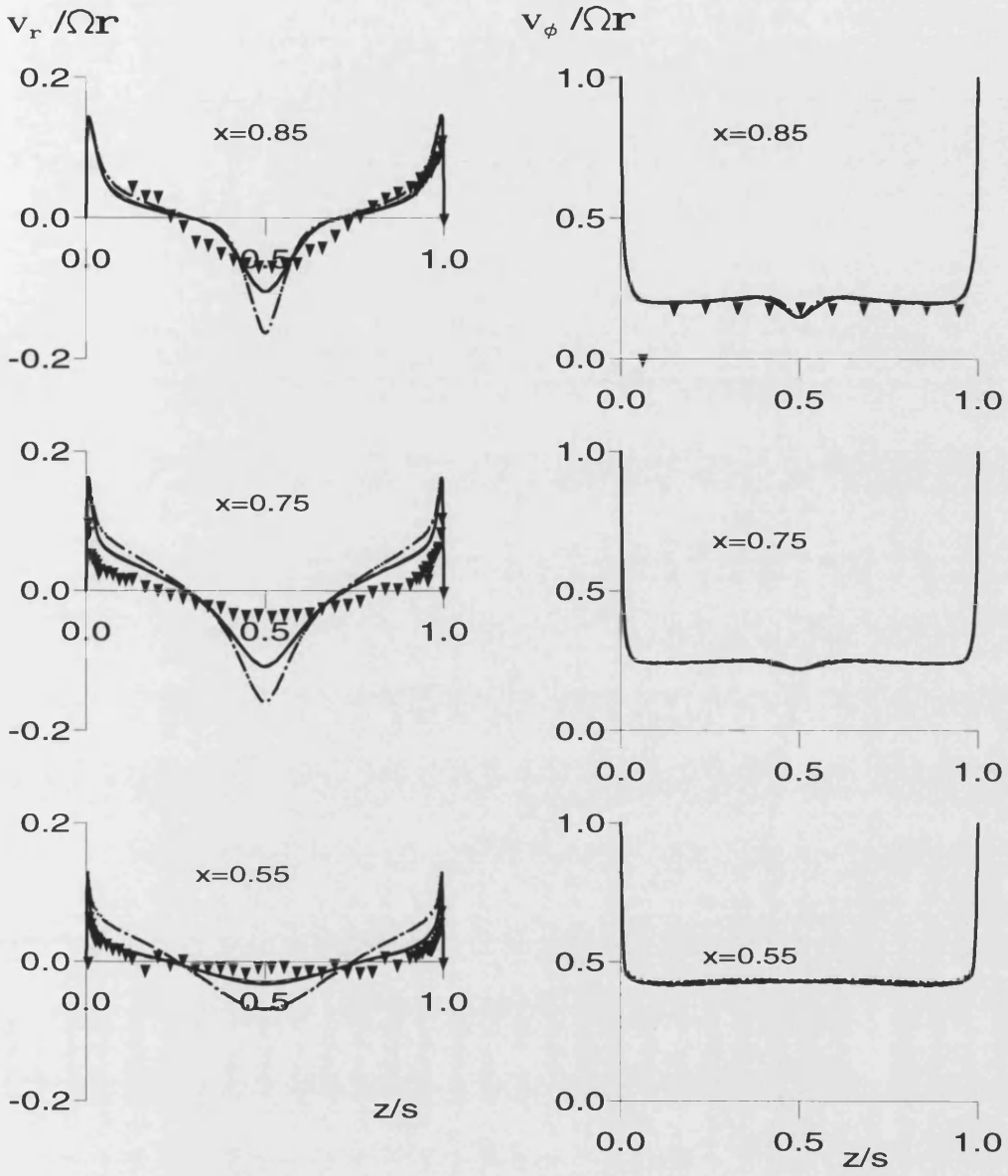

Figure 6.37. Effect of slot-width on axial variation of $V_r/\Omega r$ and $V_\phi/\Omega r$ for rotating cavity with flat-shroud:
G=0.3, C_w = -3000, Re_ϕ = 3.75 x 10^5 and λ_T = -0.104.

— · — G_c = 0.004 ····· G_c = 0.008
—— G_c = 0.0288 ---- G_c = 0.055
—— G_c = 0.086 ▾ Data of Gan (1994)

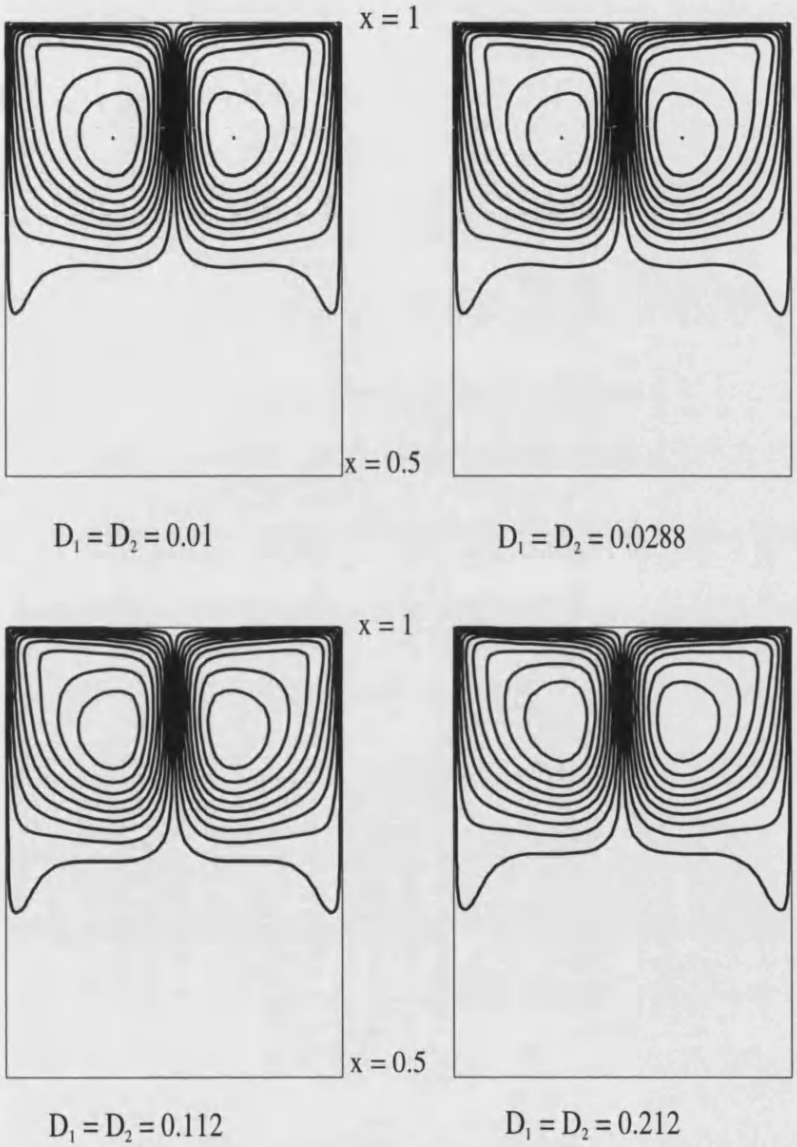

Figure 6.38. Effect of slot spacing on the computed streamlines: G = 0.30 $G_{C1} = G_{C2} = 0.01$, $C_W = -1500$, $Re_\phi = 1.5 \times 10^6$ and $\lambda_T = -0.0172$

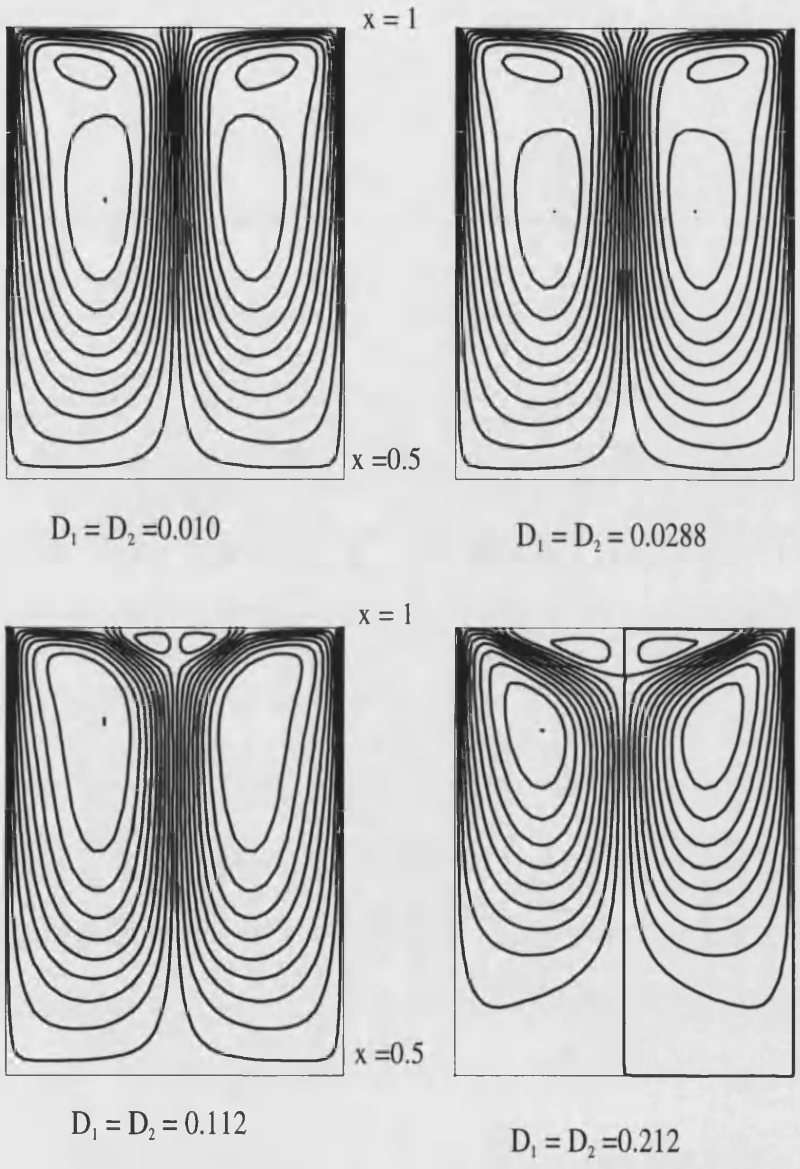

Figure 6.39. Effect of slot spacing on the computed streamlines: G = 0.30 $G_{C1} = G_{C2} = 0.01$, $C_W = -3000$, $Re_\phi = 3.75 \times 10^5$ and $\lambda_T = -0.104$

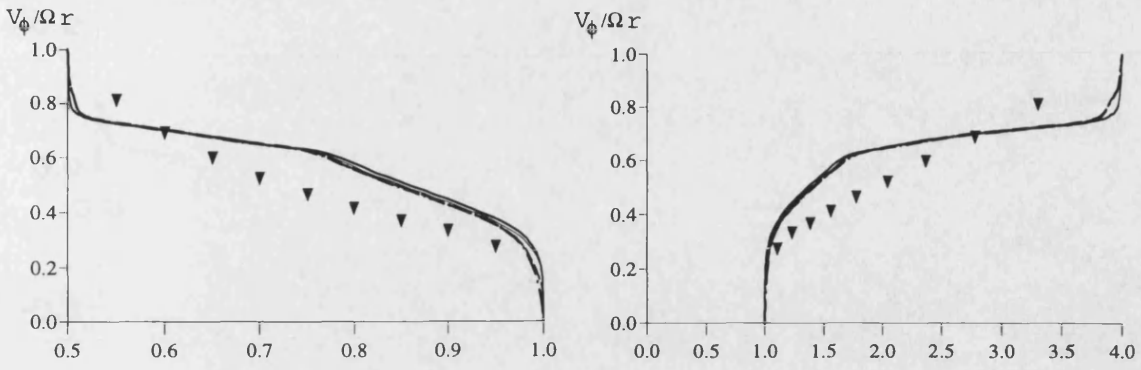

a) C_W = -1500 and Re_ϕ = 3.75 x 10^5

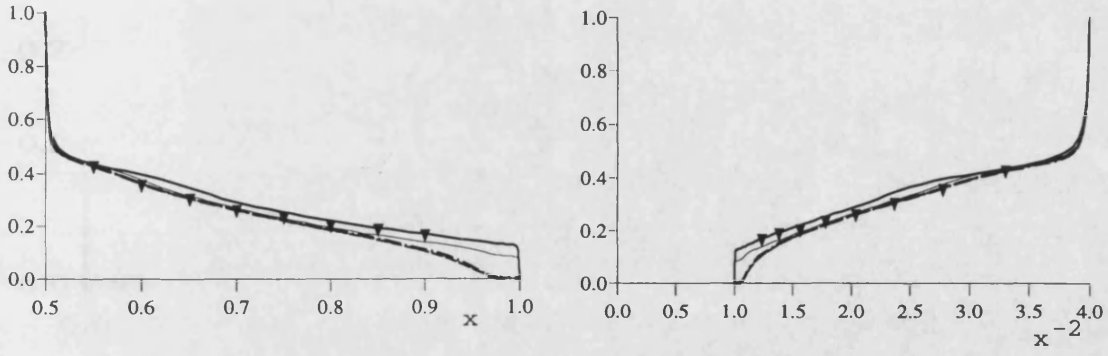

b) C_W = -3000 and Re_ϕ = 1.5 x 10^6

Figure 6.40. Effect of slot-spacing on variation of $V_\phi/\Omega r$ with x and x^{-2} for rotating cavity with flat-shroud.

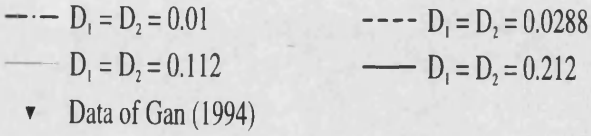

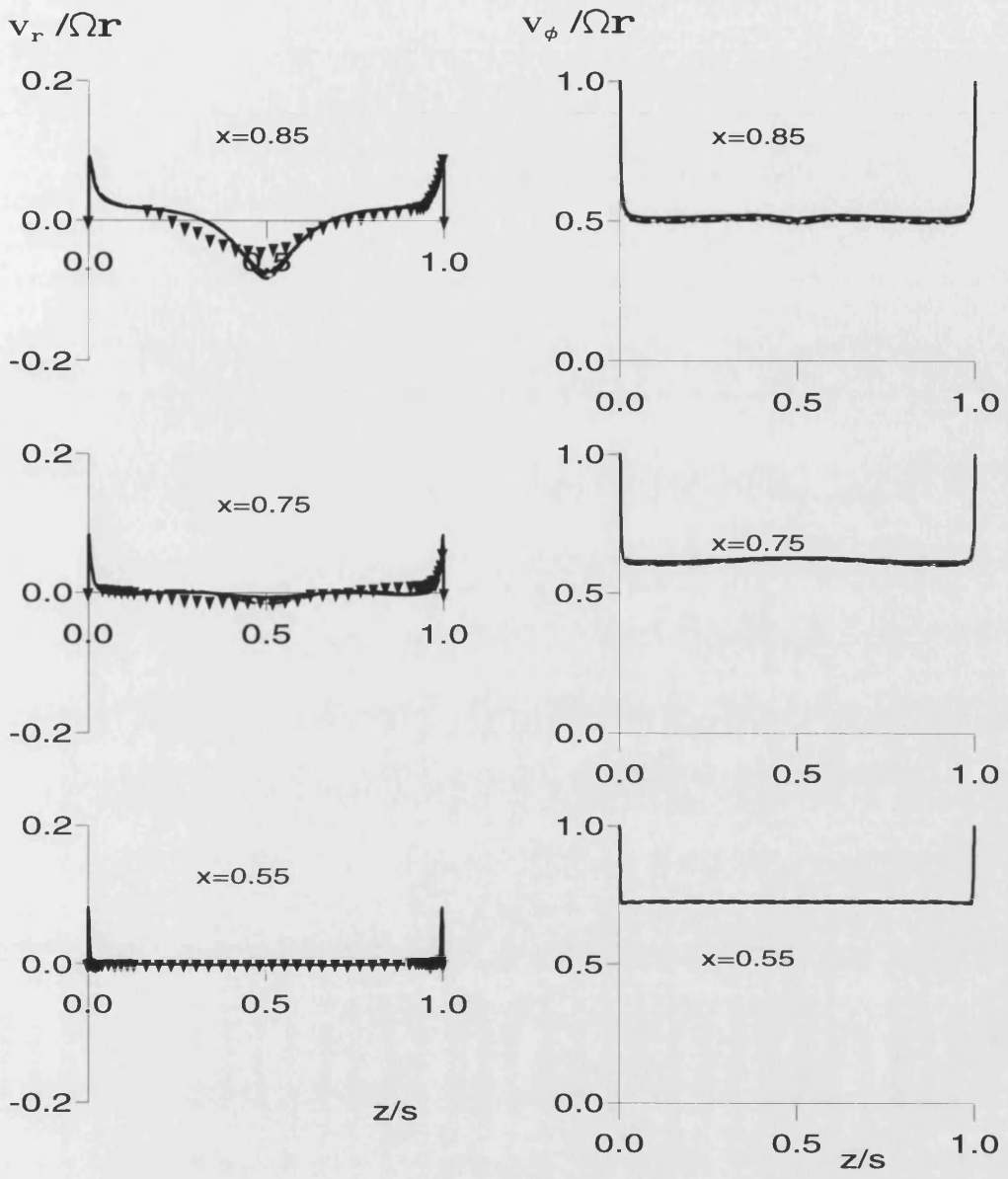

Figure 6.41. Effect of slot spacing on axial variation of $V_r/\Omega r$ and $V_\phi/\Omega r$ for rotating cavity with flat-shroud: G=0.3, $G_{C1} = G_{C2}$=0.01, C_W=-1500, $Re_\phi = 1.5 \times 10^6$ and λ_T = -0.0172.

$D_1 = D_2 = 0.01$ $D_1 = D_2 = 0.0288$

$D_1 = D_2 = 0.112$ $D_1 = D_2 = 0.212$

▼ Data of Gan (1994)

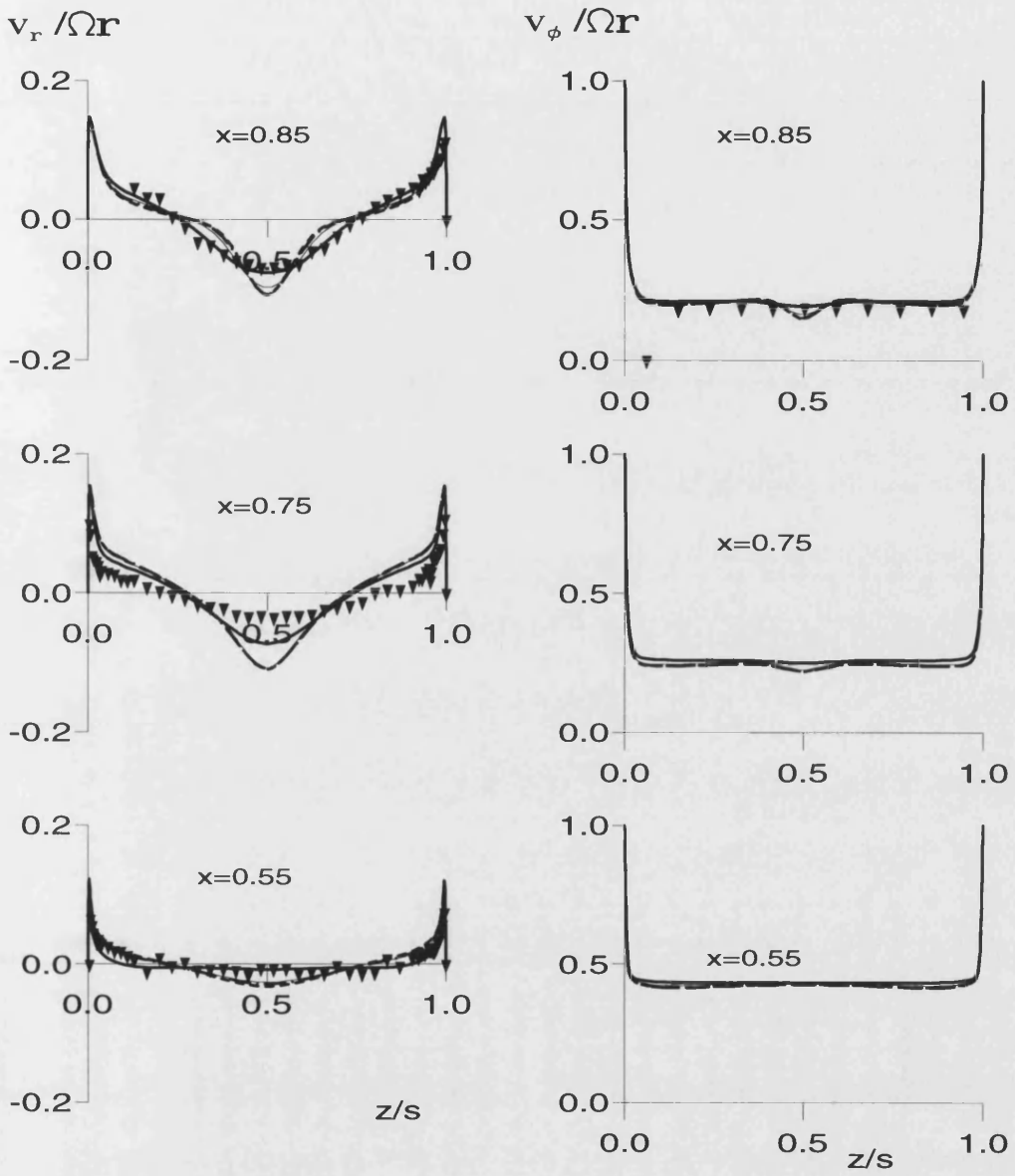

Figure 6.42. Effect of slot spacing on axial variation of $V_r/\Omega r$ and $V_\phi/\Omega r$ for rotating cavity with flat-shroud: G=0.3, $G_{C1}=G_{C2}=0.01$, $C_w=-3000$ $Re_\phi=3.75 \times 10^5$ and $\lambda_T=-0.104$.

—·— $D_1 = D_2 = 0.01$ ---- $D_1 = D_2 = 0.0288$

$D_1 = D_2 = 0.112$ —— $D_1 = D_2 = 0.212$

▼ Data of Gan (1994)

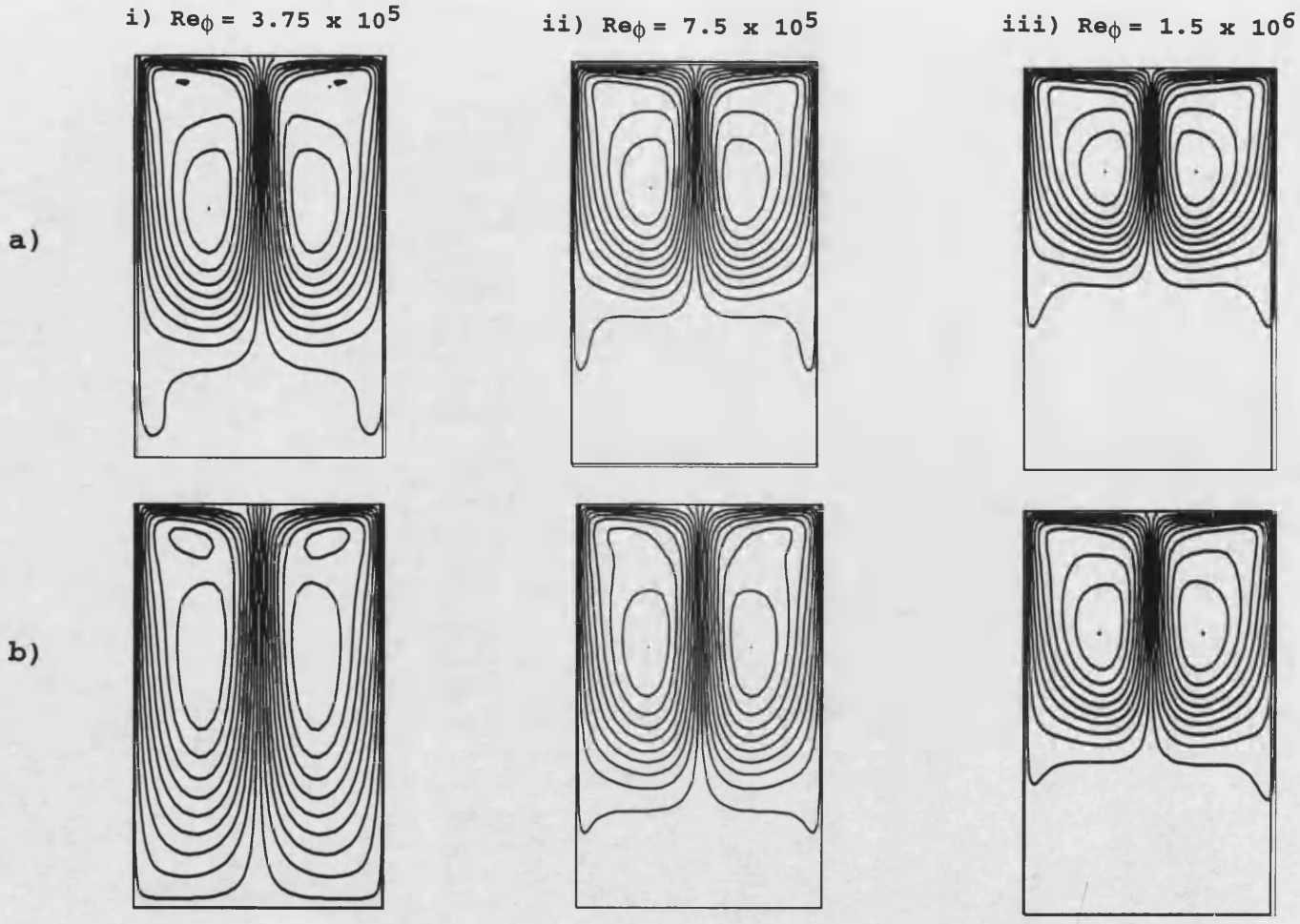

Figure 6.43. Effect of Re_ϕ on computed streamlines for rotating cavity with flat-shroud: a) C_W = -1500, b) C_W = -3000.

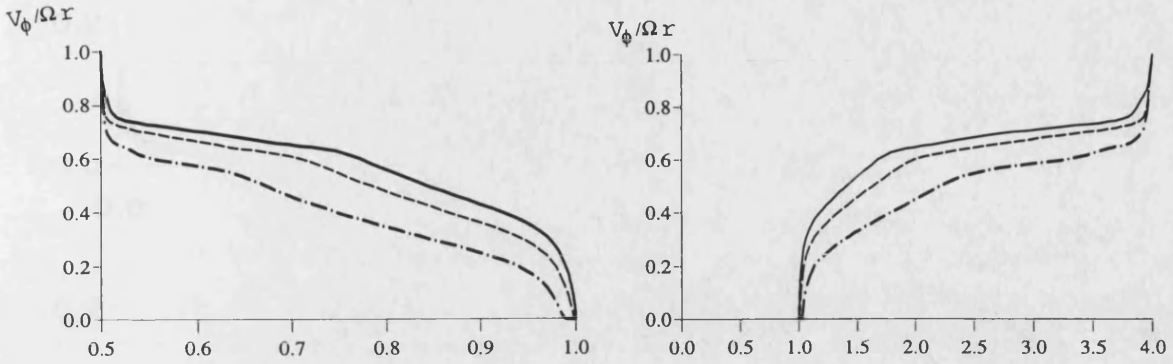

a) C_W = -1500

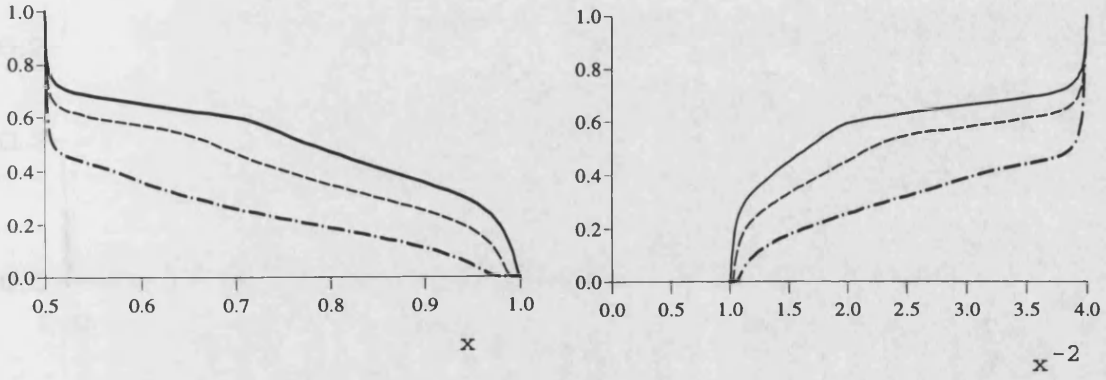

b) C_W = -3000

Figure 6.44. Effect of Re_ϕ on variation of $V_\phi/\Omega r$ with x and x^{-2} for rotating cavity with flat-shroud.

——— $Re_\phi = 1.5 \times 10^6$

- - - - $Re_\phi = 7.75 \times 10^5$

—·— $Re_\phi = 3.75 \times 10^5$

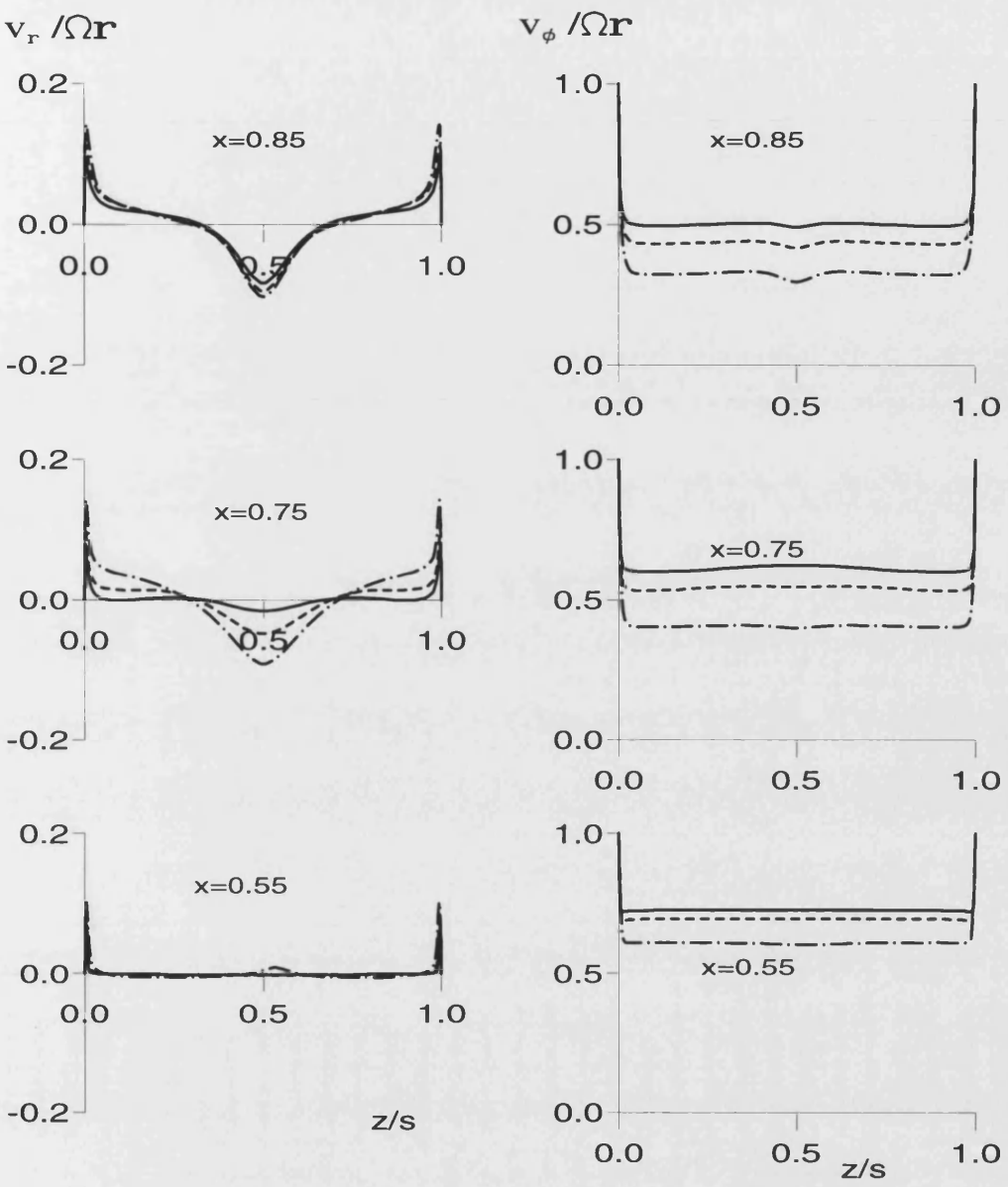

Figure 6.45. Effect of Re_ϕ on the axial variation of radial and tangential components of velocity for rotating cavity with flat shroud: C_w = -1500.

—— $Re_\phi = 1.5 \times 10^6$

---- $Re_\phi = 7.75 \times 10^5$

—·— $Re_\phi = 3.75 \times 10^5$

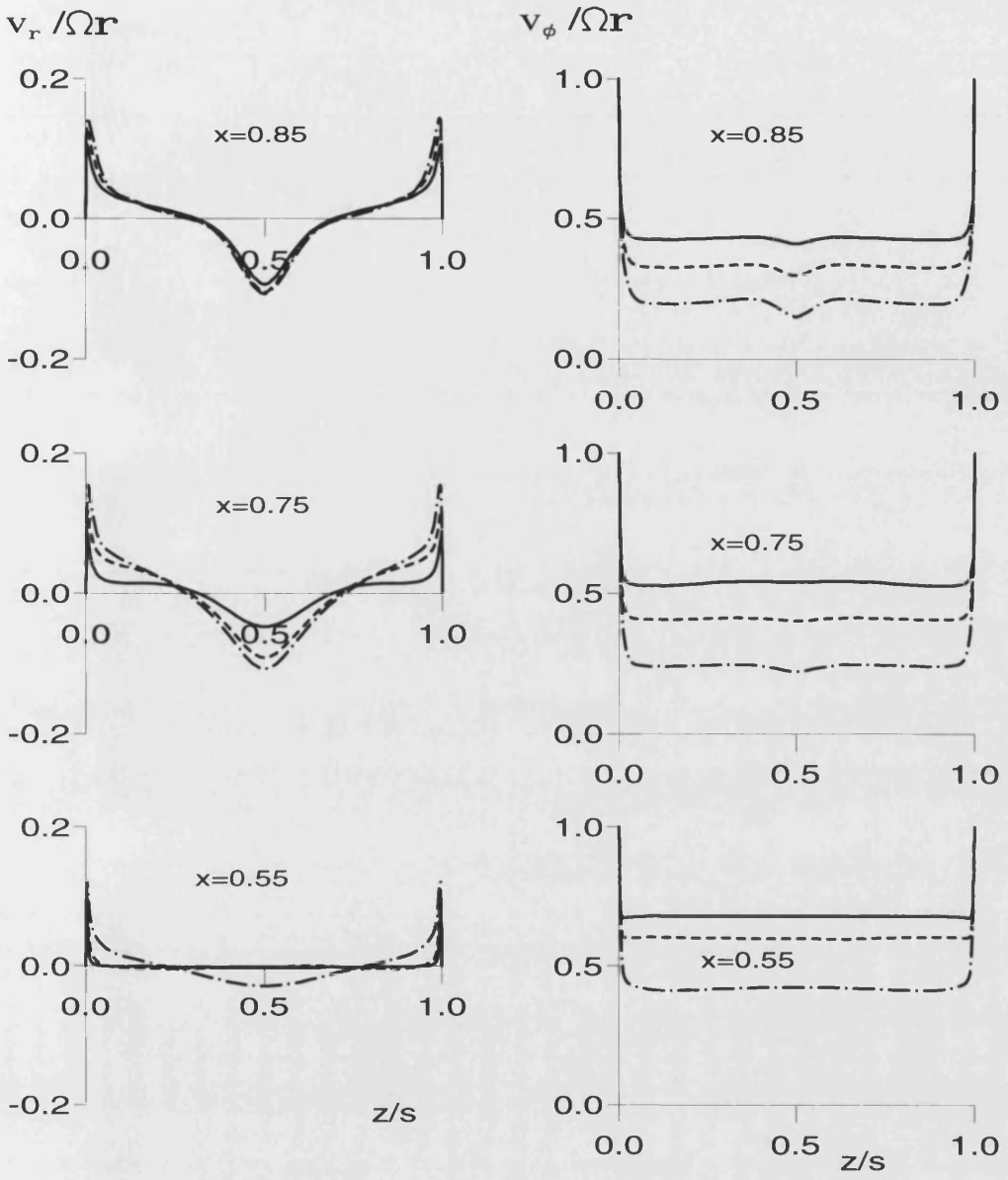

Figure 6.46. Effect of Re_ϕ on the axial variation of radial and tangential components of velocity for rotating cavity with flat-shroud: C_w =-3000.

——— $Re_\phi = 1.5 \times 10^6$

- - - - $Re_\phi = 7.75 \times 10^5$

—·— $Re_\phi = 3.75 \times 10^5$

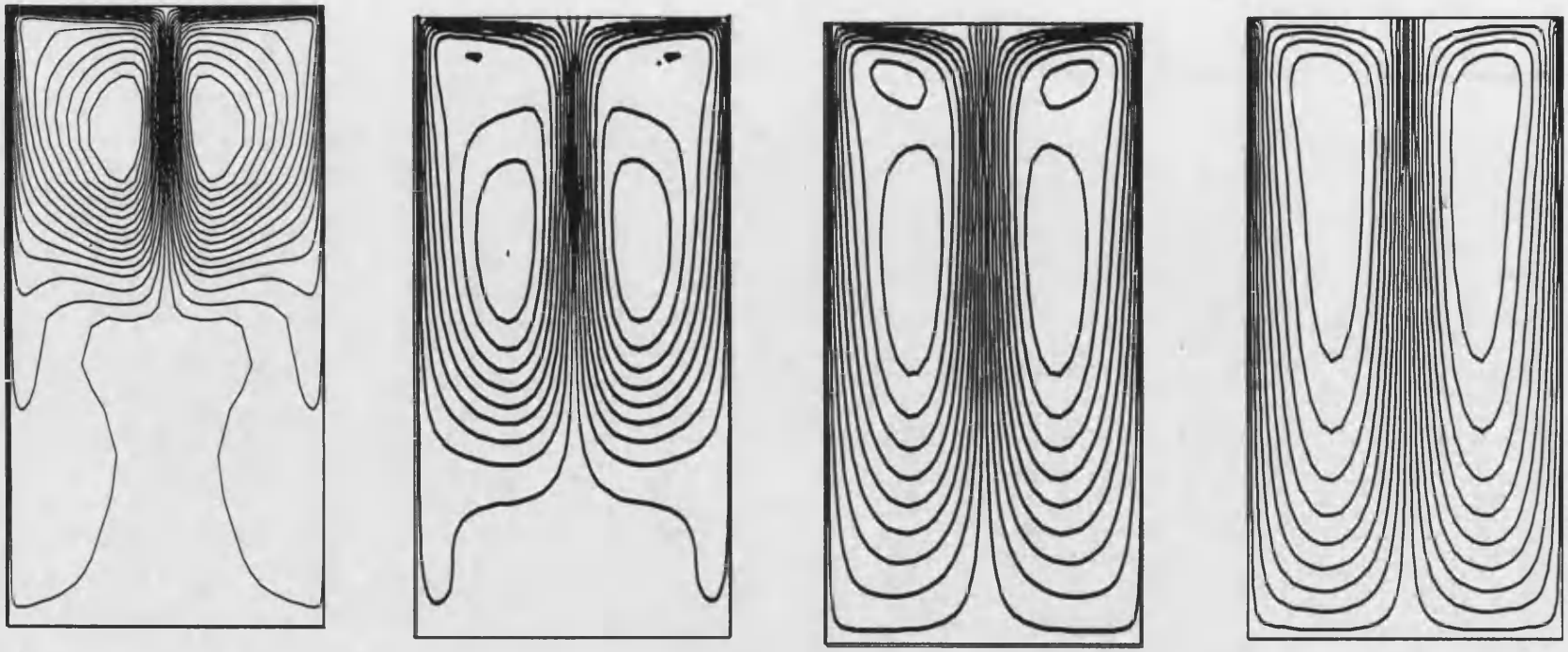

a) $C_W = 0$ b) $C_W = -1500$ c) $C_W = -3000$ d) $C_W = -6000$

Figure 6.47. Effect of C_W on computed streamlines for rotating cavity with flat-shroud: $Re_\phi = 3.75 \times 10^5$

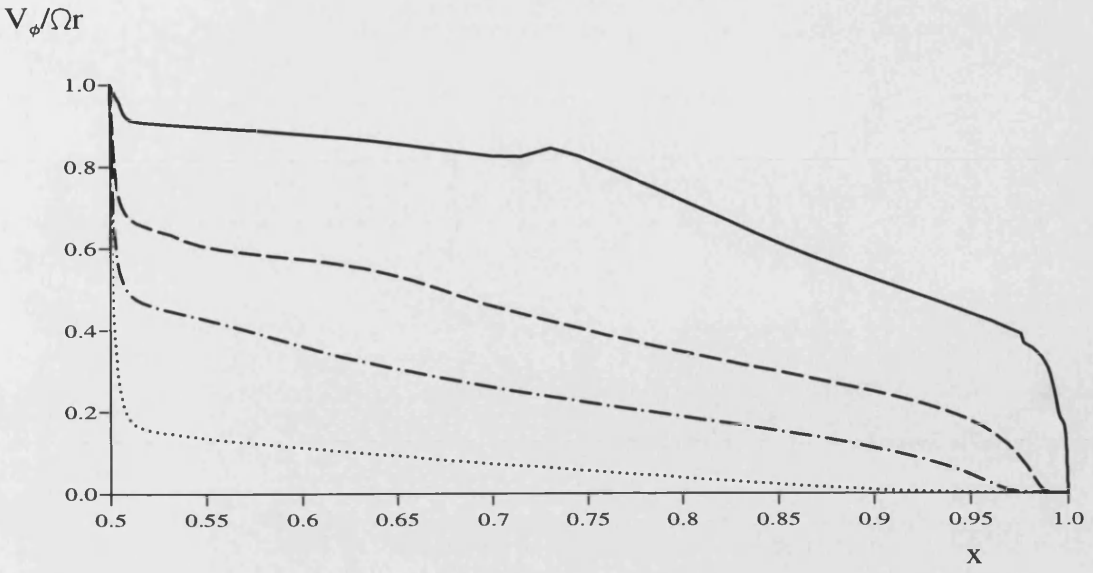

a) variation with x

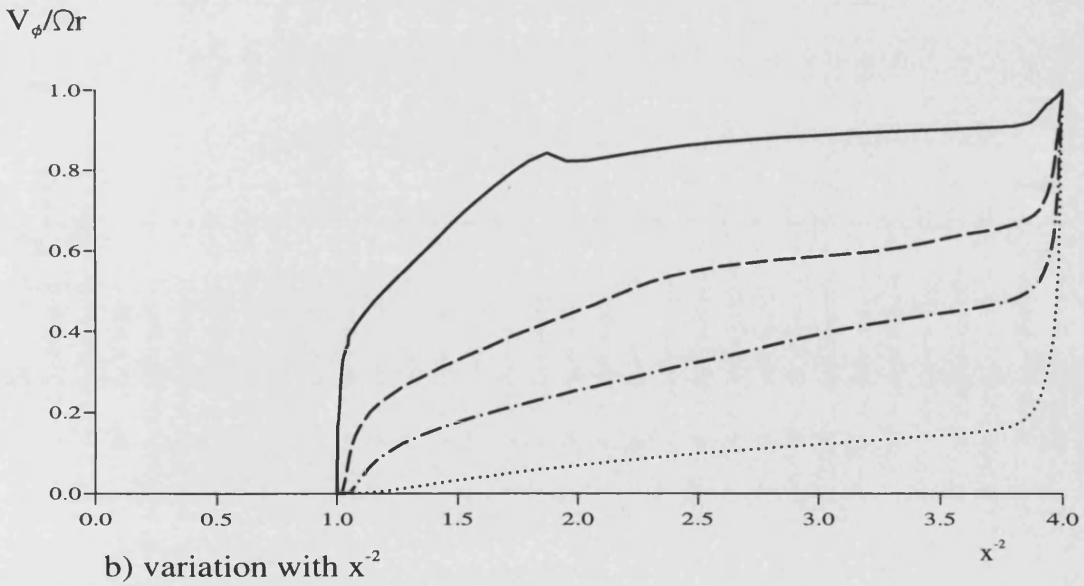

b) variation with x^{-2}

Figure 6.48. Effect of C_w on variation of $V_\phi/\Omega r$ with x and x^{-2} for rotating cavity with flat-shroud: G=0.3 and $Re_\phi = 3.75 \times 10^5$.

——— $C_w = 0$

– – – $C_w = -1500$

—·— $C_w = -3000$

..... $C_w = -6000$

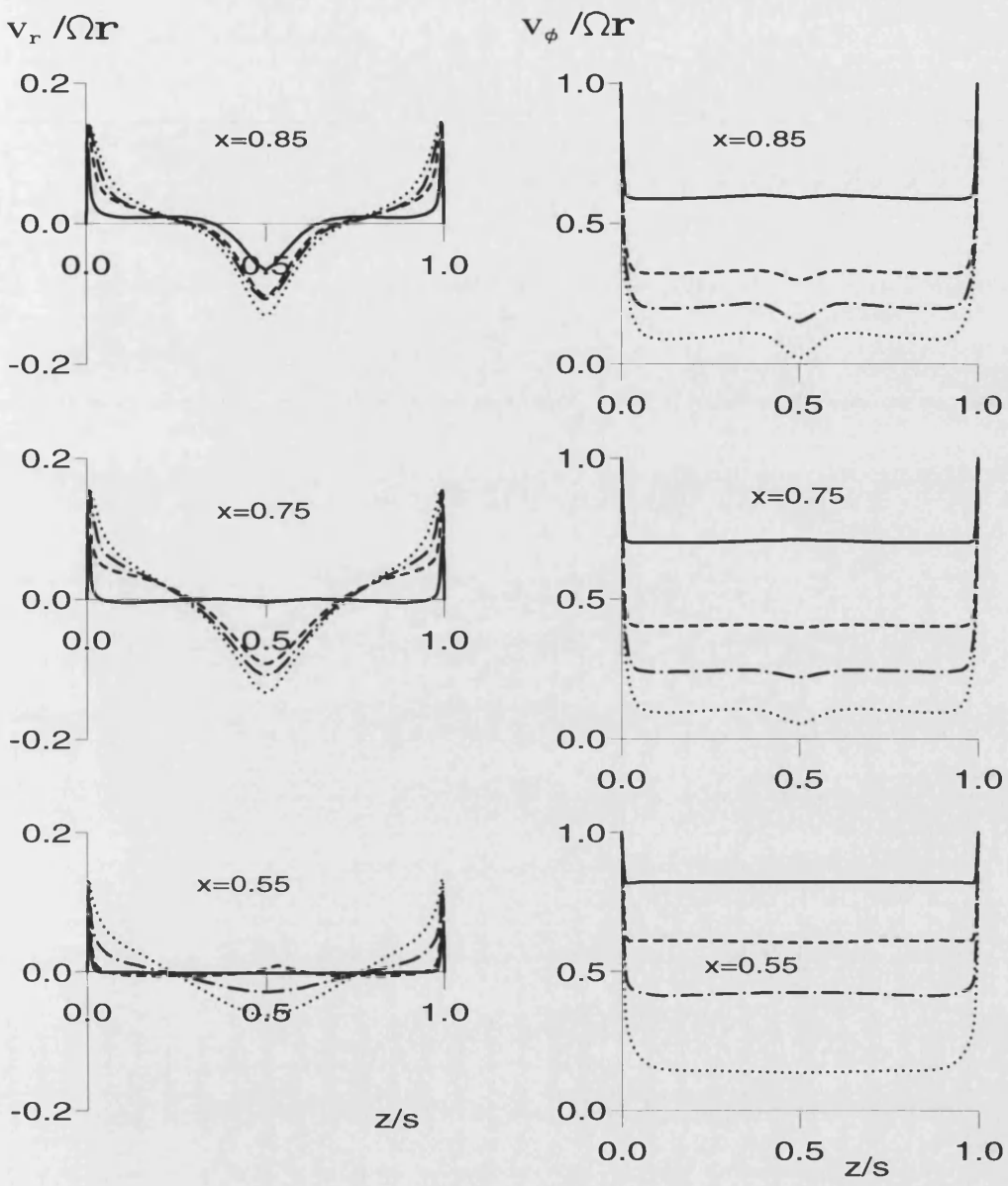

Figure 6.49. Effect of C_w on the axial variation of radial and tangential components of velocity for rotating cavity with flat-shroud: $Re_\phi = 3.75 \times 10^5$.

—— $C_w = 0$

---- $C_w = -1500$

—·— $C_w = -3000$

····· $C_w = -6000$

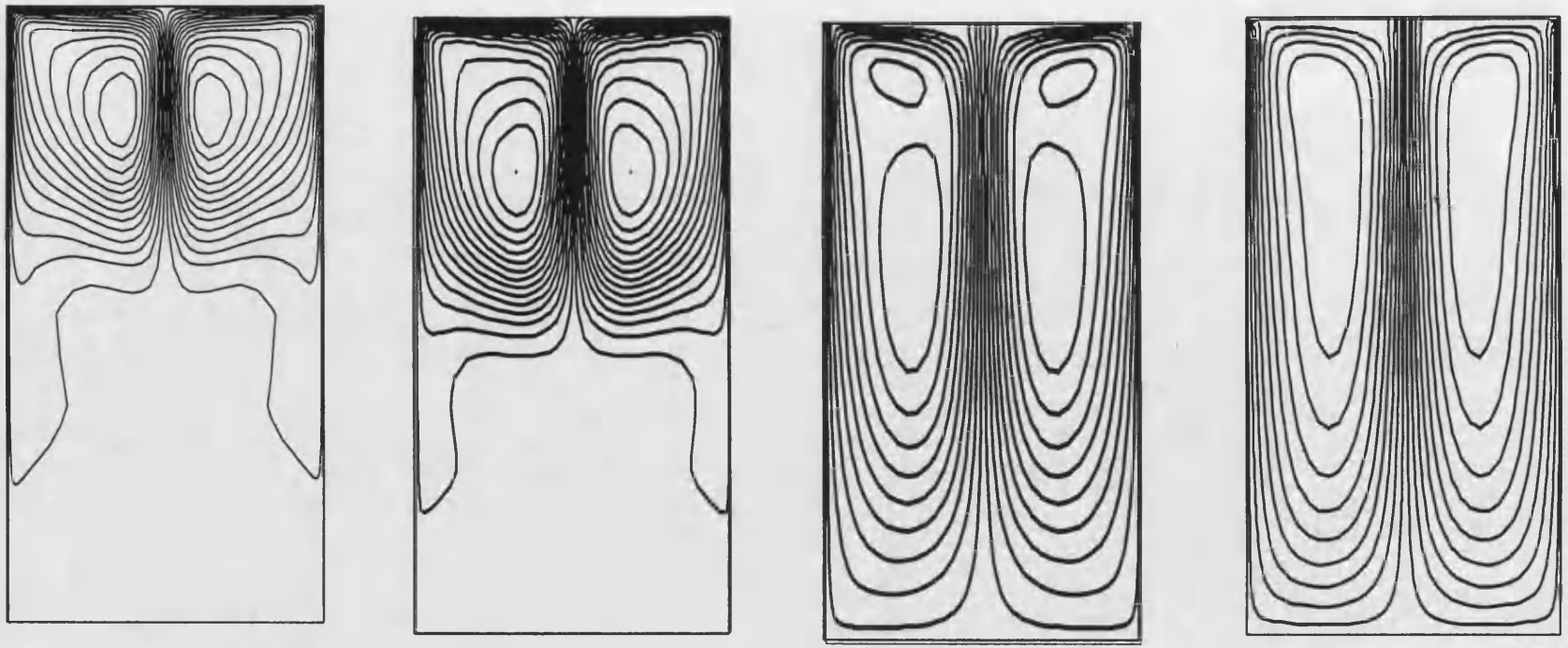

a) $\lambda_T = 0$ ($C_W = 0$, $Re_\phi = 1.5 \times 10^6$)

b) $\lambda_T = -0.017$ ($C_W = -1500$, $Re_\phi = 1.5 \times 10^6$)

c) $\lambda_T = -0.104$ ($C_W = -3000$, $Re_\phi = 3.75 \times 10^5$)

d) $\lambda_T = -0.2$ ($C_W = -6000$, $Re_\phi = 3.75 \times 10^5$)

Figure 6.50. Effect of λ_T on computed streamlines for rotating cavity with flat-shroud.

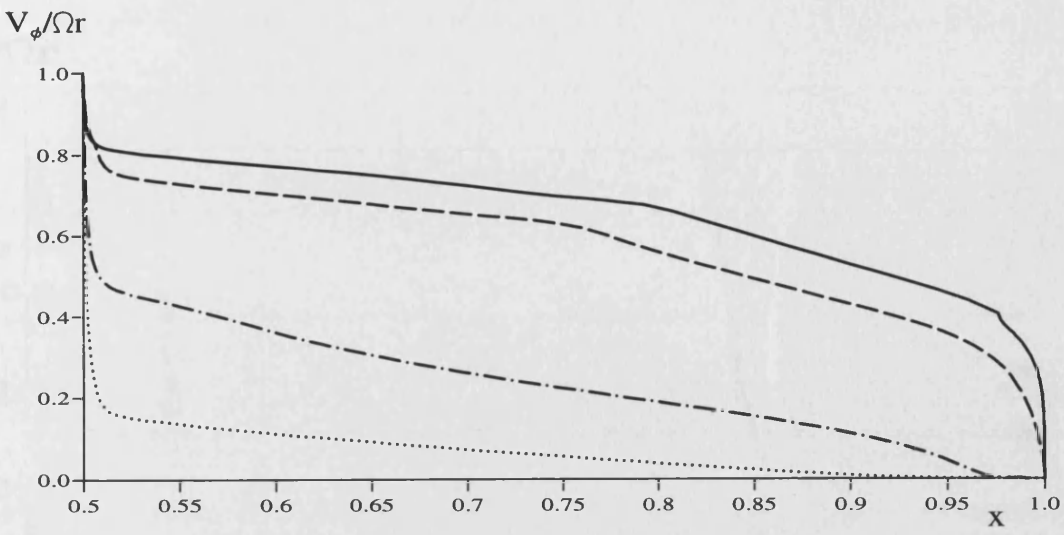

a) variation with x

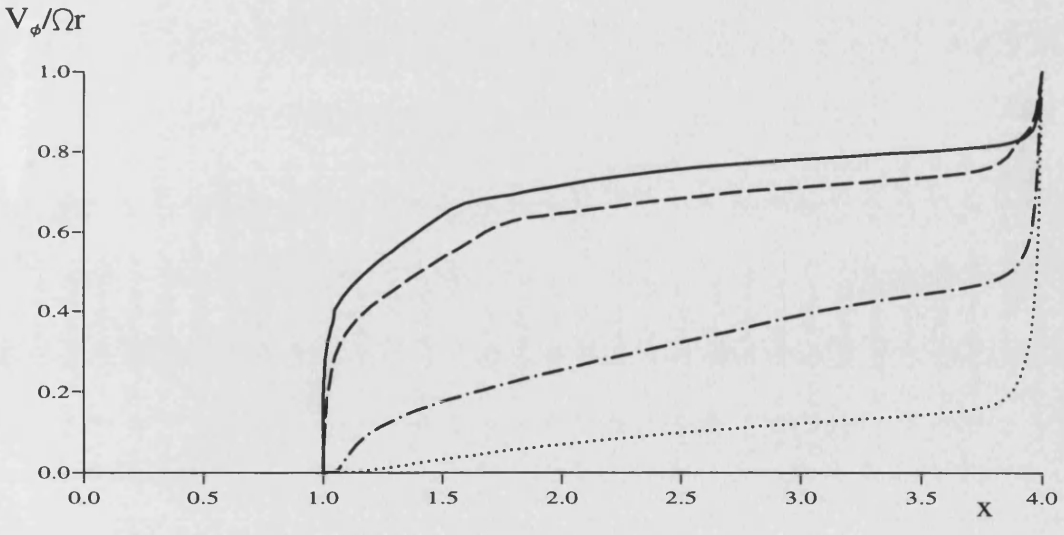

b) variation with x^{-2}

Figure 6.51 Effect of λ_T on variation of $V_\phi/\Omega r$ with x and x^{-2} for rotating cavity with flat-shroud: G=0.3

——— λ_T =0 (C_w =0 and Re_ϕ = 1.5 x 10^6)

– – – λ_T = -0.017 (C_w = -1500 and Re_ϕ = 1.5 x 10^6)

—·— λ_T = -0.104 (C_w = -3000 and Re_ϕ = 3.75 x 10^5)

..... λ_T = -0.2 (C_w = -6000 and Re_ϕ = 3.75 x 10^5)

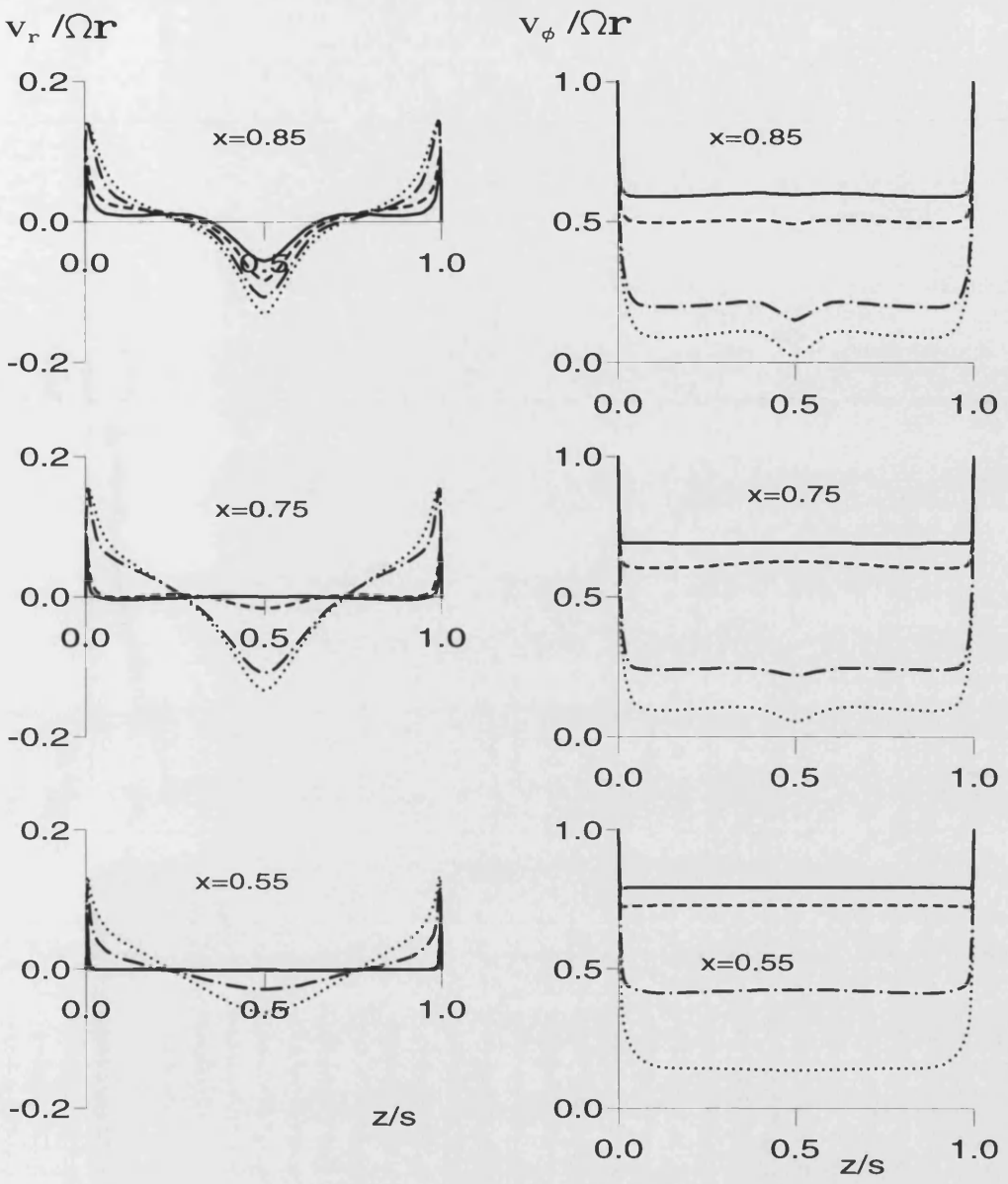

Figure 6.52. Effect of λ_T on the axial variation of radial and tangential components of velocity for rotating cavity with flat-shroud.

—— $\lambda_T = 0.$ (C_w =0.0 and $Re_\phi = 1.5 \times 10^6$)

- - - - $\lambda_T = -0.017$ ($C_w = -1500$ and $Re_\phi = 1.5 \times 10^6$)

—·— $\lambda_T = -0.104$ ($C_w = -3000$ and $Re_\phi = 3.75 \times 10^5$)

····· $\lambda_T = -0.2$ ($C_w = -6000$ and $Re_\phi = 3.75 \times 10^5$)

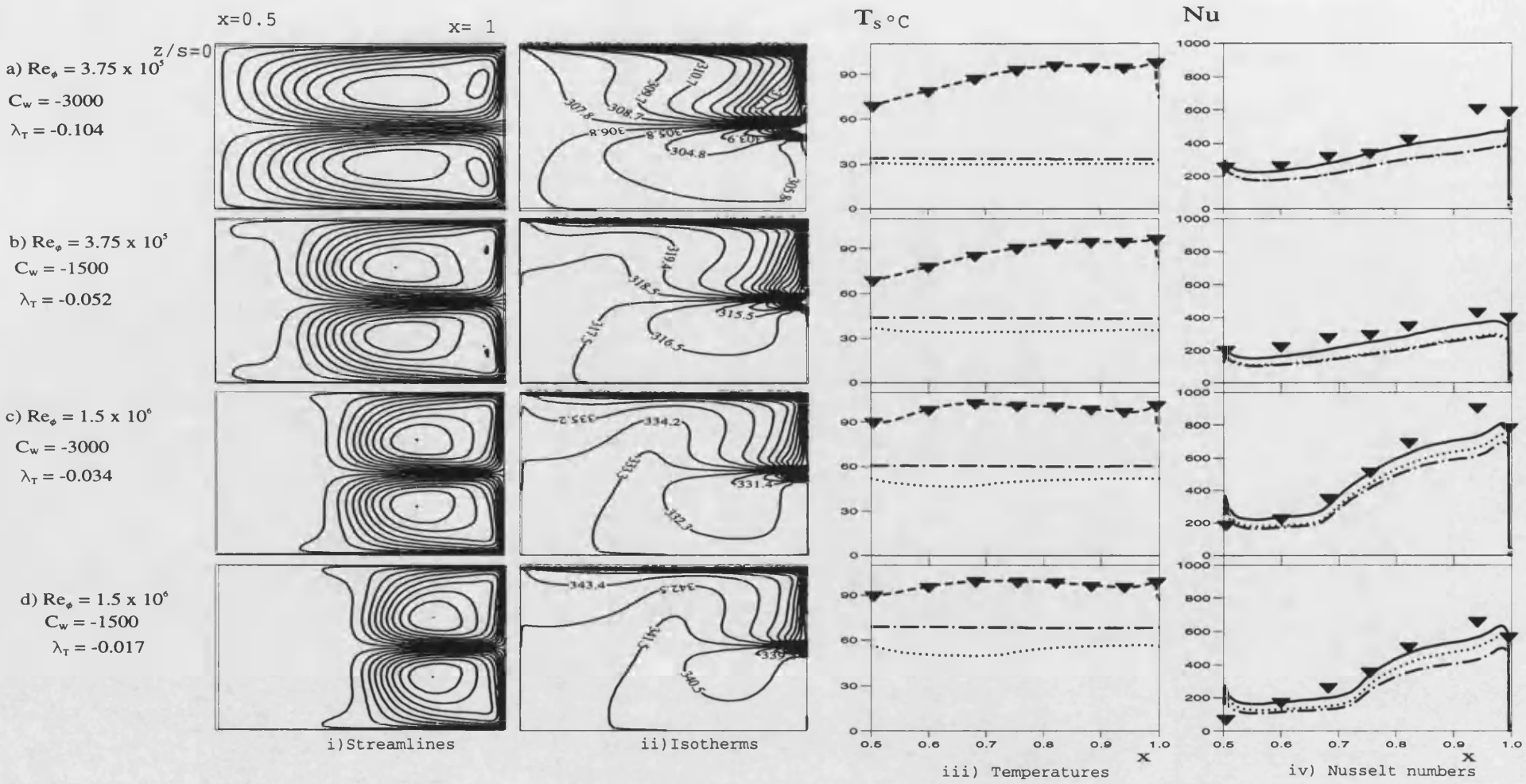

Figure 6.53. Comparison between computed and measured temperatures and Nusselt numbers for rotating cavity with flat-shroud.

▼ Measured temperatures and Nusselt numbers on the heated disc ——— Fitted temperature on the heated disc

{ Computed temperature on the unheated disc; Computed Nusselt numbers on the heated disc } for { —·— adiabatic-disc assumption ····· conducting-disc assumption }

——— Computed Nusselt numbers on the heated disc: conducting-disc assumption with radiation correction

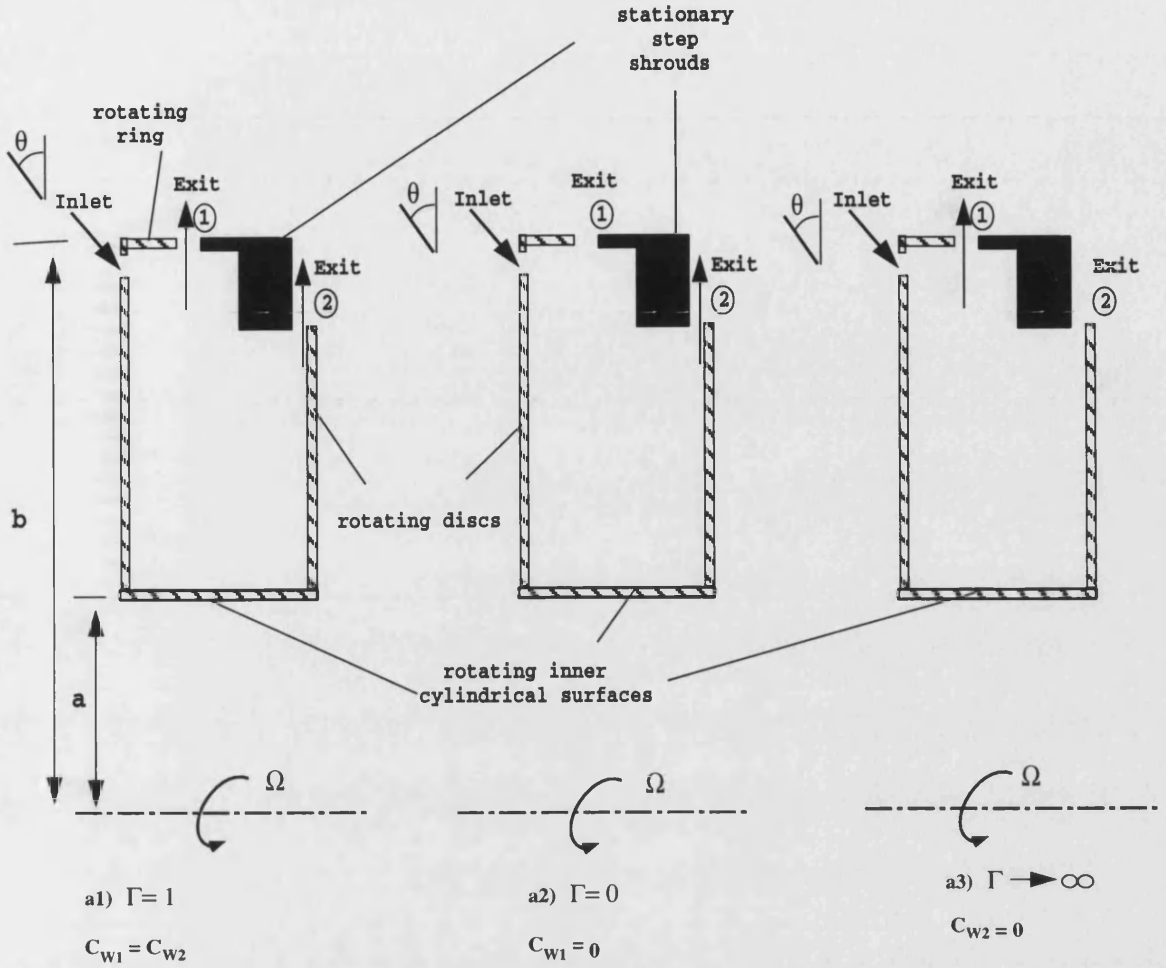

a) schematic diagram

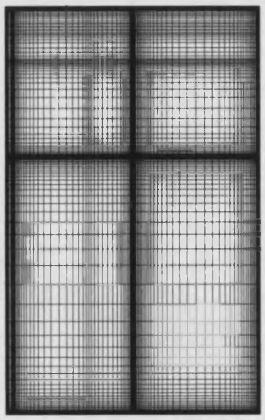

b) grid distribution

147 x 131 grid nodes in r-z plane

Figure 7.1. Schematic diagram and typical grid distribution for stepped-shroud.

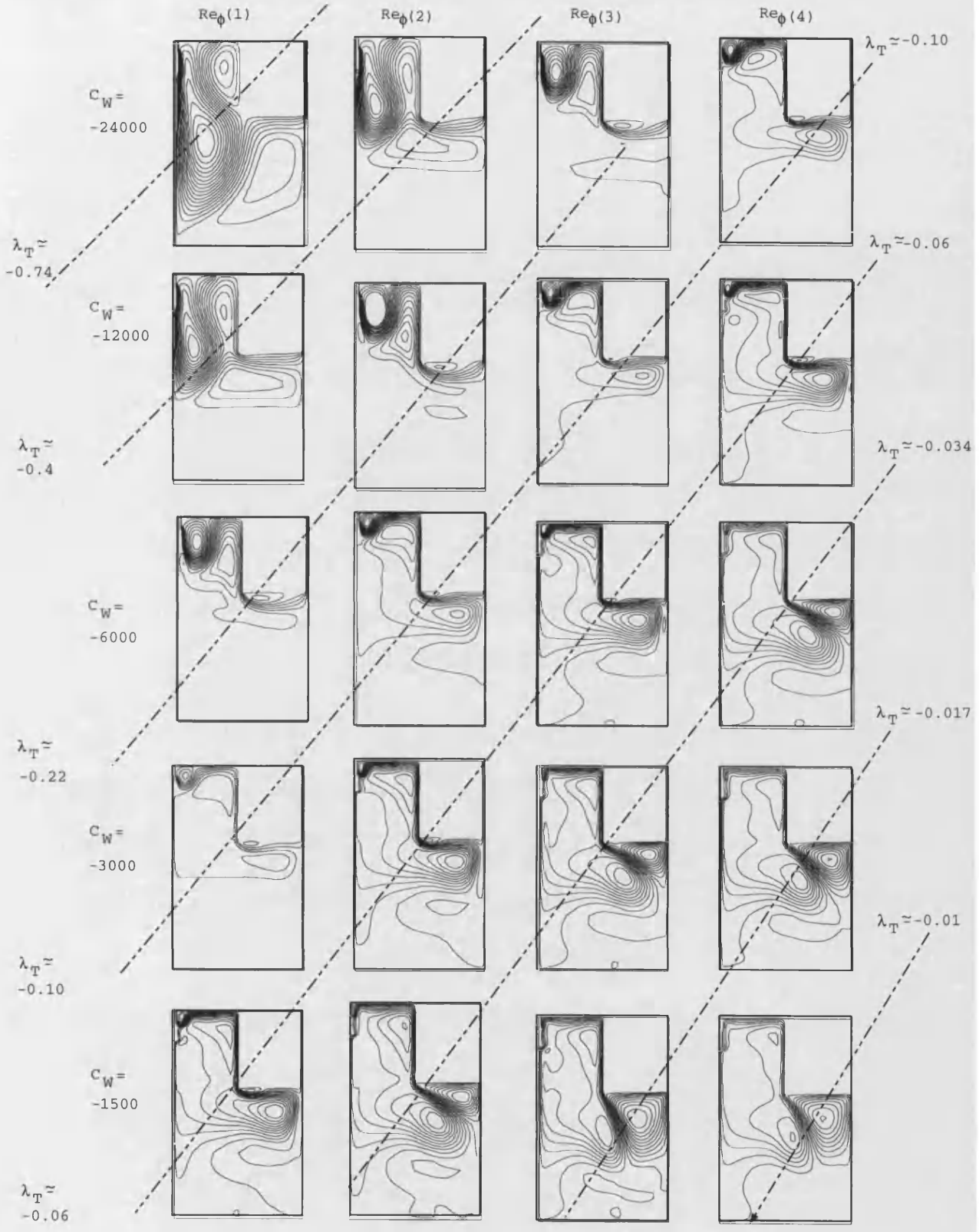

Figure 7.2. Effect of Re_ϕ, C_W and λ_T on the computed streamlines for peripheral flow with stepped shroud: $\Gamma = 1$

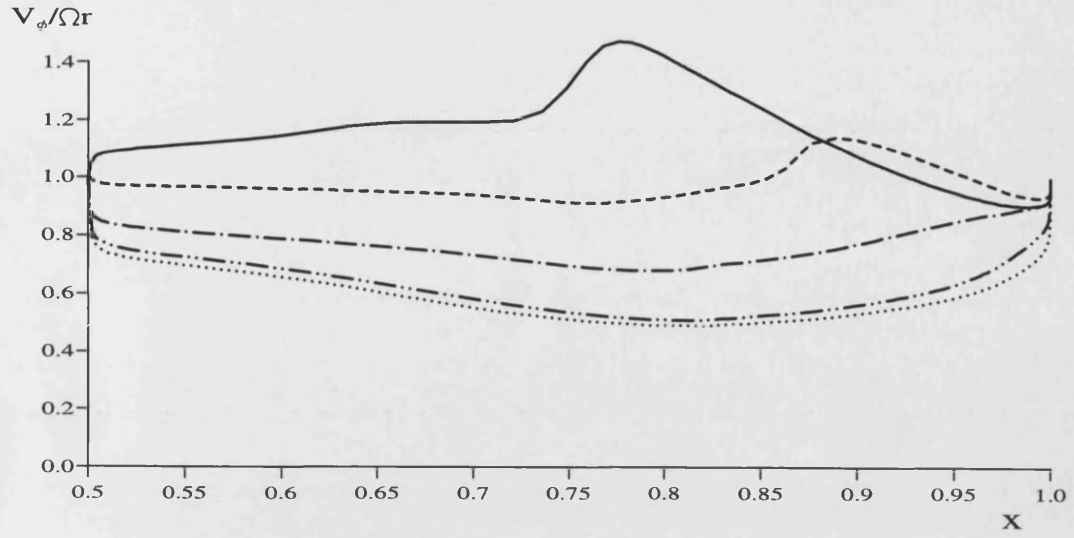

a) Variation of $V_\phi/\Omega r$ with x

$\lambda_T = -0.4$

$\lambda_T = -0.22$

$\lambda_T = -0.10$

$\lambda_T = -0.034$

$\lambda_T = -0.01$

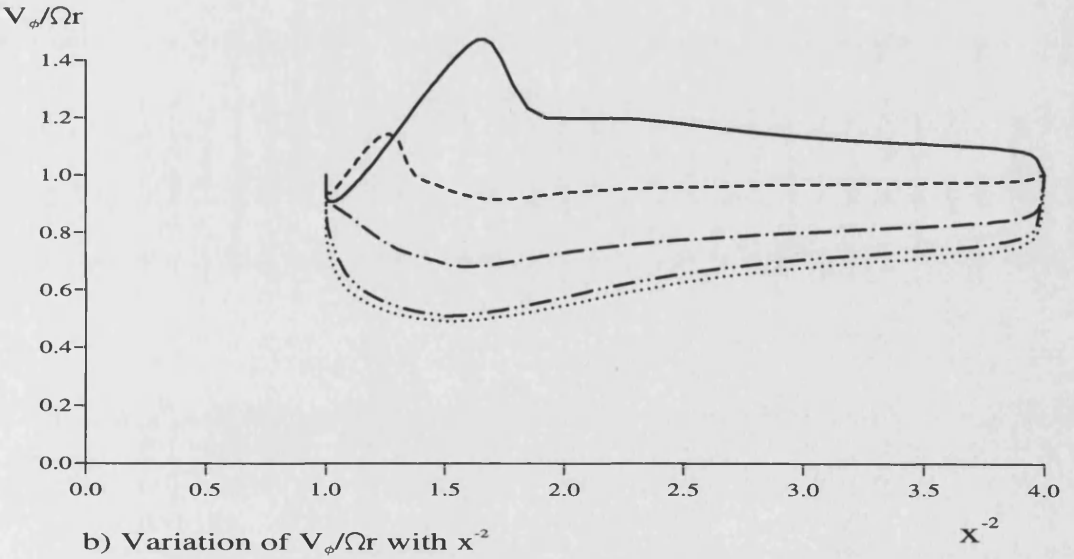

b) Variation of $V_\phi/\Omega r$ with x^{-2}

Figure 7.3. Effect of λ_T on variation of $V_\phi/\Omega r$ with x and x^{-2} for rotating cavity with stepped-shroud: $\Gamma = 1$.

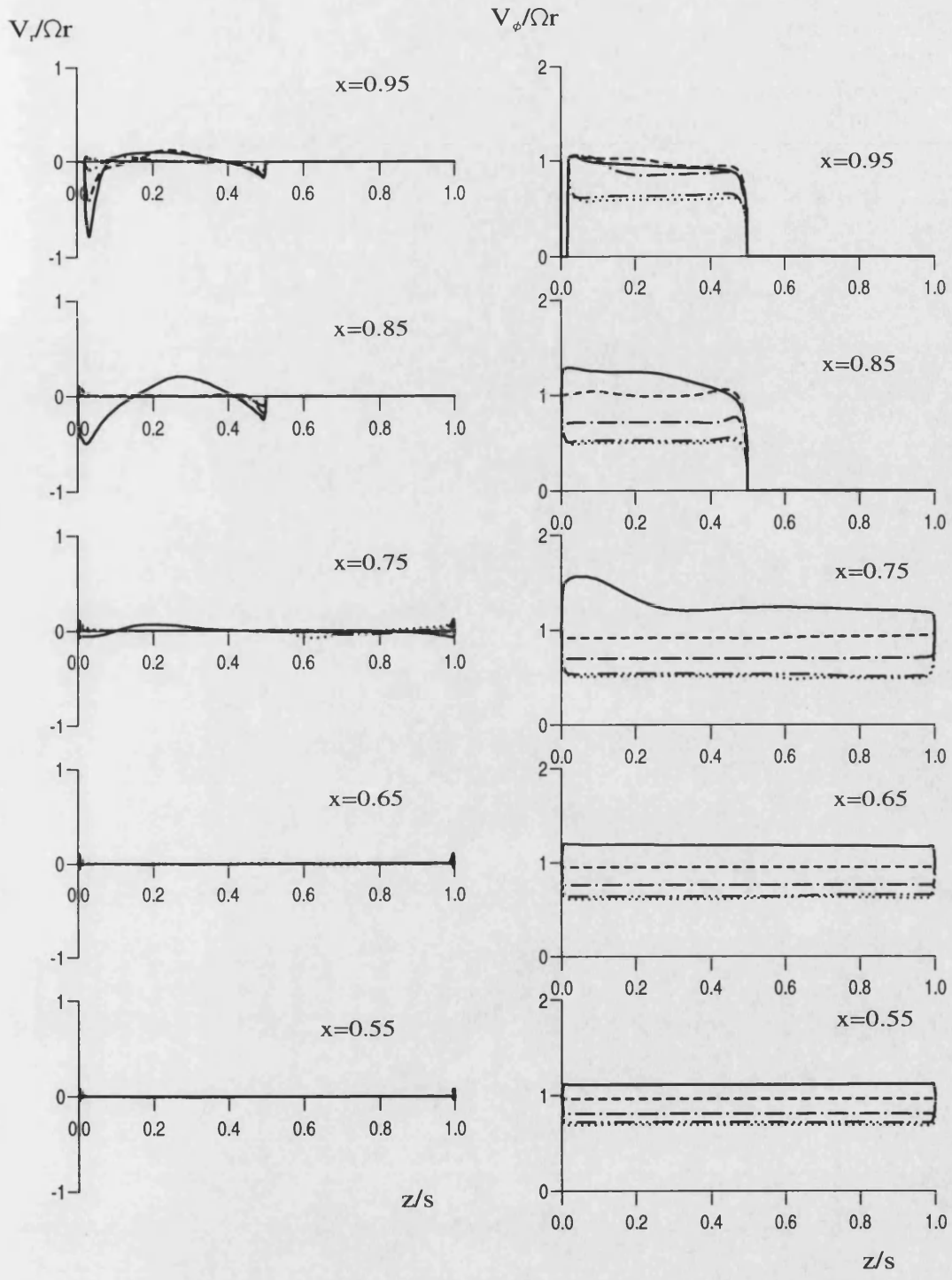

Figure 7.4. Effect of λ_T on axial variation of $V_r/\Omega r$ and $V_\phi/\Omega r$ for rotating cavity with stepped-shroud: $\Gamma = 1$.

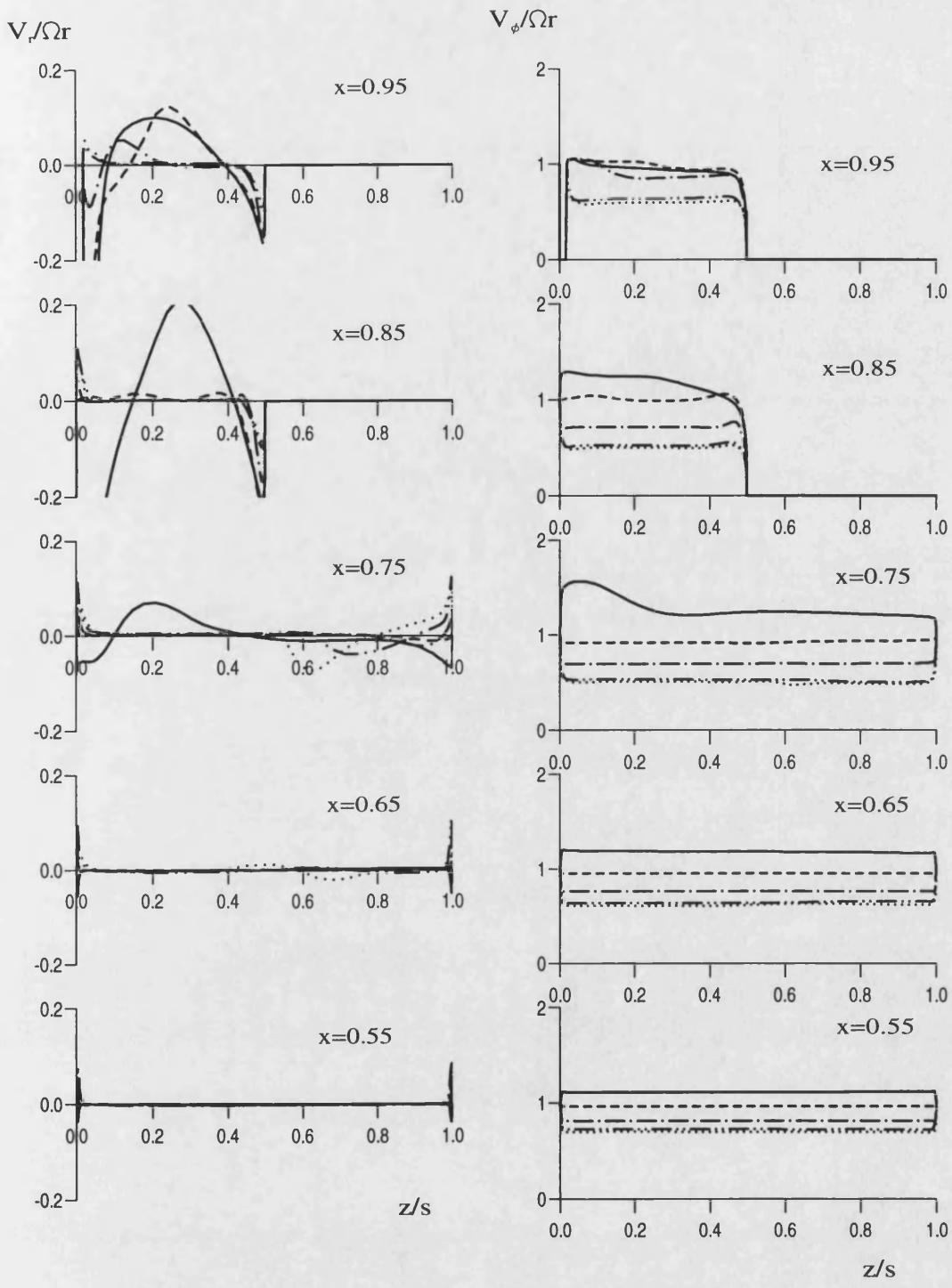

Figure 7.5. Effect of λ_T on axial variation of $V_r/\Omega r$ and $V_\phi/\Omega r$ for rotating cavity with stepped-shroud: $\Gamma = 1$.

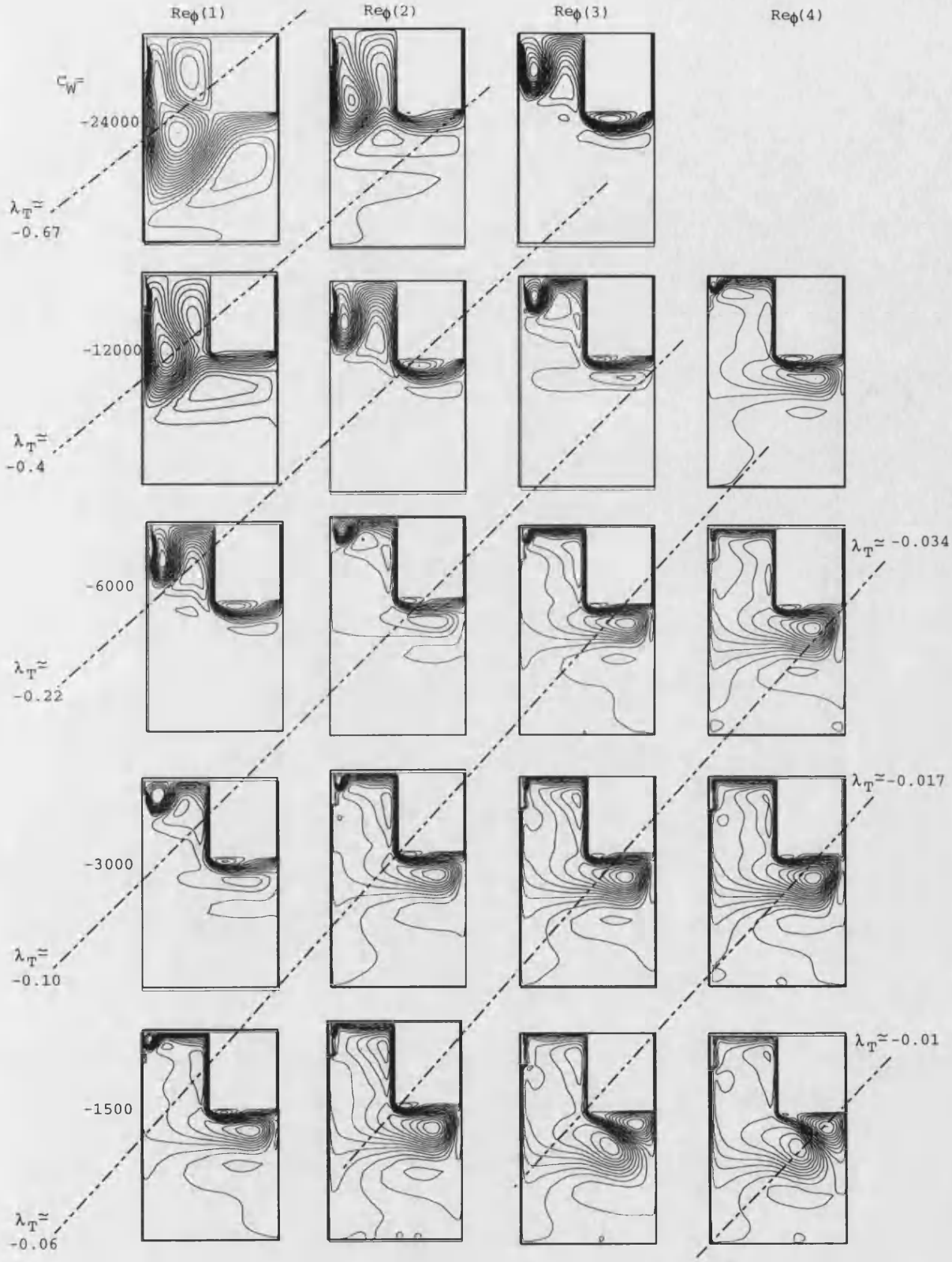

Figure 7.6. Effect of Re_ϕ , C_W and λ_T on the computed streamlines for peripheral flow with stepped shroud: $\Gamma = 0$

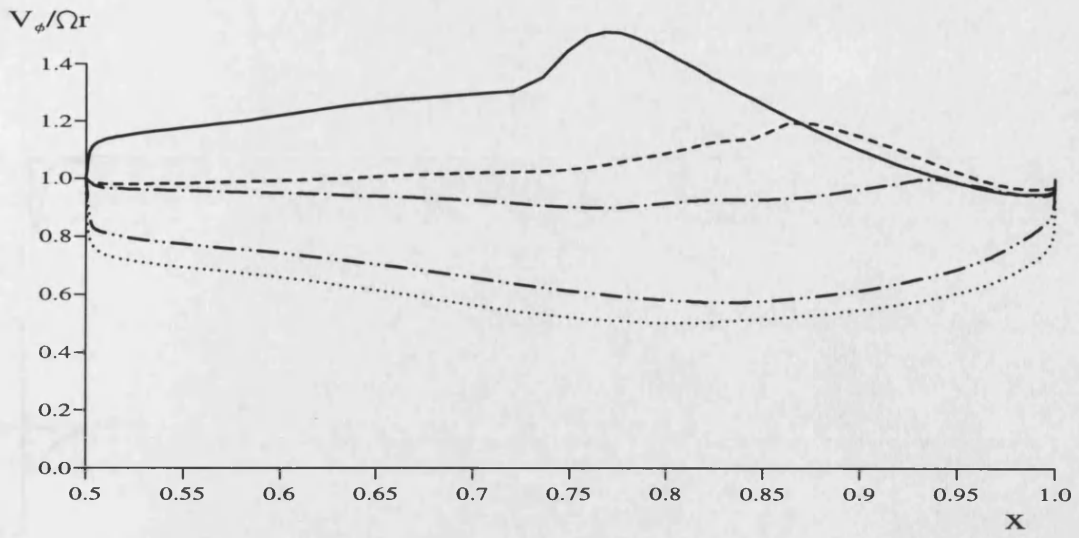

a) Variation of $V_\phi/\Omega r$ with x

$\lambda_T = -0.4$

$\lambda_T = -0.22$

$\lambda_T = -0.10$

$\lambda_T = -0.034$

$\lambda_T = -0.010$

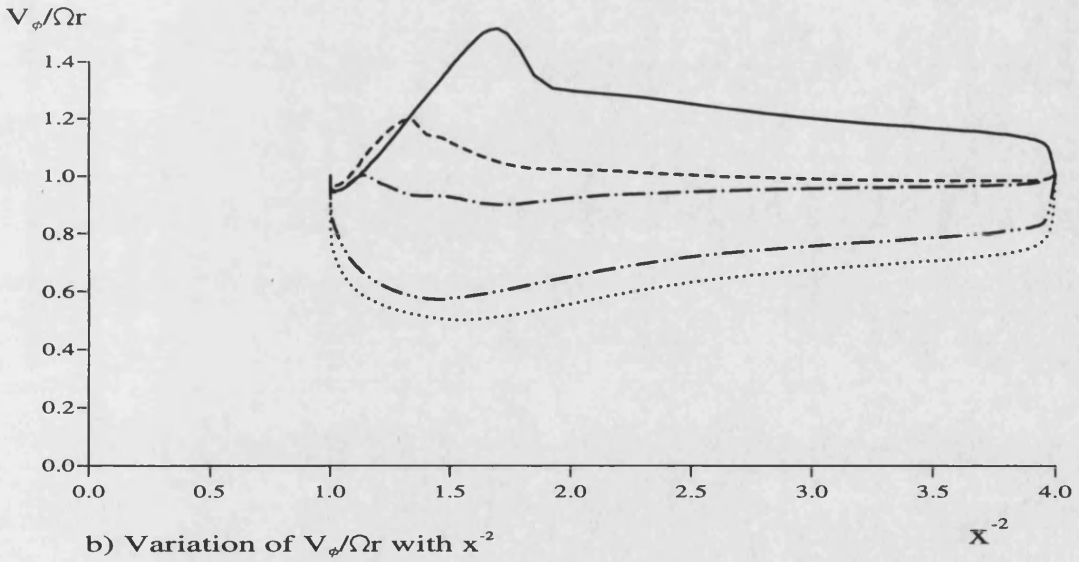

b) Variation of $V_\phi/\Omega r$ with x^{-2}

Figure 7.7. Effect of λ_T on variation of $V_\phi/\Omega r$ with x and x^{-2} for rotating cavity with stepped-shroud: $\Gamma = 0$.

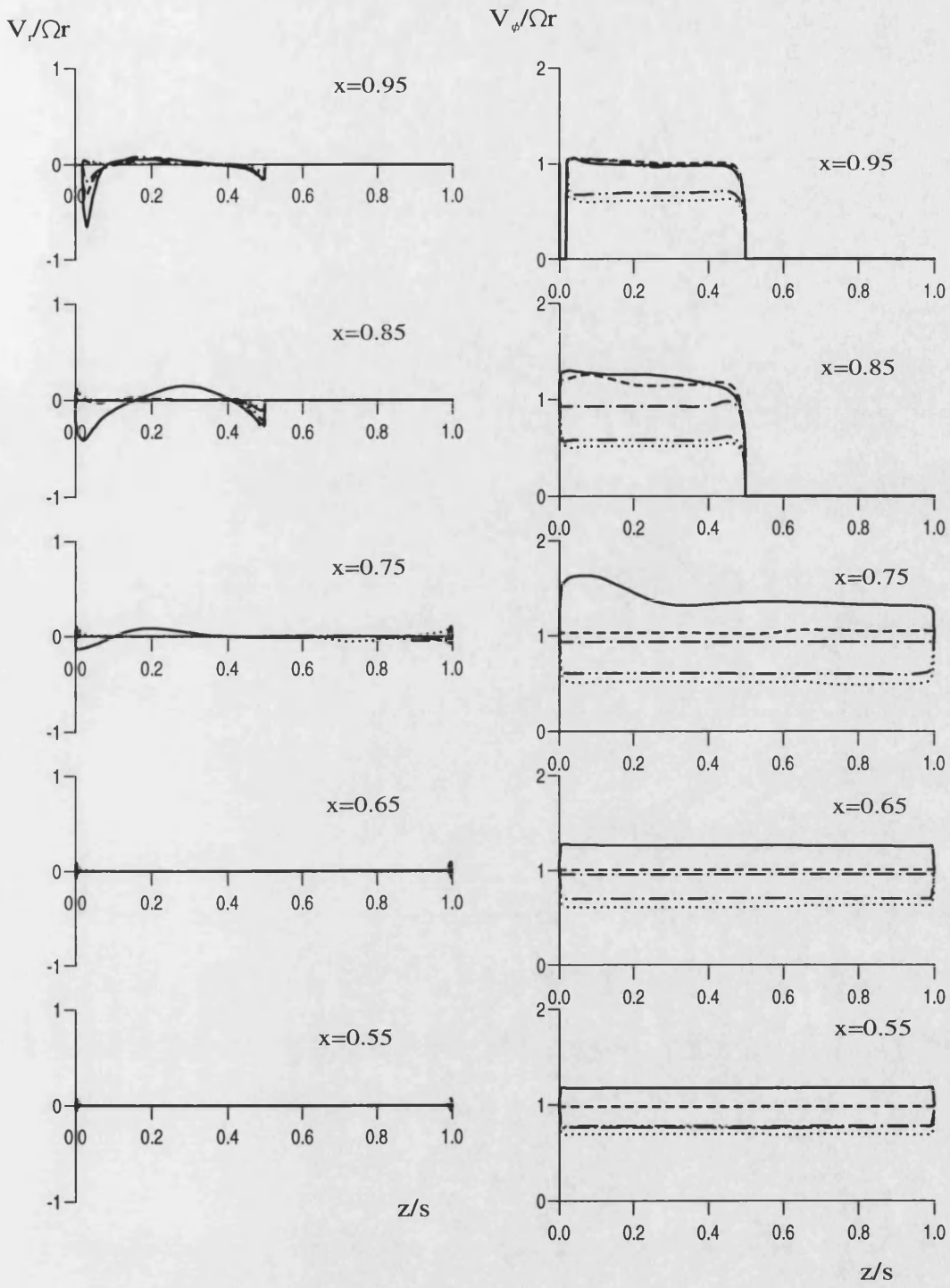

Figure 7.8. Effect of λ_T on axial variation of $V_r/\Omega r$ and $V_\phi/\Omega r$ for rotating cavity with stepped-shroud: $\Gamma = 0$.

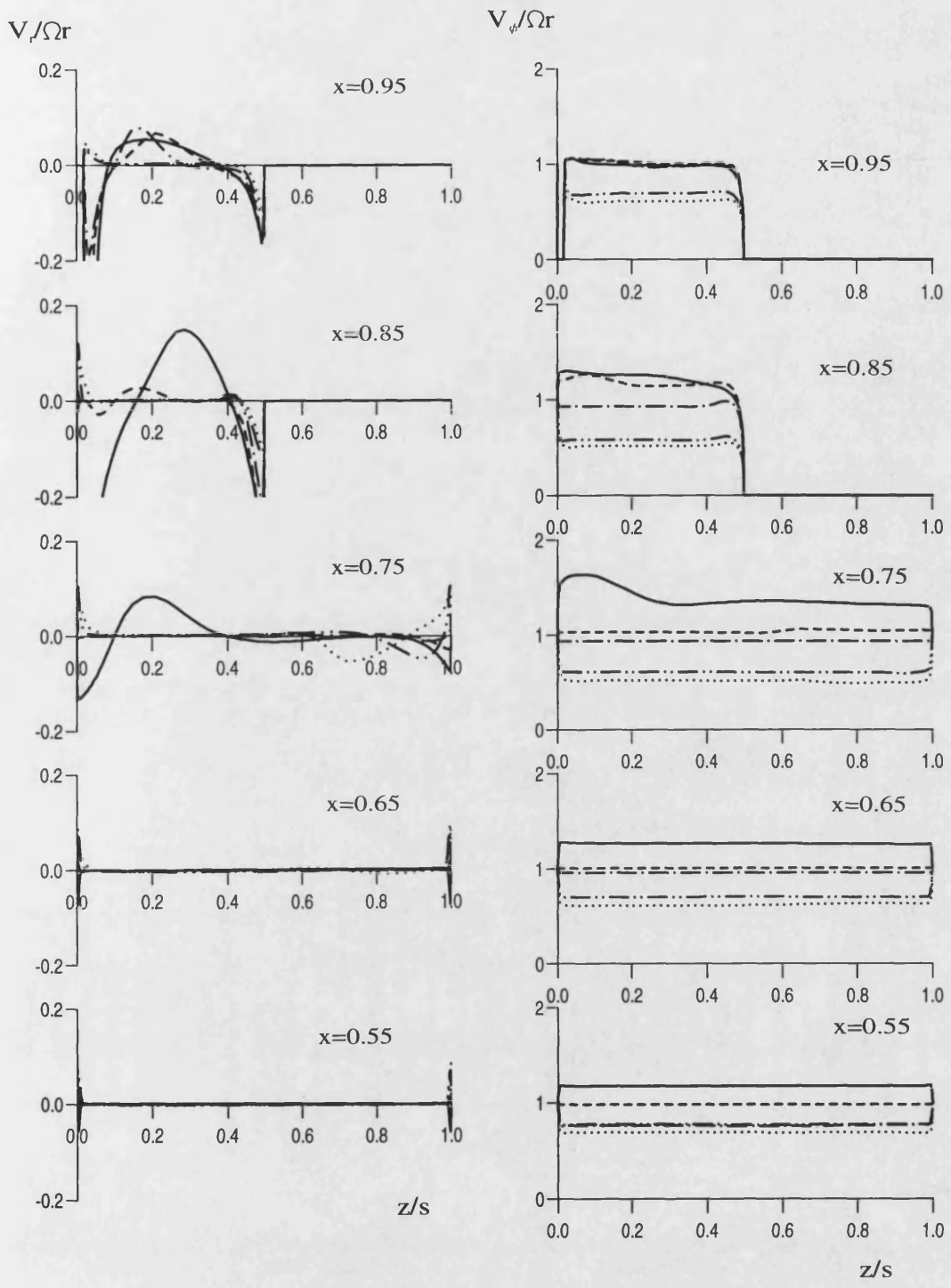

Figure 7.9. Effect of λ_T on axial variation of $V_r/\Omega r$ and $V_\phi/\Omega r$ for rotating cavity with stepped-shroud: $\Gamma = 0$.

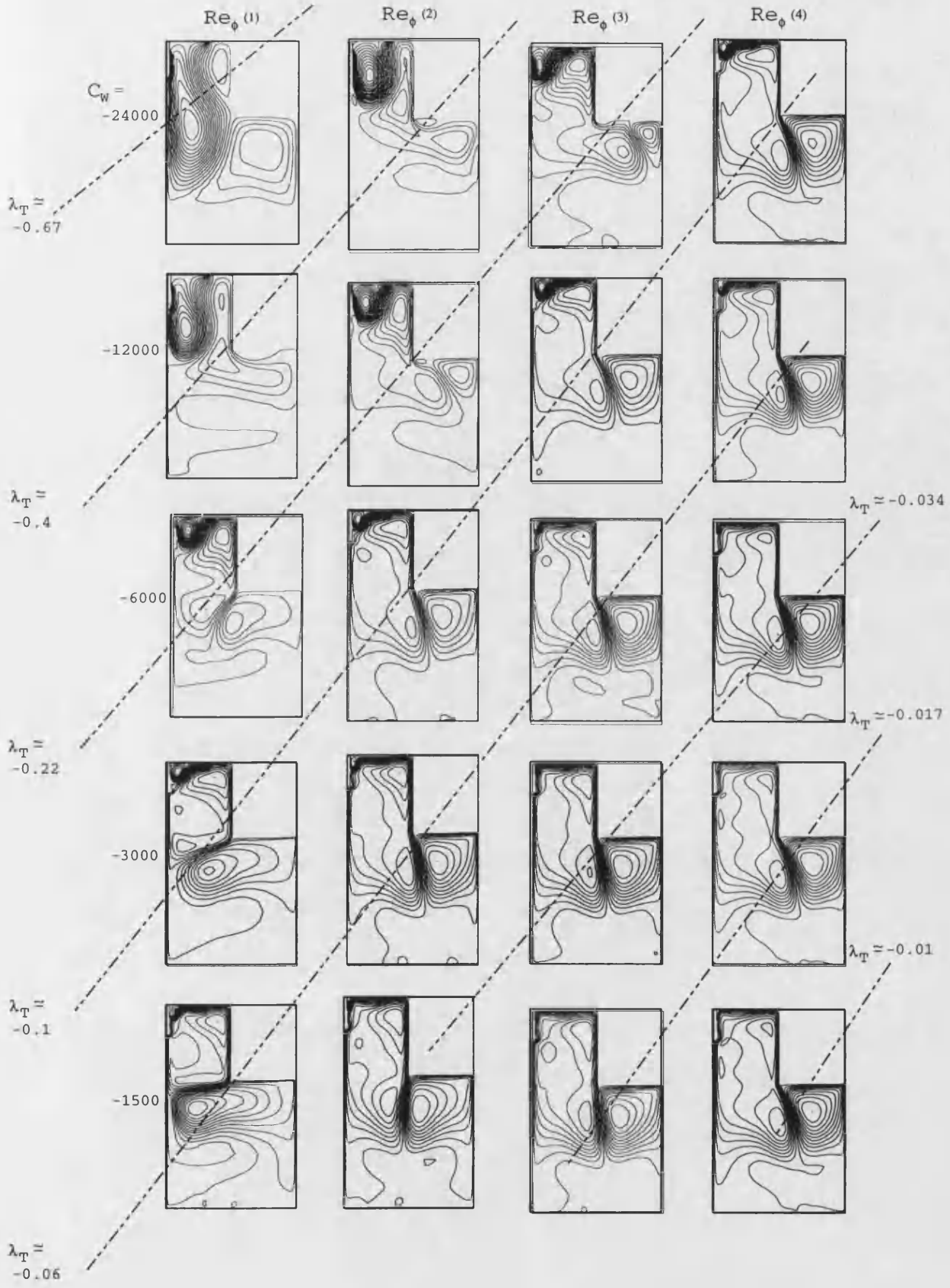

Figure 7.10. Effect of Re_ϕ , C_W and λ_T on the computed streamlines for peripheral flow with stepped shroud: $\Gamma \to \infty$

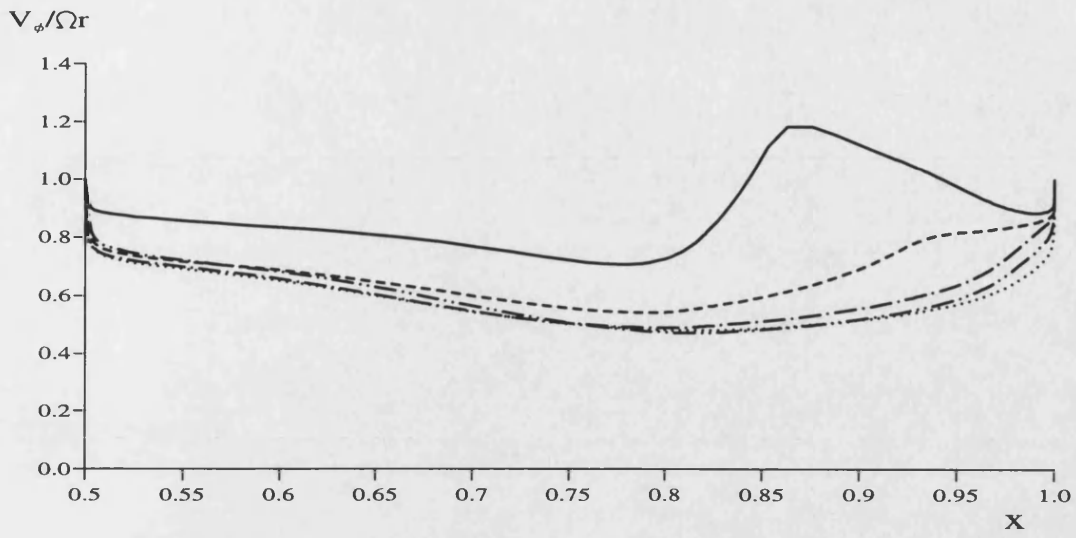

a) Variation of $V_\phi/\Omega r$ with x

$\lambda_T = -0.4$

$\lambda_T = -0.22$

$\lambda_T = -0.10$

$\lambda_T = -0.034$

$\lambda_T = -0.01$

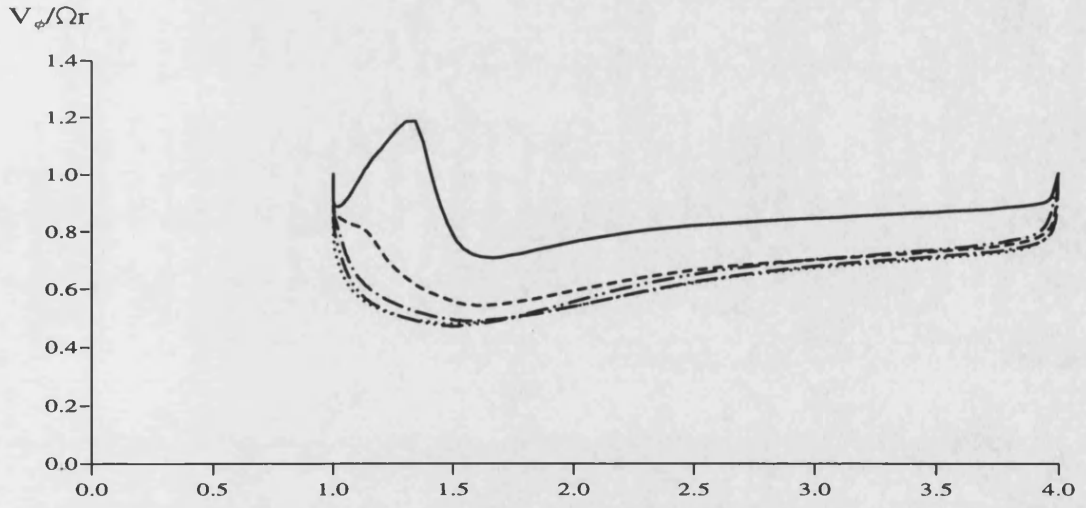

b) Variation of $V_\phi/\Omega r$ with x^{-2}

Figure 7.11. Effect of λ_T on variation of $V_\phi/\Omega r$ with x and x^{-2} for rotating cavity with stepped-shroud: $\Gamma \to \infty$

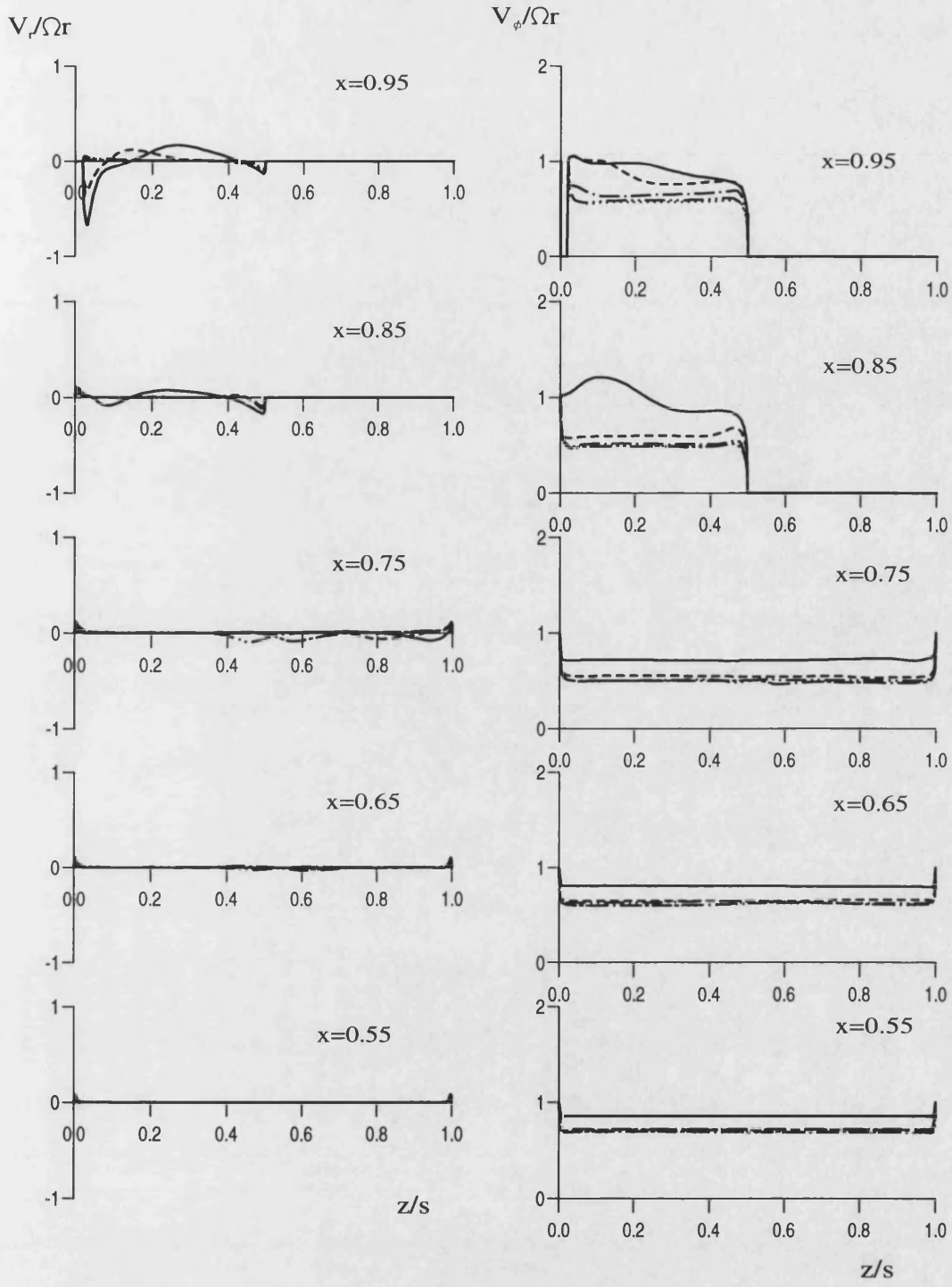

Figure 7.12. Effect of λ_T on axial variation of $V_r/\Omega r$ and $V_\phi/\Omega r$ for rotating cavity with stepped-shroud: $\Gamma \rightarrow \infty$

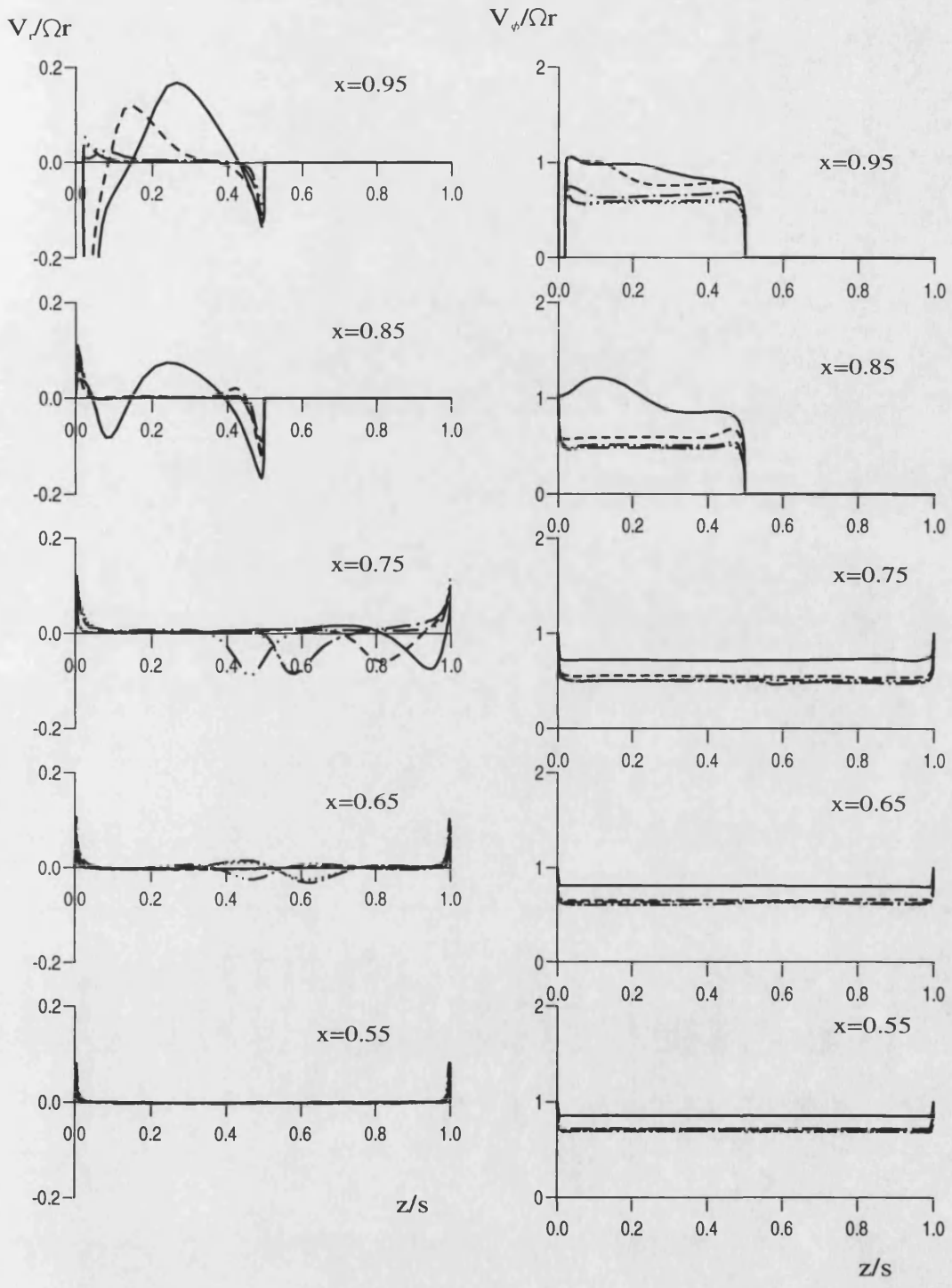

Figure 7.13 Effect of λ_T on axial variation of $V_r/\Omega r$ and $V_\phi/\Omega r$ for rotating cavity with stepped-shroud: $\Gamma \rightarrow \infty$

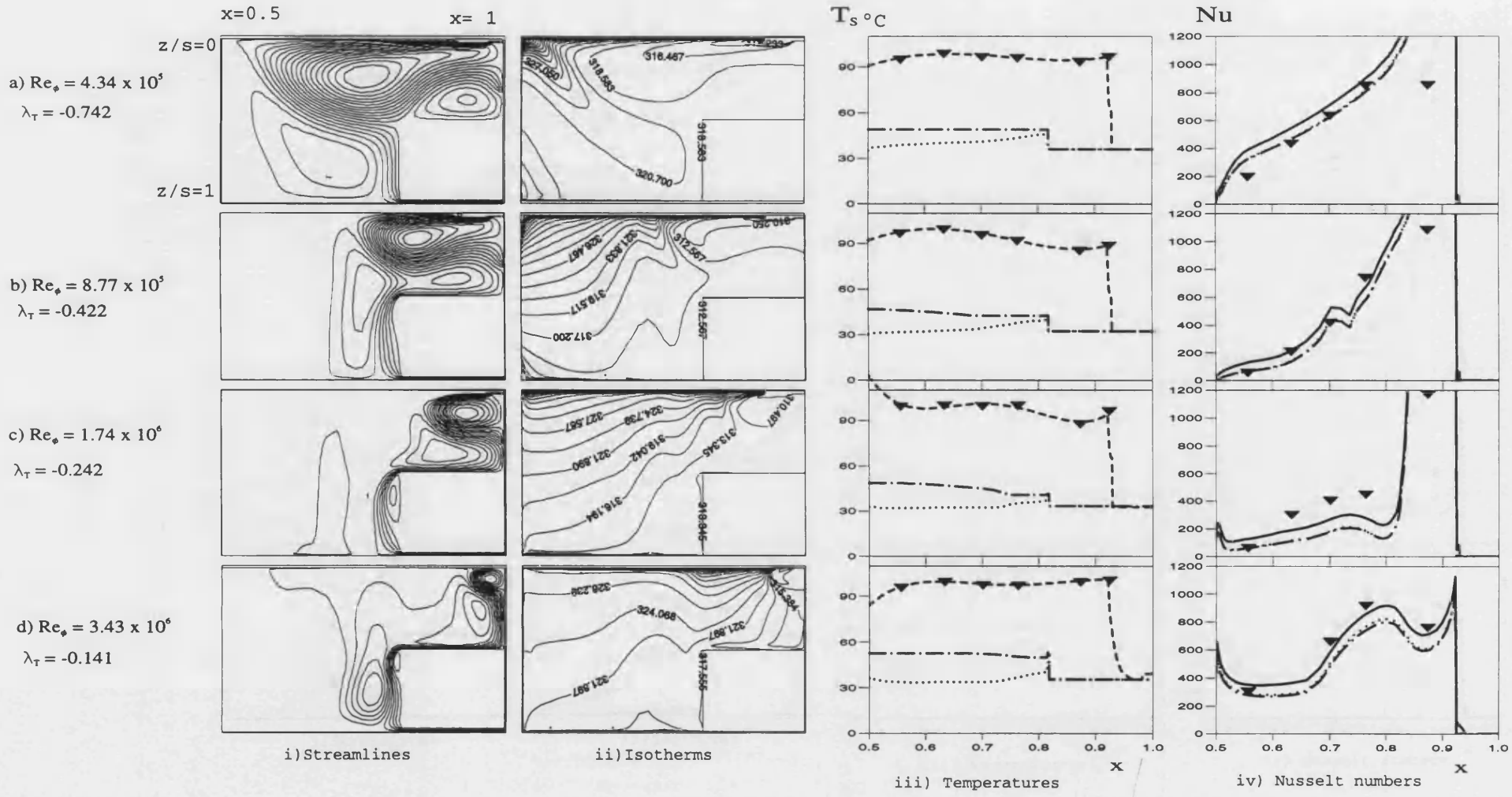

Figure 7.14. Comparison between computed and measured temperatures and Nusselt numbers for rotating cavity with stepped-shroud: $\Gamma = 1$ and $C_w = -24000$

▼ Measured temperatures and Nusselt numbers on the heated disc — — — Fitted temperature on the heated disc

{ Computed temperature on the unheated disc; Computed Nusselt numbers on the heated disc } for { —·— adiabatic-disc assumption ····· conducting-disc assumption }

——— Computed Nusselt numbers on the heated disc: conducting-disc assumption with radiation correction

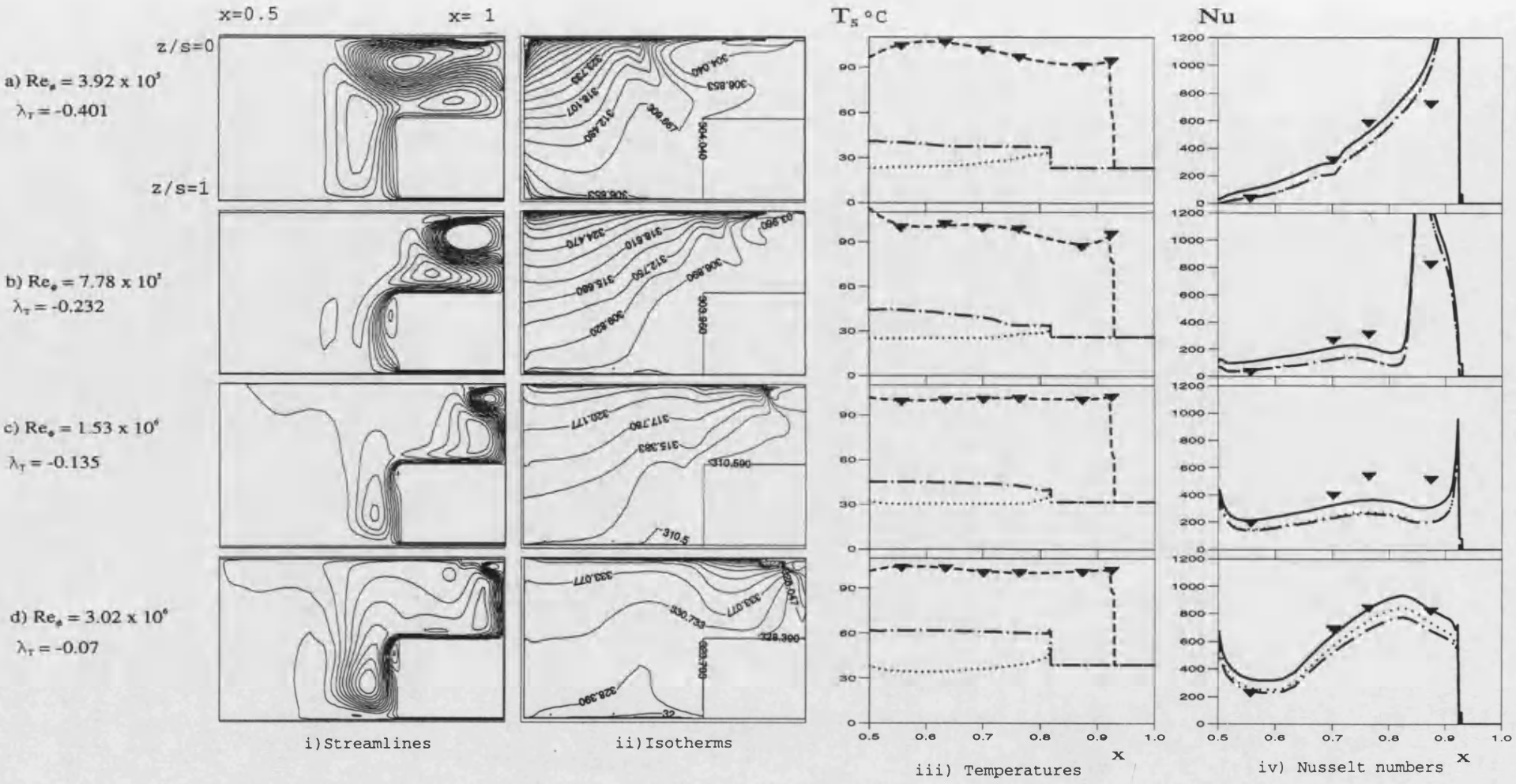

Figure 7.15. Comparison between computed and measured temperatures and Nusselt numbers for rotating cavity with stepped-shroud: $\Gamma = 1$ and $C_w = -12000$

▼ Measured temperatures and Nusselt numbers on the heated disc — — — Fitted temperature on the heated disc

{ Computed temperature on the unheated disc; Computed Nusselt numbers on the heated disc } for { —·— adiabatic-disc assumption ····· conducting-disc assumption }

——— Computed Nusselt numbers on the heated disc: conducting-disc assumption with radiation correction

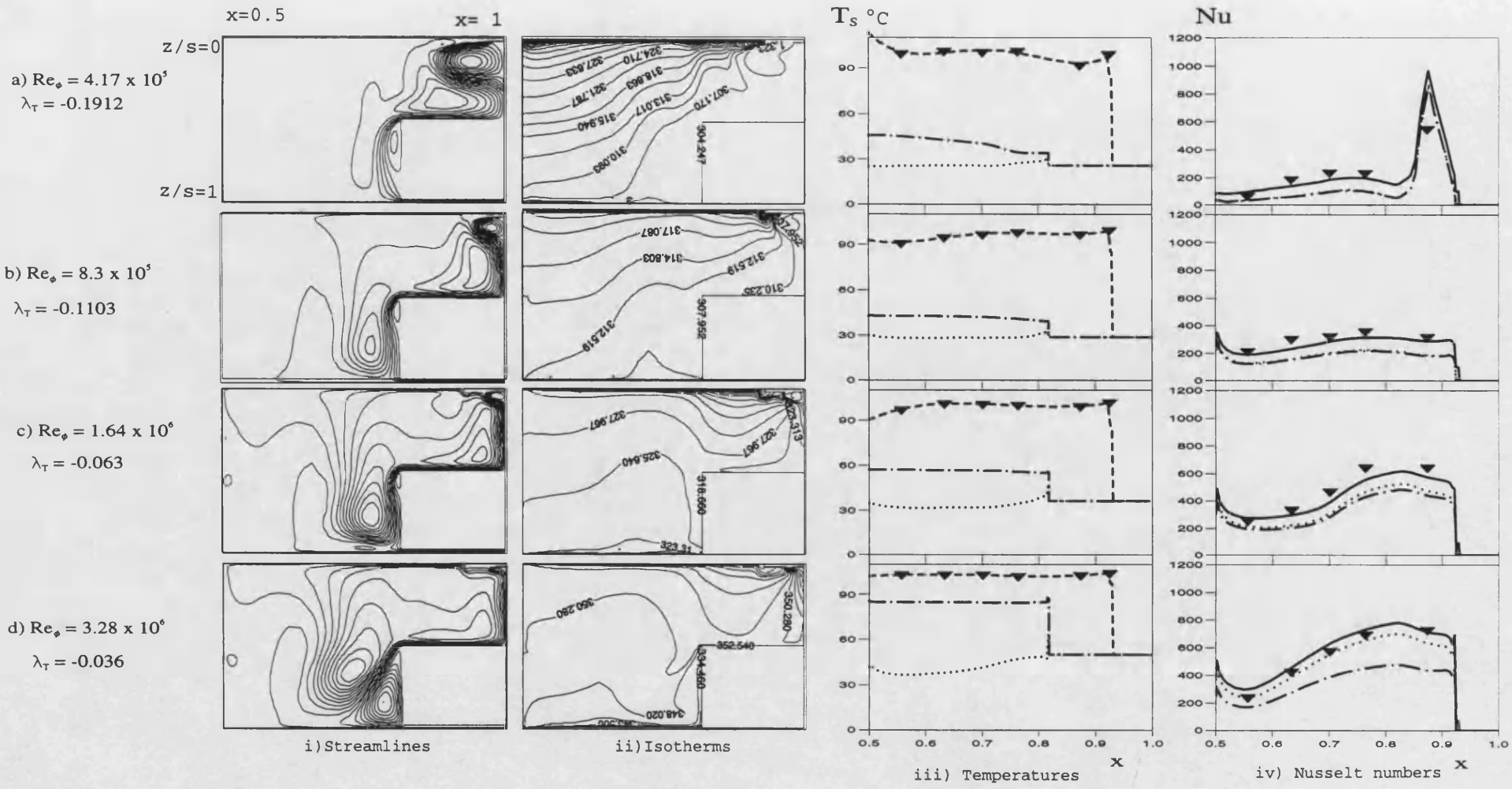

Figure 7.16. Comparison between computed and measured temperatures and Nusselt numbers for rotating cavity with stepped-shroud: $\Gamma = 1$ and $C_w = -6000$

▼ Measured temperatures and Nusselt numbers on the heated disc — — — Fitted temperature on the heated disc

{ Computed temperature on the unheated disc; Computed Nusselt numbers on the heated disc } for { —·— adiabatic-disc assumption ····· conducting-disc assumption }

——— Computed Nusselt numbers on the heated disc: conducting-disc assumption with radiation correction

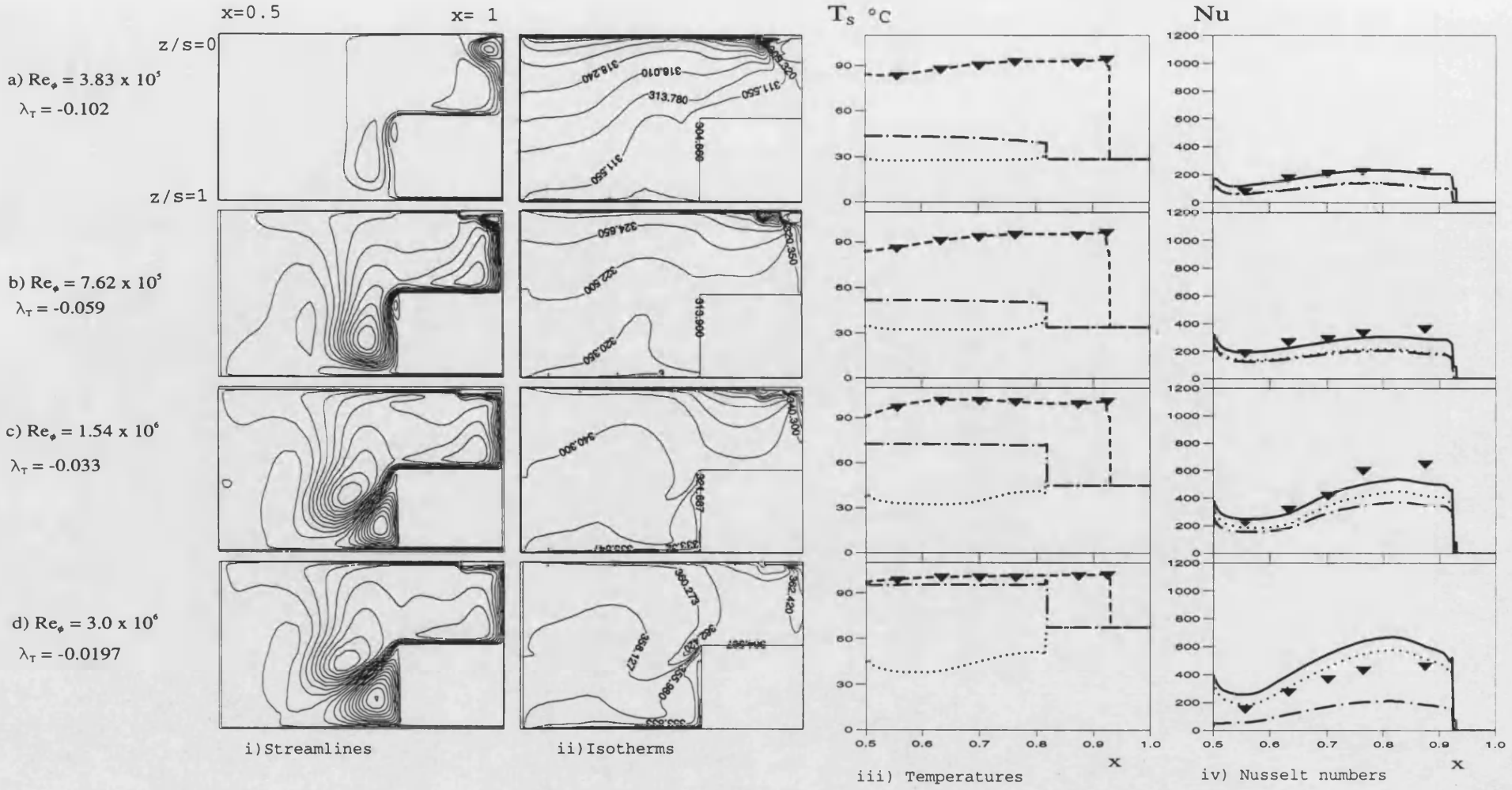

Figure 7.17. Comparison between computed and measured temperatures and Nusselt numbers for rotating cavity with stepped-shroud: $\Gamma = 1$ and $C_w = -3000$

▼ Measured temperatures and Nusselt numbers on the heated disc — — — Fitted temperature on the heated disc

{ Computed temperature on the unheated disc; Computed Nusselt numbers on the heated disc } for { —·— adiabatic-disc assumption ····· conducting-disc assumption }

——— Computed Nusselt numbers on the heated disc: conducting-disc assumption with radiation correction

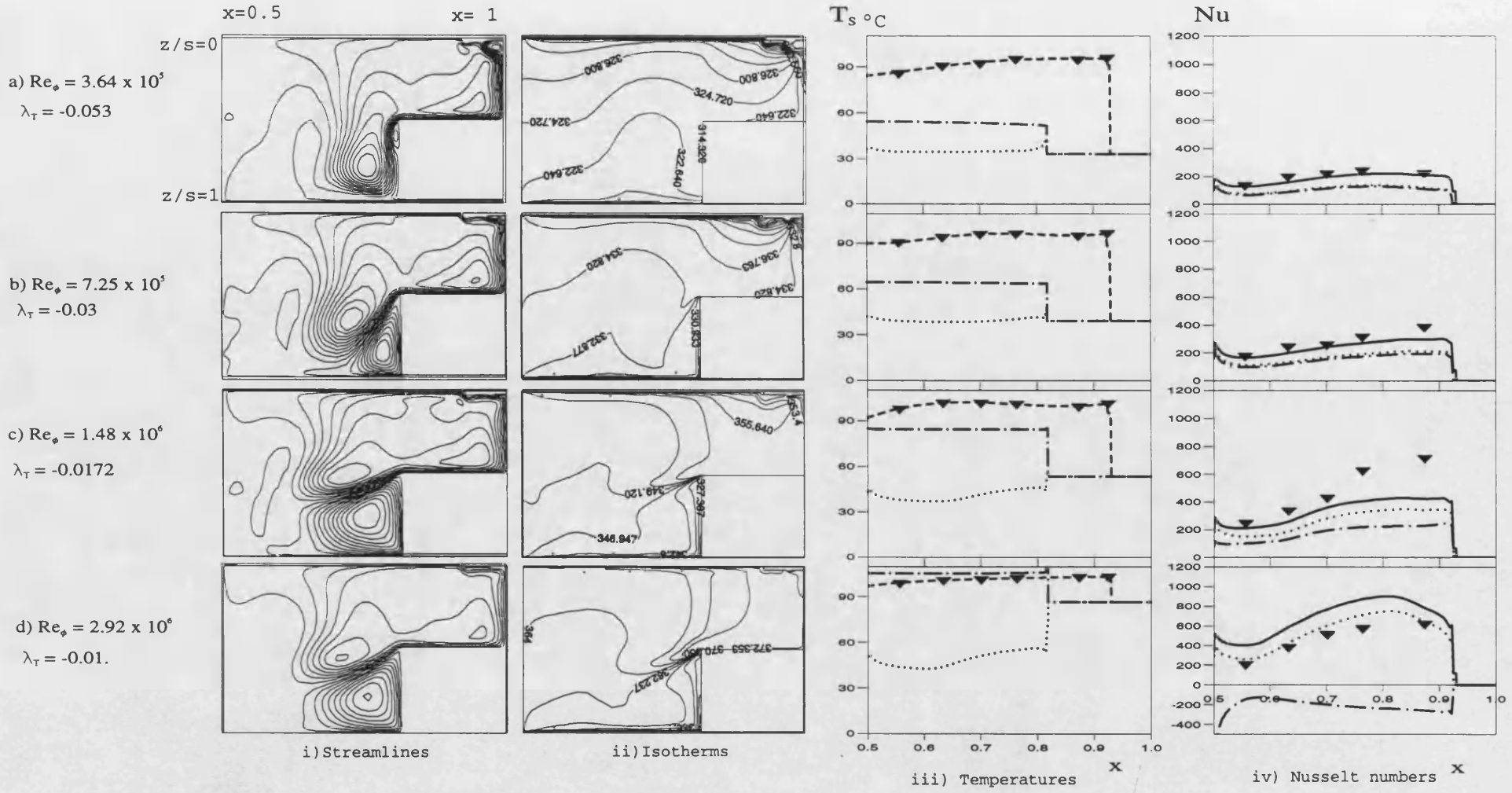

Figure 7.18. Comparison between computed and measured temperatures and Nusselt numbers for rotating cavity with stepped-shroud: $\Gamma = 1$ and C_w= -1500

▼ Measured temperatures and Nusselt numbers on the heated disc — — — Fitted temperature on the heated disc

{ Computed temperature on the unheated disc; Computed Nusselt numbers on the heated disc } for { —·— adiabatic-disc assumption ····· conducting-disc assumption }

——— Computed Nusselt numbers on the heated disc: conducting-disc assumption with radiation correction

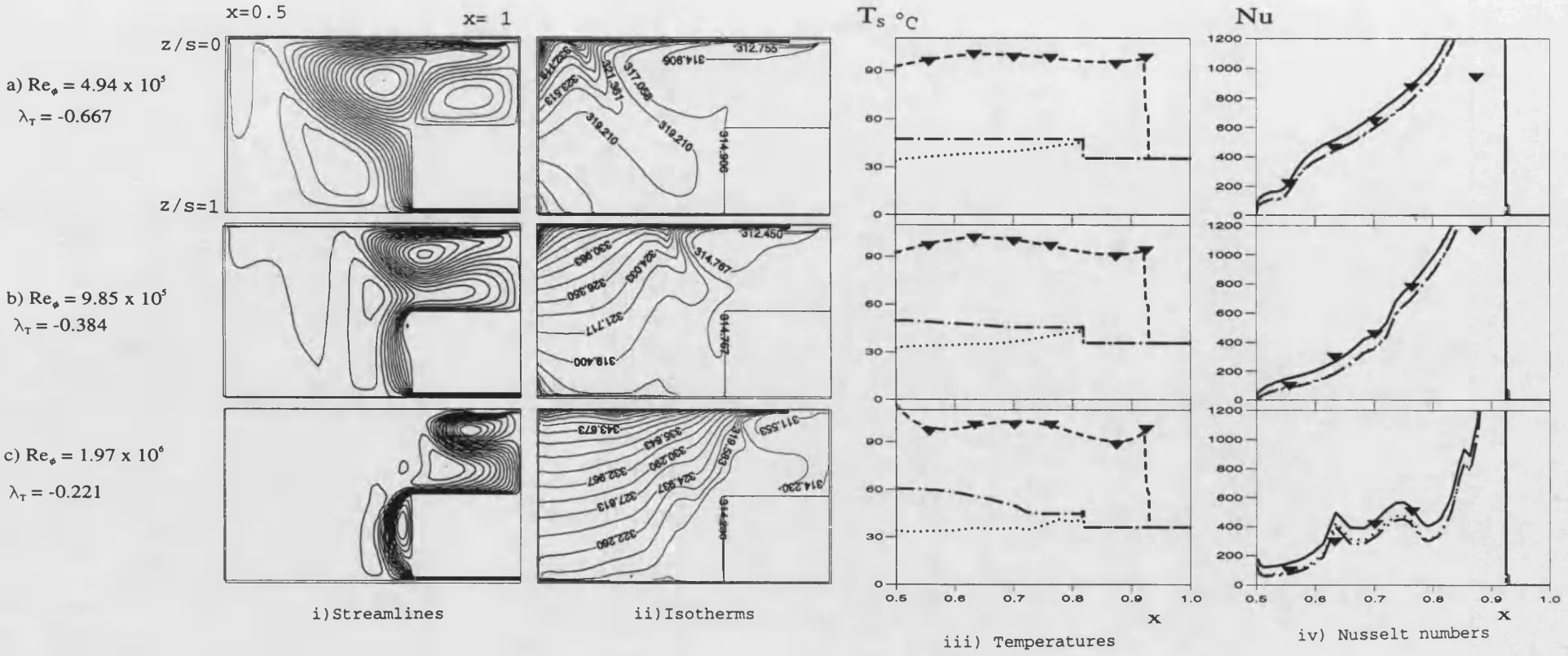

Figure 7.19. Comparison between computed and measured temperatures and Nusselt numbers for rotating cavity with stepped-shroud: $\Gamma = 0$ and $C_w = -24000$

▼ Measured temperatures and Nusselt numbers on the heated disc — — — Fitted temperature on the heated disc

{ Computed temperature on the unheated disc; Computed Nusselt numbers on the heated disc } for { —·— adiabatic-disc assumption ····· conducting-disc assumption }

——— Computed Nusselt numbers on the heated disc: conducting-disc assumption with radiation correction

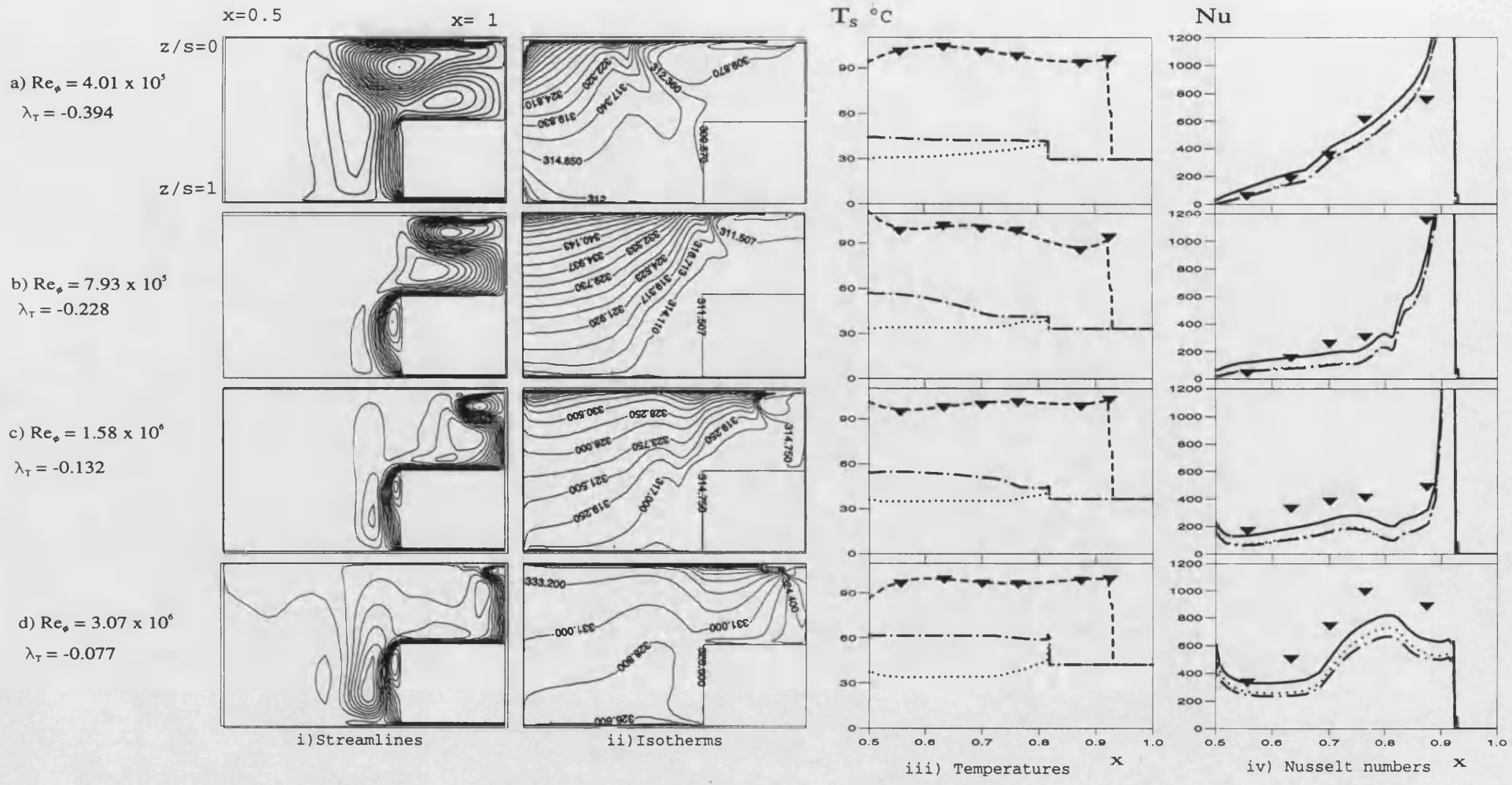

Figure 7.20. Comparison between computed and measured temperatures and Nusselt numbers for rotating cavity with stepped-shroud: $\Gamma = 0$ and C_w = -12000

▼ Measured temperatures and Nusselt numbers on the heated disc — — — Fitted temperature on the heated disc

{ Computed temperature on the unheated disc; Computed Nusselt numbers on the heated disc } for { —·— adiabatic-disc assumption ····· conducting-disc assumption }

——— Computed Nusselt numbers on the heated disc: conducting-disc assumption with radiation correction

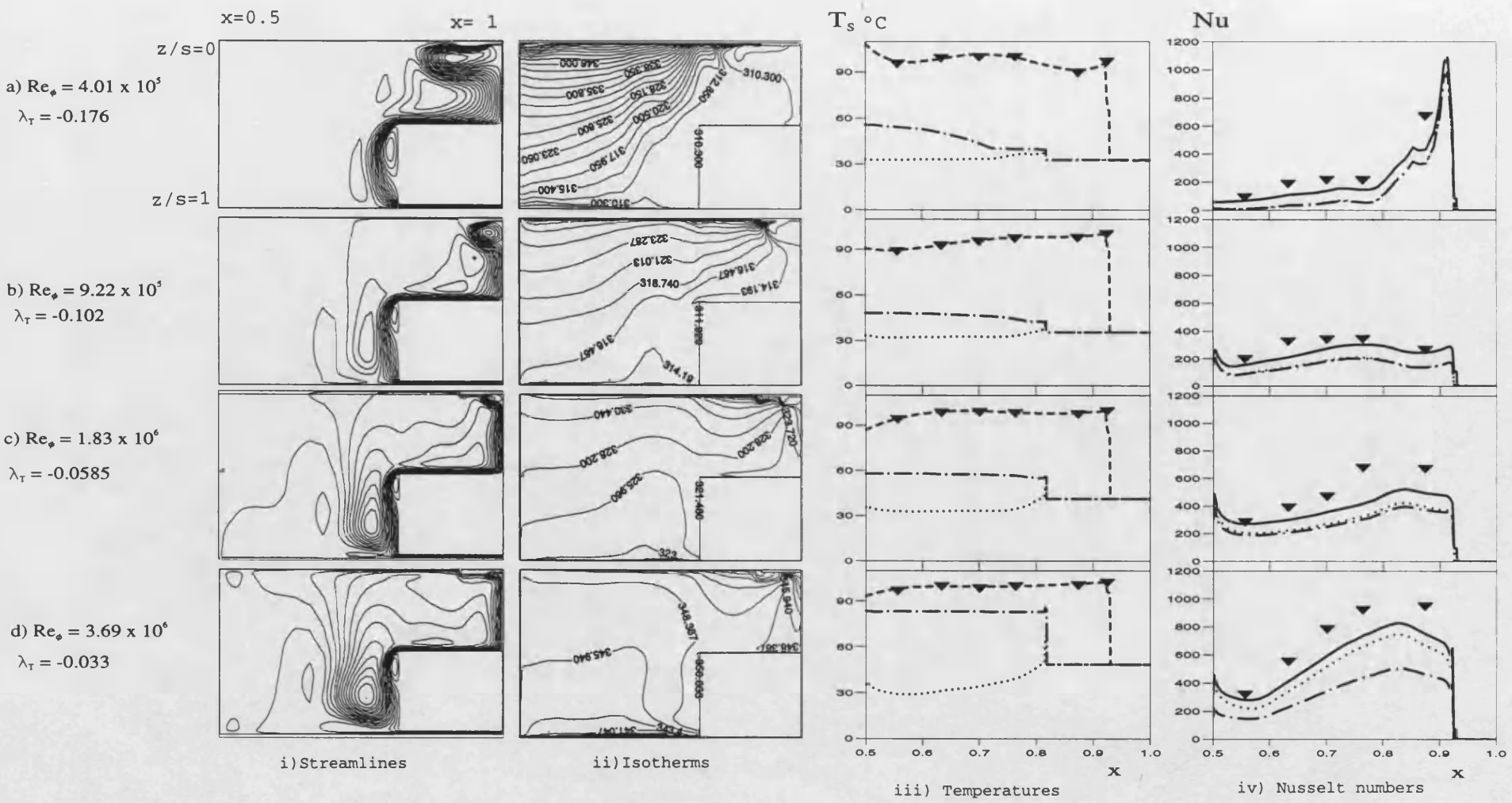

Figure 7.21. Comparison between computed and measured temperatures and Nusselt numbers for rotating cavity with stepped-shroud: $\Gamma = 0$ and C_w= -6000

▼ Measured temperatures and Nusselt numbers on the heated disc ——— Fitted temperature on the heated disc

{ Computed temperature on the unheated disc; Computed Nusselt numbers on the heated disc } for { —·— adiabatic-disc assumption ····· conducting-disc assumption }

——— Computed Nusselt numbers on the heated disc: conducting-disc assumption with radiation correction

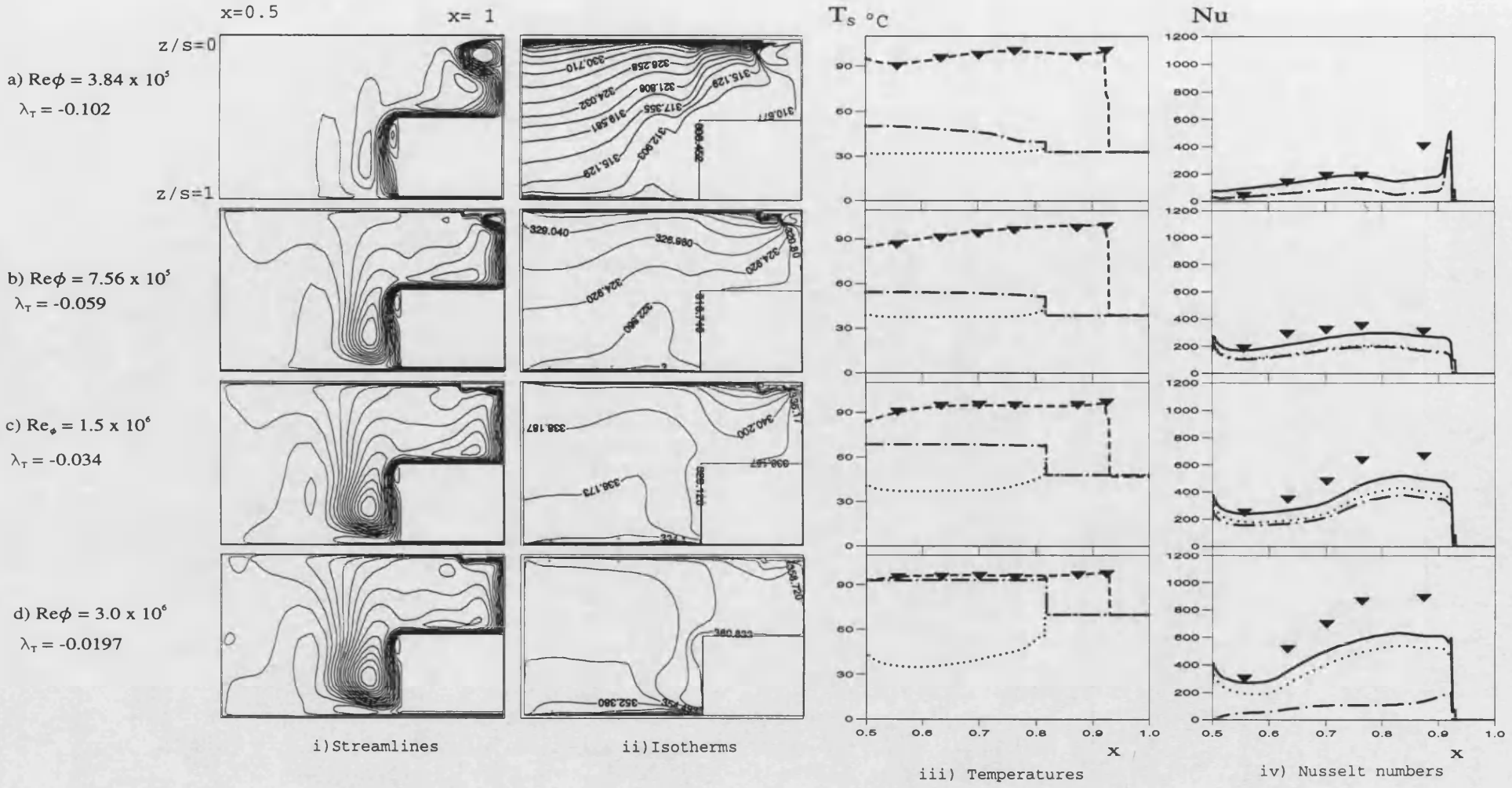

Figure 7.22. Comparison between computed and measured temperatures and Nusselt numbers for rotating cavity with stepped-shroud: $\Gamma = 0$ and $C_w = -3000$

▼ Measured temperatures and Nusselt numbers on the heated disc — — — Fitted temperature on the heated disc

{ Computed temperature on the unheated disc; Computed Nusselt numbers on the heated disc } for { —·— adiabatic-disc assumption ····· conducting-disc assumption }

——— Computed Nusselt numbers on the heated disc: conducting-disc assumption with radiation correction

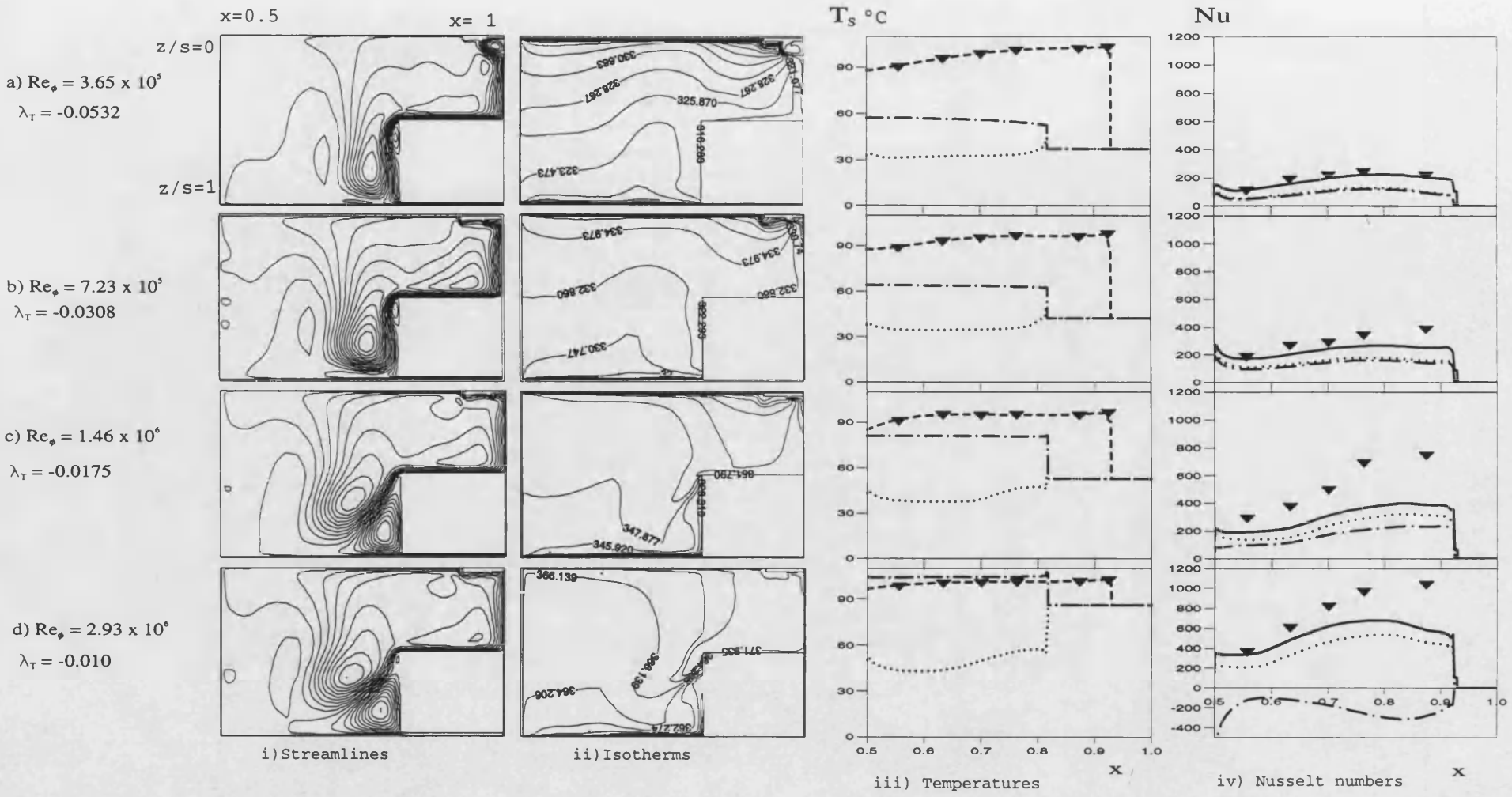

Figure 7.23. Comparison between computed and measured temperatures and Nusselt numbers for rotating cavity with stepped-shroud: $\Gamma = 0$ and C_w= -1500

▼ Measured temperatures and Nusselt numbers on the heated disc — — — Fitted temperature on the heated disc

{ Computed temperature on the unheated disc; Computed Nusselt numbers on the heated disc } for { —·— adiabatic-disc assumption ····· conducting-disc assumption }

——— Computed Nusselt numbers on the heated disc: conducting-disc assumption with radiation correction

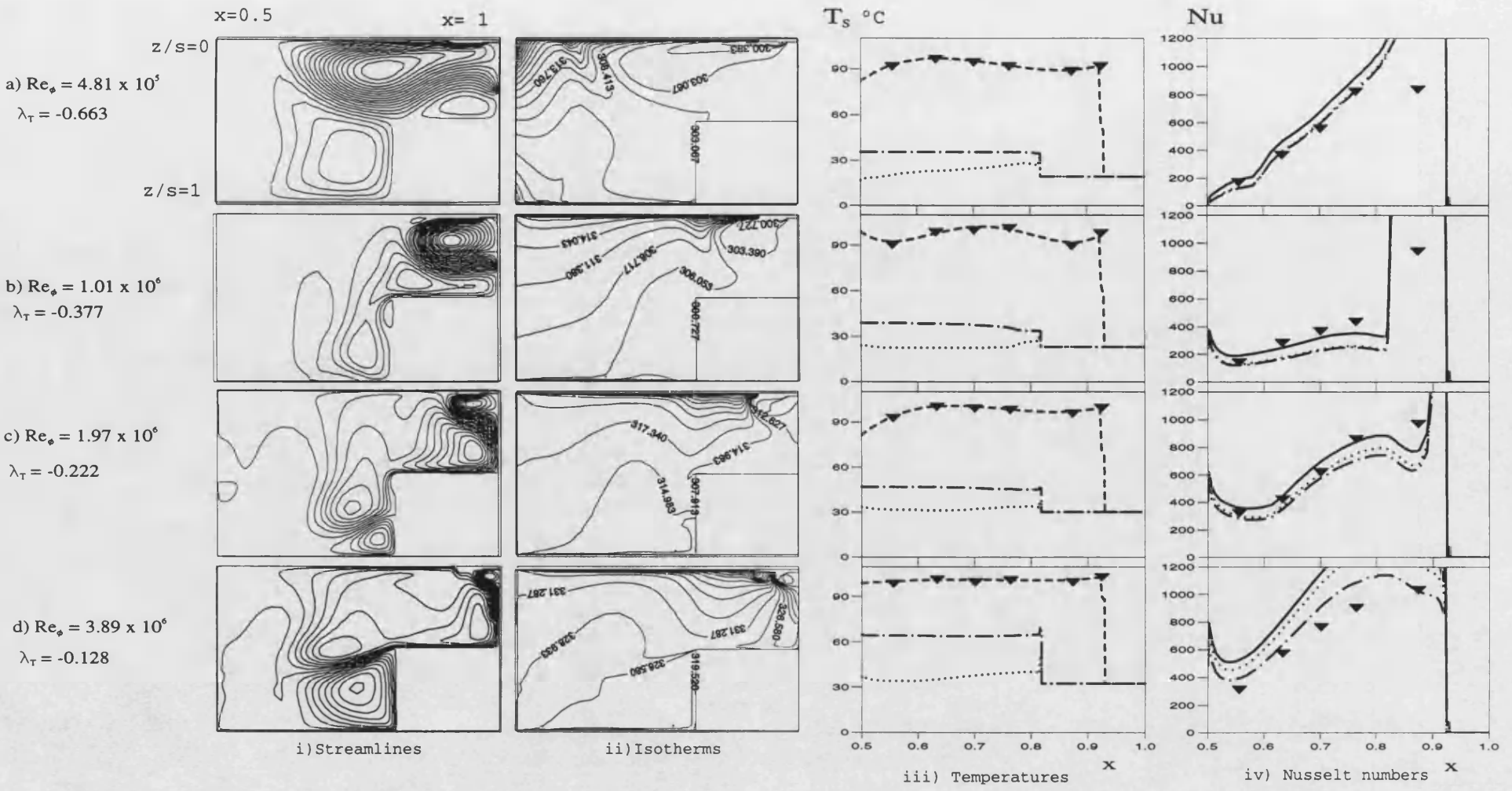

Figure 7.24. Comparison between computed and measured temperatures and Nusselt numbers for rotating cavity with stepped-shroud: $r \to \infty$ and C_w = -24000

▼ Measured temperatures and Nusselt numbers on the heated disc — — — Fitted temperature on the heated disc

{ Computed temperature on the unheated disc; Computed Nusselt numbers on the heated disc } for { —·— adiabatic-disc assumption ····· conducting-disc assumption }

——— Computed Nusselt numbers on the heated disc: conducting-disc assumption with radiation correction

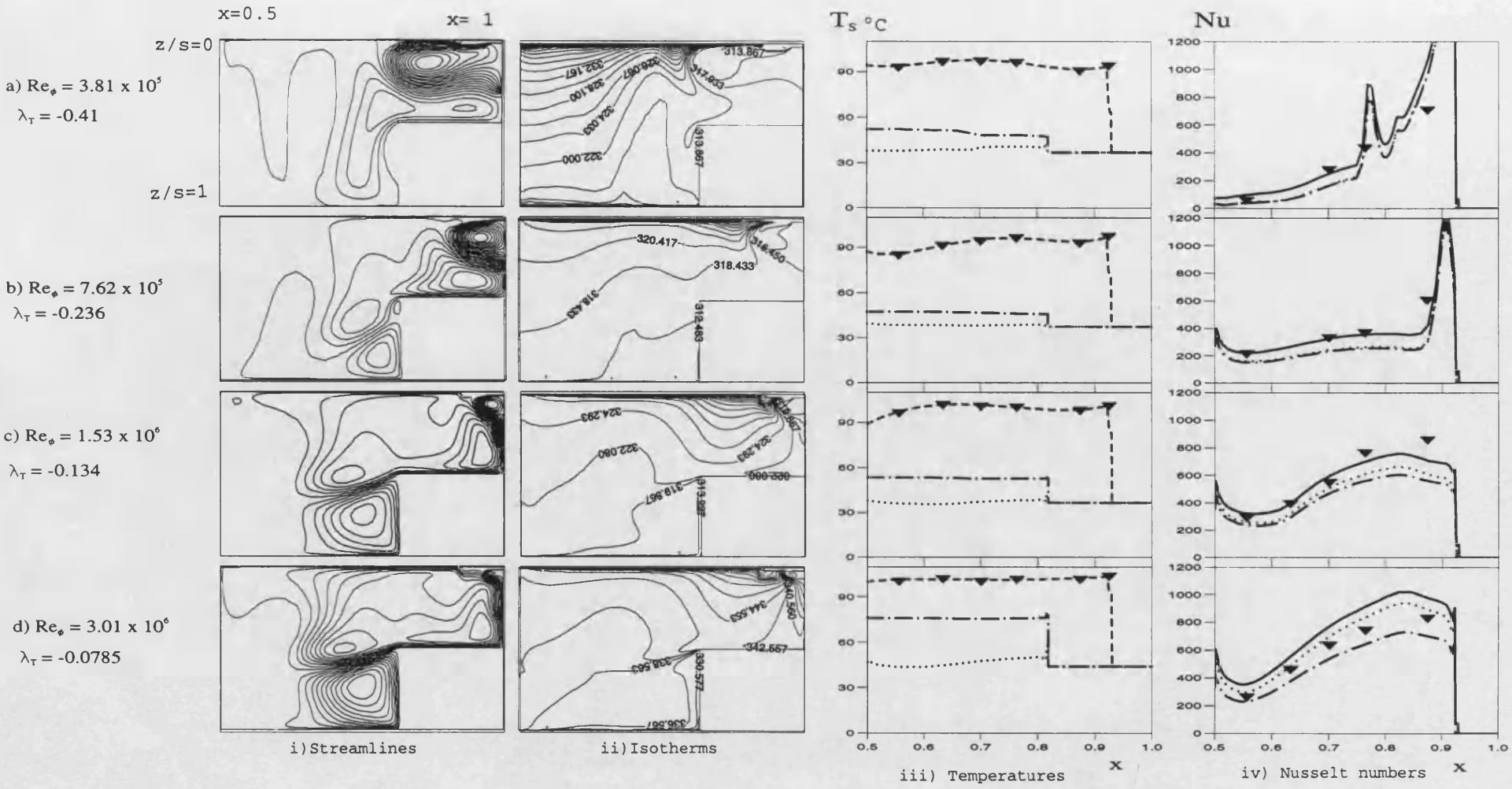

Figure 7.25. Comparison between computed and measured temperatures and Nusselt numbers for rotating cavity with stepped-shroud: $\Gamma \to \infty$ and $C_w = -12000$

▼ Measured temperatures and Nusselt numbers on the heated disc ——— Fitted temperature on the heated disc

{ Computed temperature on the unheated disc; Computed Nusselt numbers on the heated disc } for { —·— adiabatic-disc assumption ····· conducting-disc assumption }

——— Computed Nusselt numbers on the heated disc: conducting-disc assumption with radiation correction

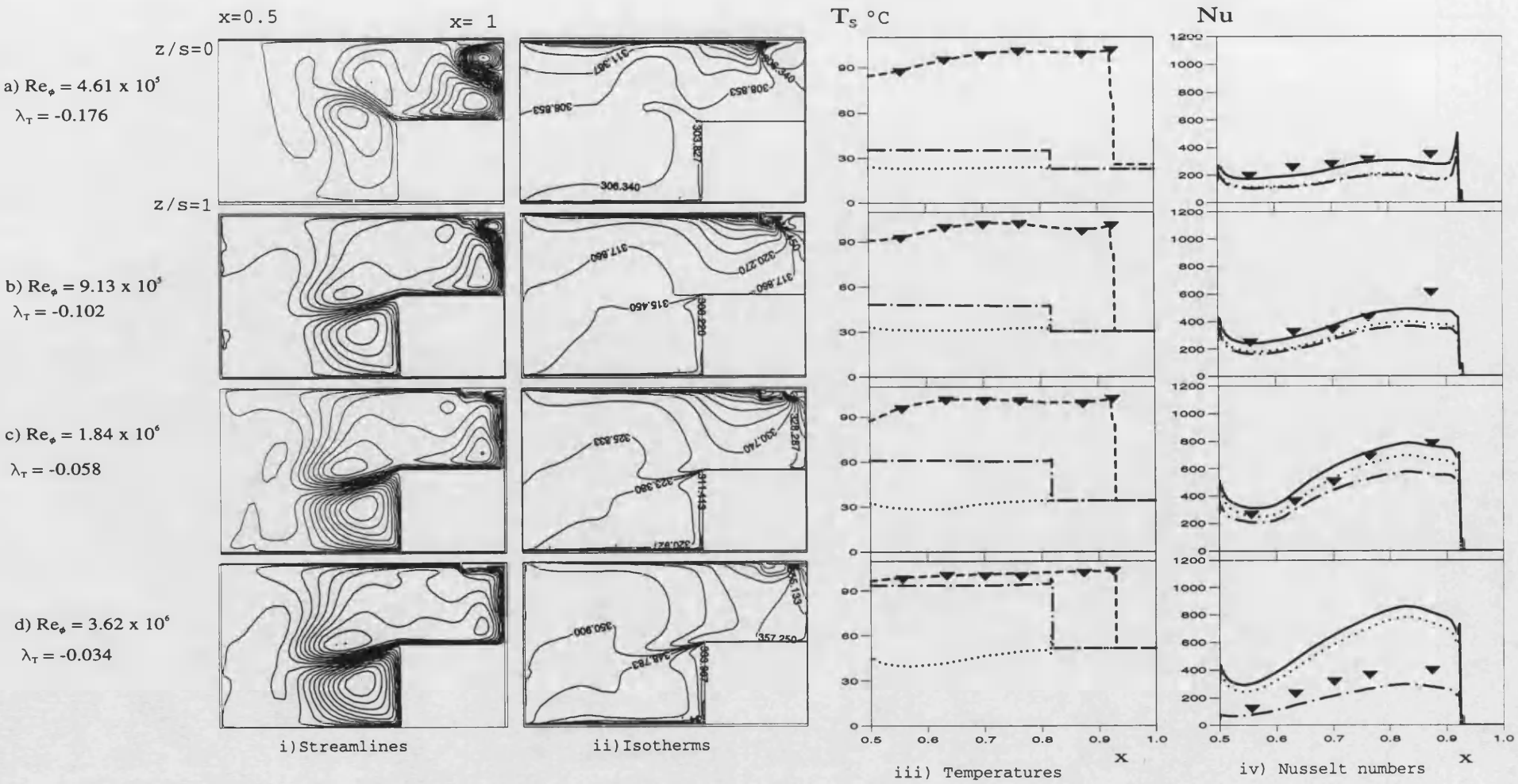

Figure 7.26. Comparison between computed and measured temperatures and Nusselt numbers for rotating cavity with stepped-shroud: $P \to \infty$ and $C_w = -6000$

▼ Measured temperatures and Nusselt numbers on the heated disc — — — Fitted temperature on the heated disc

{ Computed temperature on the unheated disc; Computed Nusselt numbers on the heated disc } for { —·— adiabatic-disc assumption ····· conducting-disc assumption }

——— Computed Nusselt numbers on the heated disc: conducting-disc assumption with radiation correction

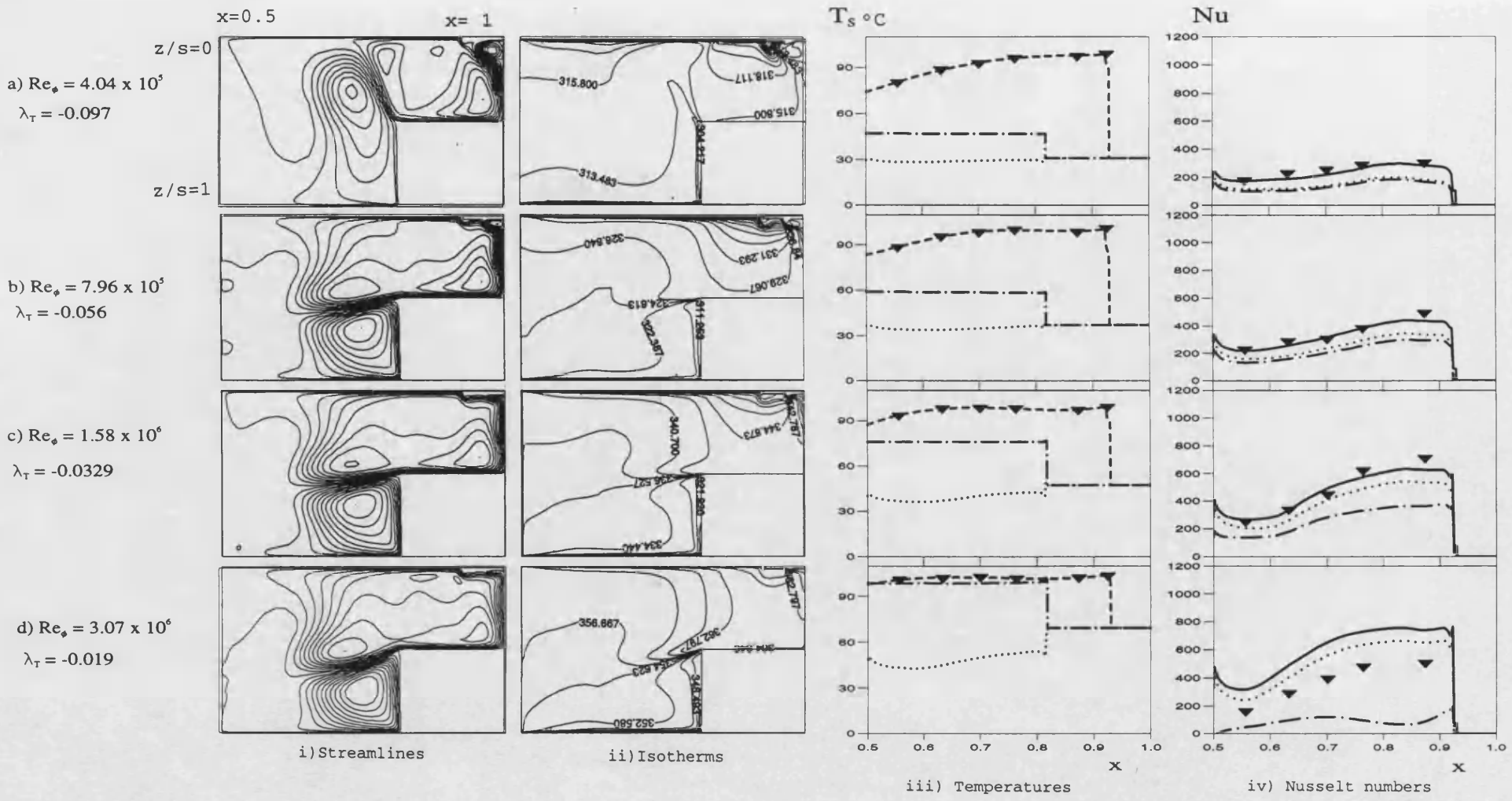

Figure 7.27. Comparison between computed and measured temperatures and Nusselt numbers for rotating cavity with stepped-shroud: $\Gamma \to \infty$ and C_w = -3000

▼ Measured temperatures and Nusselt numbers on the heated disc — — — Fitted temperature on the heated disc

{ Computed temperature on the unheated disc; Computed Nusselt numbers on the heated disc } for { —·—·— adiabatic-disc assumption ····· conducting-disc assumption }

——— Computed Nusselt numbers on the heated disc: conducting-disc assumption with radiation correction

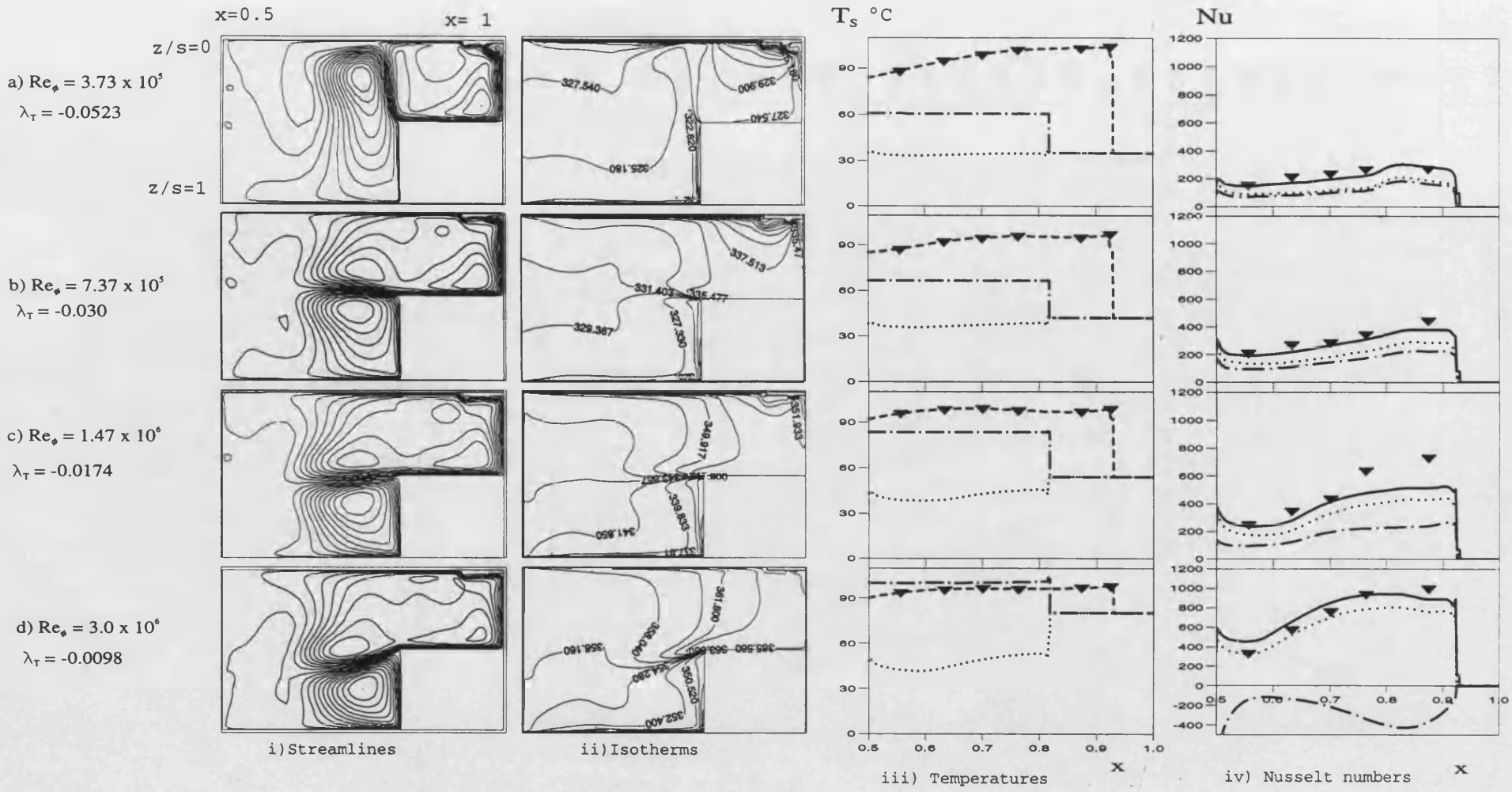

Figure 7.28. Comparison between computed and measured temperatures and Nusselt numbers for rotating cavity with stepped-shroud: $\Gamma \to \infty$ and $C_w = -1500$

▼ Measured temperatures and Nusselt numbers on the heated disc — — — Fitted temperature on the heated disc

{ Computed temperature on the unheated disc; Computed Nusselt numbers on the heated disc } for { —·— adiabatic-disc assumption ····· conducting-disc assumption }

——— Computed Nusselt numbers on the heated disc: conducting-disc assumption with radiation correction

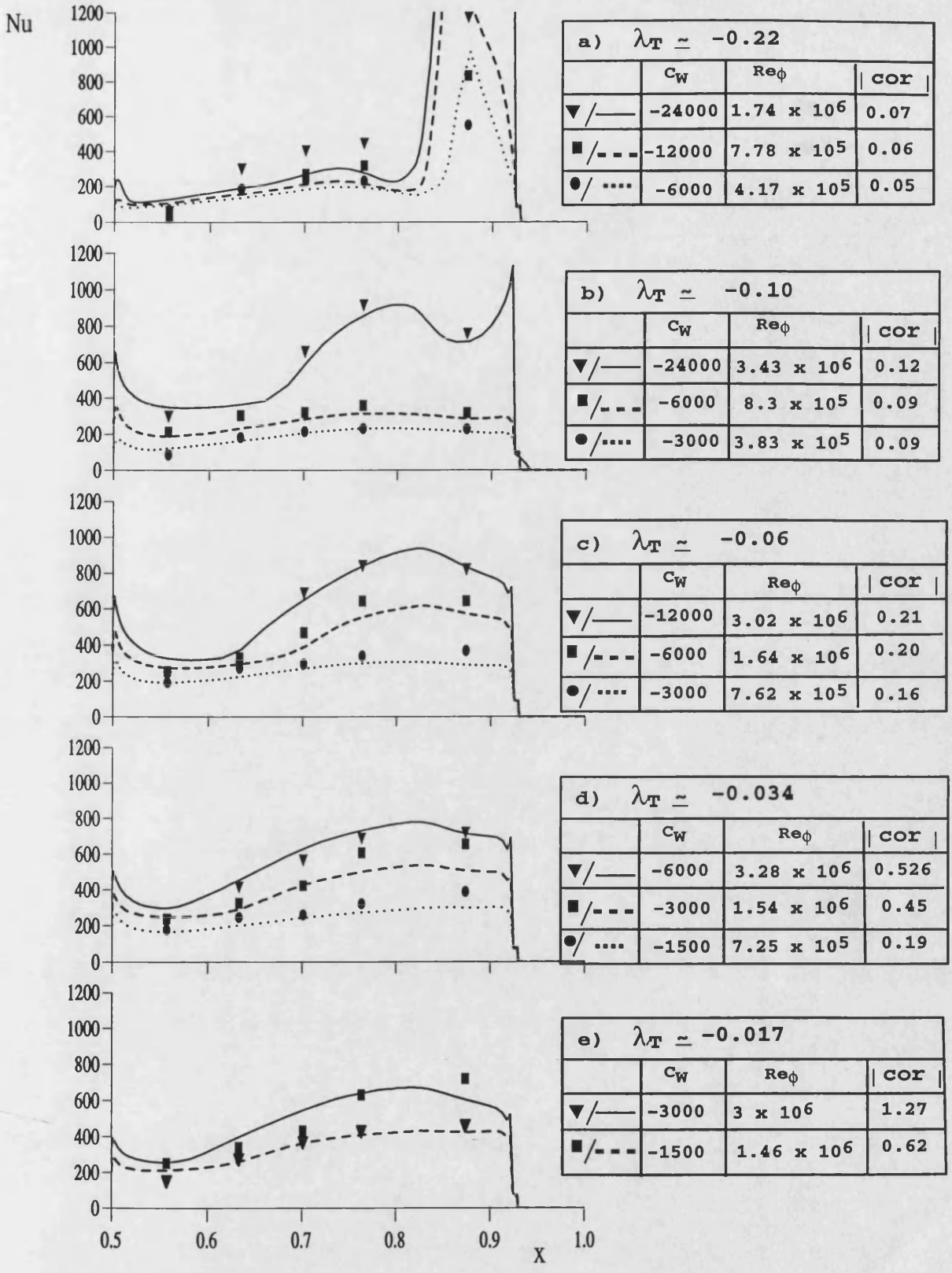

a) $\lambda_T \simeq -0.22$

	C_W	Re_ϕ	cor
▼/——	-24000	1.74 x 10^6	0.07
■/- - -	-12000	7.78 x 10^5	0.06
●/ ····	-6000	4.17 x 10^5	0.05

b) $\lambda_T \simeq -0.10$

	C_W	Re_ϕ	cor
▼/——	-24000	3.43 x 10^6	0.12
■/- - -	-6000	8.3 x 10^5	0.09
●/····	-3000	3.83 x 10^5	0.09

c) $\lambda_T \simeq -0.06$

	C_W	Re_ϕ	cor
▼/——	-12000	3.02 x 10^6	0.21
■/- - -	-6000	1.64 x 10^6	0.20
●/ ····	-3000	7.62 x 10^5	0.16

d) $\lambda_T \simeq -0.034$

	C_W	Re_ϕ	cor
▼/——	-6000	3.28 x 10^6	0.526
■/- - -	-3000	1.54 x 10^6	0.45
●/ ····	-1500	7.25 x 10^5	0.19

e) $\lambda_T \simeq -0.017$

	C_W	Re_ϕ	cor
▼/——	-3000	3 x 10^6	1.27
■/- - -	-1500	1.46 x 10^6	0.62

Figure 7.29. Effect of C_w, Re_ϕ and λ_T on computed and measured Nusselt numbers for stepped-shroud: $\Gamma = 1$.
(symbols represent measured values; lines represent computed values)

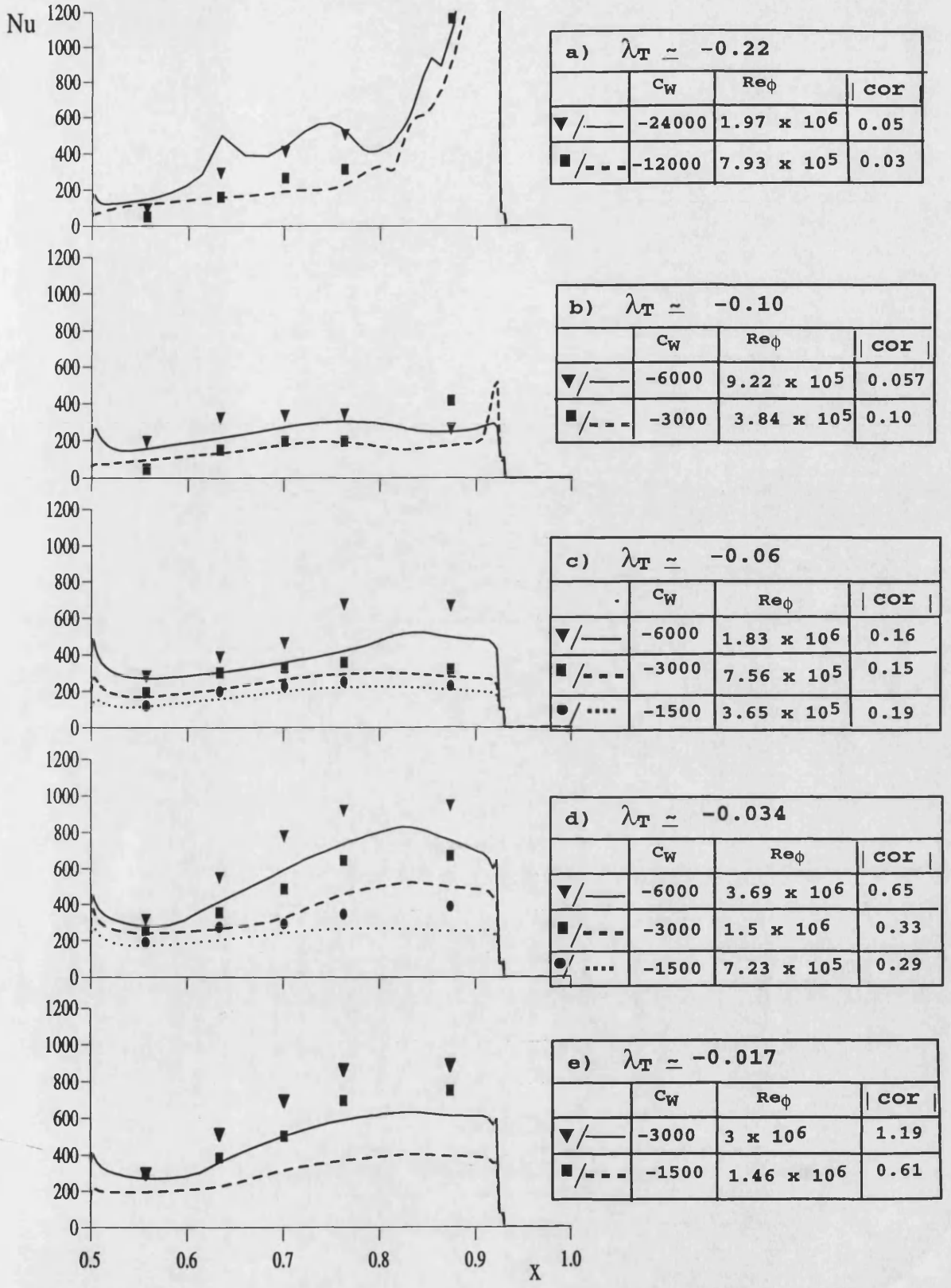

Figure 7.30. **Effect of C_w, Re_ϕ and λ_T on computed and measured Nusselt numbers for stepped-shroud: $\Gamma = 0$**

(symbols represent measured values; lines represent computed values)

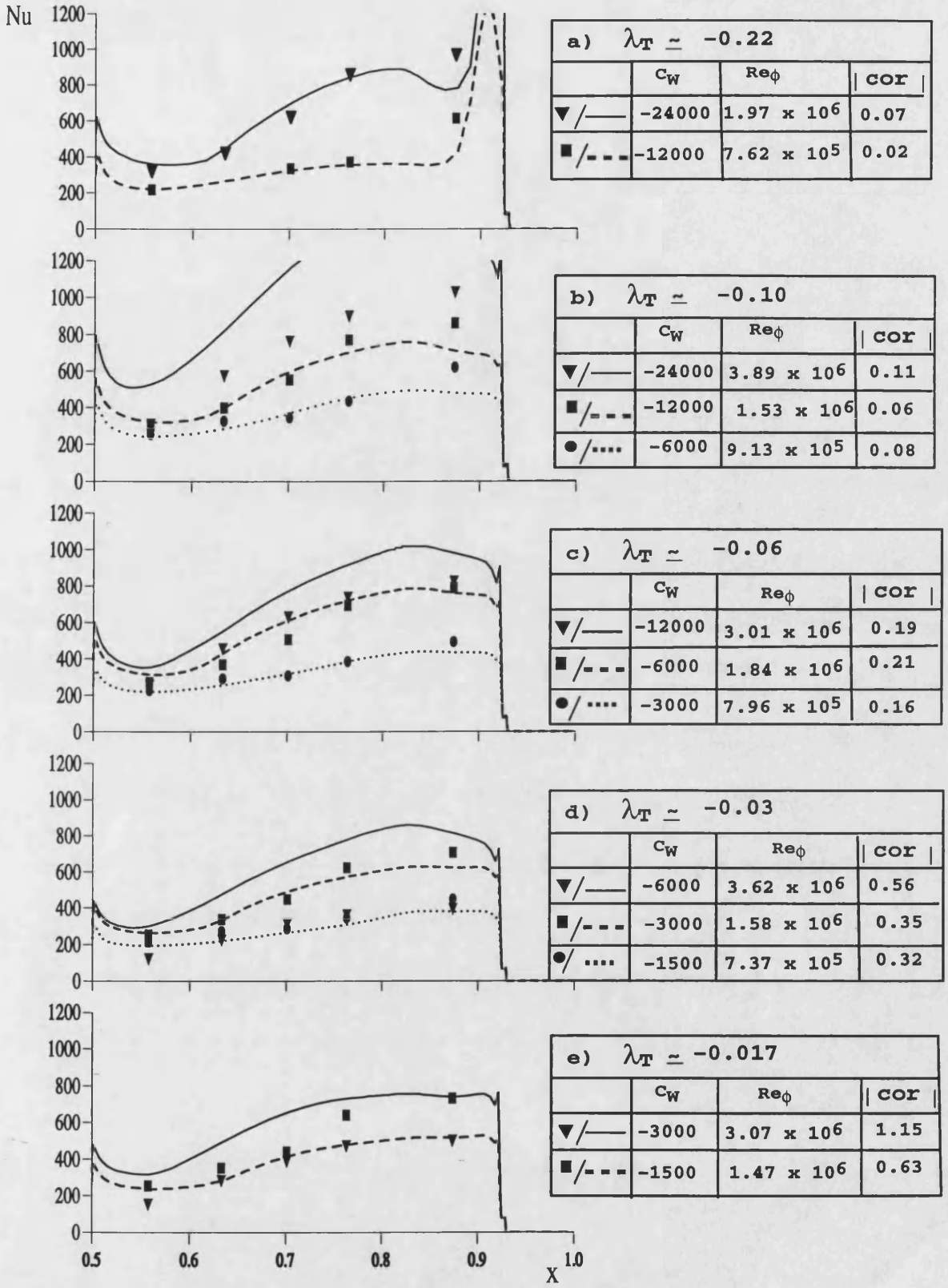

Figure 7.31. Effect of C_w, Re_ϕ and λ_T on computed and measured Nusselt numbers for stepped-shroud: $\Gamma \to \infty$
(symbols represent measured values; lines represent computed values)